Title

On Thermal Characterization of Breeder Pebble Beds with Microscale Numerical Modeling of Thermofluid and Pebble-pebble Interactions

Author

Van Lew, Jon Thomas

Publication Date

2016

Peer reviewed|Thesis/dissertation

University of California
Los Angeles

On Thermal Characterization of Breeder Pebble Beds with Microscale Numerical Modeling of Thermofluid and Pebble-pebble Interactions

A dissertation submitted in partial satisfaction
of the requirements for the degree
Doctor of Philosophy in Mechanical Engineering

by

Jon Thomas Van Lew

2016

Abstract of the Dissertation

On Thermal Characterization of Breeder Pebble Beds with Microscale Numerical Modeling of Thermofluid and Pebble-pebble Interactions

by

Jon Thomas Van Lew

Doctor of Philosophy in Mechanical Engineering

University of California, Los Angeles, 2016

Professor Mohamed A. Abdou, Chair

Lithium ceramic pebble beds are a proposed form for tritium breeding volumes in fusion reactors. In application, the beds will endure high volumetric energy deposition densities but must maintain within relatively-narrow prescribed temperature operating windows for efficient tritium release, while also providing continued transport of high quality heat into coolants for power production. The ceramic pebble beds, as non-cohesive granular material, exist with metastable packing structures defined by the local equilibrium between normal forces and static friction force chains in the assembly. Differential rates of heating and thermal expansion coefficients between ceramic pebble beds and their structural container induce stresses in the bed volume. If sufficiently large, the stresses overcome the local equilibrium of inter-pebble forces and irreversibly compel the pebble bed into a new metastable packing state. Transport of heat from pebble bed to coolant structure is divided between contact conductance between pebbles in the ensemble and convection with a helium purge gas filling the interporous voids. Thus thermal characteristics of pebble beds are intimately linked with its mechanical ones. As a consequence, predictive models of solid breeder heat transfer characteristics must contend with both flowing interporous fluid as well as transitory packing structures and the changing modes of heat transfer they present. To provide such predictive modeling, microscale numerical models were developed allowing investigation of thermal transport in pebble beds operating in environmental conditions relevant to planned

fusion reactors. Specific effort was made to apply the predictive models toward simulating pebble bed thermomechanical responses to the fault condition of crushed individual pebbles.

In this work, the thermal discrete element method (DEM) has been used to model forces and heat transfer between individual pebbles in assemblies. Pebble interaction with slow-moving, interstitial helium purge gas is accomplished by means of two coupling approaches. First, the fluid is considered with a volume-averaged computational fluid dynamic (CFD) method. Volume-averaged models of helium are computationally efficient and provide an overall view of helium influence on heat transfer in solid breeder pebble beds. Second, the lattice-Boltzmann method (LBM) is employed to gain insight into complete fluid flow patterns and conjugate heat transfer. The lattice-Boltzmann method is well-suited to modeling complex porous structures (such as packed beds) due to its inherent parallelizability and simple application of solid-fluid interface boundary conditions on structured grids.

Several open-source codes have been used as platforms for launching the numerical experiments. The codes provided basic numerical frameworks for, *e.g.* time integration, particle tracking, mesh decomposition, and streaming/colliding operators. However to apply the numeric codes on the unique environment of fusion pebble beds, the following contributions to the code were necessarily developed: stochastic numerical implementation of 'apparent' elastic moduli distributions; model of surface roughness effects for heat transfer contact conductance; a mass- and energy-conserving pebble fragmentation algorithm; implementation of the Jeffreson correction to the inter-phase exchange coefficient for moderate-to-high Biot number conditions. The models were validated against experiments measuring effective thermal conductivity of pebble beds with a stagnant interstitial gas. The DEM and CFD-DEM models first agreed well with experiments of lithium ceramic pebble beds in both vacuum and stagnant helium; simulation results of beds with helium match very well with experimental data. The predictive capability of the models were then demonstrated with validation against a broad range of non-fusion-type packed bed experimental data as well as the commonly-applied SZB correlation. The predictive models developed in this thesis were used to address several of the most pressing thermomechanical issues for solid breeder ceramic pebble beds: fragmentation of Li_2TiO_3 or Li_4SiO_4 pebbles and gap formation between

pebble beds and structural materials.

In ITER-like representative volumes, mass re-distribution in pebble beds due to fragmentation was shown to induce subtle changes to local packing fractions yet have the ability to result in macroscopically consequential changes to temperature distributions with volumetric heating. Pebble fragmentation had the largest impact when fragments were significantly smaller than the original pebble (fragments 1/125 the volume of the original) and a comparably large number of pebbles were crushed, 5%. In this case, maximum pebble bed temperatures increased approximately 20% compared to the well-packed bed with a nuclear heating rate of $8\,\mathrm{MW\,m^{-3}}$. Yet when pebbles broke into larger fragments and the amount of broken pebbles was less extensive, the thermomechanical response of pebble beds was significantly more tame; less than 5% increases in maximum bed temperatures were seen in all pebble beds considered when only 1% of the pebbles fragmented.

From the same parametric range of ITER representative pebble bed configurations, the models predict that horizontal-style configurations of breeder zones, such as in the EU HCPB design for ITER, produced *no gap* between the upper layer of pebbles and coolant surface even up to 5% of all pebbles fragmenting during operation. In fact, the configuration's orientation relative to gravity resulted in slight broadening of temperature profiles, and even slightly lower peak-to-average temperatures than vertical-style configurations, as packing structures evolved due to fragmentation. Interstitial helium was seen to accommodate much of the loss of contact conductance on overall thermal transport in packed beds, in spite of the possibility of gap formation. The role of flowing helium purge gas has been considered for the first time by the models of fusion pebble beds developed for this thesis, and its impact on thermal transport was given some careful attention in an LBM-based model.

From LBM results, the laminar nature of low-Reynolds flow in packed beds implies conduction is the dominant mode of heat transfer through the packed bed. The maximum difference between temperature profiles predicted with CFD-DEM and LBM-DEM models was only 6%, the difference arising entirely from the pure conduction model (volume-averaged CFD-DEM) versus the consideration of fluctuation terms (LBM) adding to a transverse thermal dispersion on effective conductivity. For a design which will have such low-Re flow,

CFD-DEM simulations were run in considerably less time than the full models of LBM-DEM (hours compared to days) and the error from neglecting thermal dispersion may be acceptable. Nevertheless, the small differences between LBM and CFD-DEM results arose due to increases in transverse dispersive conductivity of the fluid which itself suggest larger Reynolds or higher packing fraction pebble beds may increase transverse dispersion and thereby the ability to handle higher heat deposition due to increased effective conductivity. The LBM model of fluid and solid interaction should be used for future studies of this topic.

The dissertation of Jon Thomas Van Lew is approved.

Jaime Marian

Nasr Ghoniem

Pirouz Kavehpour

Alice Ying

Mohamed A. Abdou, Committee Chair

University of California, Los Angeles

2016

To my parents, for nurturing curiosity, confidence, and skepticism.

JVL

Table of Contents

List of Figures

List of Tables

Vita

2005 B.S., Mechanical Engineering, Cum Laude
University of Arizona
Tucson, AZ

2006 Mechanical Design Engineer
US Monolithics
Chandler, AZ

2010 M.S., Mechanical Engineering
University of Arizona
Tucson, AZ

2010 Liu, H., Li, P., & Van Lew, J. T., CFD Study On Flow Distribution Uniformity In Fuel Distributors Having Multiple Structural Bifurcations Of Flow Channels. International Journal of Hydrogen Energy, 35(17), 9186–9198.

2011 Van Lew, J. T., Li, P., Chan, C., Karaki, W., & Stephens, J., Analysis Of Heat Storage And Delivery Of A Thermocline Tank Having Solid Filler Material. Journal of Solar Energy Engineering, 133(2), 021003.

2011 Li, P., Van Lew, J. T., Karaki, W., Chan, C., Stephens, J., & Wang, Q., Generalized Charts Of Energy Storage Effectiveness For Thermocline Heat Storage Tank Design And Calibration. Solar Energy, 85(9), 2130–2143.

2012 Li, P., Van Lew, J. T., Chan, C., Karaki, W., Stephens, J., & O'Brien, J. E., Similarity And Generalized Analysis Of Efficiencies Of Thermal Energy Storage Systems. Renewable Energy, 39(1), 388–402.

2012 Liu, H., Li, P., Van Lew, J. T., & Juarez-Robles, D., Experimental Study Of The Flow Distribution Uniformity In Flow Distributors Having Novel Flow Channel Bifurcation Structures. Experimental Thermal and Fluid Science, 37, 142–153.

2012 Valmiki, M. M., Karaki, W., Li, P., Van Lew, J. T., Chan, C., & Stephens, J., Experimental Investigation Of Thermal Storage Processes In A Thermocline Tank. Journal of Solar Energy Engineering, 134(4), 041003.

2014 Van Lew, J. T., Ying, A., & Abdou, M. A., A Discrete Element Method Study On The Evolution Of Thermomechanics Of A Pebble Bed Experiencing Pebble Failure. Fusion Engineering and Design, 89(7-8), 1151–1157.

2015 Van Lew, J. T., Park, Y.-H., Ying, A., & Abdou, M., Modifying Young's Modulus In DEM Simulations Based On Distributions Of Experimental Measurements. Fusion Engineering and Design, 98-99, 1893–1897.

2015 Van Lew, J. T., Ying, A., & Abdou, M., Coupling Discrete Element Models Of Ceramic Breeder Pebble Beds To Thermofluid Models Of Helium Purge Gas Using Volume-averaged Navier-Stokes And The Lattice-Boltzmann Method. Fusion Science And Technology, 68(2), 288–294.

2016 Van Lew, J. T., Ying, A., & Abdou, M., Numerical Study On Influences Of Bed Resettling, Breeding Zone Orientation, And Purge Gas On Temperatures In Solid Breeders. Fusion Engineering and Design, 109-111, 539-544

CHAPTER 1

Introduction

Fusion research and development activities are proceeding on the expectation that the D-T reaction,

$$\mathrm{D} + \mathrm{T} \longrightarrow {}^{4}\mathrm{He} + n + 17.6\,\mathrm{MeV} \tag{1.1}$$

will be used for the first generation fusion reactors based on its energetics and attainability. While deuterium can be readily separated from water and is in great abundance on Earth, tritium is radioactive with β^- decay with a half-life of only 12.32 years, rendering it extremely scarce, expensive, and challenging to store and produce. As a consequence, the feasibility of a fusion power reactor hinges on the sustained availability of tritium. Accordingly, fusion reactor designs include a self-sustaining fuel cycle – breeding tritium in blankets surrounding the fusion core. Breeding blankets will generate tritium *in-situ* from interactions of lithium with neutrons originating either from the fusion reaction directly or neutron multiplication reactions. Relevant lithium reactions are

$$n + {}^{7}\mathrm{Li} \longrightarrow n + {}^{4}\mathrm{He} + \mathrm{T} - 2.47\,\mathrm{MeV} \tag{1.2}$$

$$n + {}^{6}\mathrm{Li} \longrightarrow {}^{4}\mathrm{He} + \mathrm{T} + 4.78\,\mathrm{MeV} \tag{1.3}$$

Solid lithium materials are potential candidate forms for tritium generation in fusion power plants. Many different potential solid materials have been studied in the past; including inter-metallic compounds (*e.g.* Li_7Pb_2), lithium oxide (Li_2O), and ternary oxides (*e.g.* Li_4SiO_4, Li_2TiO_3, $LiAlO_2$, Li_2ZrO_3, *etc.*). Solid breeder materials offer a number of potential safety advantages including relatively low tritium mobility and low stored chemical energy.

In the years since the solid breeder concept inception, the fusion community has come to recognize that lithium-based oxides (including ceramic oxides) are the most promising

tritium-breeding materials for fusion reactor solid breeder blankets. This conclusion is based on oxides having many desirable characteristics, such as:

- high Li density
- high melting temperature
- good tritium release (sufficiently high T release rates, low solubility, and open porosity for purging T)
- good thermophysical and thermomechanical characteristics
- ability to withstand the rigors of long-term irradiation at high temperature and under large temperature gradients
- desirable neutronics and irradiation characteristics (no bad transmutation nuclides)
- chemical stability & compatibility with structural material at operating temperatures (in particular thermal stability and chemical inertness are attractive from a safety point of view)

Calculations of other candidate materials indicate that inter-metallic compounds have unacceptable operating temperatures (exceedingly narrow temperature windows) and are unattractive for in-situ tritium recovery. In addition, the compounds of Li_7Pb_2 and $Li_{62}Pb_{38}$ were shown to vigorously react with water and do not offer significant safety advantages compared to liquid breeders.[2,40] And a major emphasis of blanket/breeder design is placed on safety and environmental acceptability, with primary goals of low tritium inventory in the blanket and minimal long-lived activation products. Therefore this research is focused entirely on discussion of lithium ceramics and modeling thereof.

Reference solid breeder engineering designs have converged toward liquid-cooled pebble beds of lithium ceramics. Pebble bed designs incorporate packed ceramic pebbles (spherical particles) that are filled into containment structures of a reduced-activation ferritic steel. In a typical solid breeder module, the breeding volume is subdivided into several alternating

layers of neutron multiplication material (generally beryllium) and tritium breeding material. The layers are separated by plates with internal channels for flowing liquid coolant. Coolants are typically a high pressure helium, though some designs call for pressurized water, in spite of the dangers of the highly exothermic reaction of lithium with oxygen from water vapor in the case of coolant leak. The coolant, heated as it passes through tritium breeding modules, proceeds into a standard electricity production cycle. After tritium is generated inside the ceramic, the bred hydrogen isotope is ultimately picked up by a low-pressure, slow-moving purge gas (primarily helium) and extracted in a closed loop for fuel.

Pebble bed forms of tritium breeding volumes have several advantages which include: ease of assembly of granular materials into complex geometries; bred tritium can be readily removed *via* the helium purge gas through interstitial porous networks; ceramic material is unaffected by the large magnetic fields confining the plasma, and temperature gradients across any single pebble are small enough to avoid damage from thermal stress. A sketch of a generic ceramic pebble bed volume depicting all the features described above is given in Figure 1.1.[135]

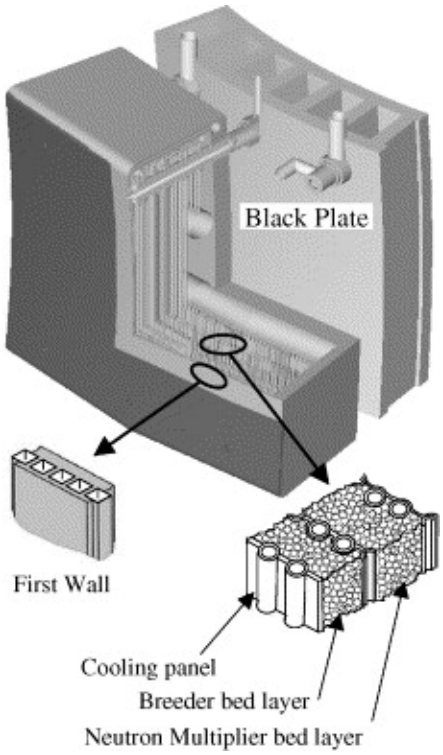

Figure 1.1: Example sketch of a typical solid breeder design (from a Japanese ITER concept sketch given in Ref.[135]). Showing: the first wall upon which a large heat flux from plasma radiation will be deposited, layered solid breeder and neutron multiplier beds, separated by a cooling panel structure with internally flowing coolant.

1.1 Solid Breeder Thermal Management and Imposed Temperature Window

The feasibility of the solid breeder concept is based on the capability of tritium to readily transport from the solid ceramic into the purge gas. Tritium release, itself, is a function of grain size, microsctructure, and open/closed porosity. To understand the capability of tritium removal, five mechanistic steps are identified for bred tritium to be recovered (visualized in Figure 1.2). The steps follow as[40]

1. bulk diffusion,

2. grain boundary migration,

3. desorption of tritium (T_2O),

4. percolation of tritium through pores internal to the solid ceramic toward the flowing purge gas,

5. convective mass transfer out of the blanket via purge channels.

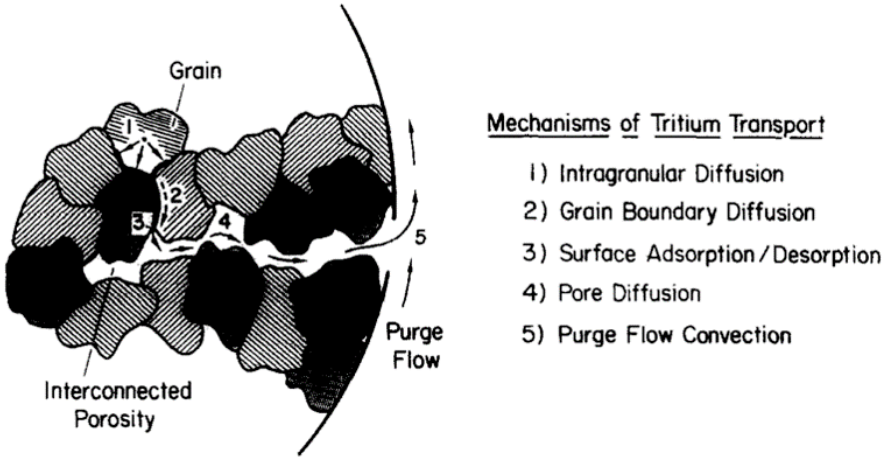

Figure 1.2: Mechanistic steps of tritium transport through ceramic materials into the purge gas for removal. Image reproduced from Ref.[147]

Bulk diffusion of tritium is considered to be a significant contributor to tritium inventory. For spherical particles of radius r_p, assuming zero surface concentration, the tritium inventory T is given by

$$T = \frac{1}{15}\dot{T}\frac{r_p^2}{D} \tag{1.4}$$

where $\dot{T}$ is the tritium generation rate and D is diffusivity of tritium in the ceramic. It is significant to note that the tritium inventory is a function of the square of the particle size. Thus it is clear that: (i) small grain sizes are required for minimum tritium inventory and (ii) grains should not significantly grow during the lifetime of a reactor blanket. Diffusivity values of tritium in ceramics are extremely scarce and with much uncertainty. Kinetic experiments of post-irradiation tritium release from several candidate breeders have been performed. The kinetics in the experiments are non-steady-state and the diffusivity is given by

$$D = 0.16\frac{r_p^2}{\tau} \tag{1.5}$$

where τ is the mean residence time, defined as the time required to extract 87.4% of the tritium. Combining Equation (1.4) and Equation (1.5) eliminates diffusivity and radius (with large variation between particles and grains), yielding:

$$T = 0.42\dot{T}\tau \tag{1.6}$$

We can then estimate the diffusive inventory in a blanket based on the readily-measured residence time, τ. It must be kept in mind that the particular micro-structure of the ceramics measured in kinetic experiments must correspond to the micro-structure of the material in the blanket in order for the diffusivity predictions to hold. In other words, residence times of 1 mm Li_2TiO_3 with average grain sizes of $\mu = 1\,\mu m$ are utterly inappropriate to calculate tritium diffusion in 0.5 mm pebbles of Li_4SiO_4 with average grain sizes of $\mu = 5\,\mu m$, for example.

The tritium generation rate, $\dot{T}$ is a function of the fusion reactor power output and blanket design. Residence times have been measured to be temperature dependent which is consistent with diffusion-controlled processes. Therefore, based on the present model, the range of operating limitations are defined on the low end where bulk diffusion is the rate-limiting step. A minimum temperature is defined as the temperature at which the tritium inventory exceeds $1\,kg\,GW^{-1}$. The minimum temperatures for many candidate materials are shown (with slight variation between sources) in Figure 1.3. Minimum temperatures generally range from 300 up to 400 °C.

As we saw from Equation (1.4), tritium inventory goes with the square of grain size and thus another operating limit on temperature arises. An upper limit of temperature is based on restructuring or grain growth in ceramics which can greatly affect the diffusive inventories. When ceramic materials are heated above their sintering temperature, generally in excess of $0.8T_{melt}$ (in absolute temperature), grains will grow.

Moreover, when lithium depletion (or lithium burn-up) occurs to a significant extent (around 5%), the resultant nonstoichiometry in ternary oxides could establish, rather than single-phase conditions. For example, under irradiation and lithium burn-up, Li_4SiO_4 ceramics would develop an excess of silica and the melting point of 1300 °C would drop to a eutectic

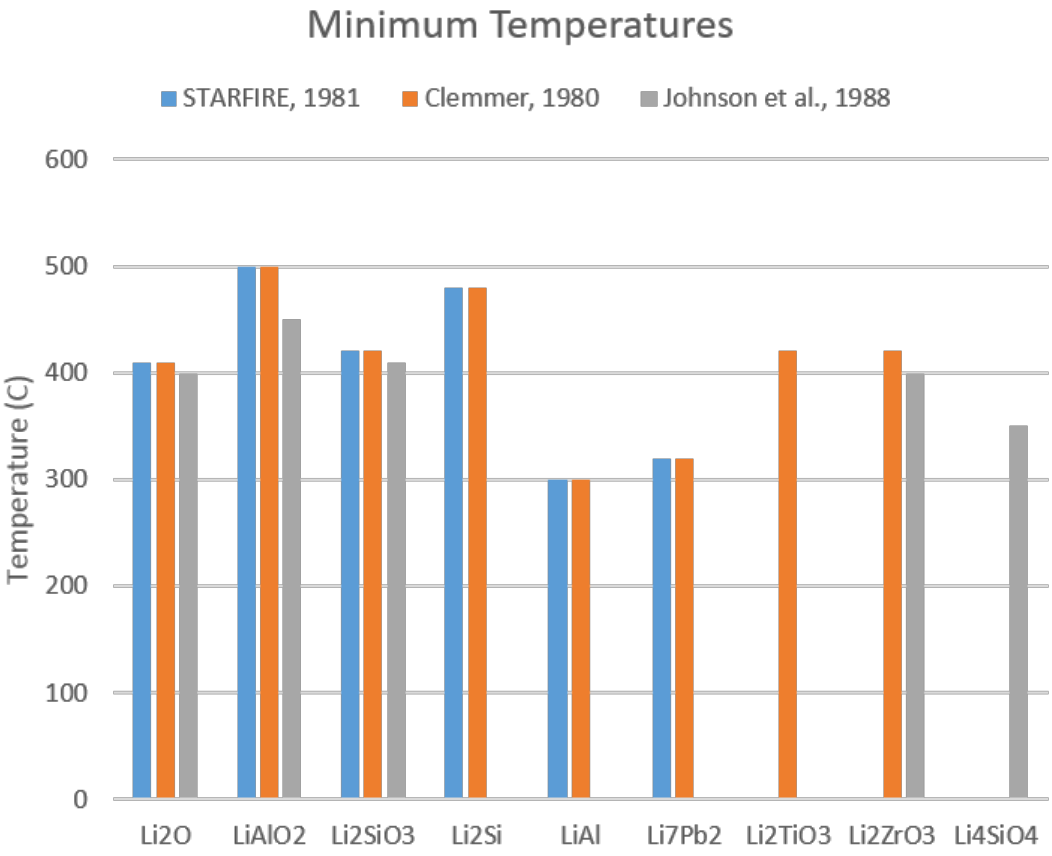

Figure 1.3: Minimum temperatures for various candidate materials (compiled from various sources) based on rate-limiting diffusion processes. STARFIRE data from Ref.,[103] Clemmer from Ref.,[40] Johnson *et al.* from Ref.[104]

temperature of 1024 °C. Such a reduction in melt temperature would have significant impact on sintering and tritium inventory in the solid breeders.[103] Therefore, neutron radiation influences are generally expected to lower the maximum operational temperature to $0.6T_{\text{melt}}$.[103] Candidate materials are compared in Figure 1.4. In general, acceptable candidate materials have their maximum temperature between 750 and 900 °C.

As a consequence of the tritium inventory of solid breeder material, we are faced with a relatively narrow operational temperature to which solid breeder designers must adhere, roughly between 350 and 800 °C. Thus to provide designers the ability to optimize breeder volumes for tritium breeding and subsequent tritium release, we must understand the important physics and phenomena dictating thermophysical properties and thermomechanical

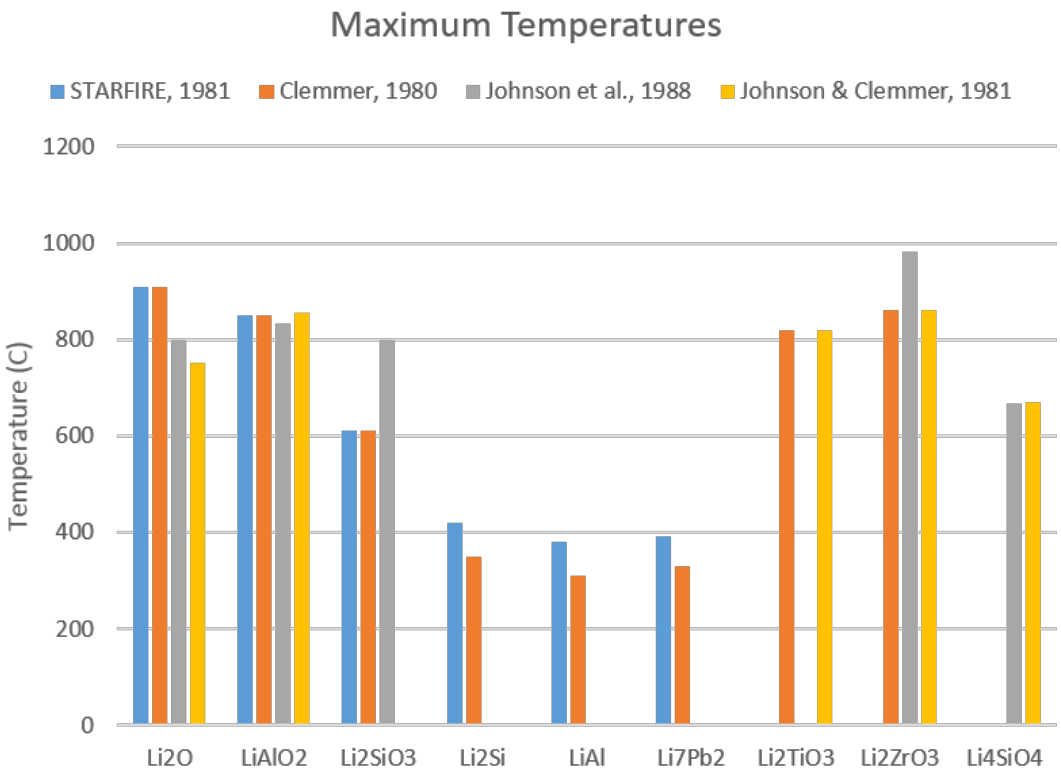

Figure 1.4: Maximum temperatures for various candidate materials (compiled from various sources) based on irradiated sintering temperatures ($0.6T_{\text{melt}}$). STARFIRE data from Ref.,[103] Clemmer from Ref.,[40] Johnson *et al.* from Ref.[104]

responses of pebble beds during operation in a fusion reactor.

Tritium breeding blankets will experience high volumetric heating as deposited by high-energy neutrons that are carrying away approximately 80% of the fusion reaction energy in addition to heating from secondary γ rays. Heat deposited in breeders must be transported through pebble bed regions into the walls of containing structures, then ultimately into the coolant gas. Heat deposited into pebble beds will transfer *via* inter-particle contact conduction, inter-particle radiation, and convection with the helium purge gas. At the interface with the structural material, similar modes of heat transfer are present: particle-wall contact conduction, particle-wall radiation, and communication *via* helium purge gas convection.

There exists a coupling between mechanical forces acting upon beds and their heat trans-

port capabilities, thus we must understand packing structures in order to understand heat transfer. The structure of packed beds can be considered as a metastable configuration that will last indefinitely unless acted upon by an external perturbation such as vibration or compressive pressure.[101] The ability of a metastable configuration to resist perturbations can, in some way, be quantified by the initial packing fraction. For more compliant beds (lower packing fractions), stresses from thermal expansion can cause significant rearrangement of the packing structure which is not recoverable after stress removal. This phenomena has been observed in numerous experiments as so-called plastic rearrangement of pebble beds.[150,151,206] Plasticity of beds may have significant consequences for the ability of the pebble bed to maintain contact with the containing structure and routes for heat out of the bed due to gap formation between pebble volumes and coolant walls.

Moreover, as pebbles heat under nuclear loads, thermal expansion of pebbles in the packed volume will be contained by cooler structural material. Confined expansion will give rise to increased contact pressure between pebbles. Increased pressure between pebbles can cause, among other effects, brittle pebbles to fragment. Therefore, some amount of restructuring of pebble beds (and internal contact force networks) are also likely to occur from crushing/cracking of individual pebbles, or the effects of inter-pebble sintering and creep arising from the high-temperature, high-stress environment in a solid breeder unit. Contact conduction in beds, intimately linked to the packing structure, will be impacted during operation of ceramic pebble beds in fusion reactors.

Because tritium inventory requirements impose a relatively narrow operational temperature window on lithium ceramic pebble beds, and given the high power densities in fusion power reactors, it is necessary to have accurate knowledge of ceramic pebble bed thermo-mechanical behavior and comprehensive characterization; reliable models of heat transfer in solid breeders are critical for solid breeder designs. In addition, due to the complicated nature of granular materials, heat transfer in these solid breeder volumes remains transient during fusion operation. Concurrently, interaction of the slow-moving purge gas with tightly packed pebble beds is an additional route of heat transfer that must be understood. Thus, heat transfer in pebble beds is quite different from standard solid materials and requires

specialized modeling of the synergistic physics. Knowledge and characterization of thermal transport must anticipate changes to the heat transfer capabilities and predict temperature profiles for pebble bed packing structures that will emerge after initially-packed pebble beds react to prolonged exposure to fusion reactor environments.

1.2 Objectives of this Study

The goal of this work is to develop more comprehensive and accurate models for predicting temperature distributions in ceramic breeder pebble beds, accounting for many important phenomena including pebble crushing and fragmentation, dynamic analysis of packing restructuring, and considerations of slow moving inter-porous helium purge gas.

Modeling will be done with discrete element method (DEM) models coupled to computational fluid dynamics (CFD) and lattice-Boltzmann method (LBM) descriptions of fluid flow. In particular detailed relationships between topological changes to packing structures, arising from fragmented pebbles, and the resulting changes to heat transfer in packed beds will be considered. For the first time, attention will be given to nuclear heating of pebble fragments as they redistribute through pebble beds and come to rest without strong mechanical contact (and therefore contact conductance) to neighboring pebbles. This includes analyzing changes to temperature distributions in pebble beds with different models of pebble damage, analyzing the impact of helium flow on temperatures in beds with fragmented pebbles, and changes to bed stresses and contact forces in beds with restructured packing. Furthermore, changes to effective thermal conductivity in packed beds with simulated reduction in solid conductivity due to irradiation damage of ceramic pebbles will be considered.

While it is the aim of this study to provide fusion blanket designers with the most complete models possible for predictive capabilities of temperature distributions in solid breeders such that operability margins to tolerate irradiation damage or crushed pebbles may be expanded, it is understood that the models developed here will not, on their own, provide a total description of physics governing heat transfer in solid breeder pebble beds during operation. As will be pointed out later in this thesis, effects of radiation, fluid slip,

sintering, and creep are all phenomena that can play a role in pebble bed heat transfer but are beyond the scope of the current work. Therefore, it is also the goal of this thesis to develop modeling tools in a modular method on well-supported, open-source frameworks which will facilitate adoption of this code and permit future expansion to conjoin with modules describing other physics. In this way, the code developed for thesis can be adopted by the community at large and expanded upon in future research.

CHAPTER 2

Literature Review

Ceramic pebble beds in solid breeders can be seen as belonging to a larger class of generalized granular material, and specifically dry granular material. Granular materials can be described as an aggregation of discrete, macroscopic particles (mean size greater than 100 µm) that are characterized with energy dissipation during interaction.[55] The main outcome of this definition is that granular materials cannot be described by conventional thermal or hydrodynamic variables. Granular materials require their own treatment and modeling for description.

The study of ceramic pebble bed thermomechanics for tritium breeding have their roots connnected to historical treatment of granular material and it is instructive to begin with a short review of this field. Following that, many generalized studies of heat and momentum transfer, specifically correlations that have been developed in the classical continuum treatment of pebble beds are presented. The correlations will not only be instructive by view of their limitations, but they will help inform the numerical modeling of coupling fluid and pebble bed conservation equations. Finally, the literature review will focus specifically on the progress that has been made in temperature predictions from numerical models of tritium breeders for fusion reactors.

2.1 Brief History of Granular Material Research

The science and modeling of granular materials has a long and rich history. Coulomb proposed ideas of static friction in 1773, Faraday in 1831 discovered the convective movement of powders, and even Reynolds in 1885 introduced notions on granular expansion and shear.[100]

Granular materials are only second to water in terms of most-used industrial material. Granular materials play in important role in civil, geotechnical, chemical, and mechanical engineering in industries as diverse as pharmacy, automative, agriculture, and construction to name just a few.[55,91] A resurgence of interest in granular materials has also happened in the fields of applied mathematics and physics as metaphors for other dynamical systems.[100] Yet despite the diverse fields interested in granular materials, descriptions of granular material with classic continuum mechanics is still far from complete; quite different from the conclusively described constitutive equations of elastic theory, hydrodynamics, and gas dynamics that have existed for two centuries.[161]

Even if we restrict our consideration to static packings of non-cohesive granular materials (neglecting the complex, unusual granular hydro- and gas dynamics), modeling is complicated by the heterogeneity (and indeterminancy) of contact forces running through the packed grains and the packing structure of the grains. The granular medium introduces complexity to modeling, in part, due to its significant difference between compression and tension experiments; under compression the granular medium behaves as if an elastic or elasto-plastic body but offers no resistance to tension. Furthermore, when an external excitation, such as vibration, is introduced into the metastable packing state of a granular system, the packing is unlocked to slowly travel through packing phase space at a logarithmically slow pace.[17,109]

Nonetheless, many material models have been developed in an attempt to describe the mechanics of a granular system as a fictitious continuum with varying success and applicability. Researchers in geophysics have long viewed granular materials as continuous materials for which they painstakingly developed equations as if the granular material obeyed laws of classical mechanics.[54,55,91] Heat transfer in granular materials has also been treated in a continuum manner and the correlations will be covered in explicit detail in § 2.2.

Granular systems became important to fusion power reactors after the introduction of ceramic pebble beds in solid breeders for fusion reactors. Because of the large size scale and complex interactive physics of solid breeders, it is desirable to employ the continuum-based models of packed beds of ceramics with effective thermomechanical properties derived from

experiments on granular beds. In § 2.4, the status and success of early continuum-based models will be discussed in more detail.

In 1979, Cundall & Strack opened a new avenue for studying granular materials when they introduced the distinct element method (later renamed by the community as the *discrete* element method).[42] Since then, grain-scale descriptions of granular systems have taken prominence for their ability to enrich the macrosopic models when they are insufficient to describe the rheology of a granular material. In the approach of Cundall & Strack, all of the individual grains in a system are described as rigid elements for which the equations of motion can each be simultaneously integrated based on the (typically localized) interacting forces.

2.2 General Studies of Heat Transfer in Granular Material

For packed beds of ceramic spheres filled into tritium breeding modules, we identify the following modes of simultaneous heat transfer:

1. Inter-granular conduction
    - Conduction through the contact area between contacting particles.
    - Conduction through the contact area between particles in contact with structural walls.
2. Granular-fluid interaction
    - Conduction through the stagnant fluid between near, non-contacting particles.
    - Conduction through the stagnant fluid between contacting particles.
    - Smoluchowski effect of non-Knudsen fluid conduction in near-granular regions.
    - Advection of energy by the fluid to contacting- and downstream particles.
3. Radiation effects
    - Radiation between the surfaces of contacting particles.

- Radiation between the surfaces of particles through adjacent voids.
- Heat generation internally in the particle from incident neutron fluxes.

Historically, granular materials are treated as a fictitious continuous media for which effective properties or correlations are derived. In this section. The volume of a pebble in a tritium breeder is on the scale of $10 \times 10^{-9}\,\mathrm{m}^3$ while the typical container volume can be on the order of $10 \times 10^{-2}\,\mathrm{m}^3$.[35] Thus a single breeder volume will house upwards of $N = 10 \times 10^7$ pebbles. Statistically then, it is reasonable to assume that a ceramic pebble bed can be treated as a fictitious granular material for which continuum theory is applicable. This assumption is the basis of many correlations for heat transfer in granular material. The continuum assumption also underpins application of finite element method (FEM) models for breeder pebble beds; constitutive equations are developed from experimental measurements of the macroscopic behavior of pebble beds which are fed into FEM models. In the following sections, historical correlations for heat transfer in packed beds as continua are reviewed.

2.2.1 Effective Thermal Conductivity of Granular Media

Deissler and Boegli, in 1958, proposed upper and lower bounds of effective thermal conductivity, k_{eff}, in two-phase granular media to be given by alternating layers of the two phases arranged in parallel or series, respectively.[45] In the case of parallel layers, effective conductivity, normalized by fluid conductivity, is

$$\frac{k_e}{k_f} = \epsilon + (1-\epsilon)\kappa \tag{2.1}$$

where k_f is the fluid conductivity, $\kappa = k_s/k_f$ is the ratio of solid to fluid conductivity, and ϵ is the void fraction in the porous media. Similarly, the minimum effective conductivity is found in a serial layering of the solid and fluid phases,

$$\frac{k_e}{k_f} = \frac{1}{\epsilon + (1-\epsilon)/\kappa} \tag{2.2}$$

Equations (2.1) and (2.2) act as theoretical upper and lower limits to true effective thermal conductivities of real material.

One of the most widely-used correlations was put forth by Zehner and Schlunder in 1970.[204,205] They considered a cylindrically-shaped unit cell and made the analogy between heat and mass transfer to derive an empirical fit to data in the bulk of two-phase porous media. The Zehner-Schlunder (ZS) correlation is

$$\frac{k_e}{k_f} = \left(1 - \sqrt{1-\epsilon}\right) + \frac{2\sqrt{1-\epsilon}}{1-B/\kappa}\left[\frac{(1-1/\kappa)B}{(1-B/\kappa)^2}\ln\left(\frac{\kappa}{B}\right) - \frac{B+1}{2} - \frac{B-1}{1-B/\kappa}\right] \tag{2.3}$$

where B is a deformation parameter related to porosity as

$$B = 1.25\left(\frac{1-\epsilon}{\epsilon}\right)^{1.11} \tag{2.4}$$

Following the success of the ZS correlation, other researchers considered the specialized cases of high thermal conductivity ratio $\kappa \geq 10^3$ when loads on the grains in the bed (due to either an external pressure or the grains own weight) resulted in large contact areas. In these cases, ZS correlations under-predicted the actual effective conductivity.[5] An extensive review of correlations for effective thermal conductivity with consideration of contact between grains is provided by van Antwerpen *et al.*[178] Hsu *et al.* considered three lumped parameters models of varying two-dimensional unit cells for which they derived an effective conductivity.[97] The first was for contact square-cylinders. The effective conductivity for this model is

$$\frac{k_e}{k_f} = \gamma_a\gamma_c\kappa + \frac{\gamma_a(1-\gamma_c)}{1+(1/\kappa-1)\gamma_a} + \frac{(1-\gamma_a)}{1+(1/\kappa-1)\gamma_a\gamma_c} \tag{2.5}$$

where Hsu *et al.* used the same fitting parameter of Nozad *et al.*, γ_c;[136] they found best agreement with experimental data when $\gamma_c = 0.01$. The other geometric parameter is related to γ_c and ϵ as

$$0 = \gamma_a^2 + 2\gamma_a\gamma_c(1-\gamma_a) + \epsilon - 1 \tag{2.6}$$

Hsu *et al.*'s second correlation had the square-cylinder unit cell replaced with circular-cylinders. The correlation is given with dependence on conductivity ratios. For $(1/\kappa-1)\gamma_a < 1$,

$$\begin{aligned}\frac{k_e}{k_f} = \gamma_c\gamma_a\kappa + \frac{1-\gamma_a\sqrt{1-\gamma_c^2}}{\gamma_a\gamma_c(1/\kappa-1)+1} + \frac{\kappa(\pi/2-2\theta_c)}{1-\kappa} - \frac{2\kappa}{(1-\kappa)\sqrt{1-(1/\kappa-1)^2\gamma_a^2}} \\ \times\left[\tan^{-1}\left(\frac{\tan(\pi/4-\theta_c/2)+(1/\kappa-1)\gamma_a}{\sqrt{1-(1/\kappa-1)^2\gamma_a^2}}\right) - \tan^{-1}\left(\frac{\tan(\theta_c/2)+(1/\kappa-1)\gamma_a}{\sqrt{1-(1/\kappa-1)^2\gamma_a^2}}\right)\right]\end{aligned} \tag{2.7}$$

For $(1/\kappa - 1)\gamma_a > 1$,

$$\frac{k_e}{k_f} = \gamma_c\gamma_a\kappa + \frac{1-\gamma_a\sqrt{1-\gamma_c^2}}{\gamma_a\gamma_c(1/\kappa-1)+1} + \frac{\kappa(\pi/2-2\theta_c)}{1-\kappa} - \frac{\kappa}{(1-\kappa)\sqrt{(1/\kappa-1)^2\gamma_a^2-1}} \times \left[\ln\left(\frac{\tan(\pi/4-\theta_c/2)+(1/\kappa-1)\gamma_a-\sqrt{(1/\kappa-1)^2\gamma_a^2-1}}{\tan(\pi/4-\theta_c/2)+(1/\kappa-1)\gamma_a+\sqrt{(1/\kappa-1)^2\gamma_a^2-1}}\right) - \ln\left(\frac{\tan(\theta_c/2)+(1/\kappa-1)\gamma_a-\sqrt{(1/\kappa-1)^2\gamma_a^2-1}}{\tan(\theta_c/2)+(1/\kappa-1)\gamma_a+\sqrt{(1/\kappa-1)^2\gamma_a^2-1}}\right)\right] \tag{2.8}$$

and for $(1/\kappa - 1)\gamma_a = 1$

$$\frac{k_e}{k_f} = \frac{\gamma_c\gamma_a^2}{\gamma_a+1} + \frac{1-\gamma_a\sqrt{1-\gamma_c^2}}{\gamma_c+1} + \gamma_a(\pi/2-2\theta_c) - \tan(\pi/4-\theta_c/2) + \tan(\theta_c/2) \tag{2.9}$$

where $\gamma_c = 0.01$ was again found to fit best to experimental data. And the other geometric parameter relationship became

$$0 = 1 - \gamma_a\gamma_c - \frac{\gamma_a^2}{2}\left(\frac{\pi}{2} - 2\theta_c\right) \tag{2.10}$$

where the contact angle is $\theta_c = \sin^{-1}(\gamma_c)$. The last correlation of Hsu *et al.* came from three-dimensional unit cell extension of the square-cylinder to cubes,

$$\frac{k_e}{k_f} = 1 - \gamma_a^2 - 2\gamma_a\gamma_c + 2\gamma_a^2\gamma_c + \gamma_a^2\gamma_c^2\kappa + \frac{\gamma_a^2 - \gamma_a^2\gamma_c^2}{1-\gamma_a+\gamma_a/\kappa} + \frac{2(\gamma_a\gamma_c - \gamma_a^2\gamma_c)}{1-\gamma_a\gamma_c+\gamma_a\gamma_c/\kappa} \tag{2.11}$$

where $\gamma_c = 0.13$ fit best for cubes and the relationship between γ_c, ϵ and γ_a became

$$0 = (1-3\gamma_c^2)\gamma_a^3 + 3\gamma_c^2\gamma_a^2 + \epsilon - 1 \tag{2.12}$$

Hsu *et al.* also proposed a correction to the ZS model for conductivity ratios of $\kappa \geq 10^3$. The assumption built into the ZS model was of a point contact between grains in the bed. Incorporating the effects of finite-sized contact area, Hsu *et al.* corrected the ZS model as

$$\frac{\kappa_e}{\kappa_f} = (1-\sqrt{1-\epsilon}) + \kappa\sqrt{1-\epsilon}\left(1 - \frac{1}{(1+\alpha_0 B)^2}\right) + \frac{2\sqrt{1-\epsilon}}{1-B/\kappa+(1-1/\kappa)\alpha_0 B}\left[\frac{(1-1/\kappa)(1+\alpha_0)B}{(1-B/\kappa+(1-1/\kappa)\alpha_0 B)^2}\ln\left[\frac{1+\alpha_0 B}{(1+\alpha_0)B/\kappa}\right] - \frac{B+1+2\alpha_0 B}{2(1+\alpha_0 B)^2} - \frac{B-1}{(1-B/\kappa+(1-1/\kappa)\alpha_0 B)(1+\alpha_0 B)}\right] \tag{2.13}$$

where B is no longer found from as a simple deformation parameter but is instead related to ϵ and α_0. Hsu *et al.* found best agreement with experimental data when $\alpha_0 = 0.002$ and $\epsilon = 0.42$. B can then be found from the solution of

$$0 = 1 - \frac{B^2}{(1-B)^6(1+\alpha_0 B)^2}\left[(B^2 - 4B + 3) + 2(1+\alpha_0)(1+\alpha_0 B)\ln\left(\frac{(1+\alpha_0)B}{1+\alpha_0 B}\right) + \alpha_0(B-1)(B^2 - 2B - 1)\right]^2 - \epsilon \tag{2.14}$$

Bauer and Schlunder[19] also improved on the earlier model of Zehner and Schlunder to include the additional effects of thermal radiation, gas heat transfer in the Knudsen regime, and finite-sized contact areas. The combined model, often called the Zehner-Schlunder-Bauer (ZSB) model is calculated as

$$\frac{k_e}{k_f} = \left(1 - \sqrt{1-\epsilon}\right)\epsilon\left[(\epsilon - 1 + 1/\kappa_G)^{-1} + \kappa_r\right] + \sqrt{1-\epsilon}\,(\phi\kappa + (1-\phi)k_c) \tag{2.15}$$

where

$$k_c = \frac{2}{N}\left[\frac{B(\kappa + \kappa_r - 1)}{N^2\kappa_G\kappa}\ln\left(\frac{\kappa + \kappa_r}{B(\kappa_G + (1-\kappa_G)(\kappa + \kappa_r))}\right) + \frac{B+1}{2B}\left(\frac{\kappa_r}{\kappa_G} - B\left(1 + \frac{1-\kappa_G}{\kappa_G}\kappa_r\right)\right) - \frac{B-1}{N\kappa_G}\right] \tag{2.16}$$

and

$$N = \frac{1}{\kappa_G}\left(1 + \frac{\kappa_r - B\kappa_G}{\kappa}\right) - B(1 - 1/\kappa_G)(1 + \kappa_r/\kappa) \tag{2.17}$$

and B is given in Equation (2.4). Radiation is incorporated in κ_r parameter, given as

$$\kappa_r = \frac{4\sigma}{2/\epsilon_r - 1}\bar{T}^3\frac{d_p}{k_f} \tag{2.18}$$

where σ is the Stefan-Boltzmann number ($\sigma = 5.67 \times 10^{-8}\,\mathrm{W\,m^{-2}\,K^{-4}}$), ϵ_r is the emissivity of the material in the packing, d_p is the packing diameter (assumed spherical), and $\bar{T}$ is the average, absolute temperature of the system (in K).

Effects due to interstitial gas in the Knudsen regime are defined by the term, κ_G given as

$$\kappa_G = \left[1 + \left(\frac{l}{d_p}\right)\right]^{-1} \tag{2.19}$$

where l is a modified mean free path of gas molecules,

$$l = 2\frac{2-\alpha_T}{\alpha_T}\left(\frac{2\pi\tilde{R}\bar{T}}{M_g}\right)^{1/2} \cdot \frac{k_f}{P(2c_p - \tilde{R}/M_g)} \tag{2.20}$$

where P is the gas pressure (in Pa), $\tilde{R}$ is the universal gas constant (in $\mathrm{J\,mol^{-1}\,K^{-1}}$), and M_g is the molecular mass of the gas (in $\mathrm{kg\,mol^{-1}}$). The accommodation factor, α_T is given by Bahrami *et al.* (originally given by Song & Yovanovich) as[16,169]

$$\alpha_T = \exp\left[-0.57T_r\right]\left(\frac{M^*}{6.8+M^*}\right) + \frac{2.4\mu}{(1+\mu)^2}\left[1-\exp\left(-0.57T_r\right)\right] \tag{2.21}$$

where $T_r = \frac{T_s - 273\,\mathrm{K}}{273\,\mathrm{K}}$, $M^* = M_g$ for monatomic gases or $M^* = 1.4M_g$ for diatomic gases, and $\mu = \frac{M_g}{M_s}$ is the ratio of gas and solid molecular masses. The α_T term, as described by Bahrami *et al.* represents the fraction of kinetic energy that a gas molecule leaves behind as thermal energy on a solid after collision.

In Figure 2.1, we see comparisons of effective conductivity predictions by the three models of Hsu *et al.* , Hsu *et al.* modification of ZS model, ZSB correction model, and their differences with the simple ZS correlation.

Van Antwerpen compiled data from numerous publications to compare the accuracy of effective conductivity correlations.[178] For our discussion, experimental data with all the correlations discussed above are also plotted. The plots are given in Figure 2.2.

Near $\kappa = 1$, all correlations collapse to predict a $\frac{k_e}{k_f} = 1$, and experiments naturally match predictions. From the range of $\kappa > 1$ to $\kappa < 1000$, experimental data is well-bound by the predictions of the simple ZS model and the complex two-dimensional models of Hsu *et al.*. Above $\kappa > 1000$, the ZS model, not taking into account heat transfer through finite-sized contacts, is no longer reliable as a model for k_{eff}. In high ranges of κ, the models incorporating contact-conduction in the granular material remain well-matched to experimental data. The results here show the worth of these general models for predictions of effective conductivity in some granular material.

As part of the Ceramic Optimal Material Experiments for Thermomechanics (COMET) project at UCLA, we measured the effective conductivity of $d_p = 1\,\mathrm{mm}$ graphite (IG11) pebbles for 135 °C to 544 °C. The results will be discussed in more detail later, though the results

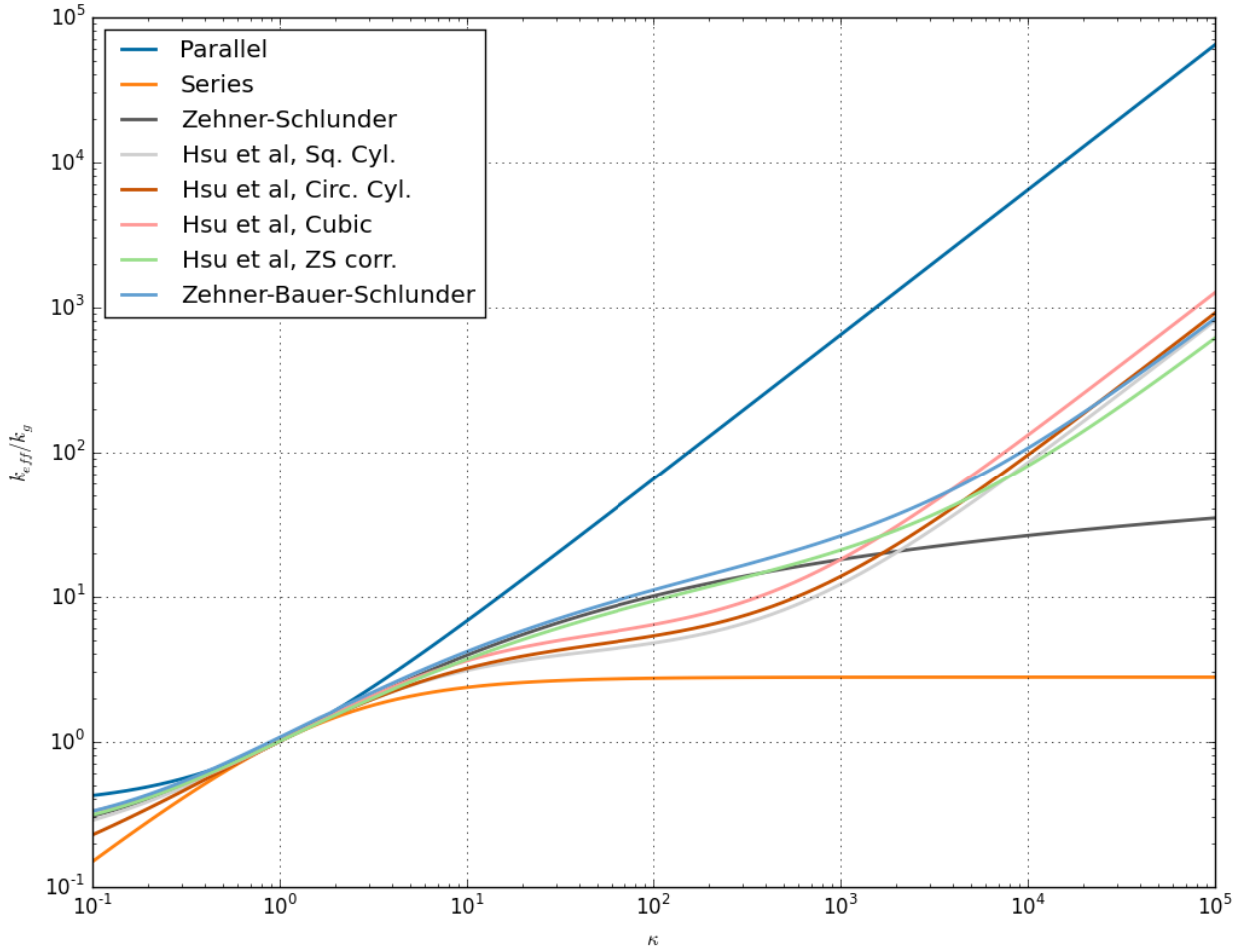

Figure 2.1: Models incorporating contact area demonstrate signficant deviation from the ZS correlation above $\kappa > 10^3$. All correlations are still bound by parallel and series approximations of the material.

will be presented here for comparison with the correlations; Figure 2.3 shows the COMET data. The measured conductivity from COMET is well above the lower bounds of series approximation for effective conductivity, though is just below the lowest values predicted from Hsu *et al.*'s square-cylinder two-dimensional model. We attribute the smaller values of effective conductivity on the surface roughness of the graphite pebbles in conjunction with their small size and small mass. In short, however, the measurements of COMET are also demonstrative of the inaccuracies in general predictions of granular material thermal properties.

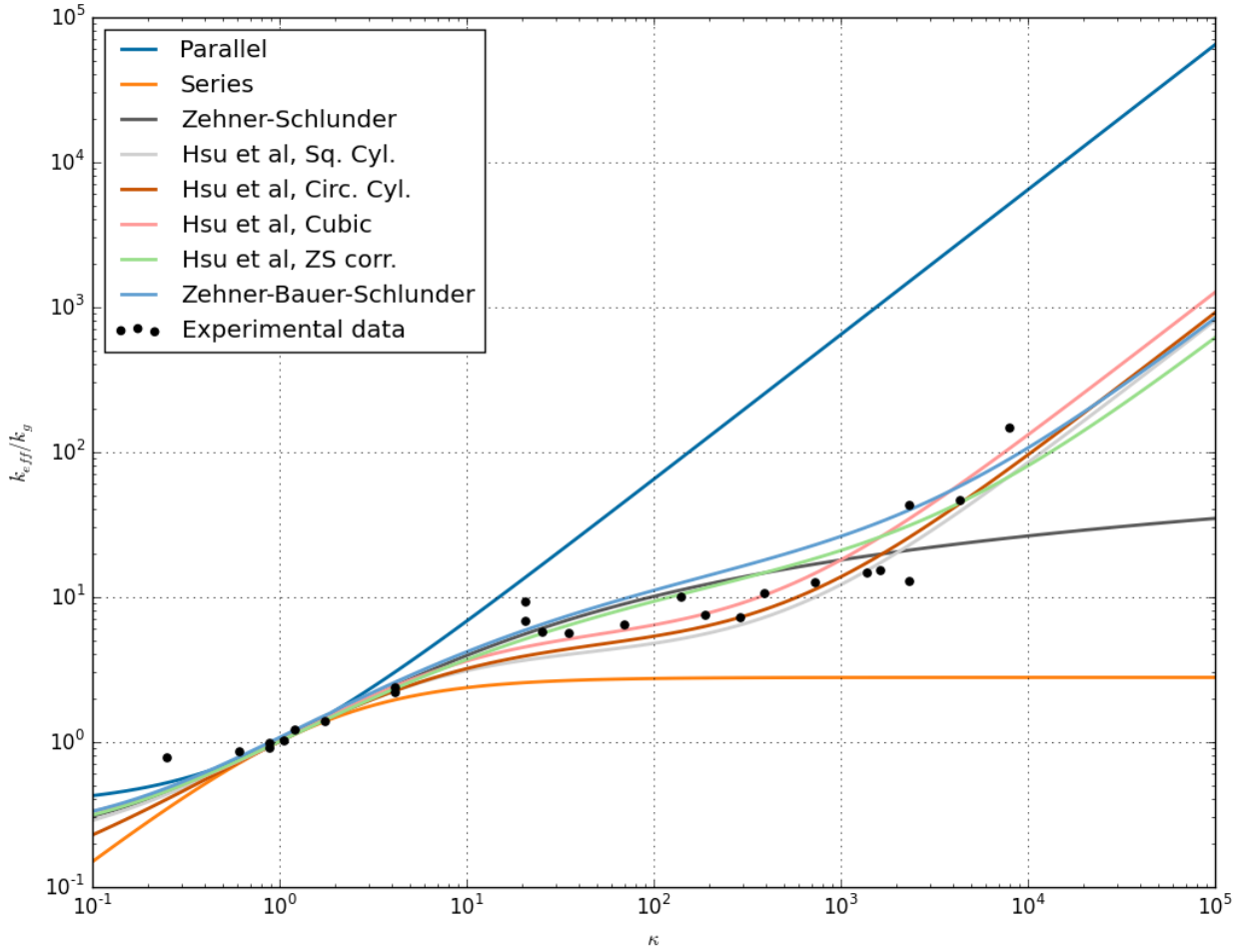

Figure 2.2: Comparison of k_{eff} correlations with compiled experimental data over a broad range of conductivity ratios, κ. Data compiled by Ref.[178] from many sources.

Lastly, one commonly-used correlation from Breitbach & Barthels.[25] Breitbach & Barthels began with the unit cell defined by Zehner & Schlunder, though noted that the closed cell precluded radiation from voids outside the cell volume. Therefore they modified the correlation *via* closing the bases of the unit cells with black surfaces instead of with surfaces of the same emissivity as the grains in the bed. The result is given as the BB correlation,[25]

$$F_E^* = \left[\left(1 - \sqrt{1-\epsilon}\right) \epsilon + \frac{\sqrt{1-\epsilon}}{2/\epsilon_r - 1} \cdot \frac{B+1}{B} \cdot \frac{1}{1 + \frac{1}{(2/\epsilon_r - 1)\Lambda_f}} \right] \tag{2.22}$$

where B is again given by Equation (2.4), and $\Lambda_f = \frac{k_s}{4 d_p \sigma \bar{T}^3}$ is a dimensionless solid conductivity for the granular packing.

An IAEA technical report provides effective conductivity measurements of $d_p = 6\,\text{cm}$

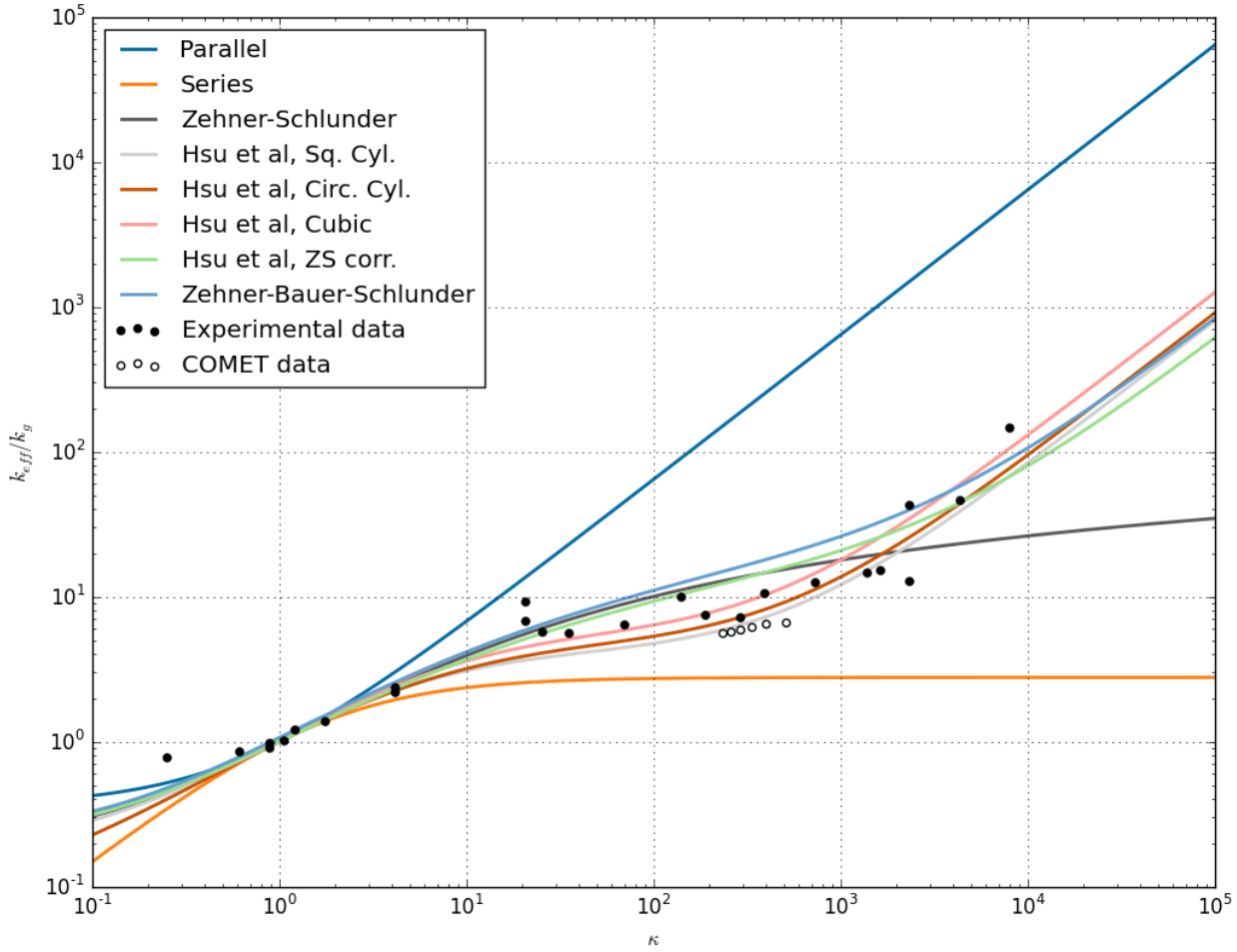

Figure 2.3: Comparison of COMET data on IG11 graphite, k_{eff} correlations, and experimental data. Data compiled by[178] from many sources and measured data at UCLA.

graphite pebble beds.[134] The data is used to compare against the combined correlations of ZS and BB. The k_{eff} measurements in Helium are given in Figure 2.4, measurements in Nitrogen are given in Figure 2.5. We see that the effective thermal conductivity correlations are significantly under-predicting, over the entire range of temperatures, when compared to experimental values. For the graphite pebble beds measured in the SANA report, we consider the Grashof number for the packing. The Grashof number is indicative of natural convection effects in the voids. The Grashof number is written as

$$\text{Gr} = \frac{g\beta(T_s - T_0)l^3}{\nu_f^2} \tag{2.23}$$

where we estimate it in voids of size $l = \frac{d_p}{2}$, a temperature drop of $T_s - T_0 = 10\,\text{K}$ is an

lower estimate. The kinematic viscosity, ν_f of the gases is known, and thermal expansion of an ideal gas is $\beta = \frac{1}{T}$. Let us assume a situation where temperatures and materials are all identical and the only variation is in length. Grashof numbers for these cases would be

$$\frac{\mathrm{Gr}_1}{\mathrm{Gr}_2} = \left(\frac{l_1}{l_2}\right)^3 \tag{2.24}$$

Zehner & Schlunder derived their correlation from mass-diffusion experiments of Curie.[43] The data of Curie was done primarily on grains of around 1 mm. Thus comparing $\frac{l_1}{l_2}$ between the size of particles for which the ZS correlation was derived and particles for which it was applied for SANA data yields

$$\frac{\mathrm{Gr}_1}{\mathrm{Gr}_2} \sim 10^{-6} \tag{2.25}$$

With a Grashof number significantly higher for the SANA experiments, it is indicative that the amount of natural convection present in the SANA experiment will have a much greater impact on heat transfer than the ZS correlation, derived on data for stagnant interstitial gas, is able to predict. This demonstrates limited applicability of effective conductivity correlations for packed bed conditions either different from those for which the correlations were derived or when convection effects are present.

2.2.2 Convection in Granular Media

Before discussing the correlations for Nusselt number of particles with forced convection in two-phase porous media, we consider a simple case of an axisymmetric sphere completely immersed in a quiescent fluid. The steady-state energy equation of the fluid surrounding the sphere is

$$\frac{\partial}{\partial}(k_f r^2 T) = 0 \tag{2.26}$$

for which the solution is

$$T = -\frac{C_1}{r} + C_2 \tag{2.27}$$

subjected to a boundary condition of

$$k_f \frac{\partial T}{\partial r}\bigg|_R = -h(T_R - T_f) \tag{2.28}$$

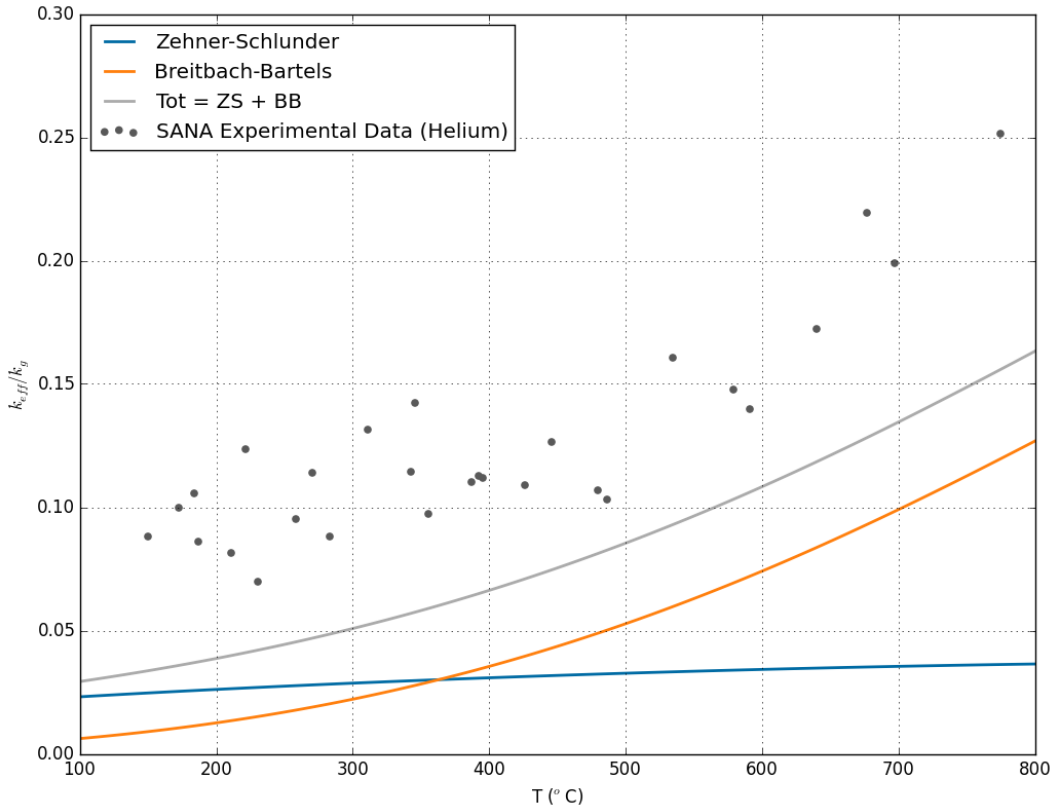

Figure 2.4: Comparison of SANA data in Helium gas with ZS and Breitbach-Bartels correlations. Data from IAEA Tecdoc-1163.[134]

where T_R is the temperature of the fluid in contact of the sphere of radius R and T_f is the temperature of the fluid infinitely far away from the sphere – which naturally leads to the second boundary condition of $T(r \to \infty) = T_f$. These two boundary conditions yield a temperature solution of

$$T = \frac{hR}{k_f}\frac{R}{r}(T_R - T_f) + T_f \tag{2.29}$$

We can also say $T(r = R) = T_R$ to show,

$$T_R = \frac{hR}{k_f}\frac{R}{R}(T_R - T_f) + T_f \tag{2.30}$$

or simply

$$\frac{hR}{k_f} = 1 \tag{2.31}$$

The Nusselt number for a sphere is defined as

$$\mathrm{Nu}_p = \frac{hd_p}{k_f} \tag{2.32}$$

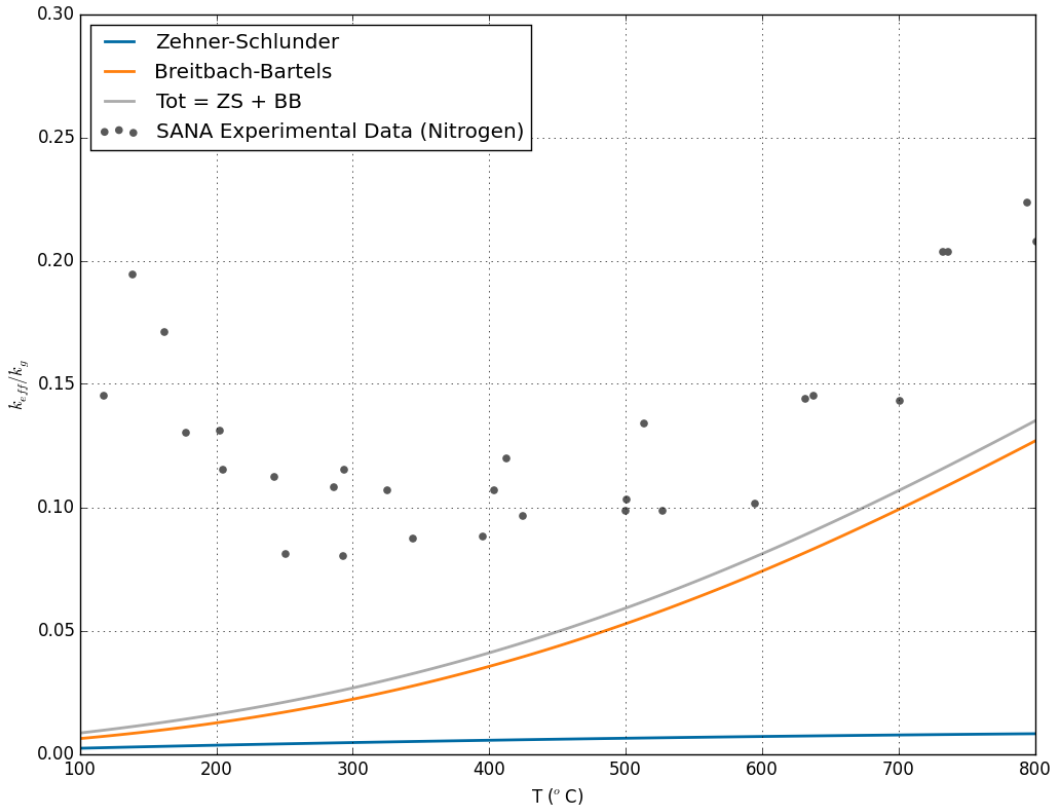

Figure 2.5: Comparison of SANA data in Nitrogen gas with ZS and Breitbach-Bartels correlations. Data from IAEA Tecdoc-1163.[134]

which is simply

$$\mathrm{Nu}_p = 2\frac{hR}{k_f} = 2 \tag{2.33}$$

showing that in the limit of $\mathrm{Re}_p \to 0$, the Nusselt number for a sphere in fluid will asymptotically approach $\mathrm{Nu}_p = 2$. This value is a natural limit for a Nusselt number correlation for particle-to-fluid heat transfer.

2.2.2.1 Nusselt number correlations for an individual sphere

For a particle falling through a fluid or a fluid moving past a single particle, a number of correlations exist for the Nusselt number of that individual sphere. One common correlation is from Ranz & Marshall,[148] developed from heat and mass transfer analogies with experiments

on evaporating drops. Their correlation is

$$\mathrm{Nu}_p = 2.0 + 0.6\mathrm{Pr}^{1/3}\mathrm{Re}_p^{1/2} \tag{2.34}$$

Generally considered valid for $\mathrm{Re}_p < 200$. The Ranz & Marshall correlation is used by Sasdisevi *et al.* in a CFD-DEM study of heat transfer in 2D fluidized spouts.[172] Romkes *et al.* did direct CFD studies of particle-to-fluid heat transfer and validated against Ranz & Marshall;[158] though they noted the correlation was valid over particle Reynolds numbers of $10 < \mathrm{Re}_p < 10^4$. Wu *et al.* also employed the correlation in a DEM study of granular material.[195] Li & Mason studied the correlation against their CFD-DEM studies,[118] they found the Ranz & Marshall's correlation to be adequate for small $\mathrm{Re}_p < 200$ also.

Gnielinski[80] developed a semi-empirical method where the Nusselt number for an arbitrary shape is related to the solution for a flat plate with appropriate transformations of the length scale. The solution is a function of the asymptotic laminar, turbulent, and $\mathrm{Re}_p \to 0$ solutions,

$$\mathrm{Nu}_p = 2 + \sqrt{\mathrm{Nu}_{lam}^2 + \mathrm{Nu}_{tur}^2} \tag{2.35}$$

where

$$\mathrm{Nu}_{lam} = 0.664\mathrm{Re}_p^{1/2}\mathrm{Pr}^{1/3} \tag{2.36}$$

and

$$\mathrm{Nu}_{turb} = \frac{0.037\mathrm{Re}_p^{0.8}\mathrm{Pr}}{1 + 2.443\mathrm{Re}_p^{-0.1}(\mathrm{Pr}^{2/3} - 1)} \tag{2.37}$$

The two single-particle correlations are shown over a range of Reynolds numbers in Figure 2.6. The two correlations are in good agreement near low Reynolds number.

2.2.2.2 Nusselt number correlations for a sphere as part of a packing

The above correlations were generally developed from measurements of a single particle in flow. The influence of neighboring grains will disrupt the flow field and result in a different Nusselt number. Thus, for the Nusselt number for a single grain in a packed bed, Nu_i, is often related to the Nusselt number of a single particle (alone in an infinite fluid), Nu_p, *via*

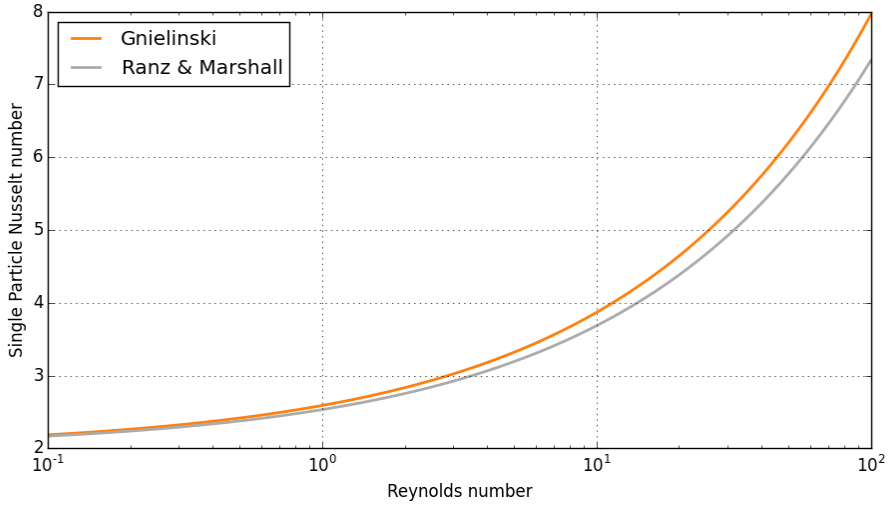

Figure 2.6: Comparison of correlations for Nusselt number of a single spherical particle in forced flow.

the packing fraction. The subscripts i and p will be used consistently below to signify the Nusselt for a particle in a packing or a correlation for a single particle.

The data of Ranz suggested the following for spherical particles in a fixed bed

$$\mathrm{Nu}_i = 2 + 1.8\mathrm{Re}_p^{0.6}\mathrm{Pr}^{1/3} \tag{2.38}$$

Another commonly-cited correlation is that of Wakao *et al.*[192,193] Combining a large amount of data over a broad range of particle Reynolds numbers and Prandlt numbers found a fitting function of

$$\mathrm{Nu}_i = 2 + 1.1\mathrm{Re}_p^{0.6}\mathrm{Pr}^{1/3} \tag{2.39}$$

Flueckiger *et al.*[63–65] as well as Yang & Garimella,[200] both implemented the Wakao *et al.* correlation in their studies of heat transfer in solar thermal storage tanks.

Zhou *et al.*[215] used a modified form from Kunii and Levenspiel, to fit their experimental data. They gave

$$\mathrm{Nu}_i = 2 + 1.2\mathrm{Re}_p^{1/2}\mathrm{Pr}^{1/3} \tag{2.40}$$

In another study, Li & Mason[117] also employed a modified form of Ranz & Marshall to account for the packing in the assembly with a function of void fraction in front of the

Reynolds and Prandtl terms,

$$\mathrm{Nu}_i = 2 + 0.6\epsilon^n \mathrm{Re}_p^{1/2} \mathrm{Pr}^{1/3} \tag{2.41}$$

where they found $n = 3.5$ fitting for 3 mm pellets in dilute flows.[117] Kloss *et al.*[108] and Di Maoi *et al.*[49] also use the modified Ranz & Marshall correlation provided by Li & Mason in their CFD-DEM studies. This correlation, however, conflicts with the correlations of Ranz, Wakao, and the Kunii & Levenspiel. In the asymptotic limit of $\epsilon \to 1$, the correlation correctly approaches the single particle correlation of Ranz & Marshall, Equation (2.34). For a dense packing, $\epsilon = 0.36$, the correlation gives

$$\mathrm{Nu}_i = 2 + 0.0168 \mathrm{Re}_p^{1/2} \mathrm{Pr}^{1/3} \tag{2.42}$$

which is significantly less than any of the correlations of Equations (2.38) to (2.40)

Achenbach defined an empirical arrangement factor, $f(\epsilon) = 1 + 1.5(1 - \epsilon)$ to related the single particle Nu of Gnielinski, Equation (2.35), to a sphere in a packing,

$$\mathrm{Nu}_i = (1 + 1.5(1 - \epsilon))\, \mathrm{Nu}_p \tag{2.43}$$

The modified form of Achenbach was used in a CFD-DEM study by Rickelt *et al.*,[156] which covers Re_p up to 10×10^5 and Pr from 0.7 to 7×10^4. The Gnielinski correlation[80] is also used in the ANSYS calculations of helium-cooled pebble bed breeders, reported by Hernandez *et al.*,[90] Cismondi *et al.*,[39] Poitevin *et al.*,[145] *etc.* However, Visser notes[191] that the correlation of Gnielinksi is valid for Re_p in 500 to 1000, for ϵ in the range 0.26 to 1.0. Thus he uses the correlation of Gunn for his situation of lower Reynolds number[84]

$$\mathrm{Nu}_i = (7 - 10\epsilon + 5\epsilon^2)(1 + 0.7\mathrm{Re}_p^{0.2}\mathrm{Pr}^{1/3}) + (1.33 - 2.4\epsilon + 1.2\epsilon^2)\mathrm{Re}_p^{0.7}\mathrm{Pr}^{1/3} \tag{2.44}$$

which Gunn developed to be valid for: heat transfer to particles at low and high Reynolds number, at low and high porosities; single particle at low Reynolds number, particles and particles in ensembles with high Reynolds number and moderate Prandtl. Amritkar *et al.* also employ the Gunn correlation in their simulations of spout-fluidized flow.[6]

The correlations are given as functions of Re at a specified value of $\epsilon = 0.36$ and $\mathrm{Pr} = 0.7$ in Figure 2.7. We see the correlation from Li & Mason (a modified form of Ranz & Marshall),

from Equation (2.41), predicts very small Nusselt numbers over this entire range of Reynolds number. Additionally, the modified Gnielinski of Equation (2.43) and the correlation of Gunn in Equation (2.44) predict much higher Nusselt numbers at low Reynolds number than any other correlation, and are well above the single particle limit of $\mathrm{Nu} = 2$ when $\mathrm{Re} \to 0$. In the studies of Achenbach and Rickelt, which employed the modified Gnielinski studies, the authors were interested in larger Reynolds number regimes. Above $\mathrm{Re} > 10$, Gnielinski correlation is similar to Wakao and Ranz correlations, thus the over-prediction at very small Re may not have been observed. Gunn rejects the notion that the Nusselt number should approach 2 in the no-flow limit.[84] The discrepancy appears to arise because of definitions of either particle or bed heat transfer coefficients. It seems Gunn's definition was meant for representative cross sections of packed beds with voidage defined by the void fraction rather than for an individual particle communicating with forced flow in a packed bed.

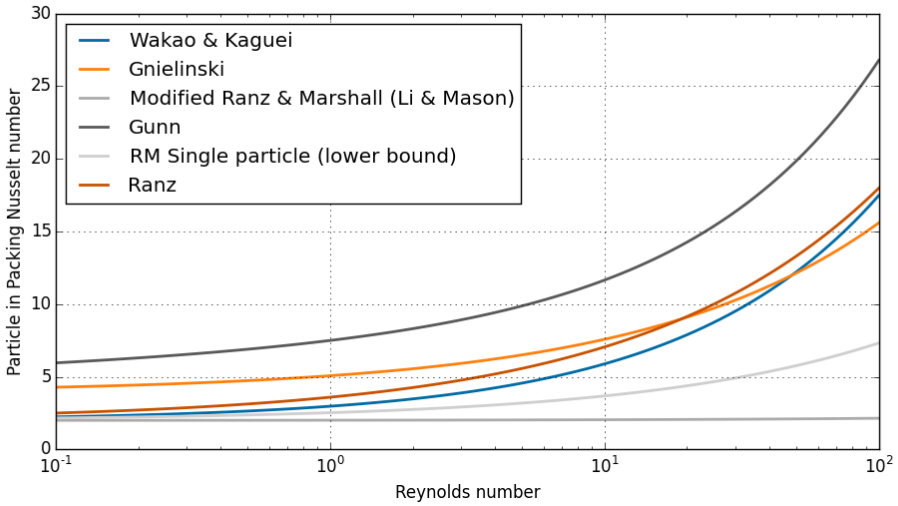

Figure 2.7: Comparison of correlations for Nusselt number of a single spherical particle in forced flow.

After discussing many popular correlations for Nusselt number in packed beds, considering the very small Reynolds number ($\mathrm{Re} \sim 1$) and packing fraction expected with the purge gas of helium in tritium breeders, the correlation of Wakao *et al.*, as given in Equation (2.39), is sufficient. However, we note the debate that still exists in literature for determining Nusselt number for a specific particle in a packed bed. If experimental validation shows the

Wakao correlation to be inaccurate, we will revisit the implementation in our modeling.

2.2.2.3 Natural convection in porous media

Natural convection is a concern in fusion packed beds due to exceptionally high temperature gradients, adverse to the gravity vector, that arise in some configurations of packed beds. The issue of natural convection has been addressed in Appendix F. The conclusion is that, in spite of temperature gradients as high as $400\,\mathrm{K\,cm^{-1}}$, viscous forces in the porous media dominate any buoyant forces that might arise in ceramic breeders. Therefore, natural convection is not considered for modeling in this thesis.

2.2.3 Radiation in Granular Media

In order to quantify radiative heat transfer compared to conduction heat transfer, consider particle i at temperature T_i with material properties of E, ν, radius R, emissivity ϵ, and solid conductivity k_s in contact with particle j of the same material at temperature T_j, the amount of heat transfered through a single contact of these two pebbles can be calculated from Equation (3.13), where conductance is given by Equation (3.16). Together, these are,

$$Q_c = 2k_s \left(\frac{3}{4}\frac{R^*}{E^*}\right)^{1/3} F_n^{1/3}(T_i - T_j) \tag{2.45}$$

Radiation exchange from particle i to j can be found from a radiative transfer equation, assuming the surfaces are grey and diffuse,

$$Q_r = \epsilon\sigma A_s F_{ij}\left(T_i^4 - T_j^4\right) \tag{2.46}$$

where, $A_s = 4\pi R^2$ and the pebbles have an emissivity of $\epsilon = 0.5$, and mechanical properties of Li_2TiO_3 are used. Feng and Han provide view factors between spheres of equal size in various packing structures.[61] Between two pebbles, regardless of the packing structure, the view factor is approximately $F_{ij} = 0.075$. The value of view factor can also be approximated as slightly less than 1/12, which is the number of contacts in the most dense packing of spheres, hexagonal-close packing.

The amount of energy transfered between the two particles is a function of: (i) temperature differences, (ii) absolute temperatures, and (iii) contact force. In the following figures, the temperature of T_i is varied between 300 °C to 800 °C, T_j is varied between $T_i - 100$ °C to T_i, and F_n is varied between 0 and 100 N. We report the radiative heat transfer as normalized against the conductive heat transfer at the given combination of temperatures and forces, and thus the values in Figure 2.8 are the direct fractional amounts of radiation compared to conduction.

From the results, we see that at the lower end of temperatures, 300 °C, radiation is negligible compared to conduction even when contact forces approach 0. At slightly higher pebble temperatures, 467 °C, radiation heat transfer is still significantly less than conduction, the highest percent is around 14% when contact forces are very small. When the pebble temperature increases to 667 °C, radiation is still small but potentially no longer negligible for pebbles with contact forces less than 20 N, which is common for many pebbles not existing as part of large force chains in packed beds. For these pebbles, radiation is around 20% or more of the energy transfer from contact conductance. Finally, at the higher end of 800 °C, even at very high contact forces of 100 N, radiative exchange is more than 20% of conduction. At lower forces, contribution of radiation to energy exchange between the two pebbles is nearly half of that from conduction.

Temperatures expected in the solid breeder will range between, approximately, 300 °C and 800 °C. Forces will also vary between pebbles in a probability distribution where the majority have small forces and some have very high contact force (as will be discussed from DEM results, to follow). Additionally, when we will later consider fragmentation particles which are significantly smaller than the original pebbles, view factors from small-to-large spheres will increase significantly. Thus we can not say that for the entirety of the pebble bed, under all conditions, radiation heat transfer is negligible. Nevertheless for the present study we must maintain with the assumption to neglect any contribution of radiation. The challenge of incorporating radiation into DEM is due to the non-locality of radiative exchange beyond contacting neighbors in the ensemble. In the work of Feng and Han to calculate view factors in packed beds, they found that in random packings, pebbles as far away as 5 diameters from

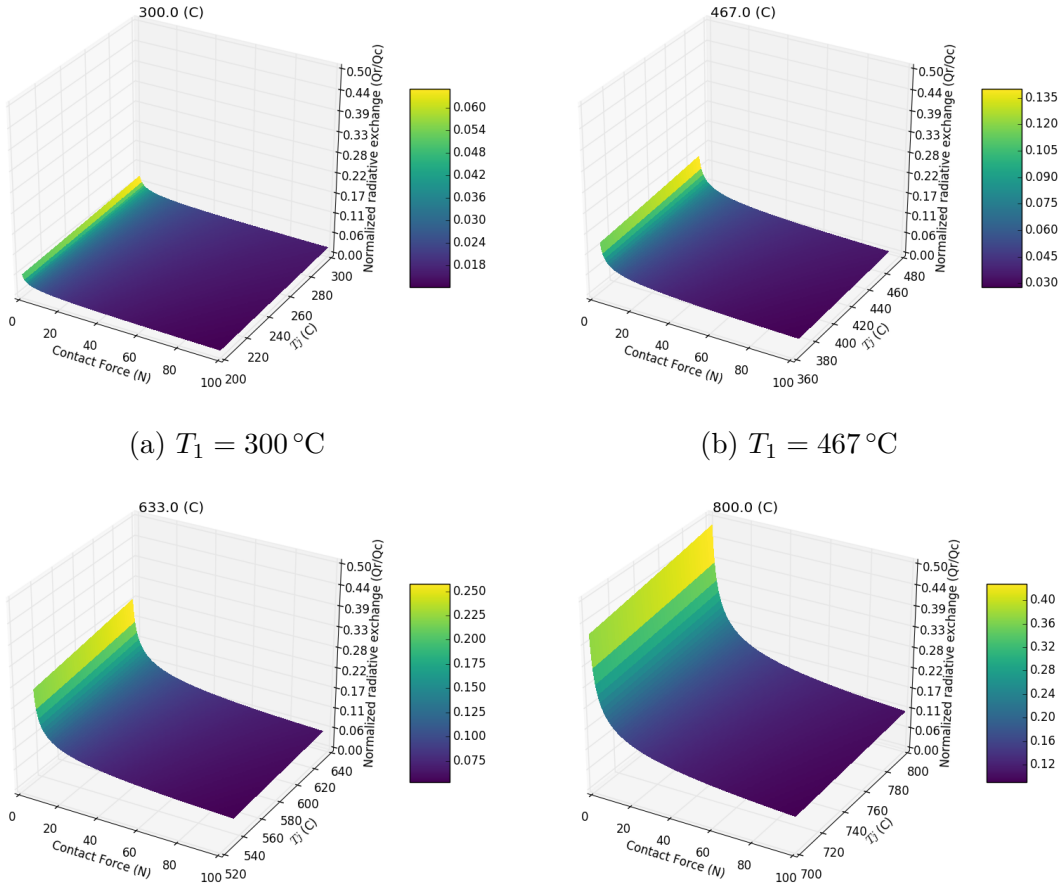

(a) $T_1 = 300\,^{\circ}\mathrm{C}$ (b) $T_1 = 467\,^{\circ}\mathrm{C}$

(c) $T_1 = 633\,^{\circ}\mathrm{C}$ (d) $T_1 = 800\,^{\circ}\mathrm{C}$

Figure 2.8: Comparison of radiative heat transfer with conduction heat transfer between two example pebbles at various temperatures.

the pebble of interest contribute to radiative transfer, as shown in Figure 2.9.[61] Tracking neighbors in an algorithmically expedient fashion among thousands or hundreds of thousands of particles is a challenge that is not attempted in the present work. We leave it to future iterations of the DEM model to incorporate the view factor calculation and radiative heat transport in DEM.

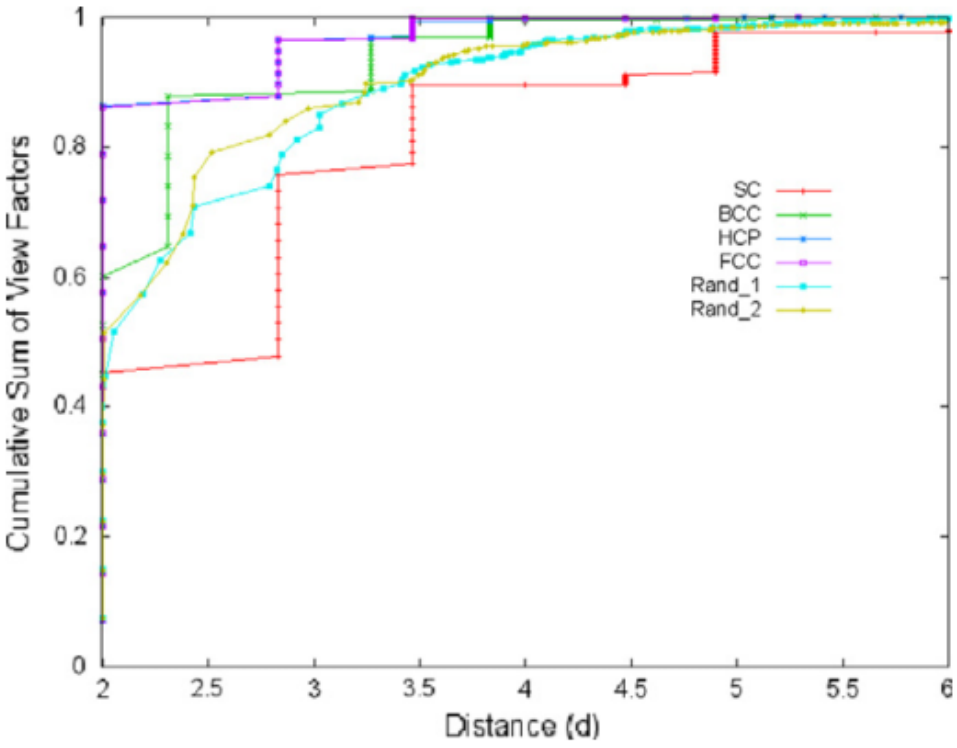

Figure 2.9: Cumulative view factors for different packing structures. Reproduced from Ref.[61]

2.3 Momentum Transfer in Packed Beds with Fluid Flow

P.C. Carman,[30] using Kozeny's Equation as a starting point, derived a formula for the average velocity of a laminar flow through randomly packed beds at the close-packed limit,

$$\bar{U} = \left(\frac{L}{L_e}\right)^2 \frac{\epsilon^3}{k_0 \mu S^2} \frac{\Delta p}{L} \tag{2.47}$$

where μ is the viscosity, Carman called the tortuosity (L_e/L) the ratio of the actual path of a streamline through the pore space, L_e, to the length of packing, L. S is the particle surface area per unit volume of the bed. For a bed of spheres this is $S = 6(1-\epsilon)/d_p$, ϵ is the void fraction, and constant, k, varies between materials and packings but for regular spheres is found experimentally to be $k \approx 5.0$. The pressure drop per unit length of flow is $\Delta p/L$.

We rearrange Equation (2.47) as

$$\frac{\Delta p}{L} = \frac{180 \bar{U} \mu}{d_p^2} \frac{(1-\epsilon)^2}{\epsilon^3} \tag{2.48}$$

The pressure gradient acting upon the fluid in the packed bed must be balanced by the drag force of all the particles in the bed. If we assume some average force, $\langle f \rangle$, as the ensemble average of the particle drag forces, we can write

$$\frac{\Delta p}{L} = n\langle f \rangle \tag{2.49}$$

where n is the number density of particles in the bed. We relate the number density in terms of the packing fraction as

$$n = \frac{6\phi}{\pi d_p^3} = \frac{6(1-\epsilon)}{\pi d_p^3} \tag{2.50}$$

Thus the average drag per particle in this flow is

$$\langle f \rangle = \frac{\Delta p}{L} \frac{\pi d_p^3}{6(1-\epsilon)} \tag{2.51}$$

We will nondimensionalize the average drag force based on the classic Stokes force – the drag force of a single particle in unbounded fluid,

$$F = \frac{\langle f \rangle}{3\pi\mu d_p U} \tag{2.52}$$

and when we plug in Equation (2.51) to Equation (2.52) we have

$$F_{kc} = \frac{\Delta p}{L} \frac{\pi d_p^3}{6(1-\epsilon)} \frac{1}{3\pi\mu d_p U} \tag{2.53}$$

which, with the substitution of the Kozeny-Carman pressure (Equation (2.48)), becomes

$$F_{kc} = \frac{180 U\mu}{d_p^2} \frac{(1-\epsilon)^2}{\epsilon^3} \frac{\pi d_p^3}{6(1-\epsilon)} \frac{1}{3\pi\mu d_p U} \tag{2.54}$$

or simply

$$F_{kc} = 10\,\frac{1-\epsilon}{\epsilon^3} \tag{2.55}$$

Carman himself[31] points out the limitations of applicability of the Kozeny-Carman (KC) equation: built into the equation is the assumption that the range of pore size and shape is fairly isotropic and similarly the tortuosity through the packed bed is relatively uniform. In the form we have used with Equation (2.55), we have also assumed spherical particles in random packing near the close-packed limit ($\phi \to 0.64$) with laminar flow at low Reynolds

numbers. Carman provided modifications to cases of extremely high porosity and non-spherical, non-regular packings in his book from 1956.[31]

Another correlation that is perhaps more commonly used in general is the Ergun equation.[59] Ergun's equation is an empirical fit to a vast amount of experimental data. His pressure drop per length is given as

$$\frac{\Delta p}{L} = \frac{150 U \mu}{d_p^2} \frac{(1-\epsilon)^2}{\epsilon^3} + \frac{1.75 \rho U^2}{d_p} \frac{1-\epsilon}{\epsilon^3} \tag{2.56}$$

We nondimensionalize the Ergun equation of Equation (2.56) by Stokes flow solution, as done to derive Equation (2.55), to find

$$F_e = 8.33 \frac{1-\epsilon}{\epsilon^3} + 0.18 \frac{\mathrm{Re}}{\epsilon^3} \tag{2.57}$$

where we see the Reynolds number dependence in the second term on the right side of Equation (2.57). Comparing this to the nondimensionalized drag force of the Kozeny-Carman relation (Equation (2.55)), we see that the first term on the right hand side is essentially the same but Ergun's equation underpredicts Stokes flow by roughly 20% (comparing the leading coefficient of 8.33 to 10.0). This is understandable as Ergun's equation was meant to fit a wide range of flow (finite-to-large Re), including turbulent flow, whereas the Kozeny-Carman was meant specifically to apply to Stokes flow-type laminar packed beds.

Koch, Hill, & Ladd studied packed bed flow with high-precision lattice-Boltzmann simulations to develop correlations for drag in a packed bed over a wide range of packing fractions and Reynolds numbers.[92,93,110] They studied ordered arrays of spheres at various flow angles with dilute arrays (interstitial Reynolds number greater than particle Reynolds number), up to dense ordered arrays, and random arrays.

They consider the drag force as a sum of viscous and inertial stresses. Based on scaling arguments, the viscous and inertial contributions to F are expected to be independent of Re and linearly proportional to Re, respectively (in much the same form as Ergun's empirical fit of Equation (2.57)). Thus their numerical results were fit to the form

$$F = F_0(\phi) + F_3(\phi)\mathrm{Re} \tag{2.58}$$

where, from their lattice-Boltzmann simulations they found,

$$F_0 = \begin{cases} \frac{1+3(\phi/2)^{1/2}+(135/64)\phi\ln\phi+16.14\phi}{1+0.681\phi-8.48\phi^2+8.16\phi^3} & \text{if } \phi < 0.4 \\ 10.0\,\frac{\phi}{(1-\phi)^3} & \text{if } \phi > 0.4 \end{cases} \tag{2.59}$$

and

$$F_3 = 0.0673 + 0.212\phi + 0.0232\frac{1}{(1-\phi)^5} \tag{2.60}$$

Koch, Hill, & Ladd[23,82,92,110] also compared their results with data from experiments. They found that at smaller Reynolds number and larger solid volume fractions, the rate of increase of drag force increases with the Reynolds number in much the same way predicted by Ergun's equation. However, at solid volume fractions smaller than those that can be achieved in physical experiments, at the largest Reynolds numbers, the rate of drag force increase is significantly smaller than the value predicted by Ergun's equation.

For Stokes-flow (and near-Stokes-flow), the drag force computed from their lattice-Boltzmann simulations were indistinguishable from experimental data over all ranges of packing fractions achievable in controlled experiments. Their correlation for small Reynolds number and large packing fraction is simply the Kozeny-Carman relationship – which was itself generated with coefficients matching experimental data so it is no surprise their correlation fits that phase space of $\phi - \mathrm{Re}$.

Three correlations relating a nondimensional drag force to packing fraction and Reynolds number have been presented. The first, the Kozeny-Carman equation, Equation (2.55), was derived assuming small Reynolds numbers with a broad range of packing fraction. The second, the Ergun equation, Equation (2.57), is meant to be applicable over a broad range of Reynolds number due to its origins as an empirical fit from experimental data but, by the same token, is limited to experimentally attainable packing fractions. Finally, the third correlation by Koch, Hill, & Ladd (KHL), Equations (2.58) to (2.60) was numerically developed to provide drag correlations over a much more broad packing fraction and Reynolds numbers than is possible with physical experiments.

A graphical comparison of the relationships that compares the three correlations: KC, Ergun, and KHL is presented here.

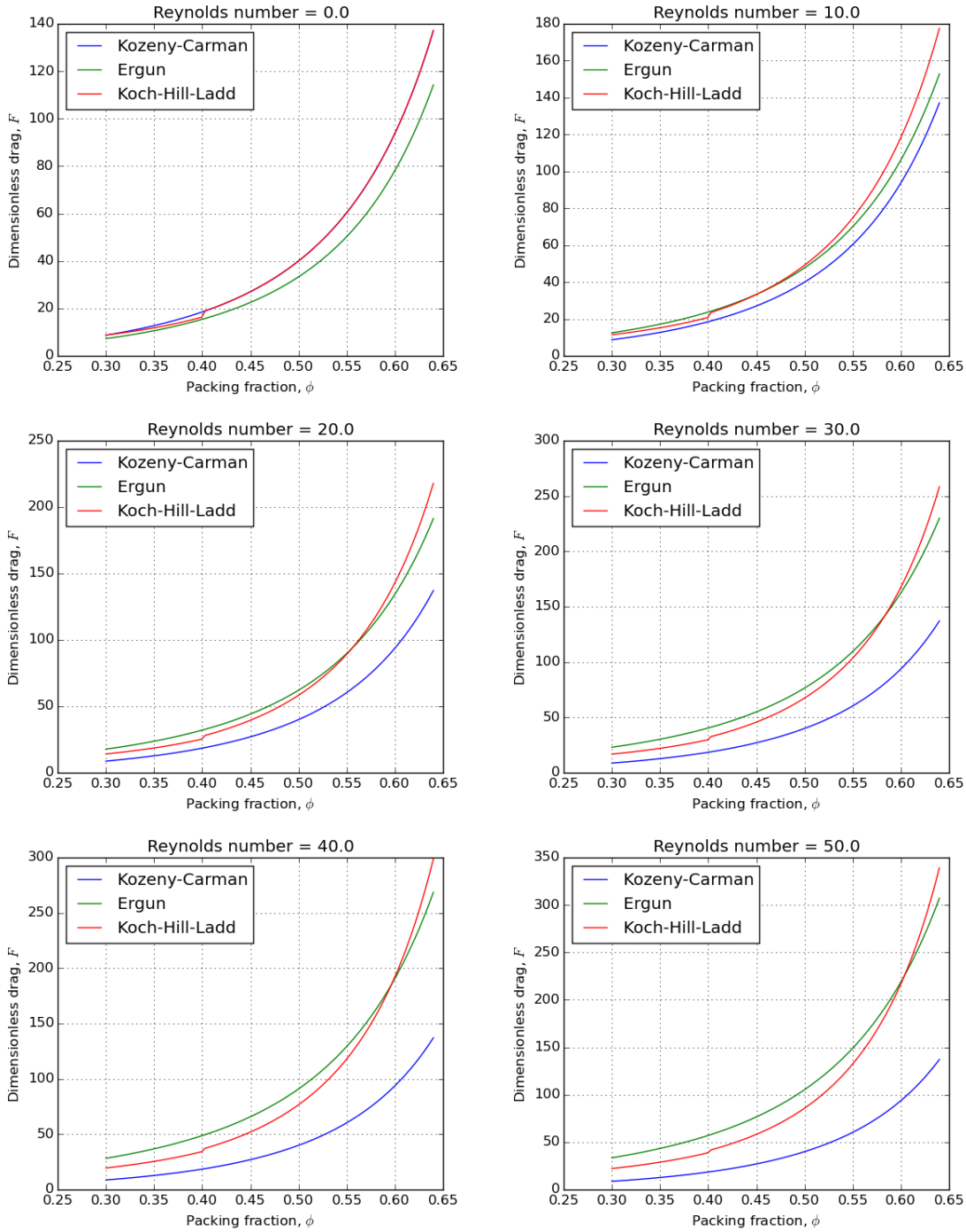

Figure 2.10: Comparison of pressure drop correlations over a range of packing fractions and Reynolds numbers.

2.4 Status of Ceramic Breeder Modeling and Analysis

Research efforts have been aimed at developing an understanding and characterization of thermomechanics of ceramic breeder pebble beds. Such an understanding is essential to providing confidence in performance and lifetime of ceramic breeder blanket designs. In particular, a significant effort of pebble bed thermomechanical studies is development of modeling simulation tools. In this section the current state of modeling – and experimental work feeding into modeling efforts – for ceramic breeders of tritium is presented.

2.4.1 Experiments to Develop Constitutive Equations for Pebble Beds

Many experiments have been run to measure the effective thermal conductivity of a volume of ceramic pebbles. In Figure 2.11, the effective conductivity is seen to be strongly affected by the interstitial gas but weakly affected by the mechanical loads on the bed. The main conclusions to bear in mind from Figure 2.11 are that: 1) the interstitial gas, even when stagnant, is an important facilitator of heat transfer in beds and 2) the effective thermal conductivity of the pebble bed is low and will limit the size of the ceramic pebble bed volume to satisfy the temperature window imposed on ceramic breeders.

Reimann *et al.* have conducted an extensive experimental study of stress-strain relations of ceramic breeder pebble beds using an oedometric test apparatus.[142,151,152,154,155] The most significant macroscopic experimental phenomena witnessed in pebble beds is an irreversible plastic strain when load is removed, a non-linear elasticity, a pressure-dependent plasticity, and volumetric creep. A particularly noticeable feature, clearly demonstrated in Figure 2.12, is the reduced amount of irreversible strain when subjected to additional loading cycles after the first unloading. This may suggest the existence of a semi-equilibrium packing state in the pebble bed which can be reached after applying a pre-load to account for the large strain in the first cycle of a pebble bed. This semi-equilibrium packing state is a feature which may be advantageous for use in a fusion reactor.

To study temperature effects in Reimann's studies, beds are freely heated to desired working temperatures before pressure load is applied. Under the same loading condition,

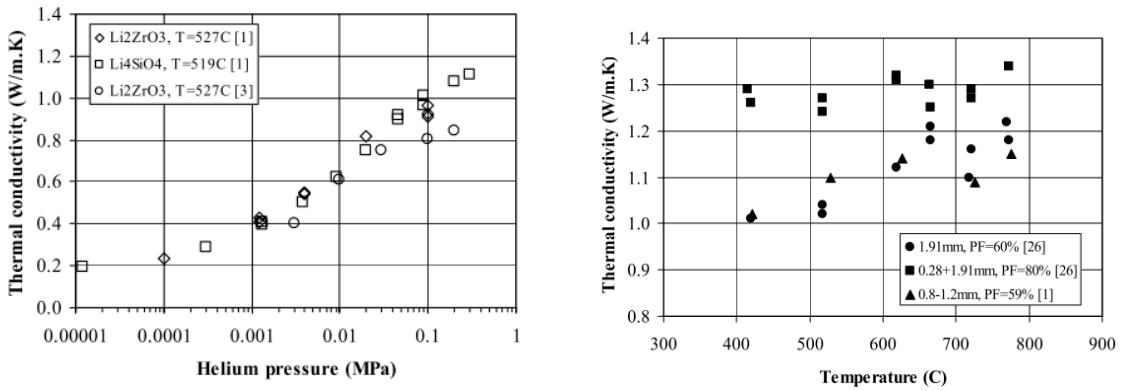

(a) Effective conductivity of ceramic pebble beds is dependent on the pressure of the interstitial gas, a minimum of about $k_{\text{eff}} = 0.2\,\text{W}\,\text{m}^{-1}\,\text{K}^{-1}$ in vacuum.

(b) The effective conductivity of several Li_2TiO_3 packing structures.

Figure 2.11: Effective conductivity of lithium ceramics. Results from Ref.[4]

beds behave much softer at higher temperatures. The bed stiffens as the pressure increases. An illustration of this phenomenon is presented in Figure 2.13 for a lithium orthosilicate pebble bed between 50 °C to 850 °C. At higher temperatures (such as > 650 °C), a creep-like behavior becomes apparent. Creep behavior allows the pebble bed to relax and sustain higher stresses, however at eleveated temperatures we must keep in mind issues of surface sintering of pebbles. The data was used to correlate creep rate as a function of temperature, stress, and time for both lithium orthosilicate, lithium metatitanate, and beryllium pebble beds.[27,153,155]

Coming from the standpoint that strain in a pebble bed is induced by thermal expansion, an experiment was conducted to characterize the pebble bed thermal expansion coefficient.[173] The thermal expansion coefficient of a packed Li_2TiO_3 pebble bed is measured under a compressive load of 0.1 MPa. The study concludes that for beds with packing factors of 65.3 to 68.5%, the average thermal expansion coefficient was $(1.4 \pm 0.2) \times 10^{-5} K^{-1}$. This thermal expansion coefficient of the pebble bed was equal to 78% of that for the bulk material under the conditions used in the study. The reduction in thermal expansion coefficient is less significant than that of the effective modulus, which is more than 2 orders of magnitude

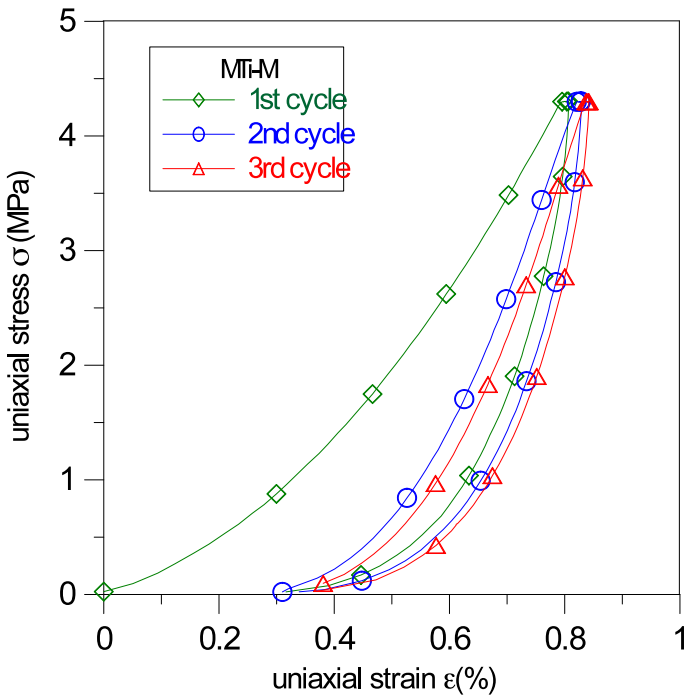

Figure 2.12: Example of uniaxial compression testing results for lithium metatitanate pebble bed.[181]

smaller than the bulk value.

The effect of thermal cycling on the packing state is of interest; in particular, it is foreseen that the ITER TBM will be subjected to such conditions. The question that arises is whether a void region will be created under thermal-cyclic loading due to the differential rates of expansion and contraction of the pebble bed and structural containing wall. This uncertainty was first addressed in an experimental set-up involving Li_2TiO_3 pebbles enclosed by two Kovar flanges while sandwiched between two commercial-grade CVD silicon carbide discs.[29] The set-up allows for generating a high stress through large differential in thermal expansion coefficients. The experimental results indicate that high thermal stresses and deformations are present during the initial thermal cycle of the assembled test article, but are successively alleviated due to a combination of pebble re-arrangement within the bed and creep induced deformation. This suggests that a few thermal cycles under a controlled atmosphere and a compressive load before final assembly of blanket sections would mitigate the severity of the thermal stresses during start-up. This is also shown in a later experiment, in which the

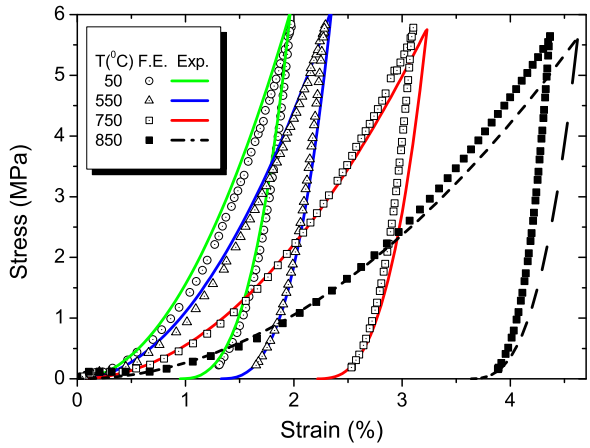

Figure 2.13: Example of uniaxial compression testing results compared with predictions from material constitutive equations for lithium orthosilicate pebble beds at different temperatures.[70]

increment of compression decreased with each heating cycle and became negligible after 30 cycles.[175] Extrapolating the finding to a prototypical blanket breeder pebble bed design, the study concludes that for a height of 1 m long pebble bed, a 51 mm high cavity may be generated at the top of the bed with an initial packing of 65% under thermal cyclic operations.

2.4.1.1 Post-irradiation experiments at Petten

The pebble bed assemblies (PBA) experiment is designed to study the effect of neutron irradiation on the thermomechanical behavior of a ceramic breeder pebble-bed under DEMO representative thermomechanical loads.[123] This was accomplished *via* analysis of changes of the in-pile temperature profiles during irradiation as wall as from the post irradiation examination of the pebble bed in the Hot Cells. Within the assemblies, there are four test elements; each resembling a small-scale mock-up of a HCPB TBM with a ceramic breeder pebble bed sandwiched between two beryllium pebble beds. Before irradiation, the beds are pre-compacted with a compressive load of 3 MPa to ensure good settling and contact.

FEM analysis was performed to study pre-compaction procedures. During progressive irradiation, temperatures are recorded at several locations in the ceramic breeder bed as well as other critical positions. Reviewing the recorded temperature data, when comparing the temperature in the center of the ceramic breeder pebble bed during later cycles and earlier cycles there appears to be a decrease in temperature for the exact same environmental conditions. Changes in the pebble beds and their characteristics are examined both in-pile by neutron radiography and out-of-pile by e.g. SEM during post-irradiation examination (PIE). The estimated bed height reduction from neutron radiographies over the course of the irradiation has shown 3% of creep compaction.

A pebble bed experiencing creep compaction is both becoming more dense as well seeing more-developed inter-pebble conduction paths. The effective thermal conductivity for a creep-compacted ceramic pebble bed is thus expected to be higher than a standard ceramic pebble bed. This phenomenon results in lower temperature gradients and a lower overall temperature magnitude, which is precisely what was observed in the experiment over the course of the cycling.

During PIE, various microscopy preparation techniques are used to study the deformation state of the pebble beds (signs of creep compaction and sintering), formation of gas gaps between the pebble beds and structural materials, and the interaction layers between eurofer-ceramic and eurofer-beryllium.

Figure 2.14 shows the cross-section of Li_2TiO_3 pebbles (left) and Li_4SiO_4 pebbles (right) post irradiation. Evident in the images is sintering of the lithium titanite and significant fracturing of the lithium orthosilicate pebbles. Importantly, however, it must be noted that the pebble beds performed reliably in spite of the changes displayed in these images.[123]

2.4.2 Continuum Modeling of Granular Material for Solid Breeders

When we consider beds of granular material from the standpoint of engineering continuum mechanics, packed beds cannot be adequately described by traditional models of either solids or liquids alone. Under compression, a packed bed responds like a solid with non-linear

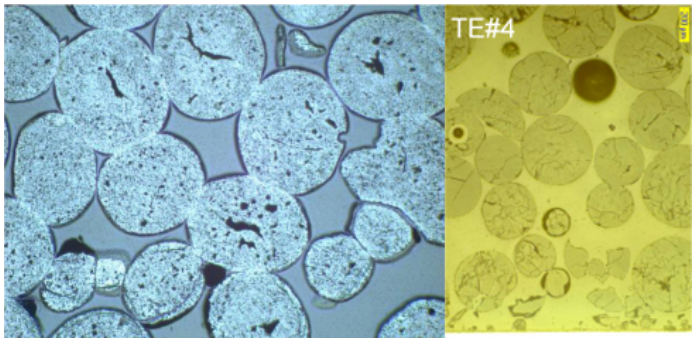

Figure 2.14: Notable features of irradiated Li_2TiO_3 and Li_4SiO_4 pebble beds from PBAcitemagielsen2011. (Left) Demonstration of significant sintering of Li_2TiO_3 pebbles with no fracturing; the visible cracks originated from production and handling. (Right) Demonstration of cracking of Li_4SiO_4 pebbles.

elasticity and a plasticity that is history-dependent. At the same time, the packed bed can obviously not support any tensile pressure and will often behave as an extremely viscous liquid as it may fill in voids under just the force of gravity. Nevertheless, phenomenological models, derived from the volumes of collected data, have been developed, using effective material properties for the ceramic pebble bed, that describe the pebble beds in an Eulerian manner that provide reliable information on the initial states of breeder volumes in the fusion reactor environment and allow reasonable design predictions of the thermomechanics of the breeding blanket.

In spite of the shortcomings of a continuum approach, it is the only option which currently allows treatment of the pebble beds with standard finite element modeling (FEM) that can be scaled up to the breeder system. To employ FEM, mathematical models written in terms of average quantities and containing effective parameters are used. These models deduce a set of constitutive equations to be implemented in the framework of a finite element code. There are two major variants of phenomenological modeling approaches developed among institutions, including: (1) A non-linear elastic model and a modified Drucker-Prager-Cap theory for plastic strain;[66,69] and (2) A hyper-porous non-linear elastic model and a Gurson model for the plastic model.[47,48,50] Another approach was taken by Ref.[66] wherein the authors employed two different elasticity laws for the loading and unloading branches.

Alongside the development of the modeling techniques, several large scale pebble bed Thermomechanics experiments were conducted. These experiments were intended to reveal the underlined thermomechanical characteristics of ceramic breeder pebble beds, and provide data for benchmarking the developed models. The vast amount of work done on modeling the pebble beds in the FEM framework can be found in literature.[47,48,51,69,71,73,74] A study was also published in 2012 that summarized, compared, and highlighted features of the models under development at the time.[201]

2.4.3 Pebble Bed Modeling Benchmarks

The constitutive equations developed for finite element models were derived from the uniaxial compression experiments, which are not fully representative of fusion operating conditions. A more prototypical experiment should subject a pebble bed to isostatic loading. This could be generated by either an in-pile pebble bed experiment or by making use of differential thermal expansion between a pebble bed and its containing structure. The latter has been attempted with several out-of-pile experiments launched by the HE-FUS 3 facility at ENEA Brasimone. The experiments investigated the thermomechanical behavior of pebble beds within geometry much more representative of current breeder designs. These include the medium-scale mock-up exercises of HELICA (HE-FUS3 Lithium Cassette) and HEXCALIBER (HE-FUS3 Experimental Cassette of Lithium Beryllium Pebble Beds).[46,50] For those experiments, the pebble layers are heated by electric heaters, and temperature and displacement were measured.

2.4.3.1 FZK Benchmarking

FZK has performed validation of their FEM code against the data collected from the HELICA experiment.[70] They have also reported the results of simulations of HEXCALIBER but have, as yet, not directly validated against the collected experimental data.[71]

In the HELICA experiment, the pebble beds experienced six thermal ramps, each applied for an hour, and then the pebble beds were actively cooled with a helium flow. After cooling,

the pebble beds were subjected to the another thermal ramp and the process was repeated. DIN reports[46] that the pebble bed temperatures exhibited cyclical behavior. FZK simulated two cycles of the HELICA test and an example of the calculated results and experimental data are shown in Figure 2.15 and Figure 2.16. In Figure 2.15 we see temperature histories at a particular location (100 mm from the first wall) during a loading-unloading cycle. The simulation results follow the temperature increase during the thermal ramps up until the seventh hour, then again follow the experimental data as the test rig is cooled with the helium coolant. Even with the two-dimensional simplification of the model, there is excellent agreement between calculations and measurements. In Figure 2.16 the displacement calculated by FZK is also in strong agreement with the average of measured displacements for the entire duration of the heating-cooling cycle. Because of the overwhelming amount of computer time necessary for the FZK model to complete a fully three-dimensional and transient simulation, the FZK computations of HELICA and HEXCALIBER are carried out in two dimensions; the helium temperature is chosen at an average value of measured inlet and outlet temperatures.

From FZK's numeric simulation arise several important observations: (i) a three-dimensional analysis would provide more detail, spatial temperature variation of *e.g.* coolants would likely explain much of the deviation between temperature profiles predicted by the simulation and measured in the HELICA experiment; (ii) gap formations, with sizes on the order of a pebble diameter, were detected at the interface of the first wall in ceramic beds; (iii) the maximum hydrostatic pressures seen in the ceramic bed are anticipated to be above the fracturing limit of the lithium ceramic. The consequences of some of these observations, if true and real, are severe enough that they merit careful attention.

Gap formation and pebble damage (due to crushing or fracturing) are important topics that must be considered in validation with future experiments. Observing the temperature profiles during the first cooling cycle, the HELICA experimental data deviate from simulation values. It is during the cooling cycle when gap formation would occur as pebbles began to thermally retract. Simulations that predict gap formation would then predict slower cooling, or higher temperatures, as the gap disrupts mechanical contact between pebble bed

and coolant structure. Such phenomena seems present in comparison of experimental and numerical results in the cooling cycle. This discrepancy seems well-suited to be answered with pebble-scale simulations of solid breeder units as the stress-induced gap could be more thoroughly studied with that modeling approach.

2.4.3.2 DIN Benchmarking

Because of the characteristics of the DIN model, full three-dimensional simulations were capable of being relatively easily performed. In the framework of benchmarking efforts, DIN has performed validation of their model against experimental results of HELICA, shown in Figure 2.17 as well as HEXCALIBER, shown in Figure 2.18.

The results of the DIN model show also good agreement with experimental results of HELICA as demonstrated in one example of temperature histories shown in Figure 2.17. In this profile, the same location as that modeled by FZK (100 mm from the first wall) is simulated by DIN. The FEM simulations from DIN (Figure 2.17) are reported over the six-hour heating portion of a single heating ramp cycle of HELICA. When comparing the results from DIN with those of FZK (in Figure 2.15 and Figure 2.16) we see the DIN model has slightly better predictive capabilities for the temperature histories. This may be due attributed to the three-dimensional variations in coolant temperature being captured by the DIN model.

Unfortunately, the ambitions of HEXCALIBER were limited due to the crippling of several heaters. Even so, the limited data was still used in efforts to validate the constitutive relationships of the DIN model. The temperature variations with time were the only major result reported by the ENEA Brasimone team, such as that shown in Figure 2.18; mechanical results were not release. From the comparisons to experimental measurements in HELICA and HEXCALIBER it is encouraging to notice that even in the absence of a creep model, satisfactorily close agreement were seen between computation and measurement. So far, no detailed displacement comparisons have been made to experimental data.

Several important observations are also made from the results of the DIN simulation: (i)

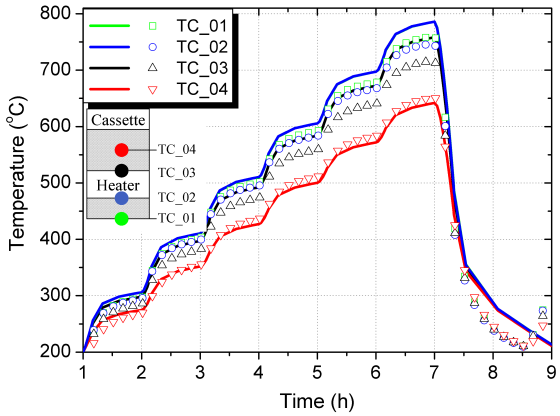

Figure 2.15: Results of the FZK benchmarking with HELICA[71] showing temperature variations with time during a loading cycle (T in °C) at 100 mm from FW.

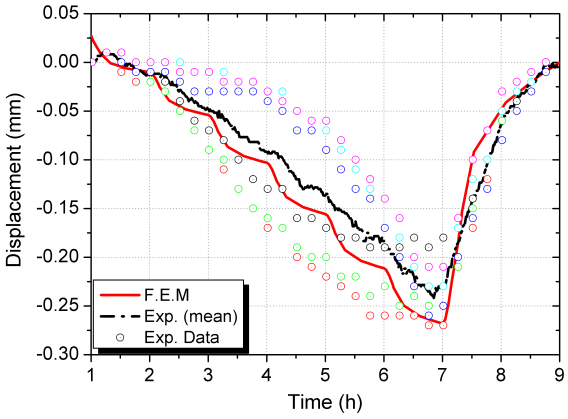

Figure 2.16: Results of the FZK benchmarking with HELICA[71] showing a comparison of displacements (in mm) in HELICA between calculated and measured LVDT values.

three-dimensional effects were important to calculations of the convective energy transport of the helium coolant; future models should continue to be analyzed in three-dimensions; (ii) DIN reports that in HELICA all ceramic beds experience a compressive force everywhere and no gap formation is ever detected.

In summary, the benchmarking efforts have only recently begun. A typical pebble bed thermomechanics simulation involves first calculating overall temperature fields of the blanket unit as it undergoes volumetric nuclear heating as well as cooling at the boundaries. The

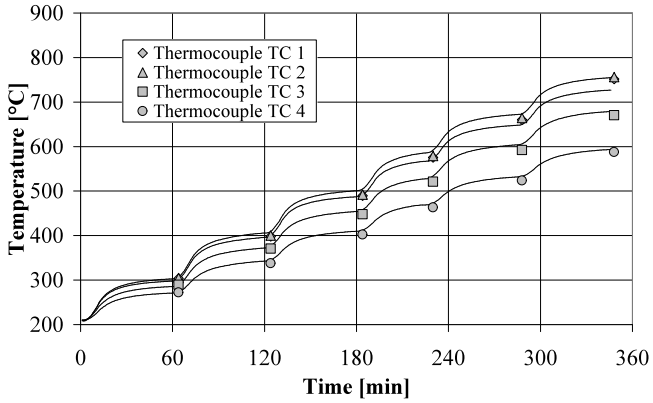

Figure 2.17: Exemplary results of the DIN benchmarking with HELICA: Temperature variations with time during a loading cycle at 100 mm from FW.[47]

non-linear mechanical analysis is then performed for stress and strain estimations. However, since the effective thermal conductivity of the ceramic breeder pebble bed is, to some degree, dependent on strain, a coupled thermal and mechanical analysis is needed. Additional details on modeling steps can be found in Refs.[46,48,50,51,71,73] The two most developed models, from FZK and DIN, have had their results compared to experimental data and have thus far shown promise.

However, it must be noted that the benchmarking efforts are incomplete and inconsistencies between the two models must be explained as they move forward. For example, the model of FZK concluded that a gap appeared between the pebble bed and structural wall, however the model from DIN reported no gap formation. The existence of a gap between pebble bed and structural wall will negatively affect the ability to cool the pebble bed and thereby impact structural and tritium release properties of the bed. That such a discrepancy exists between calculated results of the models on such a critical feature warrants either more benchmarking efforts or a careful deconstruction of the constitutive equations to discover the source of the inconsistency. Future experiments aimed at benchmarking ought to focus on creating apparatus capable of expressing, among other things, when gap formation or pebble failure occurs.

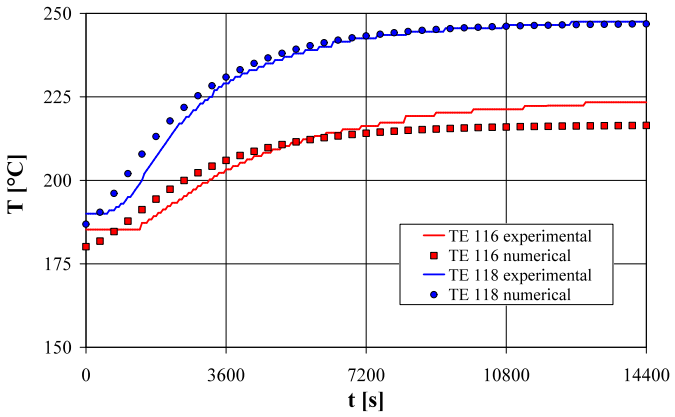

Figure 2.18: Exemplary results of the DIN benchmarking with HEXCALIBER : Temperature variations with time during a loading cycle within the first lithium-orthosilicate cell.[48]

2.4.4 Discrete Element Method for Solid Breeders of Tritium

There are many reasons to model ceramic breeders from the point of view of individual pebbles, for instance we observed the incongruity on the issue of gap formation observed during benchmarking efforts of continuum models. Correlations for effective properties of heat transfer and the constitutive equations derived from experiments are still incapable of accurate modeling of granular thermomechanics as packing structures evolves in time (based on creep, granular crushing, sintering, *etc.*), thus many researchers of ceramic pebble beds began modeling with the grain-scale discrete element method (DEM).

The Discrete Element Method (DEM) introduced by[42] has been shown to be a promising tool to study the behavior of granular systems through the interaction between the individual particles. DEM was first applied to study the micro-mechanical aspects of cyclic thermal loads on the relaxation of stress in pebble beds for fusion reactors.[121,202] An iterative relaxation strategy of DEM was used to study the internal contact forces in a pebble bed under an external load by An *et al.*[8] The same DEM tools, and the insight provided by which, were also used to initiate DEM-based investigations of creep between pebbles under thermal and mechanical loads.[7] While An *et al.* studied the pebble assemblies in rectangular and cylindrical containers bounded by a elastic walls, computational requirements prevented more

than a few thousand particles in the ensemble with rigid walls.[8] Following An's work, the DEM torch was passed across the pond to researchers at KIT where they began to improve upon the initial studies begun at UCLA.

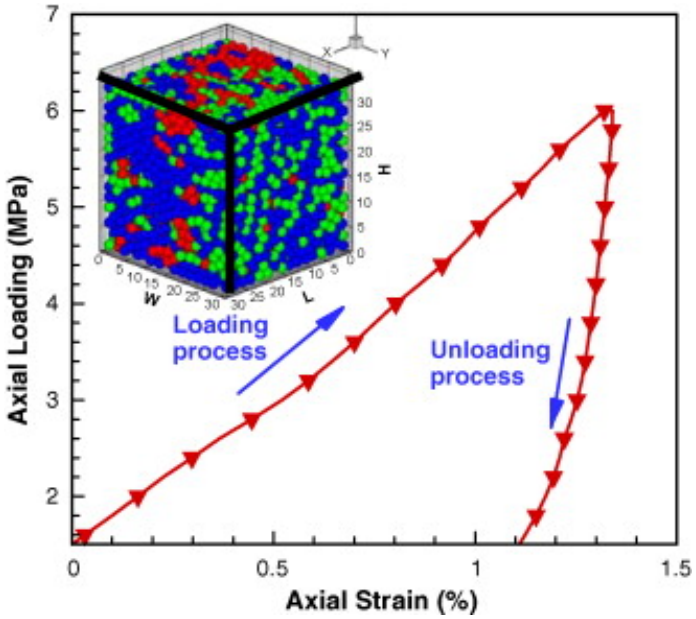

Figure 2.19: Stress–strain behaviors of granular materials in a rectangular box under uniaxial compaction from DEM are qualitatively matched to behaviors seen experimentally.

The effect of packing factor, geometry of the assembly on the overall stress-strain response under uniaxial compression tests (UCT) has been thoroughly investigated.[72] Gan *et al.* pebble assemblies in a cubic box with periodic boundary conditions to prevent the influence of boundaries dominating the ensemble response to loads.[79] In the DEM uniaxial compression studies (see Figure 2.19), a non-linear stress-strain response and a characteristic residual strain after unloading (analogous to plastic strain in continuum systems) is observed akin to the experimental results.[150] It was shown that the average coordination number, average normal contact force and the maximum normal contact force in the assembly has a unique functional relation (nonlinear, linear and linear, respectively) with the hydrostatic pressure or the applied pressure independent of the packing factor.[7,72] These functional relations may be used as master curves for the micro-macro correspondence in the pebble bed Thermomechanics studies.

Recently, the effect of the pebble size distribution on the overall thermomechanical behavior of the pebble assembly is studied by Annabattula *et al.*[11] They consider the pebble size distribution of ceramic breeder pebbles (Li_4SiO_4) with a diameter range of 0.25 mm-0.65 mm. Figure 2.20 shows a binary pebble assembly in a periodic box. The colors indicate stored elastic strain energy of the pebble (red: maximum and blue: zero). The assembly has a maximum pebble radius $r_g = 0.25$ mm with the pebble size ratio $r^* = r_s/r_g = 0.6$, relative volume fraction $V^* = V_g/V = 0.7$ and a packing factor $\eta = 0.643$. The average stress in a granular assembly can be deduced from the contact forces between individual grains.

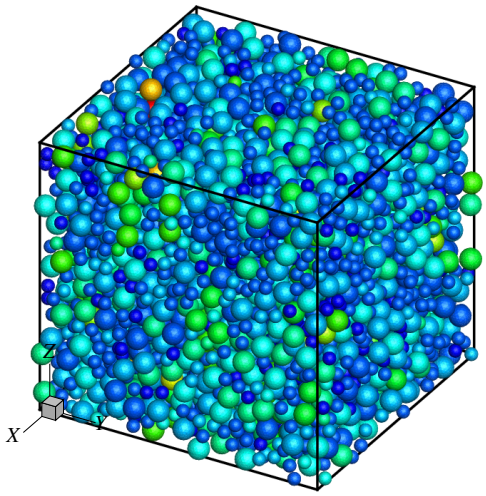

Figure 2.20: A binary pebble assembly with $r^* = 0.6$ and $V^* = 0.7$ showing the stored elastic energy of the pebbles at $\epsilon_{33} = 1.5\%$; pebbles of radius r_s (small) and r_g (large).

Another aspect of interest in the study of mechanics of pebble beds is the crush behavior of individual pebbles and their impact on the over all pebble bed response. DEM was used to study the behavior of a crushable pebble assembly with the crush load data for Li_4SiO_4 pebbles (for individual pebbles) measured at KIT for pebbles of diameter 0.5 mm.

A probabilistic method for analyzing the crush events of individual pebbles and a procedure with the combination of DEM and experimental data to obtain crush load probability has been reported by.[74] Figure 2.21 shows the cumulative distribution function as a function of the hydrostatic pressure placed on the bed. The probability analysis, derived from

DEM calculations, provides quantitative report of pebble crushing as a function of a specific hydrostatic pressure. The results of this analysis exemplify the growing strength of DEM techniques for analyses connecting global pebble bed loads to individual pebbles.

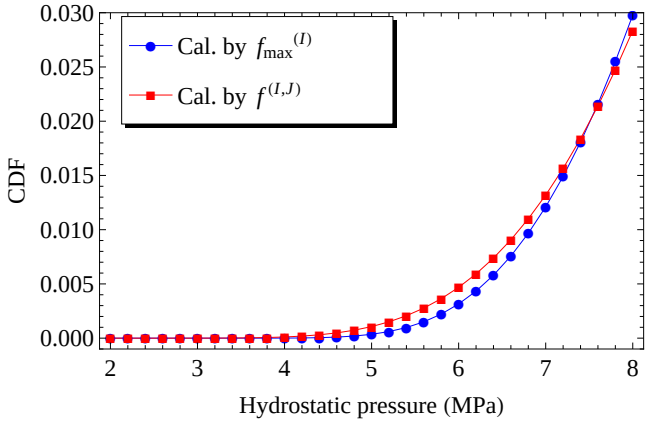

Figure 2.21: Cumulative distribution functions for crushing of individual pebbles inside the bed for as-fabricated pebbles, calculated by (1) maximum contact forces and (2) all inter-particle contact forces.[74]

However, it has been shown by Zhao *et al.* that a criterion based on critical stored elastic energy is a promising criterion for describing the Li_4SiO_4 pebble failure.[210,213] An alternative criteria is given in appendix C for reference, but has not been validated experimentally and is thus not included in this discussion. Hence, the crush load data (provided by fusion materials laboratory at KIT) has been transformed into equivalent elastic strain energy showing a Weibull distribution.[210] Critical energy, with randomly generated distribution, is used as the criterion for failure of pebbles in their DEM simulations. First, the assembly is loaded up to 3% strain in uniaxial compression and then unloaded to a stress-free state. The elastic modulus of the pebble is reduced, beginning from an initial value to a small value of 1 kPa, with increase in elastic strain energy of the pebble according to a phenomenological damage accumulation law.[12] The damage state is frozen at the end of loading step and hence there will be no further damage accumulation in the unloading step.

Figure 2.22 shows the results for two types of damage law each with three different realizations.[201] Each realization corresponds to a different random distribution of critical

energies assigned to the pebbles in the assembly. The results do not show appreciable sensitivity to random distribution of energies. In the case of gradual damage law, the reduction of the elastic modulus of the pebble starts when the stored elastic energy reaches 50% of the critical energy for that pebble and the elastic modulus reaches exponentially to its minimum value when the stored elastic energy reaches the critical energy prescribed. In the case of sudden damage this reduction starts at a much later stage when the stored elastic energy reaches 95% of the critical energy of the pebble. Clearly, the assembly with a sudden damage accumulation shows a higher maximum strength compared to the gradual damage. In the case of the gradual damage, the pebbles start to fragment at smaller strains than in the case of sudden damage. Hence the critical number of pebbles to fail for the onset of maximum strength is reached at lower strain values in gradual damage. It turns out that a mere 0.2% pebbles is the critical number for the onset of maximum strength, as manifest in observed stress plateaus.

The nature of damage evolution influences the strain at which the maximum strength is attained while the critical number of failed pebbles for this saturation is independent of the damage evolution law (also see[210]). Also note that the high frequency oscillations during loading in the stress-plateau region represent the failure of new pebbles. The analysis also shows a creep-like behavior of the stress-strain response and hence the stress-plateaus observed in experiments[150] may indicate the presence of pebble crushing in addition to the thermal creep mechanism. Furthermore, the residual strain after unloading is larger for the system with sudden damage than the system with gradual damage. It should be noted that the assembly with gradual damage has more number of damaged pebbles at the end of loading (at 3% strain) making the assembly more compliant than in the case of sudden damage.

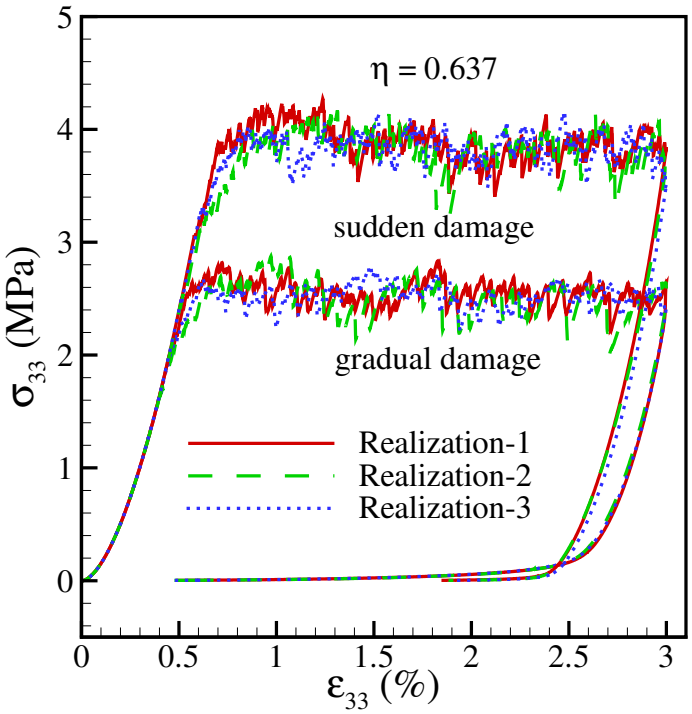

Figure 2.22: Stress-Strain response of a granular assembly under uniaxial compression for two different damage evolution laws (gradual and sudden). Each damage evolution criterion is simulated with three different realizations of randomly prescribed critical failure energy for individual pebbles following Weibull distribution. Reproduced from Ref.[201]

CHAPTER 3

Transient DEM Modeling of Solid-solid Contact Conductance and Packing Changes in Solid Breeder Pebble Beds

In this chapter thorough descriptions of mechanical and thermal interactions internal to packed beds and their governing equations as implemented with the discrete element method are given. We start with establishing a kinematics framework which simply states that physical granular interactions obey Newton's laws of motion, and the motion of interactions is integrated in time. Contact mechanics models then dictate the normal and tangential forces of interacting grains that feed into the generic kinematic equations; the choice of contact model thus largely dictates the overall behavior of the granular material. Granular heat conductance models are implemented in DEM which, too, is reliant upon the contact force modeling. Application of DEM as a tool for measuring thermomechanical interactions between pebbles for solid breeders is validated *via* numerical experiments to compare effective thermal conductivity with established measurements of effective thermal conductivity of lithium ceramic pebble beds. The contact model we use is based on Hertz's solution for elastic bodies, thus the elastic modulus of the grain is an important property for our models and we experimentally validate the application of Hertz Law; validation is possible with a new phenomenological model for the ceramic pebble elasticities. Lastly a technique for fragmentation modeling and investigate fragments and resettling in numeric ensembles is provided. The DEM model established in this chapter will form the basis for further development of tools for determining temperature distributions in solid breeder pebble beds.

3.1 Grain-scale Modeling

The observable, macroscopic behavior of particulate, or granular, systems is a complex function of myriad particle interactions. Historically, empirical relationships have been used to describe these systems as if continuous media, *e.g.* the correlations for heat transfer discussed in § 2.2. But with the advent of the discrete element method by Cundall & Strack and the acceleration of computing power, it became practical to investigate these granular materials at the particle scale without continuum assumptions.[42] With DEM, we track all the particles in the system in a Lagrangian manner. In the ensemble, the kinematics of each particle is tracked and updated based on balances (or imbalances) of forces or energy acting upon the particle.

3.1.1 Particle Dynamics

The grains in our system are allowed translational and rotational degrees of freedom. In a packed bed, we can restrict our attention to local forces between particles; neglecting, say, non-contact forces such as, van der Waals, electrostatic, or for the time being any fluid interaction forces. Assuming we know the contact forces acting upon particle i, Newton's equations of motion are sufficient to describe the particle kinematics. For translation and rotational degrees of freedom, the equations are:,

$$m_i \frac{\mathrm{d}^2 \mathbf{r}_i}{\mathrm{d}t^2} = m_i \mathbf{g} + \mathbf{f}_i \tag{3.1a}$$

$$I_i \frac{\mathrm{d}\omega_i}{\mathrm{d}t} = \mathbf{T}_i \tag{3.1b}$$

where m_i is the particle mass, $\mathbf{r}_i$ its location in space, $\mathbf{g}$ is gravity, I_i is the particle's moment of inertia, and ω_i its angular velocity.

The net contact force, $\mathbf{f}_i$, represents the sum of the normal and tangential forces from the total number of contacts, Z, acting on this grain.

$$\mathbf{f}_i = \sum_{j=1}^{Z} \mathbf{f}_{n,ij} + \mathbf{f}_{t,ij} \tag{3.2}$$

and the net torque, $\mathbf{T}_i$, is similarly,

$$\mathbf{T}_i = -\frac{1}{2}\sum_{j=1}^{Z} \mathbf{r}_{ij} \times \mathbf{f}_{t,ij} \tag{3.3}$$

When Cundall & Strack first proposed the discrete element method, they used a linear spring-dashpot structure which saw normal and tangential forces written as,

$$\mathbf{f}_{n,ij} = k_{n,ij}\delta_{n,ij}\mathbf{n}_{ij} - \gamma_{n,ij}\mathbf{u}_{n,ij} \tag{3.4a}$$

$$\mathbf{f}_{t,ij} = k_{t,ij}\delta_{t,ij}\mathbf{t}_{ij} - \gamma_{t,ij}\mathbf{u}_{t,ij} \tag{3.4b}$$

where Cundall & Strack defined the stiffness coefficients k as constants and local damping coefficients γ were proportional to them, $\gamma \propto k$, to allow dissipation of energy and the system to reach an equilibrium.

Relative normal and tangential velocities, respectively, are decomposed from particle velocities,

$$\mathbf{u}_{n,ij} = (-(\mathbf{u}_i - \mathbf{u}_j)\cdot\mathbf{n}_{ij})\mathbf{n}_{ij} \tag{3.5a}$$

$$\mathbf{u}_{t,ij} = (-(\mathbf{u}_i - \mathbf{u}_j)\cdot\mathbf{t}_{ij})\mathbf{t}_{ij} \tag{3.5b}$$

with the unit vector $\mathbf{n}_{ij}$ pointing from particle j to i

As in the solution of Hertzian interaction (see Appendix B), the surfaces of the two particles are allowed to virtually pass through each other (no deformation) resulting in normal and tangential overlaps of,

$$\delta_{n,ij} = (R_i + R_j) - (\mathbf{r}_i - \mathbf{r}_j)\cdot\mathbf{n}_{ij} \tag{3.6a}$$

$$\delta_{t,ij} = \int_{t_{c,0}}^{t} \mathbf{u}_{t,ij}\,\mathrm{d}\tau \tag{3.6b}$$

where the fictive tangential overlap, $\delta_{t,ij}$, is truncated to so the tangential and normal forces obey Coulomb's Law, $\mathbf{f}_{t,ij} \leq \mu_i \mathbf{f}_{n,ij}$ with μ as the coefficient of friction of the particle.

Thus the approach of DEM is relatively simple: calculate interaction forces between particles with Equation (3.4) based on the kinematics of velocity and position of interacting particles from Equation (3.5) and Equation (3.6), respectively, then update the positions

based on the forces. As DEM evolved and drew attention of more researchers, more complex formulas governing the spring-dashpot coefficients of Equation (3.4) emerged. But the core approach remained the same and the models all fall into the same family of so-called 'soft particle' models of DEM. A well-composed summary of the different DEM force models is given by Zhu *et al.*.[216]

The method used in this work fits into the computational skeleton of Cundall and Strack's method but with non-linear spring-dashpot coefficients defined by simplified Hertz-Mindlin-Deresiewicz model. In this model, the normal-direction stiffness coefficient of Equation (3.4a) is based on the Hertzian contact law (derived explicitly in Appendix B). The validity of Hertzian descriptions of normal forces is tested experimentally and reported in § 3.2.The tangential-direction stiffness coefficient follows from Brilliantov.[26,115,216] Together, the spring coefficients are,

$$k_{n,ij} = \frac{4}{3} E^*_{ij} \sqrt{R^*_{ij} \delta_{n,ij}} \tag{3.7a}$$

$$k_{t,ij} = 8 G^*_{ij} \sqrt{R^*_{ij} \delta_{t,ij}} \tag{3.7b}$$

where E^*_{ij} is the pair elastic modulus, G^*_{ij} is the pair bulk modulus, and R^*_{ij} is the relative radius. The terms are defined as,

$$\frac{1}{E^*} = \frac{1-\nu_1^2}{E_1} + \frac{1-\nu_2^2}{E_2} \tag{3.8a}$$

$$\frac{1}{R^*} = \frac{1}{R_1} + \frac{1}{R_2} \tag{3.8b}$$

$$\frac{1}{G^*_{ij}} = \frac{2(2+\nu_i)}{E_i} + \frac{2(2+\nu_j)}{E_j} \tag{3.8c}$$

Similar to Cundall & Strack's formulation, damping coefficients, γ, are included to account for energy dissipated from the collision of two particles.[52,176,177] Whether the damping coefficient is local or global and the exact form of the coefficient is more important for loosely confined granular systems and dictates the way the system approaches an equilibrium state.[124] For the case of our tightly packed pebble beds, it suffices to use the efficient form

of Refs.,[26,124,164,207,216]

$$\gamma_n = \sqrt{5}\beta_{\text{diss}}\sqrt{m^* k_{n,ij}} \tag{3.9a}$$

$$\gamma_t = \sqrt{\frac{10}{3}}\beta_{\text{damp}}\sqrt{k_{t,ij} m^*} \tag{3.9b}$$

with β_{damp} as the damping ratio, and the pair mass, $\frac{1}{m^*} = \frac{1}{m_i} + \frac{1}{m_j}$. For a stable system with $\beta_{\text{damp}} < 1$, the damping ratio is related to the coefficient of restitution, e, as

$$\beta_{\text{diss}} = -\frac{\ln e}{\sqrt{\ln^2 e + \pi^2}} \tag{3.10}$$

Systems to be solved by DEM models are therefore well-defined after specifying the few material properties of E, ν, ρ, and R_p and the interaction properties of μ and e.

Having expressed the contact mechanics of the discrete element method, we now must integrate the kinematic equations of the particles to resolve their evolutions. The most common means of marching in time with DEM is the velocity-Verlet algorithm.[111] In this algorithm, Equation (3.1) are integrated with half-steps in velocity, full steps in position, and then finally the full step in velocity. In practice, the two half-steps in velocity are often compressed into a single, full step. The computational time integration steps are given in explicit detail in Appendix E. Owing to the explicit nature of the velocity-Verlet algorithm, stability is a constant concern with DEM simulations. Stable, critical time steps and practical means of circumventing unreasonably small time steps are discussed in Appendix E.

A last note. Throughout this work, we required a fully quiesced bed to act as a starting point or demarcate a mechanically steady-state bed. To determine when this occurs, the total kinetic energy of the entire ensemble is monitored and a packed bed is considered to have completely settled once the magnitude of the system's kinetic energy is less than 10^{-8}. A similar process was independently determined in a similar matter in the work of Ref.[166]

3.1.2 Granular Heat Transfer in DEM

In a way analogous to handling particle momentums with Newton's laws of motion, Lagrangian tracking of particle energy is obtained *via* the first law of thermodynamics. Each

particle is treated as a single distinct object and thus internal temperature gradients are assumed negligible. The temperature of particle i is governed by

$$m_i C_i \frac{\mathrm{d}T_i}{\mathrm{d}t} = Q_{s,i} + Q_i \tag{3.11}$$

where m and C are the mass and the specific heat of the solid, respectively. Heat generation inside the particle is input with Q_s and the total heat transferred to/from particle i *via* conduction to all, Z, neighboring particles, is

$$Q_i = \sum_{j=1}^{Z} Q_{ij} \tag{3.12}$$

Assuming the particles are spherical, smooth, elastic, in vacuum, and we neglect radiation transfer between them, for two particles at temperatures T_i and T_j, we quantify the amount of energy transferred between them with a contact conductance, H_c:

$$Q_{ij} = H_c(T_i - T_j) \tag{3.13}$$

Batchelor & O'Brien[18] developed a formulation of similar form and then made a brilliant observation that "*when the radius of the circle of contact is so large that the heat flux through the thin annular matrix layer is negligible by comparison with that through the contact circle, the distribution of temperature inside the two particles is approximately the same as that of the velocity potential in irrotational flow of incompressible fluid through a circular hole in a plane wall.*" With the analogy, they made use of the fluid flow solution to write the total heat flux across the circle of contact as Equation (3.13) with heat conductance

$$H_c = 2k_s a \tag{3.14}$$

where k_s is the conductivity of the contacting solids and a is the radius of contact. Because we have assumed smooth, elastic, spherical solids, with Hertz theory (see Appendix B), contact radius can be found as a function of contact normal force, F_n,

$$a = \left(\frac{3}{4}\frac{R^*}{E^*}\right)^{1/3} F_n^{1/3} \tag{3.15}$$

where, as before, $\frac{1}{E^*} = \frac{1-\nu_1^2}{E_1} + \frac{1-\nu_2^2}{E_2}$ and $\frac{1}{R^*} = \frac{1}{R_1} + \frac{1}{R_2}$.

In the development of Equation (3.14), Batchelor & O'Brien had assumed the two contacting spheres to be of equal conductivity, k_s. Cheng *et al.*[34] proposed a slightly modified conductance which allows for contacting materials of different thermal conductivity. They give,

$$H_c = 2k^* a = 2k^* \left(\frac{3}{4}\frac{R^*}{E^*}\right)^{1/3} F_n^{1/3} \tag{3.16}$$

where $\frac{2}{k^*} = \frac{1}{k_i} + \frac{1}{k_j}$. As well as being a more general, flexible formulation, the models analyzed by Cheng *et al.*[34] are in good agreement with experiments.

The condition for validity of Batchelor & O'Brien's formulation of Equation (3.14) is in the limit where $\Psi \to \infty$, where[18]

$$\Psi = \frac{a}{R^*}\kappa \tag{3.17}$$

The term $\frac{a}{R^*}$, from Appendix B, is necessarily less than 1 for Hertz theory to be applicable. Thus for fluid in vacuum, the condition is identically satisfied but we must consider inaccuracies if we introduce an interstitial fluid with low conductivity ratios; for lithium ceramics in helium, the ratio is approximately $\kappa \approx 10$.

We step back from contact of a single pair of particles and consider a particle in an ensemble with many contacts. We must again consider the validity of applying Equation (3.16) at each contact. Vargas and McCarthy,[188] propose introducing a conduction Biot number to relate resistance of heat transfer internal to a particle with resistance between particles,

$$\mathrm{Bi}_c = \frac{H_c}{k^* d_p} = 2\frac{a}{d_p} \tag{3.18}$$

Then if $\mathrm{Bi}_c \ll 1$, the individual energy transferred between each point of contact can be decoupled. The Biot number criteria is already satisfied for Hertz theory to be valid; having assumed that $\frac{a}{d_p} \ll 1$. Therefore the total heat transferred out of a single particle with Z contacts, due to contact conductance, is the summed contribution of individual contacts,

$$Q_i = \sum_j^Z Q_{ij} \tag{3.19}$$

For the case when we do *not* have a perfectly smooth elastic sphere, we use the approach of Bahrami *et al.*, introducing a joint thermal resistance to develop a modified heat conductance

term. Bahrami *et al.*[15] use a joint thermal resistance of the superposition of macroscopic and microscopic influences; the thermal joint resistance is

$$R_j = R_s + R_L \tag{3.20}$$

where the subscript L refers to macroscopic variables and s refers to microscopic ones. Bahrami *et al.* used the constriction formulation of Yovanovich *et al.* to express the macroscopic resistance as[203]

$$R_L = \frac{(1 - a/R^*)^{3/2}}{2k_s a} \tag{3.21}$$

If the contact of the two materials obeys Hertz contact law, then $a/R^* \ll 1$ and the above becomes

$$R_L = \frac{1}{2k_s a} \tag{3.22}$$

which matches the heat conduction form of Batchelor & O'Brien,[18] Equation (3.14).

To determine the thermal resistance of the asperities in contact, Bahrami *et al.* used a superposition of many cylindrical constrictions inside of the contact area. The result is given in[15] as

$$\psi_s^* = \begin{cases} \left(\frac{\pi H' R^{*2}}{F}\right)^s & F_c = 0 \\ (R^*/a)^2 (H'/P_0)^s (1 + s\gamma) & F \leq F_c \\ (H'/P_{0,c})^s (1 + s\gamma_c) + \left[\frac{\pi H' R^{*2}}{(F - F_c)}\right]^s & F \geq F_c \end{cases} \tag{3.23}$$

where ψ_s^* is a non-dimensional form of the surface roughness thermal resistance, defined as $\psi_s^* = 1.25\pi R^{*2} k^* (m/\sigma)\psi_s$, k^* is the harmonic mean of contact grains thermal conductivity, H' is the Vicker's microhardness value, F is the contact force, P_0 is the maximum pressure of contact, s is a parameter based on the hardness constants, $\gamma = 1.5(P_0/P_{0,H})(a/a_H)^2 - 1$, F_c is the critical force where $a = R^*$, γ_c is the value of γ at the critical force, m is the mean absolute surface slope, and σ is the root-mean-square (rms) surface roughness. For Hertzian contact, $\gamma = 0.5$.

Antonetti *et al.* proposed a correlation for mean absolute surface slope related to surface asperities as[13]

$$m = 0.125(\sigma \times 10^6)^{0.402} \tag{3.24}$$

where the range of applicability of surface roughness is $0.216 \times 10^{-6}\,\mathrm{m} \leq \sigma < 9.6 \times 10^{-6}\,\mathrm{m}$. Thus the term $\sigma/m = 0.031\sigma^{0.598}$

For Hertzian contacts of the non-conforming ceramic materials, $F \ll F_c$, thus we consider only that case to write

$$R_s = \frac{(R^*/a)^2 (H'/P_0)^s (1 + s/2)}{1.25\pi R^{*2} k^* (0.031\sigma^{0.598})} \tag{3.25}$$

or

$$R_s = \frac{(H'/P_0)^s (1 + s/2)}{1.25\pi a^2 k^* \, (0.031\sigma^{0.598})} \tag{3.26}$$

For Hertzian contact, the maximum pressure is given by Equation (B.14). It is

$$P_0 = \frac{2E^*\delta_n}{\pi a}$$

Furthermore, as noted by Bahrami *et al.*, the parameter s is in the range of $0.95 \leq s \leq 0.97$. Therefore it is approximated as $s = 0.96$ here. The thermal resistance of Equation (3.26) is rewritten in a simplified form,

$$R_s = \left(\frac{H'}{E^*\delta_n}\right)^{0.96} \left(\frac{\sigma}{m}\right) \frac{1}{1.720 k^* a^{1.04}} \tag{3.27}$$

The macroscopic and microscopic thermal resistances given in Equation (3.22) and Equation (3.27), respectively, are combined to give the total joint thermal resistance of

$$R_j = \left(\frac{H'}{E^*\delta_n}\right)^{0.96} \frac{0.031\sigma^{0.598}}{1.720 k^* a^{1.04}} + \frac{1}{2k^* a} \tag{3.28}$$

and the total thermal conductance between the two grains, $H_j = 1/R_J$, is

$$H_j = \left[\left(\frac{H'}{E^*\delta_n}\right)^{0.96} \frac{0.031\sigma^{0.598}}{1.720 k^* a^{1.04}} + \frac{1}{2k^* a}\right]^{-1} \tag{3.29}$$

In the limit of zero roughness, the first term inside the bracket tends to 0 and the conductance is simply the Batchelor & O'Brien form with Hertzian assumptions of perfectly smooth elastic spheres. In our DEM model, we employ a flag to choose between the simple smooth assumption for heat conductance, Equation (3.14), or the more advanced conductance equation, Equation (3.29), if we have known hardness and roughness properties for ceramics. In practice, the hardness and roughness properties are, as yet, unknown for lithium ceramic materials and most studies in this work are done with smooth sphere approximation.

3.1.2.1 Thermal Expansion

The stresses which will act upon the solid breeder volume during operation of the fusion reactor arise from the differential rate of thermal expansion from the highly heated ceramic volume and the relatively cool structural container. Moreover, thermal settling motion is observed in pebble beds with cyclic heating.[32,53,175,189] Both of those phenomena originate from effects of thermal expansion of individual grains in the ensemble. Therefore, we introduce a simple thermal expansion method into the DEM structure that updates the diameter of each particle as,

$$d_{p,i} = d_{p_0,i}\left[1 + \beta_i \left(T_i - T_0\right)\right] \tag{3.30}$$

where β_i is the thermal expansion coefficient (in units of $1\,\mathrm{K}^{-1}$), T_i is the temperature of the pebble at the current step, and $d_{0,i}$ is the initial diameter of the pebble at temperature T_0. The update of pebble diameter based on thermal expansion could be computed at every time step as it is not computationally expensive. Nevertheless, flexibility in the code allows computation at an arbitrary interval of time, typically every $\frac{N}{\Delta t} = \frac{10^4}{10^{-7}}$ in most models of ceramic pebble beds).

3.1.3 Numerical Implementation of DEM

The primary computational tool used in this study is LAMMPS (Large-scale Atomic/Molecular Massively Parallel Simulator),[144] a classical molecular dynamics code. The package of code, maintained by Sandia National Labs (http://lammps.sandia.gov), has many features making it particularly attractive for our use of granular material simulations. LAMMPS is open-source and written in highly-portable C++ allowing customization of any core modeling feature. LAMMPS runs with distributed-memory message-passing parallelism (MPI) and provides simple control (manual or automatic) of the spatial-decomposition of simulation domains for parallelizing. Perhaps most importantly, LAMMPS provides an efficient method for detecting and calculating pair-wise interaction forces; the largest consumer of run-time in the DEM algorithm.[144] We build the LAMMPS core as a library to allow coupling LAMMPS features to other numerical tools. The scripting language of Python (Python 2.7)

to write parent routines that pass information between LAMMPS objects while accessing all of Python's numeric and scientific libraries (*e.g.* NumPy and SciPy).

LAMMPS by default provides a rudimentary method of modeling of granular particles (the term 'granular' in LAMMPS vernacular simply differentiates the discrete element of molecules or atoms from larger-scale granular particles of powders or pebbles); LAMMPS has been used for studying granular material since at least 2001 when Silbert *et al.* studied granular flow on inclined planes.[167] However, the usefulness of LAMMPS for studying granular systems was greatly enhanced by LIGGGHTS (LAMMPS Improved for General Granular and Granular Heat Transfer Simulations), a suite of modules included on top of LAMMPS. LIGGGHTS has many academic and industrial contributors from around the world, with the code maintained as open-source by DCS Computing, GmbH.

Briefly, some notable features that LIGGGHTS brings to the LAMMPS environment include: built-in Hertz/Hooke pair styles with shear history, mesh importing for handling wall geometry, moving meshes, stress analysis of imported meshes, a macroscopic cohesion model, a heat transfer model, and improved dynamic load balancing of particles on processors.[107,108] Both LIGGGHTS and LAMMPS are distributed under the open-source codes under terms of the Gnu General Public License.[67] LIGGGHTS is compiled with modified source files of heat transfer to account for the introduction surface roughness given in Equation (3.29).

3.1.4 Benchmarking Solid-Solid Conductance Models for Pebble Beds

For validation, we will compare numeric calculations of effective thermal conductivity to the few experimental campaigns which measured effective thermal conductivity of packed beds in vacuum. For comparison, in Figure 2.11a, we saw the effective thermal conductivity of a pebble bed, in near-vacuum conditions, is measured by Enoeda *et al.* as approximately $k_{\text{eff}} = 0.2\,\text{W}\,\text{m}^{-1}\,\text{K}^{-1}$ for Li_4SiO_4at 517 °C. Aquaro & Zaccari also measured the effective conductivity in vacuum, over a range of external pressures.[14] Their results are reproduced in Figure 3.1. The effective conductivity of Li_2TiO_3 pebble beds are seen to increase from approximately $k_{\text{eff}} = 0.2\,\text{W}\,\text{m}^{-1}\,\text{K}^{-1}$ to $k_{\text{eff}} = 0.3\,\text{W}\,\text{m}^{-1}\,\text{K}^{-1}$ over the range of external

pressures, 0 MPa to 7 MPa. The solid-solid conductance modeling of DEM can be seen as

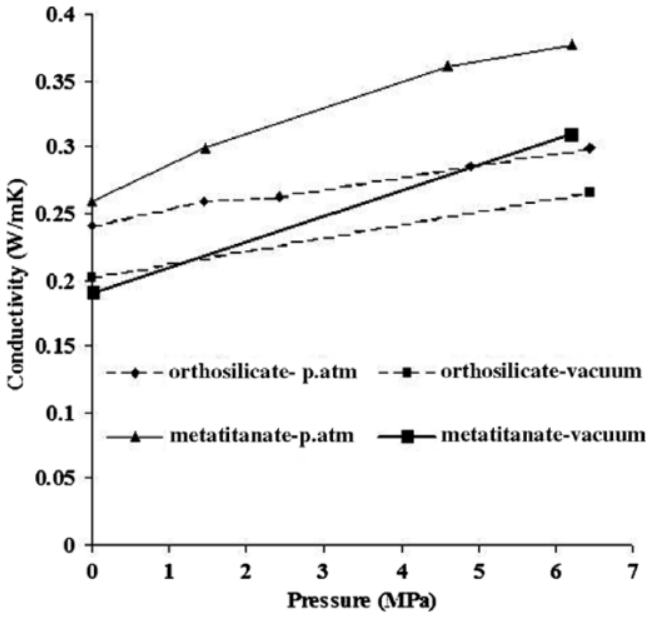

Figure 3.1: Effective conductivity of Li_2TiO_3 and Li_4SiO_4 in air and vacuum environment conditions. Reproduced from Ref.[14]

the vacuum limit when no influence of interstitial purge gas is present; the results of DEM should therefore then be in the range of 0.2 MPa to 0.3 MPa.

A recent thermal DEM study has been performed by Gan *et al.* which analyzed temperature profiles in pebble bed regions reflecting the European design of helium-cooled pebble bed.[8] In their work, they use the more generic form of heat conductance provided by Batchelor & O'Brien,[18]

$$H_c = 2\pi \frac{k_s}{\kappa} R^* \mathscr{H}(\kappa, \Psi) \tag{3.31}$$

where $\kappa = k_s/k_g$ as defined above; $\mathscr{H}(\kappa, \Psi)$ is a function of (i) the flux across contact circle, (ii) the difference between the flux across the matrix layer and the total flux between particles in point contact, and (iii) the conductivity ratio κ. In the limit of $\Psi \to \infty$ (see Equation (3.17)), $\mathscr{H} \to \frac{\kappa a}{\pi R^*}$ and thus Equation (3.14) is recovered.

For the case of $\phi = 0.645$, the temperature profile for mono-sized pebbles is reproduced in Figure 3.2.

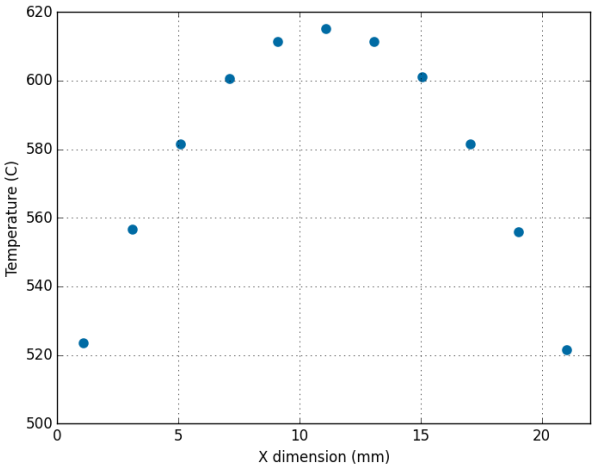

Figure 3.2: Temperature profile across a pebble bed from Ref.[8]

An effective thermal conductivity can be calculated from the data given by Gan *et al.* and using Equation (3.38). For the case of $\phi = 0.645$, an effective thermal conductivity is found to be $k_{\text{eff}} = 4.37\,\text{W}\,\text{m}^{-1}\,\text{K}^{-1}$. In the heat conductance term used by Gan *et al.*, contribution of helium is accounted for in near-contact regions of pebbles and thus the effective thermal conductivity determined from these beds should be higher than the values of vacuum, yet the value of $4.37\,\text{W}\,\text{m}^{-1}\,\text{K}^{-1}$ is exceedingly high, given the stress state in the pebble bed after heating is calculated as only 5.7 MPa. The effective conductivity was not reported in paper of Gan *et al.* and consequently no discussion on why the value is so large is given.

To validate the heat transfer capabilities of our DEM models, a three-dimensional pebble bed consisting of mono-dispersed particles of diameter d_p is analyzed. The particles are constrained by rigid y-z-planes at locations of $\frac{x}{d_p} = \pm 10$ (the walls of the container). There are periodic boundary conditions in the y-direction located at $\frac{y}{d_p} = \pm 5$. Gravity acts in the negative z-direction and the particles are resting on a rigid x-y-plane at $z = 0$ (the floor of the container) and held from the top by an x-y-plane at approximately $\frac{z}{d_p} = 50$ (the roof of the container). The precise height of the container is chosen to satisfy the requested initial packing fraction. Several initial packing fractions are chosen, $\phi_i = [59,\ 61,\ 62,\ 64]\%$ with 6875. The volume is chosen to represent the long, tall, narrow channels seen in many solid breeder module designs.[35,56,145]

Table 3.1: Material properties used in validation study of k_{eff} for Li_2TiO_3.

E (GPa)	ν	k ($W\,m^{-1}\,K^{-1}$)	C ($J\,kg^{-1}\,K^{-1}$)	α (K^{-1})
60	0.24	2.4	1156	15×10^{-6}

For this study, the material properties were chosen to represent Li_2TiO_3 pebbles, however the thermal properties of Li_4SiO_4 are roughly equal and this validation also applies to pebble beds of that material as well. All the properties come from Ref.,[78] though a modified elastic Modulus . They are summarized in Table 3.1

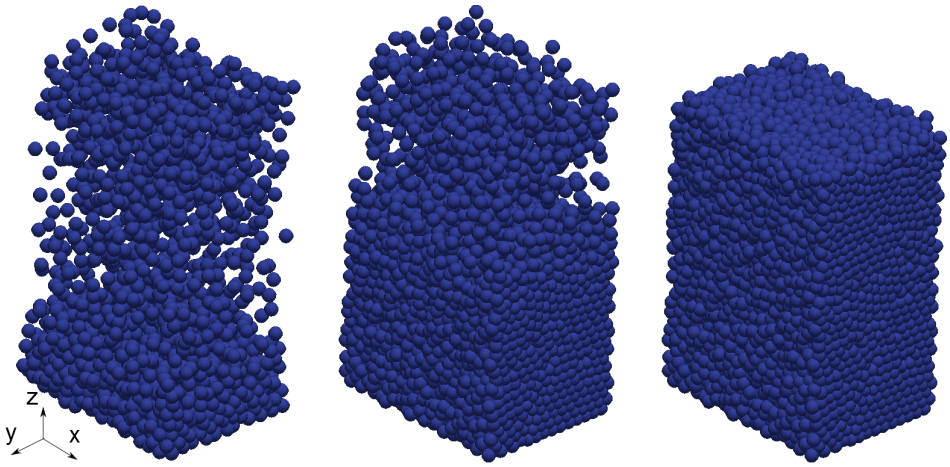

Figure 3.3: Demonstrating the pouring process of pebbles into the control volume with at an early time (left), when it is nearly filled (middle) and after the pebbles have settled to negligible kinetic energy (right).

The first attempt to pack the bed followed from the 'recipes' we had used in physical experiments in the lab. That is, the pebbles were numerically poured into the volume from above and allowed to settle under their own weight (see Figure 3.3), then the volume was vibrated while a roof was lowered to compact the system to $\phi = 0.64$, the desired packing fraction. This technique was ultimately abandoned in place of a less realistic but more computationally efficient technique which resulted in comparably packed beds.

In the preferred method, N particles are inserted randomly, with large spacing, into

a volume with an expanded y-direction. Gravity is not initialized and the coefficient of friction of the pebbles is set to $\mu = 0$. The system boundaries wrapped around the y-limits are slowly compressed until they reach the desired volume is obtained (as specified above). In the absence of friction, the pebbles move easily next to each other during the compression and there is no stored tangential forces when the pebble bed is 'packed'. Next, the coefficient of friction is increased to a realistic level, $\mu = 0.2$, and gravity in the system is initialized. The bed is then allowed to come to rest, as measured by the kinetic energy of the system. At this point, the pebble bed is considered to be packed and the system state is saved, to be loaded into the heating routine.

To simulate the conditions of a solid breeder in a fusion reactor, where the heat is removed from the pebble bed *via* contact to the containing structure, a constant temperature of T_c is assigned to the vertical walls. Nuclear heating of the pebbles is simulated through a constant source term on each pebble. A representative heating rate of $Q_s = \frac{q'''_p}{\phi_0}$, where $q'''_p = 8$ MW/m^3 and $\phi_0 = 0.64$.[8] The heating cycle runs until a thermal steady state is reached. Based on a measurement of the total thermal energy of the bed, $E_T = \sum_i^N m_i C_i T_i$, steady-state is determined as $\frac{\mathrm{d}E_T}{\mathrm{d}t} = 0$ within a specified tolerance. Once at steady state, effective thermal conductivity of the beds is analyzed for comparison to experimental data on pebbles in vacuum.

Based on the boundary conditions of the system, the heat transfer becomes symmetric and one-dimensional in the x-direction from $x = 0$ to the walls at $\frac{x}{d_p} = \pm 10$. The pebble bed has negligibly small variation of forces and temperatures in the y-direction due to the periodic boundary condition at the edges of the domain. Gravity effects are minor in the overall heat transfer and induce only a slight z-dependency to the results. Taking advantage of the pebble bed temperature profile's resemblance to a one-dimensional heat transfer problem to calculate an effective conductivity from an analytic, one-dimensional test case analogy.

Assuming a one-dimensional pebble bed, to find an effective conductivity, we step back into a continuum mechanics formulation where the pebble bed can be represented as a slab of solid material. We can analytically solve for the temperature equation in a slab with heat generation, symmetry about the centerline, and a constant boundary temperature condition.

At steady-state, the temperature of a material with constant temperature boundary conditions ($T(L) = T_s$), constant thermal conductivity (k_{eff}), and nuclear heating (q''') obeys the following equation

$$0 = \frac{\mathrm{d}^2 T}{\mathrm{d}x^2} + \frac{q'''}{k_{\text{eff}}} \tag{3.32}$$

In nondimensional form, the temperature is

$$\theta = \frac{T(x) - T_s}{T_0 - T_s} \tag{3.33}$$

where T_0 is the temperature at the centerline of this slab (a value found momentarily). The length is nondimensionalized as

$$x^* = \frac{x}{L} \tag{3.34}$$

Thus Equation (3.32) in nondimensional form is,

$$0 = \frac{\mathrm{d}^2 \theta}{\mathrm{d}x^{*2}} + G \tag{3.35}$$

where

$$G = \frac{q''' L^2}{k_{\text{eff}}(T_0 - T_s)} \tag{3.36}$$

In the nondimensionalized form, the solution is revealed to be purely geometric,

$$\theta = 1 - x^{*2} \tag{3.37}$$

as $T_0 - T_s = \frac{q''' L^2}{2k_{\text{eff}}}$. The nondimensional temperature solution of Equation (3.37) is used to prove the one-dimensional assumption of heat transfer is justified for the pebble beds.

Noting that in this continuum mechanics formulation, we are assuming that the nuclear source, q''' term is applied evenly over the entire volume. In our DEM formulation, our source term applies to a single pebble, $Q_s = \frac{q'''}{\phi}$.

From the solution of Equation (3.35), we find the effective conductivity to be

$$k_{\text{eff}} = \frac{q''' L^2}{2(T_0 - T_s)} \tag{3.38}$$

I use this formulation of Equation (3.35) to analyze and compare the pebble beds.

For our representative pebble bed, after applying the nuclear heating and wall cooling, the steady-state temperature distributions of some representative volumes are given in Figure 3.4. Evident in all three pebble beds, though increasingly so for smaller packing fractions, are loose pebbles that have poor mechanical contact with neighboring pebbles and therefore have arbitrarily high temperatures (the magnitude is only limited by the time of the simulation). We refer to these pebbles as 'rattlers'. The phenomena of hot rattlers is possible in DEM simulations because there is no other method of heat removal. This is a strong argument for the need to include helium purge gas in the thermal transport models of ceramic pebble beds. If these hot rattlers persist even in the presence of helium, it could lead to an unfavorable performance of the ceramic solid breeder – the hot rattlers would sinter and prevent the outgassing of tritium, among other issues. The observation of these isolated pebbles is another motivator for the coupling of DEM to thermo-fluid models. In Figure 3.4, we also see that, intuitively, the more loosely packed the pebble bed, the higher the temperatures.

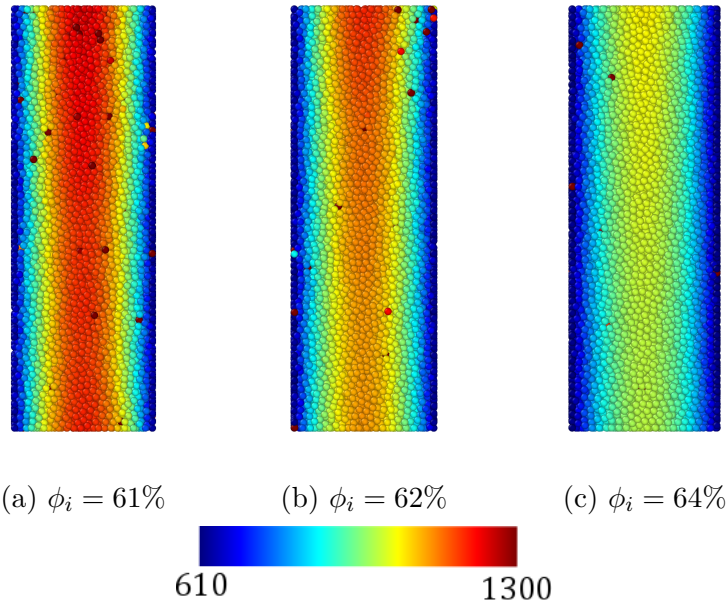

(a) $\phi_i = 61\%$ (b) $\phi_i = 62\%$ (c) $\phi_i = 64\%$

Figure 3.4: Temperature distributions in representative packed beds with given initial packing fraction.

In order to calculate an effective conductivity of the pebble bed, we find an average temperature profile through the bed. Average values of the bed, along the x direction, are

generated *via* averaging temperatures in bins. We create bins that are volumes slices of width Δx that extend through the limits of the y- and z-directions. We then find the n pebbles residing in the slices and take the mean value of their temperatures. The average, given by Equation (3.39), is also shown as the solid lines in Figure 3.6. The binned average temperature is

$$\langle T \rangle = \frac{1}{n} \sum_{i}^{n} T_i \tag{3.39}$$

Using the volume slices, average contact forces are also found,

$$\langle F^{1/3} \rangle = \frac{1}{n} \sum_{i}^{n} F_{n,ij}^{1/3} \tag{3.40}$$

Van Lew *et al.* showed that the largest parameter governing the effective conductivity of a granular material like a packed bed is the magnitude of contact forces between pebbles.[184] In Figure 3.5, we see the distribution of contact forces as scatter points. The binned average along x is also plotted in the black line. Figure 3.5a is given as reference for a pebble bed for which the packing fraction does not completely fill the volume when the pebble bed quiesces. At $\phi_i = 59\%$ there are regions of gap between the top layer of pebbles and the container, as a result the contact forces are on the order of the accumulated weight of the pebbles in the volume. For packing fraction of $\phi_i = 61\%$, we have a relatively well-packed pebble bed with small average contact forces, $\langle F_n \rangle = 5.9\,\mathrm{N}$. At an initial packing fraction of $\phi_i = 64\%$, *for the geometry of this bed*, we see somewhat larger average contact forces, $\langle F_n \rangle = 25.9\,\mathrm{N}$. In large-volume experiments on pebble beds, such a large contact force would be indicative of being under slight compression and, as such, we expect the effective thermal conductivity of the bed to be larger than the well-packed case of $\phi_i = 61\%$. The effective thermal conductivities are given in the temperature plots of Figure 3.6.

From Figure 3.6, we see that even the most compliant well-packed bed of case $\phi_i = 0.61$, the effective thermal conductivity is more than three times larger than the measured effective conductivity from experimental data.[57] We will see that part of this discrepency is due the current model not accounting for surface roughness of pebble material. For the simulations generating the data of Figure 3.6, the smooth particle contact conductance model of Batchelor & O'Brien was used (see Equation (3.16)). In experimental measurements of

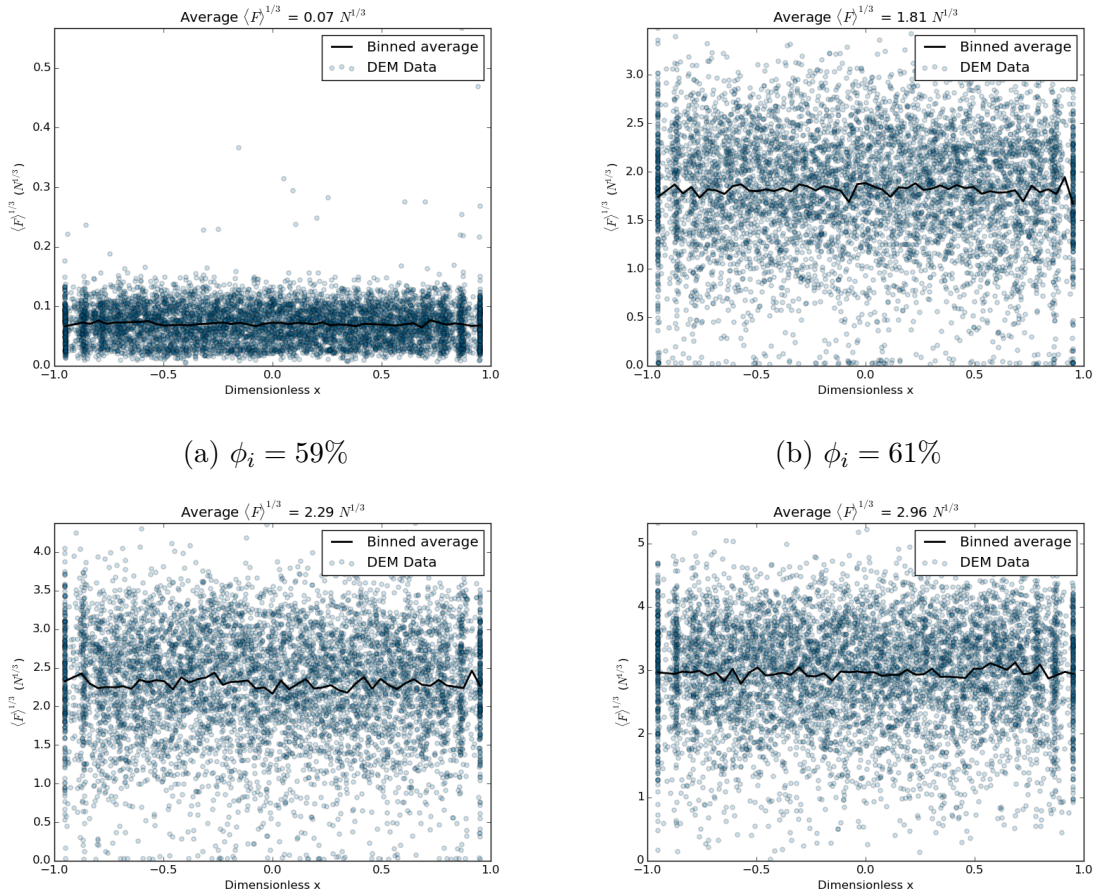

(a) $\phi_i = 59\%$

(b) $\phi_i = 61\%$

(c) $\phi_i = 62\%$

(d) $\phi_i = 64\%$

Figure 3.5: Contact forces in the initially packed beds .

effective thermal conductivity with roughness, at small loads, effective thermal conductivity of face-centered cubic steel spheroids in an air environment reduced approximately 25% between cases between a smooth surface ($\sigma = 0.03\,\mu\text{m}$) and rough ($\sigma = 1.7\,\mu\text{m}$).[28] In spite of the lack of data for roughness of the specific pebbles used in the experiments of Enoeda *et al.*, we will see that including surface roughness, *via* Equation (3.29), allows our DEM models to obtain comparable effective thermal conductivities.

Following ranges of values found in a variety of experimental data,[15] we can choose average parameters for roughness. The asperity height, ranging in experiments from 0.12 µm to 13.94 µm; we use an average value of $\sigma = 5\,\mu\text{m}$. Vickers hardness is reported for Li_2TiO_3 as $H = 363(1 - 2.36\epsilon)$ MPa, where $0.1 \leq \epsilon \leq 0.3$ is the porosity of the bulk ceramic; with

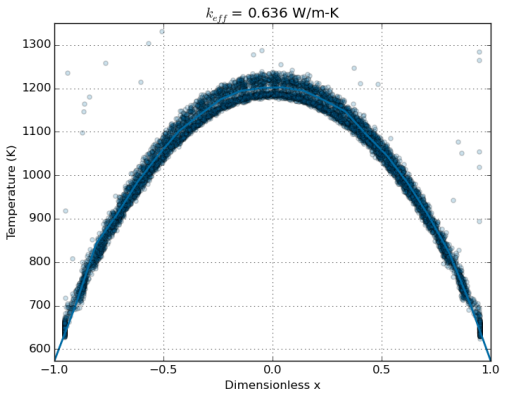

(a) $\phi_i = 61\%$

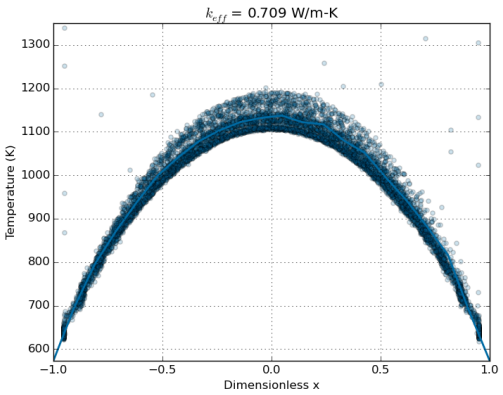

(b) $\phi_i = 62\%$

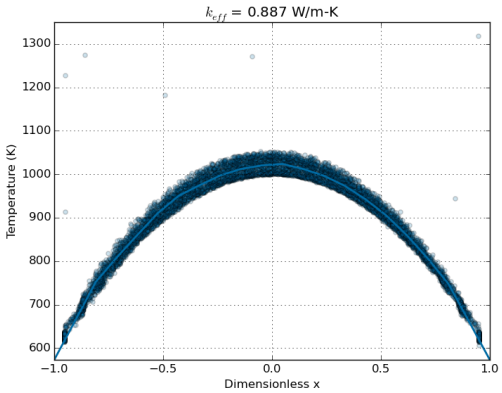

(c) $\phi_i = 64\%$

Figure 3.6: k_{eff} for the packed beds is higher than values measured in experiments in vacuum.

$\epsilon = 0.2$, $H = 192\,\text{MPa}$.[78,159] However, it is unclear if the reported value is the microhardness or macrohardness (as defined by ASTM E384). Surface microhardness can be much larger than bulk hardness.[16] Regardless, for this study we set the microhardness value equal to $H = 192\,\text{MPa}$. No Vickers hardness data has been reported for Li_4SiO_4. Using the placeholder roughness values, we use Equation (3.29) form of conductance to run the above cases again.

Before discussing the results of effective thermal conductivity with roughness, we analyze the effect of the above roughness parameters in order to have an understanding of what to expect in packed beds with rough-surface pebbles. We normalize the heat conductance of

Equation (3.29) by the smooth-sphere conductance of Equation (3.16),

$$\Gamma = \frac{H_j}{H_c} = \frac{\frac{1}{2k^*a}}{\left(\frac{H'}{E^*\delta_n}\right)^{0.96}\frac{0.031\sigma^{0.598}}{1.720k^*a^{1.04}} + \frac{1}{2k^*a}} \tag{3.41}$$

Therefore we see from Equation (3.41) that Γ is a quantification of reduction in heat conductance due to roughness parameters. Using the a hardness of $H = 15\,\text{GPa}$, we then find heat conductance reduction, Γ as a function of contact force (which determines the value of a) and asperity height, σ. The contour of Γ is given in Figure 3.7.

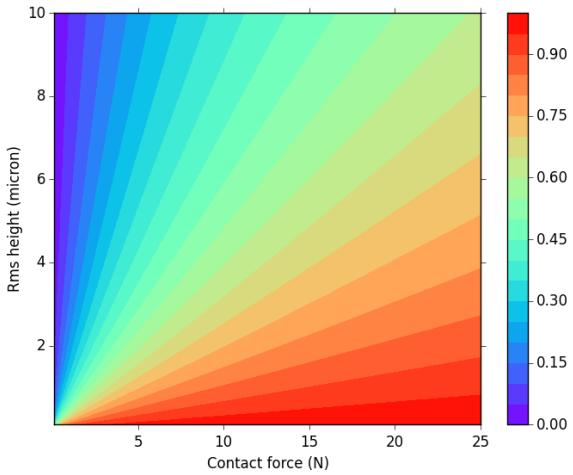

Figure 3.7: Colorbar gives value of Γ, the measure of reduction in heat conductance comparing calculations with roughness and smooth sphere approximations.

The bed initially packed to $\phi_i = 0.64$, had average contact forces of about 25 N. According to Figure 3.7, at that force level, with an asperity of 5 µm, contact heat conductance of a rough pebble is 75% of a similar contact between smooth pebbles. The bed packed to $\phi_i = 0.61$ had average contact forces of 5.9 N; in this case heat conductance has been reduced approximately 45% from the smooth approximation. The total effective thermal conductivity is the macroscopic result of heat conductance between all pebbles and can not be linearly extrapolated from heat conductance of any single contact, nonetheless, the measure of Γ provides insight into approximate scales of reduction in effective thermal conductivity we should expect when roughness is taken into account.

Temperature distributions in pebble beds with roughness, along with measures of effective thermal conductivity are given in Figure 3.8. Accounting for roughness of the pebbles in contact, the effective thermal conductivity of numeric pebble beds approaches the value found in experimental studies of pebble beds in vacuum. When the initial packing fraction is $\phi_i = 0.61$, the effective thermal conductivity falls to $k_{\text{eff}} = 0.398\,\text{W}\,\text{m}^{-1}\,\text{K}^{-1}$, which compares quite well to experimental measurement of $k_{\text{eff}} = 0.2\,\text{W}\,\text{m}^{-1}\,\text{K}^{-1}$.

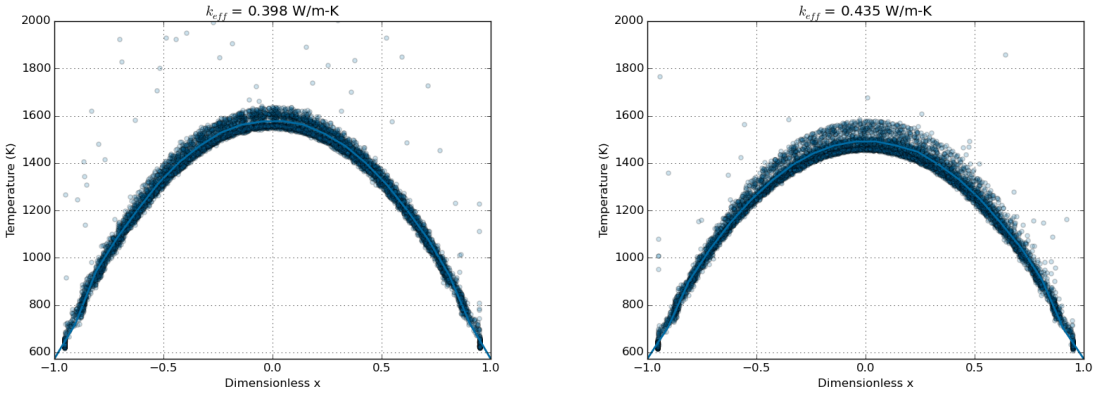

(a) $\phi_i = 61\%$ (b) $\phi_i = 62\%$

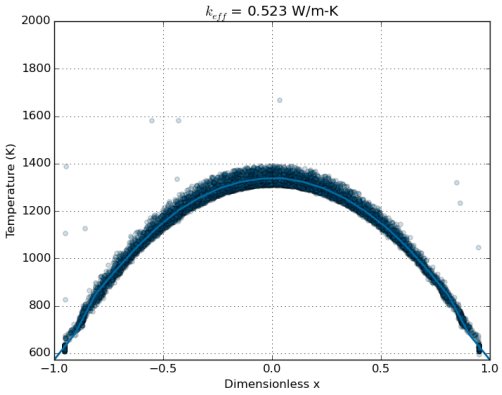

(c) $\phi_i = 64\%$

Figure 3.8: k_{eff} with roughness for given initial packing fractions. Reduced initial packing fractions had lower initial contact forces and therefore effective conductivity values closer to experimentally measured ones.

The effective conductivities of models with the smooth-sphere and roughness approximations are plotted together in Figure 3.9. For reference, the grey bar indicates the window of

experimental measurements for effective conductivity in vacuum.

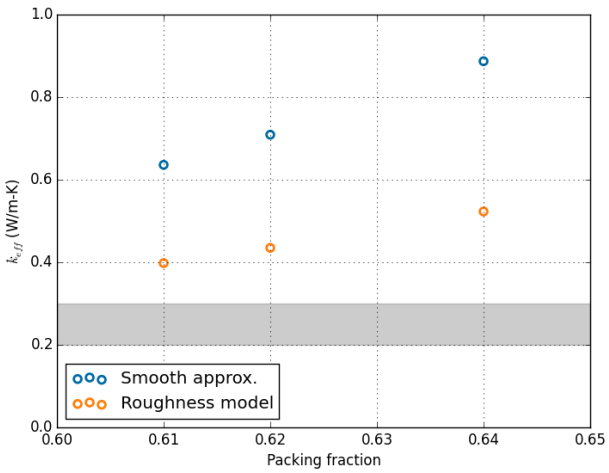

Figure 3.9: Comparison of effective conductivity measurements for Li_2TiO_3.

The combination of microhardness and asperity height resulted in substantial drops in the effective thermal conductivity of these representative pebble beds. The reductions in effective conductivity were 37%, 39%, and 41% for initial packing fractions of 61%, 62%, and 64%, respectively. While these reductions make the effective conductivity calculated with DEM approach the experimental measurements for pebble beds in vacuum, the values are still more than 25% higher. The Vicker's microhardness value used in this study could be measured again for other production techniques of lithium ceramics and variations in that value could lead to DEM results that approach even closer to experimental values. Moreover, the arbitrarily-chosen rms asperity height needs to be measured for ceramic pebbles for more accurate roughness contact resistance modeling. Lastly, the majority of ceramic pebbles produced for solid breeders have non-perfect sphericity, some are ovoid or ellipsoidal. However, in the current implementation of DEM, the pebbles are all perfectly spherical. The impact on effective thermal conductivity with geometric variations of the packing material is fertile grounds for future studies.

3.2 Elastic Modulus Implementation in DEM for Ceramic Pebbles

The discrete element method has been used by many ceramic breeder researchers to model the interaction of individual pebbles in an ensemble.[7,12,72,120,184,210] In the past studies, the elastic modulus of the ceramic materials used in DEM simulations was taken from historical data, for instance lithium metatitanate from Ref.[78] Furthermore, the assumption of Hertzian descriptions of normal contact for the pebbles is also assumed to be true without direct validation. In our experimental test stand for crushing individual pebbles, shown in Figure 3.10, our equipment was able to record accurate measurements of the force-travel relationship for each pebble. Using the data, we will directly test the validity of Hertzian contact laws for describing interactions of lithium ceramics.

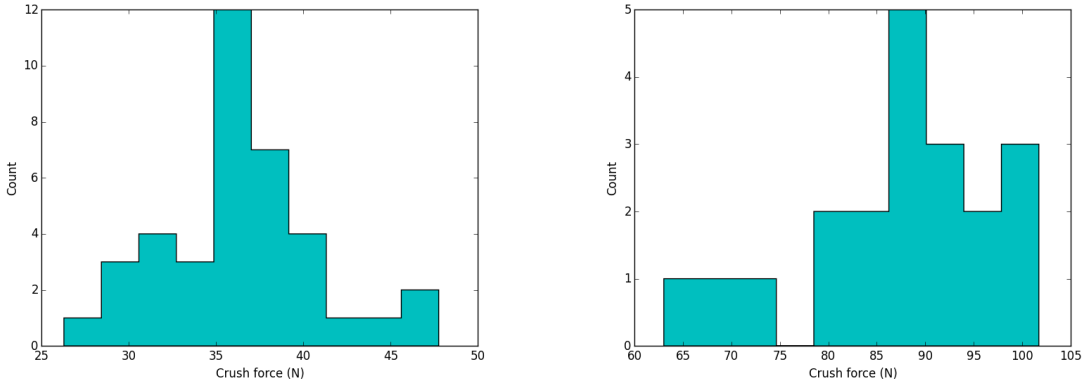

(a) $\bar{d}_p = 1$ mm (b) $\bar{d}_p = 1.5$ mm

Figure 3.10: Crush forces of Li_2TiO_3 pebbles display probability distributions around mean values for each average diameter batch.

The derivation of the Hertz force can be found on page 237. The result is given again here for reference:

$$F_{n,ij} = \frac{4}{3} E^*_{ij} \sqrt{R^*_{ij}}\, \delta^{3/2}_{n,ij}$$

and, again, the pair elastic modulus and radius are

$$\frac{1}{E^*} = \frac{1-\nu_i^2}{E_i} + \frac{1-\nu_j^2}{E_j}$$
$$\frac{1}{R^*} = \frac{1}{R_i} + \frac{1}{R_j}$$

In experiments where we press a ceramic pebble between two anvils, we measure the travel, s, of the crosshead rather than the pebble overlap. We modify Equation (B.16) to be represented in terms of travel ($s = 2\delta$). Furthermore, for a pebble ($R_i = R_p$) in contact with a smooth plane ($R_j \to \infty$), the relative radius is simply $R^* = R_p = d_p/2$. We write the elastic modulus of the pebble as E_p and for the test stand's anvil as E_s; similarly for the Poisson ratios of the two materials. The Hertz force acting upon a pebble between anvils is then expressed as a function of the pebble and anvil properties as,

$$F = \left[\frac{1}{3} \frac{\sqrt{d_p}}{\frac{1-\nu_p^2}{E_p} + \frac{1-\nu_s^2}{E_s}} \right] s^{3/2} \tag{3.42}$$

The elastic modulus and Poisson ratio of the test stand are known values that do not vary between pebble experiments. Similarly, in the application of Hertz theory, we also assume the elastic modulus and Poisson ratio of the ceramic are also known and constant. In that case, *for any given pebble diameter*, the term inside the bracket ought to be composed entirely of constants for any given pebble; there would therefore be a single force-travel response possible – based only on s. Using material properties given in Ref.[78] for Li_2TiO_3, we plot a set of parametric curves based on diameter over a range of travel. The properties we have used for the nickel-alloy anvil of our test stand and Li_2TiO_3 are given in Table 3.2. The curves are given in Figure 3.11.

Table 3.2: Material properties used for Li_2TiO_3 and nickel-alloy platen

E_{peb} (GPa)	ν_{peb}	E_{stand} (GPa)	ν_{stand}
126	0.24	220	0.27

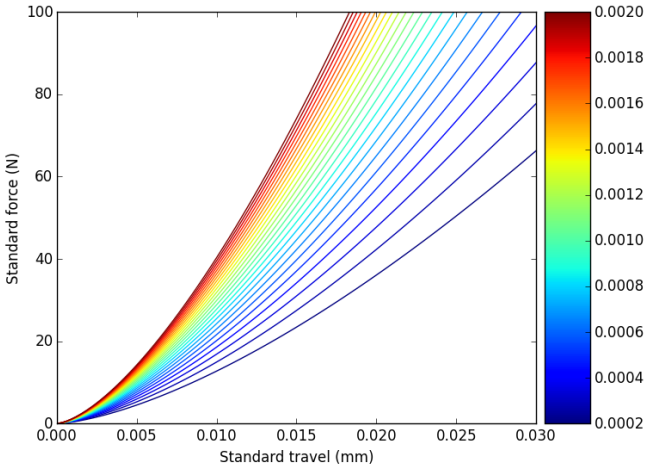

Figure 3.11: Hertzian responses of Li_2TiO_3 pebbles compressed between platens. The colormap shows pebble diameters in m. The diameters span an order of magnitude from $d_p = 0.2\,\text{mm}$ to $d_p = 2\,\text{mm}$.

Figure 3.11 shows that, for a given pebble, that is strictly obeying Hertz theory, there is only a single force-displacement curve it can follow. However, during our experiments on Li_2TiO_3 pebbles, we observed behavior such as the curves shown in Figure 3.12. The diameters of the pebbles are mapped to the colormap on the right side of the figures. These pebbles are responding much different than the expected Hertzian curve, predicted by Equation (3.42).

We can confirm that the force-travel relationship goes as $F \propto s^{3/2}$ by plotting the force-travel data on log-log plots; the slope of the data represents the power relationship of force and travel. The log-log plots are given in Figure 3.13. The slope of the response is calculated for each experimental curve and a histogram is collected in Figure 3.14. For both sets of Li_2TiO_3 pebbles, the data is heavily centered around a slope of $n = 1.5$, validating the dependence of force on travel as fitting Hertzian predictions.

We propose the experimental curves of force travel can be explained *via* unique reductions in elastic modulus of each pebble. We introduce an 'apparent' elastic modulus for each pebble which is iteratively found as the elastic modulus which provides the best fit when used in Equation (3.42) and compared to force-travel responses from experiments. The apparent

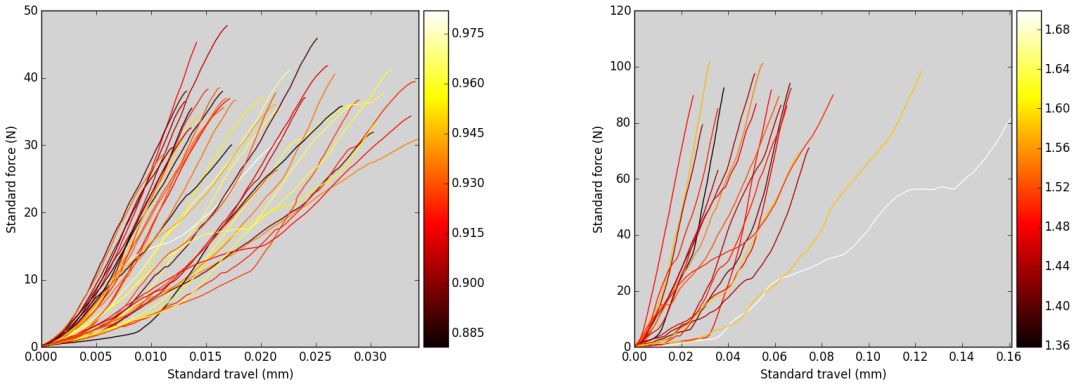

(a) $\bar{d}_p = 1$ mm (b) $\bar{d}_p = 1.5$ mm

Figure 3.12: Experimental measurements of pebble force as a function of cross-head travel.

elastic modulus is reported normalized against the Li_2TiO_3 elastic modulus from literature, E_{lit},

$$\kappa = \frac{E_{\text{peb}}}{E_{\text{lit}}} \tag{3.43}$$

where we introduce κ as a softening coefficient. The sintered pebble value of elastic modulus for Li_2TiO_3 is taken from Ref.[80] to be $E_{\text{lit}} = 124\,\text{GPa}$. Iterating over apparent elastic modulus, the L2-norm of the difference between Hertzian and experimental curves is used as the 'error'. The L2 norm, A for a given array, a is

$$||A||_F = \left[\sum_{i,j} \text{abs}(a_{i,j})^2\right]^{1/2} \tag{3.44}$$

This is a convenient way to compare the error at every point along the force-displacement curves. When the error is minimized, the apparent elastic modulus is recorded and a softening coefficient is calculated. A Hertzian curve (in black), using the apparent elastic modulus in Equation (3.42), is plotted alongside its respective experimental curve in Figure 3.15

The majority of the curves for two batches of Li_2TiO_3 pebbles analyzed (Figure 3.15) fit well to Hertzian curves with apparent elastic moduli. Apparent elastic moduli of the Li_2TiO_3 pebbles are given in Figure 3.16. Histograms of κ for two batches of Li_2TiO_3 are given in Figure 3.17. The distributions for both batches of Li_2TiO_3 pebbles more closely resemble Snedecor's F distribution with many pebbles behaving with a very small κ, then a

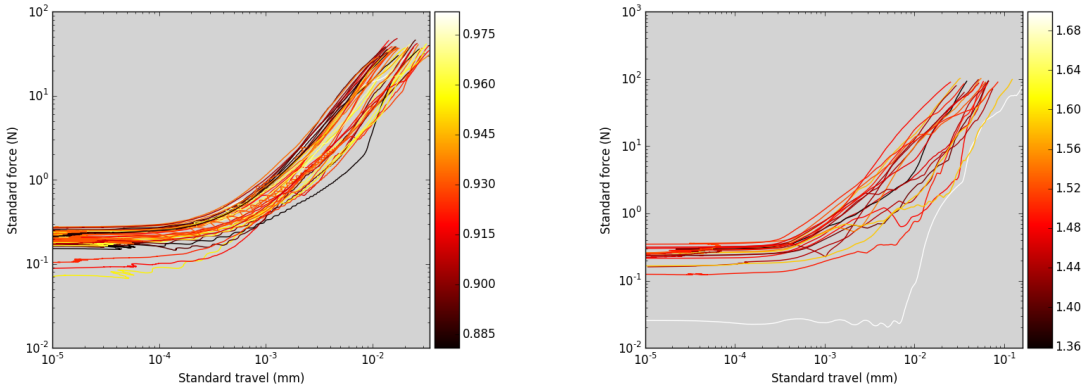

(a) $\bar{d}_p = 1$ mm (b) $\bar{d}_p = 1.5$ mm

Figure 3.13: Log-log plots of experimental measurements of pebble force as a function of cross-head travel.

long tail of few pebbles with large κ.

In Figure 3.18 we see scatter plots of the pebble diameters against κ values for the different batches of lithium ceramic pebbles. A Pearson Correlation value was calculated for each of the batches to quantify a correlation between diameter and κ. For the Li_4SiO_4 pebbles, we find $R = 0.198$ which is a weak positive correlation. For the Li_2TiO_3 pebbles we have $R = -0.385$ for $\bar{d}_p = 1$ mm and $R = -0.201$ for $\bar{d}_p = 1.5$ mm. Both of these are weakly negatively correlated.

We hypothesize that manufacturing processes of pebbles leads to slightly different internal structures in the ceramic. Those differences yield stronger or weaker pebbles in a probability around a mean value, as seen in Figure 3.10a. Different internal structure would then also cause each pebble to behave with different stiffness. Thus if the elastic modulus in Equation (3.42) for the batch of pebbles had a probability distribution, rather than a single value, we can account for the variations in responses of Figure 3.12.

The results of these single pebble experiments indicate that the elastic modulus traditionally used in DEM simulations for ceramic pebble beds in solid breeders is incorrect. Numerical re-creations of the probability distribution curves will be used to apply κ to pebbles in the ensemble. From the weak correlations between diameter and κ, we are free to

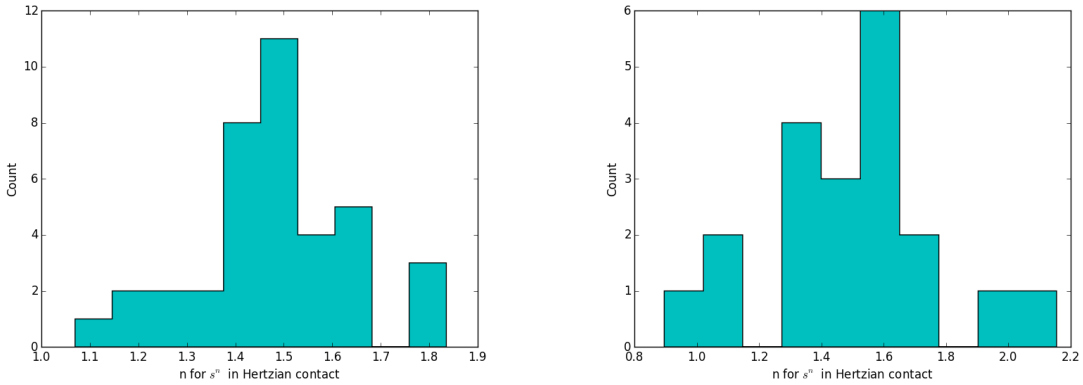

(a) $\bar{d}_p = 1$ mm (b) $\bar{d}_p = 1.5$ mm

Figure 3.14: Slopes from the log-log plots of experimental measurements of pebble force as a function of cross-head travel show the relation is approximately $F \propto s^{1.5}$.

ignore any diameter dependence when assigning κ values in the DEM framework, especially in light of the current implementation of monodisperse pebble beds. Therefore, numerically, when assigning elastic moduli to the particles in the ensemble, the κ distribution will be applied in a random fashion.

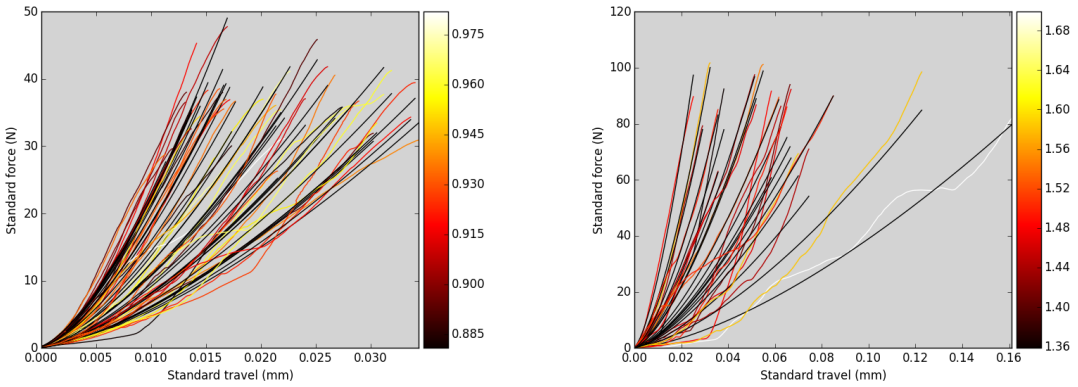

(a) $\bar{d}_p = 1$ mm (b) $\bar{d}_p = 1.5$ mm

Figure 3.15: Force-displacement curves for Li_2TiO_3 pebbles (in color) along with their Hertzian fits (in black) calculated with each pebble having a unique elastic modulus.

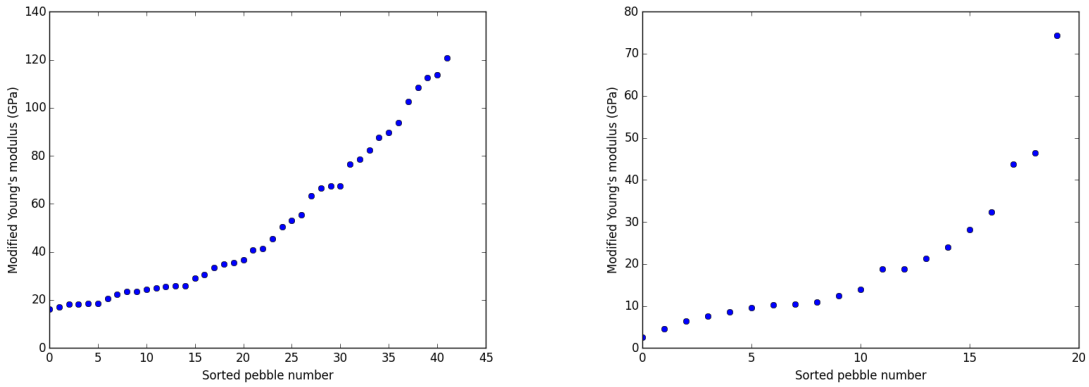

(a) $\bar{d}_p = 1$ mm (b) $\bar{d}_p = 1.5$ mm

Figure 3.16: Distribution of modified elastic modulus for a batch of Li_2TiO_3 pebbles. All pebbles responded to compression with a elastic modulus well below the sintered pellet value of 126GPa.

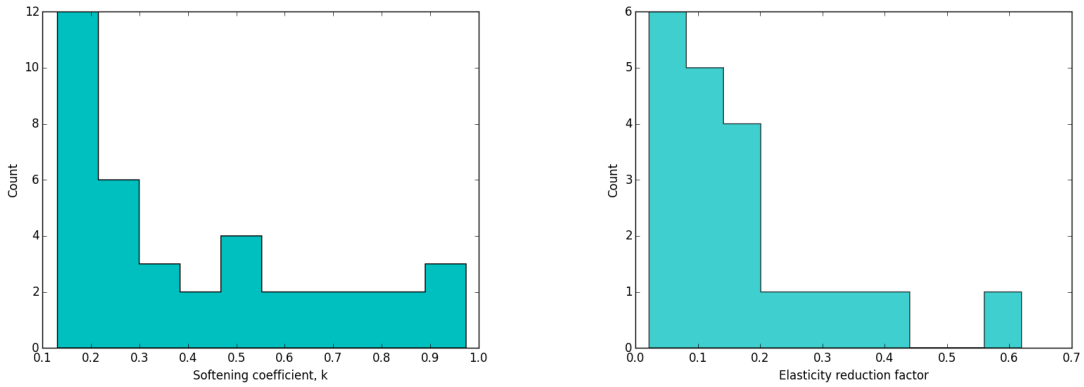

(a) $\bar{d}_p = 1$ mm (b) $\bar{d}_p = 1.5$ mm

Figure 3.17: Histogram of κ for two batches of Li_2TiO_3 pebbles. All pebbles responded to compression with a elastic modulus well below the sintered pellet value of 126GPa.

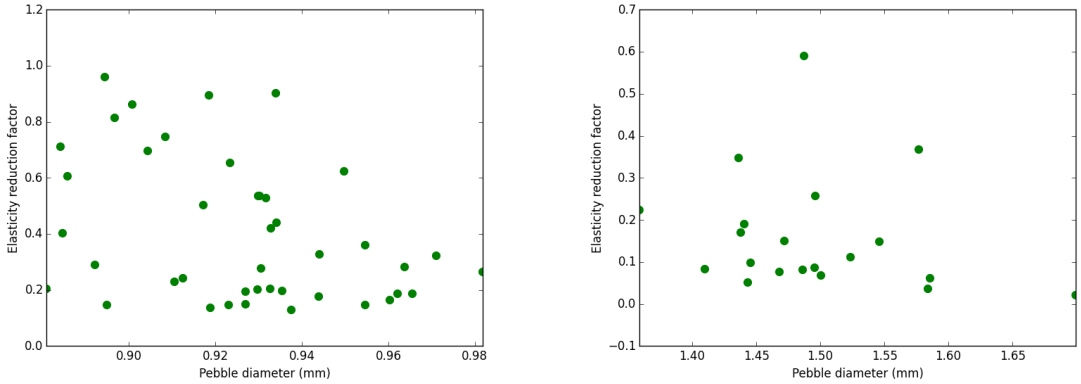

(a) $\bar{d}_p = 1$ mm (b) $\bar{d}_p = 1.5$ mm

Figure 3.18: Scatter of κ against pebble diameter for two batches of Li_2TiO_3 pebbles showing almost no relationship between apparent stiffness and diameter.

3.2.1 Elastic Modulus Influence on Mechanical Response of Pebble Beds

Proper calculation of normal force in DEM simulations is critical for accuracy in heat transfer modeling, as seen in Equation (3.16), as well as accuracy in predictions of pebble crushing, as will be shown in § 3.3. We showed in the previous section that Hertzian contact is generally valid for describing pebble interactions. The Hertzian force is linearly proportional to the pair elastic modulus of contacting spheres. Based on the softening coefficient, κ, values found in § 3.2, the apparent elastic moduli of Li_4SiO_4 and Li_2TiO_3 are, on average, less than half the values given for sintered materials in literature. For the case of Li_2TiO_3, the average value was closer to only 10% of the value from literature. Thus the actual contact forces in pebble beds may be 10% of the values found from DEM simulations with incorrect elastic modulus! In this section, we compare a number of pebble beds modeled with DEM using different elastic moduli.

We first simulate uniaxial compression tests on pebble beds. One set of beds will be composed of pebbles with the single elastic modulus from literature and the other set will be composed of pebbles with a distribution of elastic moduli that fit the distribution from experiments. The second set of numerical experiments will simply compare the effective thermal conductivity of pebble beds as a function of elastic modulus.

3.2.1.1 Uniaxial Compression Simulations: Numerical Setup

The pebble beds are modeled as undergoing a standard uniaxial compression up to 6 MPa while measuring the macroscopic stress-strain for some parametrically varied pebble beds. At the moment of maximum stress, we can investigate the differences in contact forces of the different pebble beds.

Our pebble ensemble is composed of 0.5 mm diameter Li_4SiO_4 pebbles. The pebble beds are initiated and packed in the same manner as § 3.1.4. There are two main bed groups. Set A: three beds (A.1-3) containing a single type of pebble with $E = 90$GPa. Set B: four beds (B.1-4) containing ten types of pebbles with their elastic modulus assigned in a discrete, random way to satisfy the distribution seen from experimental data. For the DEM study,

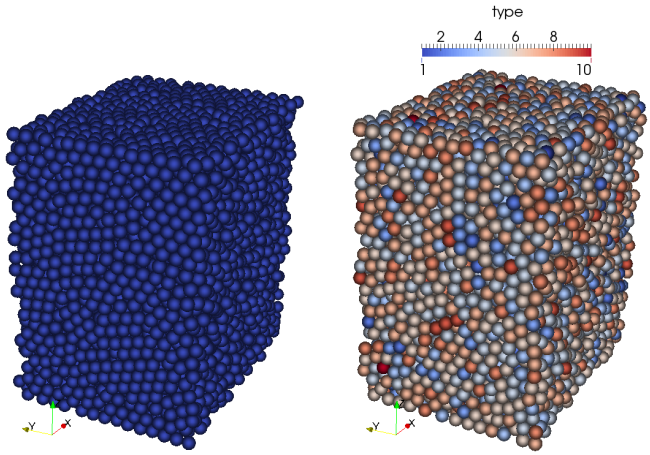

Figure 3.19: On the left, set A, a pebble bed with a single type, of $E = 120$ GPa. On the right, set B, is a pebble bed with 10, randomly distributed types; each type corresponds to a reduced, apparent elastic modulus as derived from experimental data.

Li_4SiO_4 pebbles are fit with a Weibull distribution of shape parameter $\sigma = 1.6$ where the average stiffness was $\bar{E} = 49$ GPa. The description of the two sets of pebble beds is visually represented in Figure 3.19. The pebble bed geometry was also the same used in the study of Ref.[184] : two virtual walls in the x-direction located at $x_{\text{lim}} = \pm 20R_p$, periodic boundaries at the limits of $y_{\text{lim}} = \pm 15R_p$, and a total of 8000 pebbles packed into the volume to an approximate height of $z_{\text{lim}} = 20R_p$.

Among both sets, a parametric study was done on pebble radius and coefficient of friction. The radii of pebbles in beds A.1, A.2, B.1, and B.2 were constant at R_p=.25 mm. The radii of pebbles in beds A.3, B.3, and B.4 followed a Gaussian distribution about $\bar{R}_p = 0.25$ mm: $\mu_d = R_p$ and $\sigma_d = R_p$. The coefficient of friction was set at $\mu = 0.2$ for beds A.1, A.3, B.1, and B.3; the coefficient of friction was $\mu = 0.3$ for beds A.2, B.2, and B.4.

3.2.1.2 Uniaxial Compression Simulations: Results

A constant-velocity, uniaxial compression was applied to the pebble beds. A single cycle up to 6 MPa then down to 0 MPa was used on all the beds. The macroscopic measurements of stress-strain are shown for all the pebble beds in Figure 3.20.

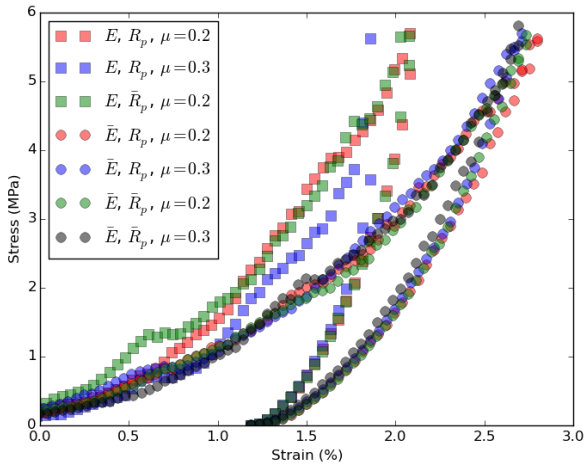

Figure 3.20: Stress-strain responses of pebble beds with: squares, constant elastic modulus; and circles, Gaussian distribution of elastic modulus. The constant elastic modulus beds all had much firmer responses for all parametric cases studied here.

Naturally, the pebble beds with smaller elastic s modulus (with circle markers) are more compliant to external loads. The result is true regardless of the coefficient of friction or distribution of pebble radius studied here. Group B moved to an average strain of about 2.6% at 6 MPa, by comparison the beds of Group A only had strained 1.9% on average to reach the same stress. Among the beds of each group, pebble beds with constant radius pebbles behaved virtually the same as similar pebble beds with a Gaussian distribution on radius. An increase in the coefficient of friction had a moderate impact on the overall stress-strain response.

The parametric study here shows that the largest contributor to stress-strain response is the elastic s modulus. The coefficient of friction and radius distribution had comparatively insignificant influence. A pebble bed geometry more directly comparable to oedometric compression experiments should be used to allow direct comparison and validation of the numerical models.

At the point of peak stress for each bed, DEM results are used to visualize the distribution of contact forces among all pebbles in the ensemble. A plot of the probability distributions of all the beds together, Figure 3.21, shows that the majority of the contacts in all the beds

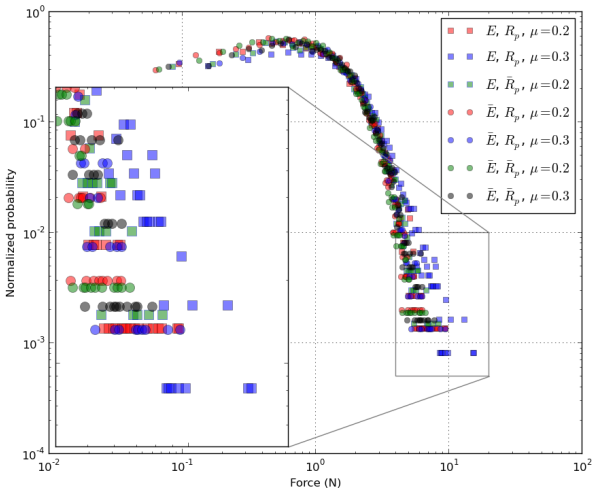

Figure 3.21: Probability distribution of contact forces in all the pebble beds studied here. Elastic moduli value is the largest contributor to higher peak contact forces among pebbles.

are equally small. There are a few overall trends we observe from the results however. The pebble beds with the constant elastic modulus are always higher for their comparable version with distributed elastic modulus. For pebble beds with comparable elastic moduli and radii, higher coefficients of friction generally have higher peak contact forces. Pebble beds' radius distributions have much less impact on peak contact forces than either coefficient of friction or elastic s modulus. Another method of comparing overall contact force distributions is to consider predictions on pebble cracking which assigns a strength value at random to pebbles in the bed (details are given in § 3.2). At the point of maximum stress, this is done and the results are shown in Table 3.3.

While overall the predicted number of broken pebbles is small, we compare similar parameteric pebble beds and in each case pebble beds with modified elastic s modulus overall predict smaller percentages of broken pebbles. Pebble crushing is a major topic for the overall evaluation of the feasibility of ceramic pebble beds in fusion reactors. This study reveals that past DEM work on pebble crushing, such as Ref.,[10,12,212] were likely over-predicting the extent of crushing if the elastic modulus used in the study was much larger than the realistic response of individual pebbles.

Table 3.3: Comparisons for the two styles of elastic moduli used in the study.

Bed label	Parameters	Predicted crushed %
A.1	E, R_p, $\mu = 0.2$	0.3
A.2	E, R_p, $\mu = 0.3$	1.0
A.3	E, $\bar{R}_p$, $\mu = 0.2$	0.9
B.1	$\bar{E}$, R_p, $\mu = 0.2$	0.6
B.2	$\bar{E}$, R_p, $\mu = 0.3$	0.8
B.3	$\bar{E}$, $\bar{R}_p$, $\mu = 0.2$	0.4
B.4	$\bar{E}$, $\bar{R}_p$, $\mu = 0.3$	0.7

3.3 Pebble Damage Modeling

To address pebble damage, there are two major modeling tasks: (i) predictive models for pebble crush events and (ii) modeling fragmentation after a crush event. For (i), the task is to develop a model to relate inter-particle pebble forces in an ensemble to measured crush loads of pebbles from experiments. Appendix Appendix C discusses predictive models developed in the fusion community as well as other theory behind a predictive model developed recently at UCLA. To address (ii), models must exist which simulate damage pebbles; *i.e.* a scheme to treat a cracked, shattered, or crushed pebble in the assembly as small particles, removed particles, or particles with modified material properties.

Modeling of 'crushed pebbles' in numerical assemblies has been attempted by a number of researchers. In most cases, indirect changes to the simulation are done with the hope of matching macroscopic features of beds that are observable in assemblies with damaged pebbles. In work by Marketos and Bolton, they treated a crushed pebble very similar to Van Lew *et al.*; when a pebble was damaged it was removed completely from the assembly.[126,184] Marketos and Bolton study the stress-strain response of a pebble bed with a predictive crushing routine while Van Lew *et al.* studied the effective thermal conductivity of a damaged pebble bed.

Annabattula *et al.*, noting the computationally expensive approach of modeling small fragments, introduced damaged pebbles *via* reduction in elastic modulus.[12] Annabattula *et al.* was also interested in the mechanics of the pebble bed with the presence of crushable materials. The study highlighted the differences in behavior of assemblies with different failure criteria and initial packings. From Figure 3.23, results are qualitatively similar to the stress-strain curves depicted by Marketos *et al.*.

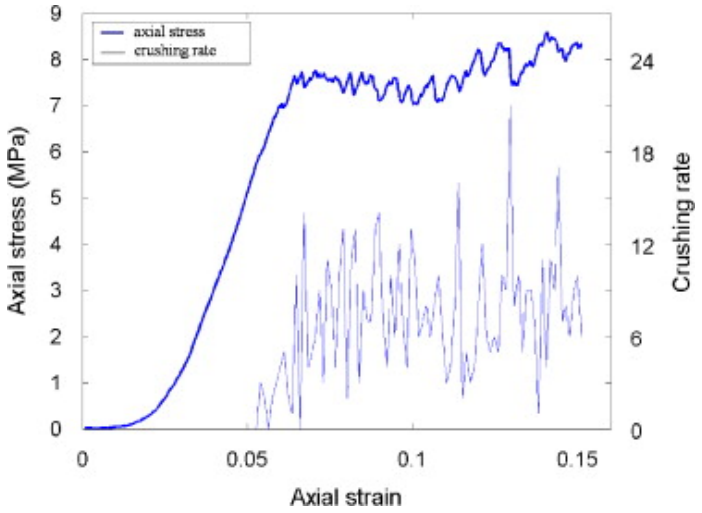

Figure 3.22: Stress-strain response of a pebble bed with crushed pebbles modeled with removal of pebbles from assembly. Reproduced from Ref.[126]

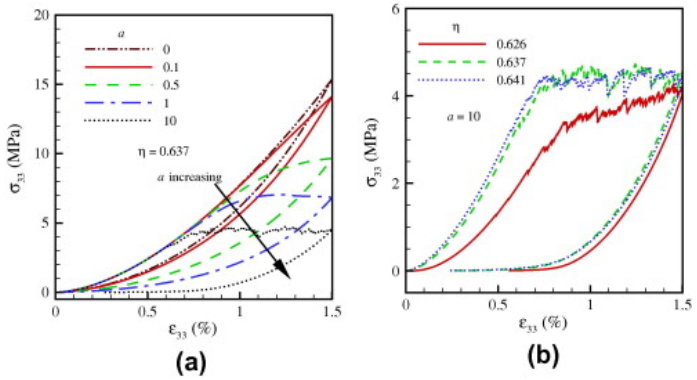

Figure 3.23: Stress-strain response of a pebble bed with crushed pebbles modeled with reduction in elastic modulus with varying failure criteria. Reproduced from Ref.[12]

Ben-Nun *et al.* studied the effects of fragmentation in two dimensional DEM studies of compressed packings.[20,21] In two dimensions, they were able to introduce small fragments

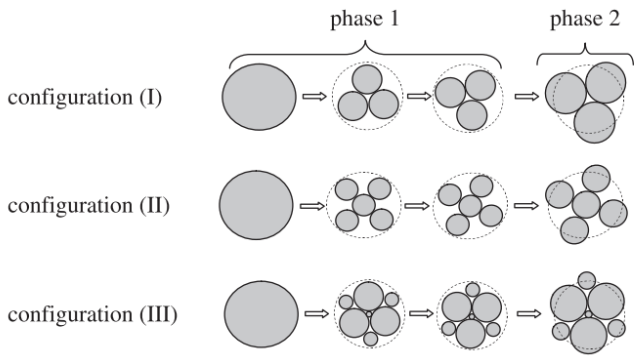

Figure 3.24: Configurations of fragmentation used in the study of Ref.[20]

after a crush event without excessive computational overhead. Under compression, they observed small fragments rearranging into smaller pores, giving rise to new force chains, until ultimately for a given initial volume an asymptotic limit is reached where fracture effectively stopped.[20] More important than his conclusions on self-organization in highly fragmented volumes were his observations that were similarly made here. In essence, any attempt to prescribe spherical fragments within the surface of a parent sphere will always fail to satisfy mass conservation (except in the limit of the fragment radius approaching 0). In order to resolve this situation Ben-Nun *et al.* conserve the mass by inserting fragments in two phases: first, non-overlapping fragments are prescribed and randomly inserted, second, a rapid linear expansion is then introduced in the second phase to gain back the overall solid mass. Our approach, to be discussed soon, will be seen to be quite similar.

The importance of mass conservation in modeling ceramic pebbles beds for fusion is critically important to conserve energy in pre- and post-fragmentation systems. In the first study of Van Lew *et al.* , where broken pebbles were removed from the system, energy input into two systems being studied were not dissimilar. This is quantified as follows. The total energy pouring into the non-damaged system is

$$E_h = \frac{q'''_{\text{nuc}} V_{\text{peb}} N}{V_{\text{bed}}} \tag{3.45}$$

where N is the total number of pebbles of volume V_{peb} that exist in the pebble bed of volume V_{bed}. After a crushing event, when pebbles are removed, the total amount of energy is

$$E'_h = \frac{q'''_{\text{nuc}} V_{\text{peb}} \eta N}{V_{\text{bed}}} \tag{3.46}$$

where η is the percent of crushed pebbles. Obviously then, the ratio of the two heating rates is

$$\frac{E_h'}{E_h} = 1 - \eta \tag{3.47}$$

and the energy deposited is not balanced between a virgin bed and one with crushed pebbles.

To continue the discussion of mass conservation of spherical packings, we consider how many fragments of a given radius would need to be inserted to conserve mass. In terms of DEM spheres we strictly wish to conserve mass between a solid pebble of radius R_p and the crushed fragments of radius R_c. Thus the number of crushed fragments (spheres) per crushed pebble is

$$N_c = \left(\frac{R_c}{R_p}\right)^{-3} \tag{3.48}$$

The number of fragments goes like the inverse of radius ratio to the third power; the number of crushed fragments to represent a single crushed pebble increases rapidly as the fragments shrink. The relationship between radius ratio and number of fragment particles is given in Figure 3.25. Note that in the DEM simulation, it is impossible to insert fractions of a particle so the number of fragment pebbles is rounded to the nearest integer in the table. While the large numbers of fragments are computationally expensive to model, they are not prohibitive at least down to $R_c/R_p = 0.20$, as will be seen later.

Table 3.4: Example values of the particle crush fragments, N_c, necessary to replace a single crushed particle and obey conservation of mass (fragment number is rounded to nearest integer).

R_c/R_p	N_c
0.20	125
0.30	37
0.40	16
0.50	8
0.75	2

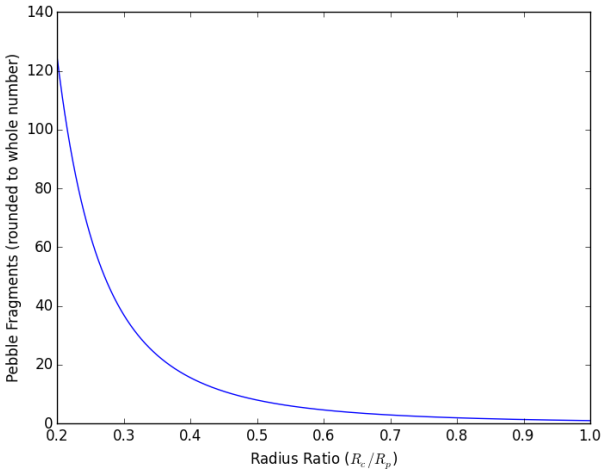

Figure 3.25: Number of fragment pebbles necessary to conserve mass increases rapidly as the size of the radius ratio ($\frac{R_c}{R_p}$) decreases.

Aside from satisfying conservation of mass, we must physically insert the particle fragments into void space in the simulation domain. During the course of the simulation, when we choose to replace the pebble with the fragments, the only available room is the spherical void left over by the damaged pebble. As mentioned previously, without allowing overlap, the condition of mass conservation will never be satisfied. Then we may consider what precisely is the smallest size sphere that could hold non-overlapped spheres of given fragment radii.

Luckily, dense packing of spheres inside a larger sphere is an interesting mathematical problem and has been tackled by many mathematicians in the past. Hugh Pfoertner keeps a compiled list of many solutions for a number of particles; many solutions are his are from Gensane.[75] If we consider, for instance, that a radius ratio of $R_c/R_p = 0.3$ requires 37 particle fragments, then we can also find from Ref.[75] that 37 particles would have to be of radius 0.2406866 to fit into a single sphere of radius of unity. We defined the particle fragment radius as R_c, the original particle as R_p, and then the radius of sphere necessary to hold the N_c fragments will be R_N, we can find a relationship between the volume of sphere V_p and necessary volume V_N,

$$r_1^* = \frac{R_c}{R_p} \tag{3.49}$$

and

$$r_2^* = \frac{R_c}{R_N} \tag{3.50}$$

then

$$R_N = R_p \frac{r_1^*}{r_2^*} \tag{3.51}$$

thus

$$\frac{V_N}{V_p} = \left(\frac{r_1^*}{r_2^*}\right)^3 \tag{3.52}$$

Choosing a linearly spaced distribution of r_1^* between 0 and 1, allows finding N_c particles necessary to conserve mass. Then from the N_c particles we can find from the database of sphere packing solutions the size of sphere that would be necessary to fit the N_c particles. The calculations are carried out and shown in Figure 3.26. The data in Ref.[75] does not go above 72 spheres so we are limited to radius ratios above about $r_1^* > 0.24$.

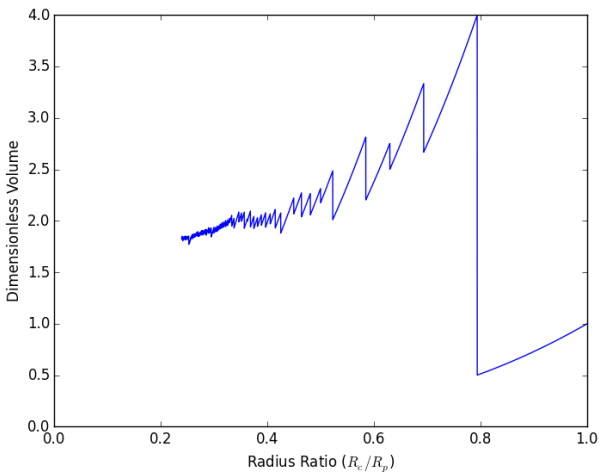

Figure 3.26: The volume necessary to house the particles of different radius ratios decreases toward unity as the radius ratio decreases. It is greater than 5 times the volume for large r_1^*.

The plot of Figure 3.26 shows that for particle fragments of reasonable numbers ($N_c \approx 20$ for $r_1^* \approx 0.3$), the volume necessary to fit the number of volume-conserving particles is greater than double the volume of the original sphere! Therefore from the point of view of having the physical space to insert the fragments, smaller sized fragments are ideal. To insert the few number of large particles would require disrupting the packing in the region of

the damaged particle. From this discussion, we conclude that an upper size limit should approximately be $r_1^* = 0.3$. This result agrees with the work from Ben-Nun *et al.* who only studied configurations with particles as large as $r_1^* = 1/3$.[20]

Our approach for inserting mass-conserving fragments is in essence similar to that described by Ben-Nun *et al.*. Whereas they would insert fragments fully enveloped in the circle and then increase their radius up to a mass-conserving value, we insert mass-conserving spheres but allow extreme overlap in the first phase. In the second phase, we permit a relaxation of the overlap by enforcing a limit to the travel during integration with the velocity-Verlet scheme. After the fragments have slowly moved away from each other and reached a local equilibrium with their neighboring particles, we re-initiate standard velocity-Verlet integration of all the particles in the ensemble to allow fragmentation resettling.

In the next section, we see some sample pebble beds where fragmentation is induced to equal amounts but with varying fragmentation sizes. We will investigate such characteristics as disruption caused by large fragments and travel of small fragments during resettling.

3.3.0.1 Example Beds with Fragmentation

To study the effects on a pebble bed of different fragmentation schemes, we begin with a bed of 6875 particles and randomly crush 1%. This was done with a range of fragments of size $r_1^* = [0.20, 0.25, 0.35, 0.50]$. The number of particles inserted for these different r_1^* followed the from Equation (3.48). In the images of Figure 3.27, Figure 3.28, Figure 3.29, and Figure 3.30, we see the initial packing of new particle fragments (in blue) settle into the interstitial gaps of the packing structure of original pebbles (yellow).

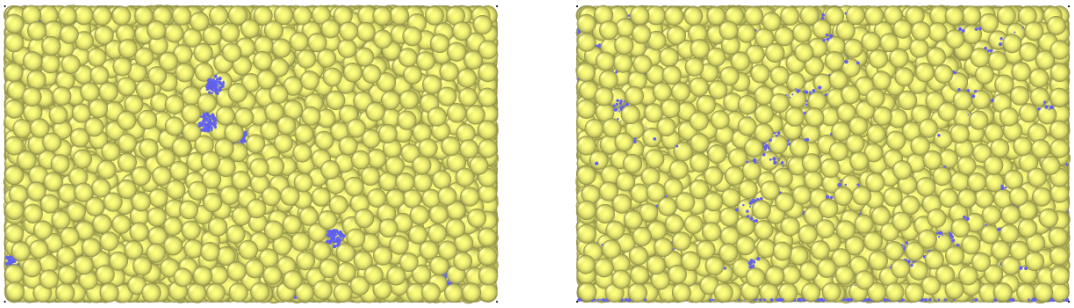

(a) initial (b) final

Figure 3.27: $N_c = 8594$, $N_{\text{tot}} = 15430$, $r_1^* = 0.20$. Side view of the packing arrangement and settling for different crush fragment sizes. The small crush fragments migrate far through the height of the bed. The yellow particles are the original pebbles and the blue are fragments inserted into the system after pebble crushing.

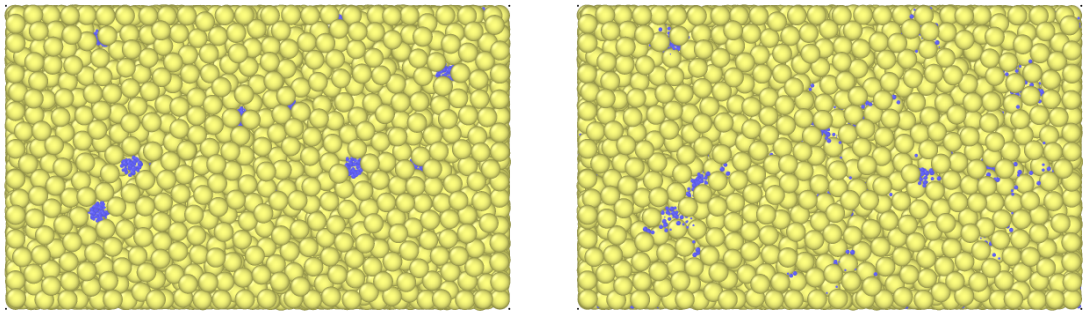

(a) initial (b) final

Figure 3.28: $N_c = 4400$, $N_{\text{tot}} = 11222$, $r_1^* = 0.25$. Side view of the packing arrangement and settling for different crush fragment sizes. The small crush fragments migrate far through the height of the bed. The yellow particles are the original pebbles and the blue are fragments inserted into the system after pebble crushing.

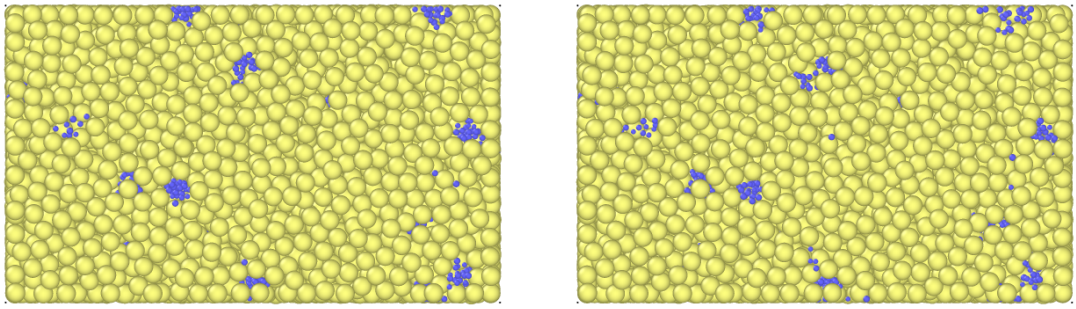

(a) initial (b) final

Figure 3.29: $N_c = 1603$, $N_{\text{tot}} = 8393$, $r_1^* = 0.35$. Side view of the packing arrangement and settling for different crush fragment sizes. The bigger fragments remain largely in place. The yellow particles are the original pebbles and the blue are fragments inserted into the system after pebble crushing.

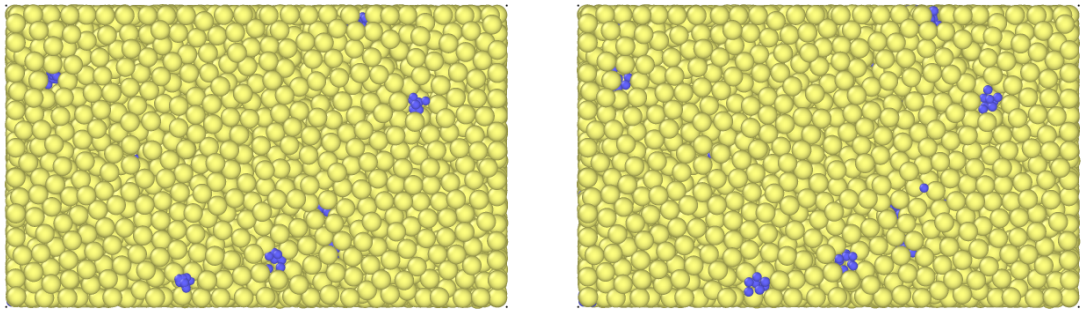

(a) initial (b) final

Figure 3.30: $N_c = 550$, $N_{\text{tot}} = 7358$, $r_1^* = 0.50$. Side view of the packing arrangement and settling for different crush fragment sizes. The bigger fragments remain largely in place. The yellow particles are the original pebbles and the blue are fragments inserted into the system after pebble crushing.

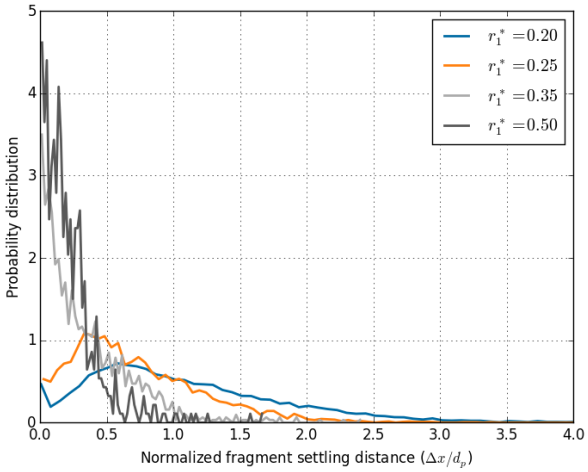

Figure 3.31: After the particle fragments are inserted into the system they re-settle due to gravity and inter-particle forces. The small fragments travel much further throughout the bed than the large fragments.

The settling of crushing fragments is also visualized in Figure 3.31. For this figure, the magnitude of displacement for all the crushed fragments is recorded based on the change between initial insertion location and final resting place. The displacement of the fragments is normalized against a pebble diameter and then a probability distribution is generated. Immediately obvious from Figure 3.31 is that larger fragments, $r_1^* = [0.35, 0.50]$ rarely travel beyond their original insertion point; very few particles have a normalized fragment settling distance larger than 1.0. In contrast, a good number of smaller fragments travel well beyond a single pebble diameter. In fact, 12% of the fragments of size $r_1^* = 0.20$ travel more than 2 diameters before coming to rest. We will return to the effects of pebble fragment travel when we consider ITER-relevant configurations and pebble bed heating.

From Figure 3.31, the impression then arises that the large displacement magnitudes of the small crush fragments may result in an overall less-dense bed with large increase in packing fraction near the floor where pebbles settle. For 1% crushed pebbles, there is some observable changes to the local packing fraction near the floor of the pebble bed, but no appreciable changes elsewhere in the bulk. In Figure 3.32, the packing fractions of the four different pebble beds are given. We look closely at the distribution within the first pebble

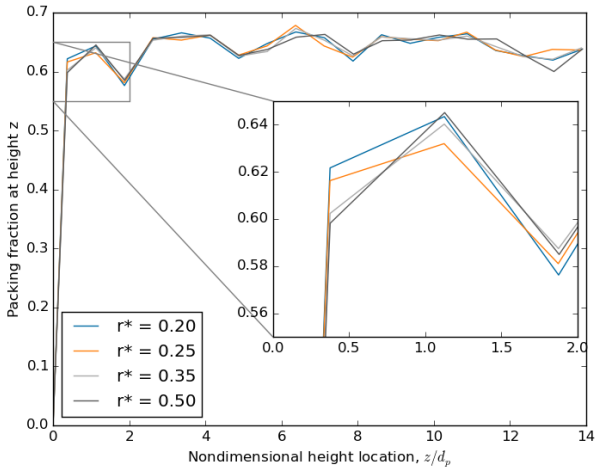

Figure 3.32: For only 1% of crushed pebbles, the re-settling of small pebble fragments has a small effect on the overall packing fraction of the pebble bed. In the inset, the main influence is seen in the slight increase of packing fraction within the first pebble radius of the floor.

diameter (see inset of Figure 3.32) and see the small crush fragments have a small change to the local packing fraction as they settled onto the floor of the container.

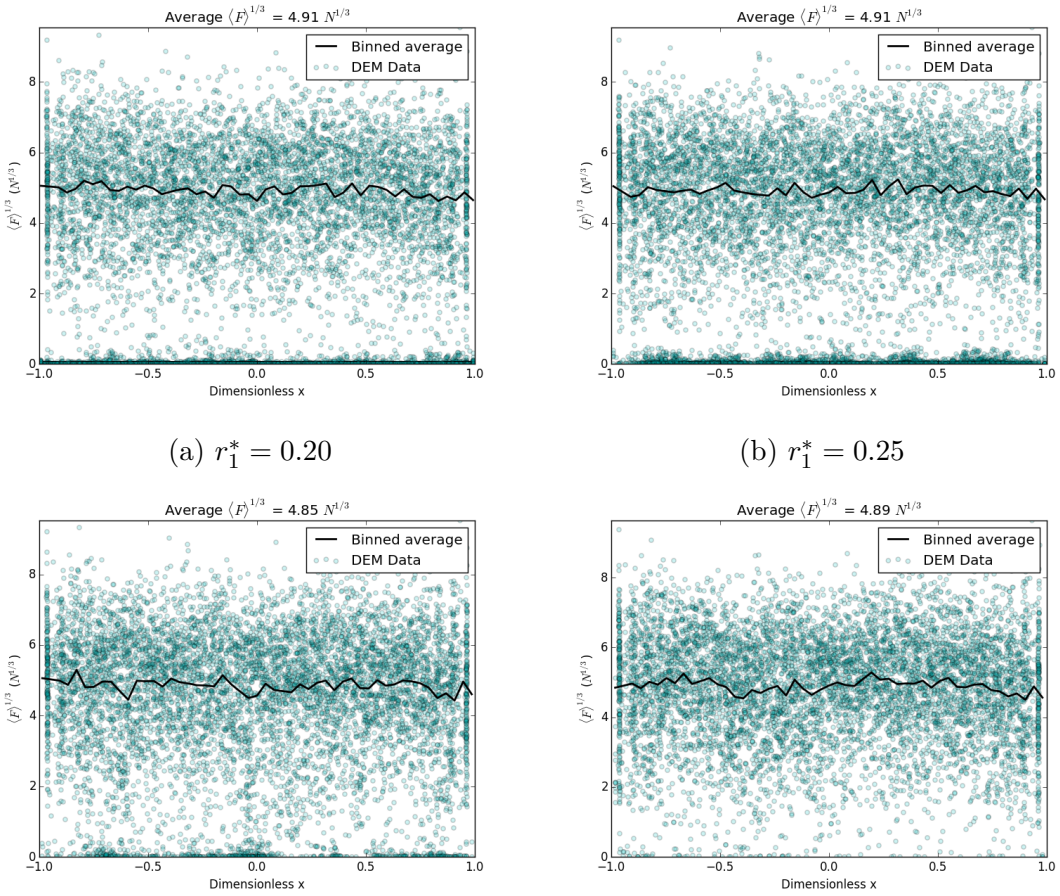

(a) $r_1^* = 0.20$

(b) $r_1^* = 0.25$

(c) $r_1^* = 0.35$

(d) $r_1^* = 0.50$

Figure 3.33: Contact force distributions throughout the pebble beds with different crush fragment sizes. Average forces in the bed are largely unaffected by the size of crushed particle fragments.

The last point to discuss is how the different size particles change the distribution of contact forces inside the ensemble. We plot the scatter of contact forces for all the pebbles in the ensemble in Figure 3.33. We are most interested in the contact loads carried by the large particles that make up the force network after crush fragments are inserted into the ensemble. The small fragments, moving through the interstitial gaps, are not expected to carry much load. Therefore in the data processing for the subplot of Figure 3.33a and Figure 3.33b, the vast number of small forces on the fragments are omitted in the average value of contact force. Opposingly, the larger fragments, $r_1^* > 0.4$, are expected to be inserted firmly into the

contact network and their contribution to the average value is included.

What we see in Figure 3.33 is that the average contact forces in the pebble bed remain mostly unchanged as a function of the size of the fragment radii. For all pebble beds, after the bed re-settles from the crushing event, the average contact forces (to the 1/3 power, which is the value important for heat transfer) are approximately 4.9 $N^{1/3}$. None of the beds have a maximum value greater than 9 $N^{1/3}$.

3.4 Summary of DEM Modeling of Solid Breeder Pebble Beds

A transient, thermal discrete element method approach to studying heat transfer in pebble beds has been introduced. Use of the method is important for blanket researchers and designers because it allows one to interrogate solid-solid interactions in pebble beds and opens a window into the micro-mechanical world of pebble beds. The DEM method recreates the constriction of heat conduction through normal-force-dependent contact areas between pebbles and between pebble-walls in an ensemble. The approach also allows exploration of evolving packing structures that will occur during operation of a ceramic pebble bed in a solid breeder unit of a fusion reactor - in this case we specifically consider packing structure changes due pebble damage. DEM-based models provide us with the ability to understand, predict, and more importantly, ultimately avoid pebble damage and associated thermomechanical changes to pebble beds.

Our DEM modeling of heat transfer was validated against experimental measurements of effective thermal conductivity of pebble beds in vacuum. The smooth-sphere approximation of pebbles was seen to over-predict the ability of pebbles to transport energy between contacts. Reductions in contact conductance due to roughness were shown to allow DEM models to approach experimental measurements. In the numeric models, we witnessed the phenomena of hot rattlers loosely settled in pebble beds and heating to a much higher degree then neighbors in the ensemble. If, in practice, the hot rattlers truly exist in solid breeders, it would be disadvantageous from the point of view of sintering or densification of pebbles leading to poorer tritium release. This observation strongly supported the need to include

helium purge gas in models of thermal transport of pebble beds with DEM.

A modified elastic modulus is shown to capture the observed scatter of elasticity of individual ceramic pebbles from experiments. The modified elastic Modulus is realized in DEM simulations with numeric re-creations of measured experimental elastic modulus distributions. The models applying modified elastic moduli predict more compliant pebble beds and smaller peak contact forces in beds and thus fewer crushed pebbles. Because normal contact forces between pebbles, a direct function of elastic modulus, are used to calculate pebble heat transfer and it is therefore imperative to have an accurate determination. The new approach to implementing elastic moduli in simulations is a necessary step towards more faithful DEM models.

In the case of a crushed pebble, a volume-conserving pebble fragmentation method is used to simulate a broken pebble. Smaller pebble fragments were seen to have the capability of traveling relatively long distances before re-settling. Redistribution of mass was seen in increased local packing fractions of beds. Nuclear heating of the beds will also be affected by mass redistribution and will be studied during applications of the models for ITER-relevant pebble beds.

We have demonstrated the usefulness of discrete element methods to model complex, transient, micro-mechanical interactions of pebbles in an ensemble and the concomitant heat transfer between them. Toward the goal of a complete model of thermal transport in solid breeder pebble beds, we must also take into account the slow-moving interstitial helium purge gas. In the next chapters, we will discuss augmentation of DEM models with two different schemes of helium flow models.

CHAPTER 4

Coupled DEM and CFD Modeling of Solid-solid and Solid-fluid Heat Transfer in Solid Breeder Pebble Beds

Our DEM model, introduced in § 3, was shown to be useful for modeling thermal transport between contacts in pebble beds in vacuum. The discrete element method's strength lies in its ability to resolve granular interactions at the pebble scale, allowing realistic modeling of contact forces and packing structure evolutions from crushed pebbles in fusion solid breeders. This is, however, insufficient on its own to model a solid breeder unit in a fusion reactor as the DEM equations neglect slow-moving helium purge gases permeating solid breeder pebble beds. Therefore, to develop a more complete model of temperature distributions in solid breeders, we will introduce the interstitial gas into our model.

Coupled granular-fluid flow is an important process used in a variety of industries.[108,214] Early work on gas-particle flow models treated the solid and gas phases as two inter-penetrating continua. The solid and gas were treated with the so-called two fluid model (TFM) by Anderson & Jackson as early as 1967.[9] Volume-averaging Theory (VAT) followed TFM. The VAT approach is similar to TFM in that the fluid computational cell is sufficiently large to include many individual particles but still smaller than the size of the system.[58] VAT allows treatment of complex porous flows with smooth continuous equations. In VAT, we average over a discrete space to replace complex geometry with a fictitious, smooth, continuous medium in which quantities of interest are defined independently of whether specific locations in that space are, for instance, solid or gas.[162,194] The governing equations of VAT required constitutive equations for closure between the fluid and solid phases. To overcome the difficulties of closure in VAT, multi-scale strategies have been devised for formulation of governing equations and constitutive relationships between solid and fluid phase.

At the microscopic level, the discrete element method describes the motion and energy transfer of particles interacting with a surrounding fluid. At the mesoscopic level, fluid flow is handled in a continuum sense with volume-averaged governing equations that are closed with constitutive relationships with the particle phase.[177,198] A numerical technique of coupling volume-averaged computational fluid dynamics (CFD) flow solvers to discrete element models was first proposed by Tsuji *et al.*. in 1992 and then Hoomans *et al.* in 1996.[94,176,177] Since then, CFD-DEM coupling approaches have grown as a tool for granular flow research and many CFD-DEM models have been experimentally validated for fluidized beds and preliminarily validated for heat transfer in packed beds.[38,44,82,108,140,141,172,179,198,208]

Noting the growth in application of coupled CFD-DEM, a systematic review of the theoretical developments behind different particular system models was given by Zhu *et al.*[216] They consider the two most common formulations, following the notation of Gidaspow, for the governing equations. The two formulations are commonly referred to simply as Model A and Model B.[77] Both of these models have been implemented somewhat interchangeably in CFD-DEM simulations. As pointed out by Zhu *et al.*, the two models differ by their treatment of the pressure drop. In Model A, the pressure drop on the system is jointly shared by the gas and solid phases. In Model B, it is only the gas phase which directly experiences the effects of pressure drop. Therefore, the two models have different forms of coupling source term, S_k (see Equation (4.9a)). The source of Model B is related to that of Model A as $S_k^B = S_k^A/\epsilon - \rho_f \phi g$.

However, as is shown by Zhou *et al.*, there is a built-in assumption to Model B which is typically overlooked in the implementation of CFD-DEM. For an accelerating fluid, there is an added-mass in the momentum equation. In the derivation of Model B, it is tacitly assumed that the fluid is steady which is not generally valid.[214] Nevertheless, the proliferation of Model B is due to the ease in numerical implementation and, except for some situations, Model B is numerically similar to Model A for most cases studied in CFD-DEM simulations.[214] In the simulations of packed beds for tritium breeding, we choose to implement Model B as it is valid for any of the flow scenarios ever experienced by the ceramic pebble bed.

4.1 Modeling Particles in the Presence of Fluid Flow Fields

Governing equations of DEM systems were given in § 3.1.1. To review, each pebble obeys Newton's equations of motion in response to a net force acting upon it. To include the influence of helium in the DEM formulation, we simply add a drag force term to Equation (3.1a). The momentum balance of our Lagrangian-tracked pebble now reads,

$$m_i \frac{\mathrm{d}^2 \mathbf{r}_i}{\mathrm{d}t^2} = m_i \mathbf{g} + \mathbf{f}_i + \beta_i V_i \Delta \mathbf{u}_{if} \tag{4.1}$$

The components of the last term are $\Delta \mathbf{u}_{if} = \mathbf{u}_f - u_i$, which is the relative velocity between the fluid and pebble, i; β_i, a volumetric drag coefficient; and the drag acts upon the entire pebble volume, V_i. A discussion on the method of determination and form of the inter-phase drag coefficient will be discussed after introducing the DEM heat transfer equation.

To similarly include the influence of helium gas field surrounding pebble, i, on its temperature, we must simply add a source term to the original energy balance equation of the DEM pebble, as given in Equation (3.11). In this case, the inter-phase exchange coefficient for energy is the heat transfer coefficient, h, for a fluid moving past a sphere in a packed bed. Heat transfer with passing fluids is added to the energy balance as

$$m_i C_i \frac{\mathrm{d}^2 T_i}{\mathrm{d}t^2} = Q_{s,i} + \sum_{j=1}^{Z} Q_{ij} + h_i A_i \Delta T_{if} \tag{4.2}$$

where again we have only needed to add the last term to account for the energy deposited/removed by the passing fluid. ΔT_{if} is the temperature difference, $T_f - T_i$, and the inter-phase energy exchange coefficient, h_i, acts upon the pebble surface area, A_i.

In the development of Equation (3.11), it was assumed that a 'conduction' Biot number was satisfied such that a lumped-capacitance method would be valid for the discrete pebbles in our ensemble. Likewise, for Equation (4.2) to be valid, we must assume that the true Biot number is also $\mathrm{Bi} \ll 1$. However, the lumped capacitance method is generally developed in heat transfer systems without heat generation. Furthermore, considering the low conductivity of our pebble material, it is not apparent *a priori* if the lumped capacitance assumption inherent in our DEM formulation is valid. The validity of the assumption is explored in § 4.2.

At present, assuming their validity, these simple additions to the governing equations of momentum and energy of each particle are all that are necessary to incorporate helium into the DEM computations of solid breeder pebbles. The computations of the inter-phase exchange coefficients, β_i and h_i are discussed next.

4.1.1 Inter-phase Exchange Coefficients

The purge gas in ceramic breeders is meant to travel at very low flow rates to maximize the absorption of tritium. The pebble beds will also always be near the close-packed limit. As such, the particle Reynolds number for these flows is often near unity and the Kozeny-Carman equation, as applicable for Stokes flow, is quite sufficient. However, we will employ the full Koch-Hill-Ladd (KHL) correlations which include terms for both the Stokes flow correlation (as a function of ϕ) in the zero Reynolds number limit and the viscous effects with a Reynolds number-dependent term. The KHL correlation is of a general form, and reduces to the Kozeny-Carman correlation in the close-packed, zero Reynolds number limits.[110] The KHL correlation allows for flexibility of discretized fluid cells to contain low volume-fraction regions of pebble beds, such as in the near-wall region. A short review of other correlations, their applicable ranges of fluid parameters, and other details is given in § 2.3. The assumptions leading to the development of the KHL correlation provide justification for our implementation in packed beds of lithium ceramics.

The nondimensional force of the KHL correlation reads,

$$F = F_0(\phi) + F_3(\phi)\mathrm{Re} \tag{4.3}$$

where the viscous term of the drag is

$$F_0 = \begin{cases} \frac{1+3(\phi/2)^{1/2}+(135/64)\phi\ln\phi+16.14\phi}{1+0.681\phi-8.48\phi^2+8.16\phi^3} & \text{if } \phi < 0.4 \\ 10.0\,\frac{\phi}{(1-\phi)^3} & \text{if } \phi > 0.4 \end{cases} \tag{4.4}$$

and the inertial component of the drag is

$$F_3 = 0.0673 + 0.212\phi + 0.0232\frac{1}{(1-\phi)^5} \tag{4.5}$$

The correlation from Koch-Hill-Ladd provide a nondimensional drag that must simply be re-written to fit into the pattern of our inter-phase momentum exchange coefficient. The momentum exchange coefficient follows the common form by Gidaspow.[77] The form used here is actually that of Van der Hoef, which differs from the classic form of Gidaspow by a factor of $1-\phi$, because numerically it is more convenient to couple the pressure gradient force to the buoyancy force.[23,180] Thus,

$$\beta_i = \frac{18\mu_f}{d_{p,i}^2}(1-\phi_k)\phi_k F \tag{4.6}$$

where μ_f is the fluid viscosity and the diameter of pebble i is $d_{p,i}$. The packing fraction, ϕ_k, in this equation is the local packing fraction in the fluid cell k. Localized packing fraction in a ceramic breeder volume may change in time due to fragmentation of pebbles or other packing rearrangement. The packing fraction will also change due to ordered packing enforced by pebble bed mechanical boundaries.[22,98,157] For example, the void fraction ($\epsilon = 1-\phi$) in narrow annular containers using the correlation from Mueller, as a function of wall-distance in a cylinder is,[130]

$$\epsilon = \epsilon_0 + (1-\epsilon_0)J_0(ar^*)e^{-br^*}$$

where r^* is the nondimensional distance from the wall; here it is defined in terms of the pebble diameter, $r^* = r/d_p$. The constants, a and b, are defined in terms of the size parameter $\alpha = D/d_p$ where D is the diameter of the annular tube. First, a is

$$a = \begin{cases} 7.383 - \dfrac{2.932}{\alpha - 9.864}, & \text{if } \alpha \geq 13 \\ 8.243 - \dfrac{12.98}{\alpha + 3.156}, & \text{if } 13 \geq \alpha \geq 2.61 \end{cases}$$

then

$$b = 0.304 - \frac{0.724}{\alpha}$$

The bulk void fraction is found from the correlation:

$$\epsilon_0 = 0.379 + \frac{0.078}{\alpha - 1.8}$$

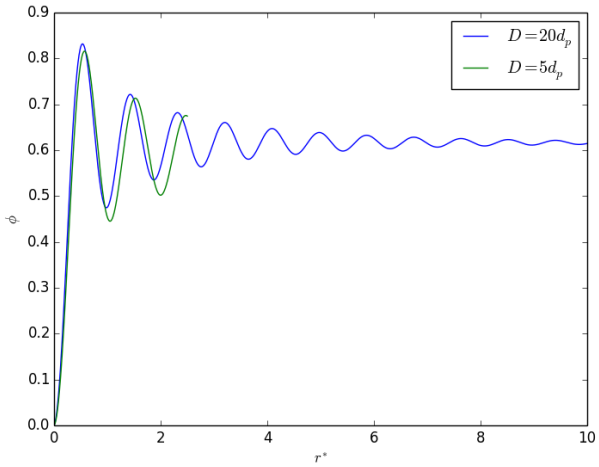

Figure 4.1: Showing the packing fraction approach the bulk value after a few pebble diameters when the pipe is $20d_p$ and that when the pipe is only $5d_p$, the packing fraction at any radius is not the same as the bed average.

The packing fractions as a function of distance from the container wall for two example sizes, diameters of $20d_p$ and $5d_p$, are plotted in Figure 4.1. This example is meant to demonstrate the varying packing fraction in a packed bed that is described with a single 'bulk' or 'global' packing fraction. It is important that the computational cell used in the CFD domain be sufficiently small to capture the variation of void fraction in near-wall regions. The size of the discretized cell relative to the pebble will dictate how much of the void fraction variation is captured in the volume-averaged equations.

The inter-phase energy transfer coefficient is calculated from the Nusselt number for the helium flow in the ensemble,

$$h_i = \frac{\mathrm{Nu} k_f}{d_{p,i}} \tag{4.7}$$

where k_f is the thermal conductivity of the fluid. Several correlations for determining the Nusselt number are given for reference in § 2.2.2. For the low-Reynolds number flows of the helium purge gas, the most appropriate correlation is from Wakao *et al.*, given in Equation (2.39).

From Eqs. 4.6 and 4.7, we have a formulation wherein knowledge of the flow field around our pebbles will allow calculation of dimensionless drag, F, and Nusselt number, Nu, and

thereby the two inter-phase exchange coefficients. The flow is coupled to our DEM computations with simple algebraic additions to the equations of motion and energy of the pebble, Equation (4.1) and Equation (4.2), respectively.

4.1.2 Volume-averaged Thermofluid Flow

The gas phase flow field will be treated in a method analogous to the approach of volume-averaging theory (VAT); the criticl difference is that with formal VAT the solid field is not handled with the discrete element strategy employed in CFD-DEM models.[177]

In this formulation of gas flow, we discretize fluid space with cells that are slightly larger than the individual particles; in the application of our CFD-DEM coupling, this meant at most roughly 5 to 6 particles per cell. With VAT, the particles themselves are not resolved in the fluid space but are simply introduced *via* closure terms.[96,162] A clear derivation of the governing equations of VAT can be found in Sbutega *et al.*.[162] The momentum and energy of a fluid flow through a solid phase with volume-averaged Navier-Stokes and energy equations are applied to each cell, k, in the discretized fluid space,

$$\frac{\partial \epsilon_k \rho_f}{\partial t} + \nabla \cdot (\epsilon_k \mathbf{u}_f \rho_f) = 0 \tag{4.8a}$$

$$\frac{\partial \epsilon_k \mathbf{u}_f}{\partial t} + \nabla \cdot (\epsilon_k \mathbf{u}_f \mathbf{u}_f) = -\frac{\epsilon_k}{\rho_f} \nabla P_f + \nabla \cdot (\nu_f \epsilon_k \nabla \mathbf{u}_f) - \frac{S_k}{\rho_f} \tag{4.8b}$$

$$\frac{\partial \epsilon_k T_f}{\partial t} + \nabla \cdot (\epsilon_k \mathbf{u}_f T_f) = \nabla (\epsilon_k \nabla T_f) - \frac{E_k}{\rho_f C_f} \tag{4.8c}$$

where the packing fraction in any fluid cell is calculated as a function of the volumes of particles residing in cell k. The computation of the void fraction is critically important and is discussed in length in § 4.1.3.

Coupling the fluid phase to the particles happens with the closure terms in momentum and energy of S_k and E_k, respectively. They are volume-weighted sums of the drag forces and energy exchanges for all particles in the discretized fluid cell,

$$S_k = \frac{1}{V_k} \sum_{\forall i \in k} \beta_i V_i \Delta \mathbf{u}_{if} \tag{4.9a}$$

$$E_k = \frac{1}{V_k} \sum_{\forall i \in k} h_i A_i \Delta T_{if} \tag{4.9b}$$

The inter-phase momentum and energy exchange coefficients act as the communicators between the particle information from the DEM solver and the fluid fields from CFD. Thus the motion and energy of the fluid field are intimately and dynamically coupled with the particle positions and energy. Computational time is preserved by only considering volume-averaged values in the fluid domain but important inter-particle forces are still calculated in the DEM space. The nature of the coupling, *i.e.* how information is mapped between the two computational spaces, is discussed next.

4.1.3 Lagrangian-Eulerian Mapping Calculations of Porosity

The simplest method for calculating the porosity of a CFD computational cell is to map all the DEM particles into the Eulerian volume *via* their centroid. We refer to this simple technique as the particle centroid method; in spite of its simplicity it is often used for large cell-to-particle volume ratios.[198] A two-dimensional demonstration of the centroid technique is given in Figure 4.2. In this figure, we see a computational cell (dashed line) in which many particles exist either partially or fully. The particles shaded in red have their centers located inside the cell and therefore in the simple technique have their entire volume contribute to the calculation of the porosity. The porosity for the centroid method is calculated as,

$$\epsilon_{\text{cell}} = 1 - \frac{1}{V_{\text{cell}}} \sum_{i=A}^{i=L} V_{p,i} \tag{4.10}$$

where $V_{p,i}$ is the volume of particle i. As the cell size begins to approach the size of the particle, erroneous calculations of porosity arise. This is visible, for instance, when considering particle A in Figure 4.2. This particle has only a quarter of its volume inside the cell but the porosity of the cell is computed as if the entire particle existed inside. Hoomans *et al.* recognized this limitation of the centroid method and introduced a fractional volume

method.[94] In the fractional volume method, the porosity is found as only partial volumes of the original sphere,

$$\epsilon_{\text{cell}} = 1 - \frac{1}{V_{\text{cell}}} \sum_{i=A}^{i=L} f_i V_{p,i} \tag{4.11}$$

where f_i is the fraction of the particle residing in the Eulerian cell. A similar approach taken by Kloss *et al.* and Zhao & Shan is the divided technique.[108,209] In this technique, the spherical particle is artificially divided into a number of regions with markers indicating their location. For example, see now how particles at the boundary, such as particle A, are treated in Figure 4.3. Instead of searching for centroids of particles, each particle has a search through the marker points (the black markers drawn in particle A) and the volume of that section of the sphere is assigned to whichever cell it falls inside. Note that in the sketch of Figure 4.3, every particle is divided with markers but particles not near the cell boundary have not had them drawn for clarity and convenience.

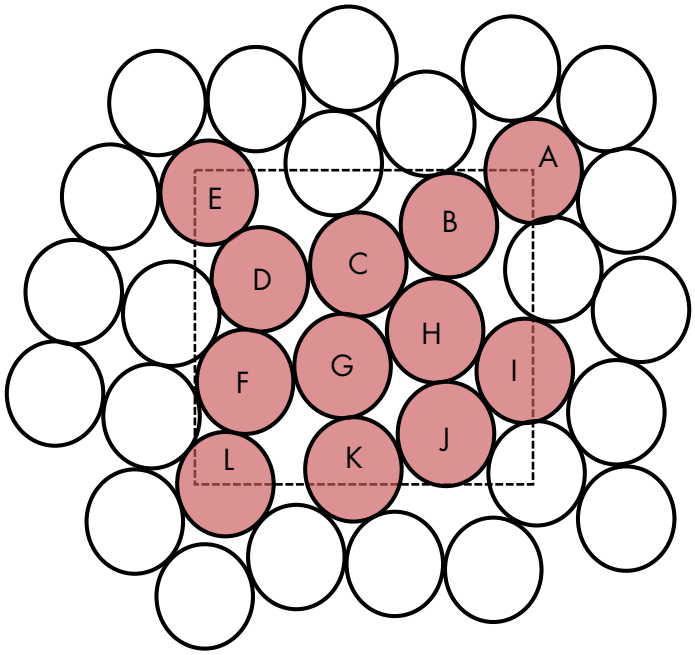

Figure 4.2: The dashed line represents a computational cell in which exist many particles. The particles with centroids inside the cell are shaded red.

As the computational cell volume approaches the size of a single particle $V_{\text{cell}} \to V_p$, the centroid and divided techniques break down. A technique introduced by Link *et al.* treats

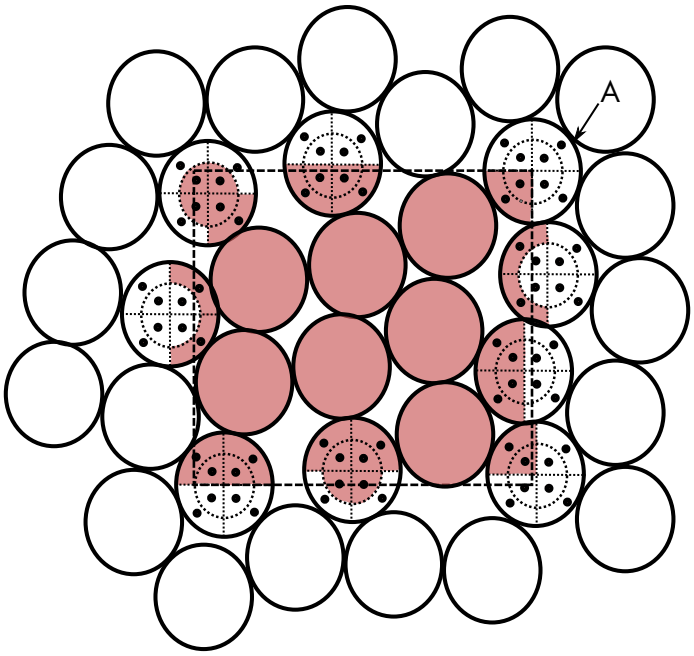

Figure 4.3: The dashed line represents a computational cell in which exist many particles. The divided portions of the particles with the sectional markers (dots) located in the cell are colored red.

the particle as a porous cube and allows computations when a cell is completely occupied by only a single particle.[119] Peng *et al.* offer an analytic technique as well as guidelines for validity of either analytic or centroid techniques.[141] However, in this work, the divided technique of Kloss *et al.* is implemented, based on the geometry of our packed bed flow and the guidelines established by Peng *et al.*[108,141]

4.1.4 Eulerian-Lagrangian Mapping Calculations of Force and Energy

Once the fluid momentum and energy fields are calculated in the Eulerian grid, the coupled inter-phase exchange coefficients must map the velocities and temperatures onto the particles in the Lagrangian DEM framework. A particle centroid method is always used in the exchange onto the particles. Referencing Figure 4.2, the velocity and temperature of the dashed cell is mapped only onto the particles highlighted in red. The approach has been used successfully by others.[108,119,198]

4.1.5 Numerical Implementation of CFD-DEM

The infrastructure for solving the DEM equations continues to be handled by LIGGGHTS. Details of the software are described in § 3.1.3. The DEM solver is a highly parallel C++ code based on the Molecular Dynamics (MD) code LAMMPS.[144]

Taking advantage of a separate, stand-alone CFD solver that is maintained by a large community, the CFD simulations are conducted by the pressure-based solver using the PISO algorithm realized within the open-source framework of OpenFOAM®.[99,137] The coupling routines, maintained by DCS Computing GmbH, are collected in a library providing a modular framework for CFD-DEM coupling with the C++ codes LIGGGHTS and OpenFOAM®.[81,108]

The routine of coupling CFD-DEM consists of several steps:

1. the DEM solver calculates the particles positions, velocities, and temperatures with time step dictated by stability of DEM

2. the particles positions and velocities are passed to the CFD solver using the Message Passing Interface (MPI)

3. for each particle, the cell in the CFD mesh that contains the particle is located

4. for each cell, the particle volume fraction is determined from the divided technique described in § 4.1.3. The ensemble-average velocity of the particles is determined

5. on the basis of ϵ and Re_p, the fluid forces and heat transfer rate acting on each particle are calculated from the inter-phase exchange coefficients of Eqs. 4.6 and 4.7

6. the momentum and energy source/sink terms are assembled from particle-based forces by ensemble averaging over all particles in a CFD cell *via* Eqs. 4.9

7. the inter-phase exchange coefficients of Eqs. 4.6 and 4.7 are sent to the DEM solver

8. the CFD solver calculates the fluid velocity and temperature from the source/sink terms determined in step 6.

4.2 Jeffreson Correction to Lumped Capacitance Method

When incorporating helium into the DEM-based modeling, the lumped capacitance assumption for each particle in the ensemble is assumed. The assumption eases the computational efforts of solving for the temperature distribution inside each particle; each particle is treated as being isothermal. The accuracy of the lumped capacitance method is described by the Biot number,

$$\mathrm{Bi} = \frac{h d_p}{k_r} \tag{4.12}$$

and for $\mathrm{Bi} \ll 1$ the lumped capacitance method accurately models the behavior of a solid interacting with a fluid. For $\mathrm{Bi} \approx 0.1$ (in cases with no heat generation), the error from the lumped capacitance method is only about 5%. In solid breeder volumes, the particles are generally small, the solid conductivity low, and heat transfer coefficient generally is also low. This leads to small-to-moderate Biot numbers expected in the packed bed. In this section we will analyze the accuracy of the lumped capacitance and introduce a correction method to account for inaccuracies of the method at moderate Biot numbers.

I simplify the case of a packed bed and only consider a single sphere with volumetric heat generation submerged in- and thermally interacting with a fluid. The sphere will be of radius $R = d_p/2$, as shown in Figure 4.4. The sphere will initially be at a uniform temperature of T_i. The fluid temperature will remain constant at T_f

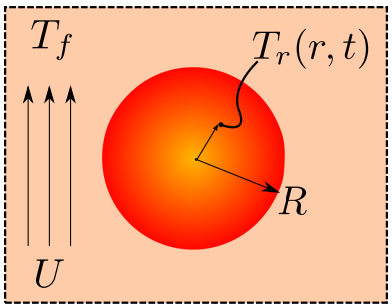

Figure 4.4: Control volume of a single spherical particle in a packed bed

4.2.1 Lumped Capacitance Solution for Sphere

I solve for a single sphere interacting with a passing fluid, as shown in Figure 4.4, while making the lumped capacitance assumption for this sphere. The solid is initially at temperature T_0, with constant volumetric heat generation, cooling in a fluid with constant heat transfer coefficient. The fluid will remain constant at T_f.

The time response of the sphere's temperature is dictated by the balance of energy to/away from the solid,

$$\rho_r C_r V \frac{dT}{dt} = -hA(T - T_f) + \dot{g}V \tag{4.13}$$

Equation (4.13) is solved in dimensionless form with the following nondimensional parameters of temperature and time,

$$\theta = \frac{T(t) - T_f}{T_0 - T_f} \tag{4.14a}$$

$$\tau = \frac{t}{R^2/\alpha} \tag{4.14b}$$

where α is the thermal diffusivity of the sphere, T_0 is the initial isothermal temperature of the sphere, and T_f is the constant fluid temperature. The resulting temperature distribution is,

$$\theta_{LC} = \left(1 - \frac{G}{3\text{Bi}}\right) \exp(-3\text{Bi}\tau) + \frac{G}{3\text{Bi}} \tag{4.15}$$

where a dimensionless heat generation is defined as,

$$G = \frac{\dot{g}R^2}{k(T_0 - T_f)} \tag{4.16}$$

The energy contained in the sphere, relative to the fluid, in nondimensional terms is

$$E^*(\tau) = \frac{E(\tau)}{E_0} \tag{4.17}$$

where E_0 is the initial energy of the sphere,

$$E_0 = \rho_r C_r V(T_0 - T_f) \tag{4.18}$$

Thus for a sphere with the lumped capacitance model, in nondimensional form, the energy is simply

$$E^*_{LC}(\tau) = \theta_{LC}(\tau) = \left(1 - \frac{G}{3\text{Bi}}\right)\exp(-3\text{Bi}\tau) + \frac{G}{3\text{Bi}} \tag{4.19}$$

The nondimensional energy profile of Equation (4.19) is plotted over the nondimensional time of $\tau \in [0, 1/\text{Bi}]$ in Figure 4.5.

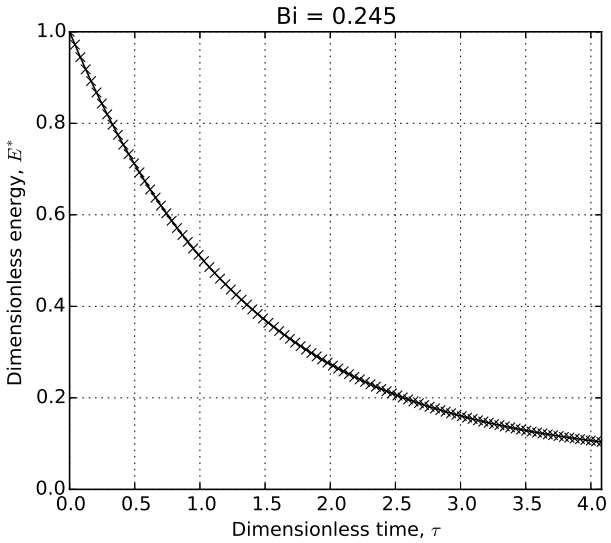

Figure 4.5: Lumped capacitance model: Sphere energy profile decaying from an initial value to a time of 1/Bi

Reviewing Equation (4.15) we see that the speed of decay is dictated by the term in the exponential, 3Bi. Meanwhile, the steady-state value being approached is given by $\frac{G}{3\text{Bi}} = \frac{gR}{h(T_0 - T_f)}$. It is important for this discussion to point out that because both the nondimensional heat generation and Biot number terms contain the solid conductivity, the steady-state value of the lumped capacitance model will not change for varying solid conductivity even if it leads to different Biot numbers.

4.2.2 Exact Solution for Sphere

I again analyze the sphere of Figure 4.4 but now will account for internal temperature gradients inside the sphere. The details of the analytic solution for a sphere with heat

generation interacting with a fluid is given in Appendix D. Again, solving in terms of the nondimensional temperature and time introduced in § 4.2.1 as well as a nondimensional radius,

$$\theta = \frac{\mathbb{T}}{\mathbb{T}_0}$$
$$\rho = \frac{r}{R}$$
$$\tau = \frac{t}{R^2/\alpha}$$

The energy conservation equation for the sphere with internal temperature gradient, in nondimensional form θ_{TG}, is

$$\frac{1}{\rho}\frac{\partial^2}{\partial\rho^2}(\rho\theta_{TG}) + G = \frac{\partial\theta_{TG}}{\partial\tau} \tag{4.20}$$

With the initial condition and boundary conditions outlined in appendix D, the nondimensional temperature distribution inside the sphere is

$$\theta_{TG}(\rho,\tau) = \left(\frac{G}{6} + \frac{G}{3\text{Bi}} - \rho^2\right) + \sum_{n=1}^{\infty} \exp(-\zeta^2\tau)\frac{\sin(\zeta_n\rho)}{\rho}\frac{Z(\zeta_n)}{N(\zeta_n)} \tag{4.21}$$

where ζ_n are the eigenvalues of the equation and the functions of ζ_n (Z,N,C) are given in appendix D.

The accompanying nondimensional energy of the sphere is integrated to,

$$E^*_{TG}(\tau) = \left(\frac{G}{15} + \frac{G}{3\text{Bi}}\right) + 3\sum_{n=1}^{\infty} \exp(-\zeta^2\tau)\frac{Z(\zeta_n)}{N(\zeta_n)}C_n(\zeta_n) \tag{4.22}$$

I now compare the exact solution from Equation (4.22) to the solution of energy given by the lumped capacitance model of Equation (4.19). The two profiles are given in Figure 4.6.

For the value of Biot number here, Bi = 0.245, the energy profile of the analytic solution of the sphere cooling in a flow is well-captured by the lumped capacitance model. The maximum relative error over the time span, as defined by

$$\text{error} = \frac{\left|E^*_{TG}(\tau) - E^*_{LC}(\tau)\right|}{E^*_{TG}(\tau)} \tag{4.23}$$

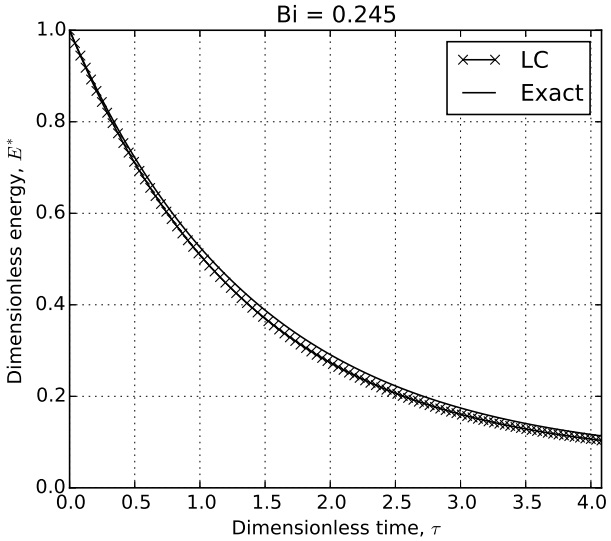

Figure 4.6: Analytic and lumped capacitance models: Sphere energy profile decaying from an initial value to a time of 1/Bi

is always less than 10%.

Consider now the same size sphere but with the Biot number increased by an order from: a) a conductivity of $k = k_r/10$ and b) a heat transfer coefficient of $h = 10h_f$. The two physical changes to the system result in the same Biot number (Bi = 2.45) but as we can see in Figure 4.7, there are drastic differences between the energy profiles.

Seen in Figure 4.7a, the lumped capacitance solution both over-predicts the speed at which the sphere reaches a thermal steady-state as well as the value of the steady-state. Comparatively, in Figure 4.7b, for the same Biot number, the lumped capacitance solution again over-predicts the speed to thermal steady-state by the same rate but is relatively accurate for the steady-state value itself.

Viewing the steady-state terms of the two solutions, the source of the error becomes apparent. From Equation (4.22), the steady-state term of the exact solution is

$$E^*_{TG,ss} = \frac{G}{15} + \frac{G}{3\text{Bi}} \tag{4.24}$$

Whereas, the steady-state term of the lumped capacitance solution from Equation (4.19)

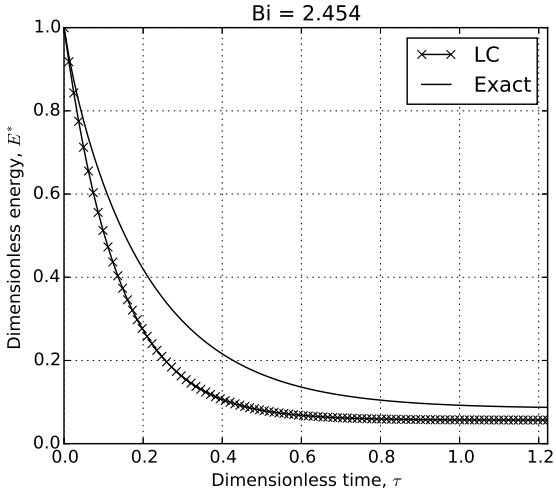

(a) $k \uparrow$, lumped capacitance error in the transient and steady-state.

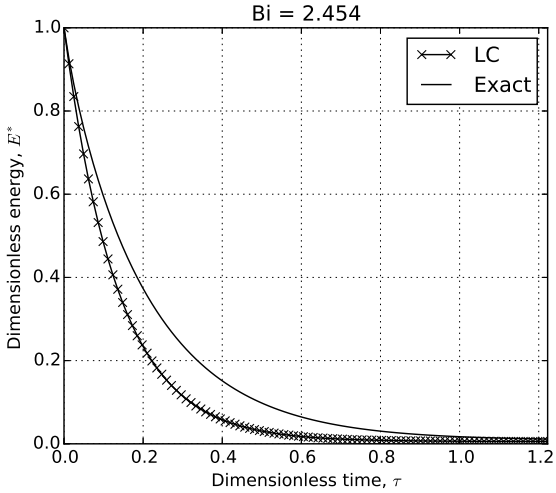

(b) $h \uparrow$, lumped capacitance error mainly in the transient.

Figure 4.7: Analytic and lumped capacitance models: Sphere energy profile decaying from an initial value to a time of 3/Bi. The same Biot number produces different results for the exact solution of a sphere with heat generation.

is,

$$E^*_{LG,ss} = \frac{G}{3\text{Bi}} \tag{4.25}$$

The two steady-state values differ only by the additional term of $\frac{G}{15}$ on the exact solution. This term appears in the exact solution from integration of the temperature gradient that exists in the pebble due to volumetric heating (see appendix D). The lumped capacitance solution assumes no internal temperature gradient in the sphere and thus by definition can not account for this $\frac{G}{15}$ term. Furthermore, the nondimensional heat generation term, G, given in Equation (4.16), is importantly a function of thermal conductivity but not the heat transfer coefficient. The lack of dependence on h explains the difference between steady-state values in Figure 4.7 When Bi is small, the steady state error between lumped capacitance and the exact solution is small. If only h increases the error in steady-state remains small. This is demonstrated in Figure 4.7b when steady-state solutions are close. However, in Figure 4.7a as k was reduced, the curves no longer converge to similar steady-states. This phenomena appears only with the combination of low conductivity materials with volumetric heating.

Even in cases without volumetric heating, when the Biot number grows large, errors appear in the transient portion of curves but ultimately converge to the same steady-state solutions. To address the inaccuracies in the time-dependent response of the lumped capacitance method with large Biot number, a correction factor, implemented by Van Lew and Xu *et al.* in situations without heat generation, is employed.[183,197] In their work, they considered a heat transfer fluid interacting with a low conductivity thermal storage material. The solar thermal storage systems they analyzed often had moderate-to-large Biot numbers but they could continue to apply the lumped capacitance model in their calculations with application of a so-called Jeffreson Correction.[102] However, because their applications did not involve heat generation, its usefulness for application in our pebble beds absorbing nuclear heat is validated.

4.2.3 Jeffreson Correction for Sphere with Nuclear Heating

The correlation to correct the heat transfer coefficient due to solids with large Biot number is given by Jeffreson as,[102]

$$h_p = \frac{h}{1 + \mathrm{Bi}/5} \tag{4.26}$$

where h_p is the modified heat transfer coefficient of the particle with an internal temperature gradient. As the Biot number increases, the modified heat transfer coefficient decreases. THe form of this correlation works to effectively slow down the rate of heat removed by the passing fluid. Recall the curves of Fig 4.7. where the lumped capacitance solution over-predicted the speed with which the energy decayed towards steady-state. A modified Biot number can then also be written as

$$\mathrm{Bi}_p = \frac{h_p d}{k_r} = \frac{\mathrm{Bi}}{1 + \mathrm{Bi}/5} \tag{4.27}$$

Applying the Jeffreson Correction to Equation (4.15), the modified lumped capacitance solution is written now in terms of the modified Biot number,

$$\theta_{JC} = \left(1 - \frac{G}{3\mathrm{Bi}_p}\right) \exp\left(-3\mathrm{Bi}_p \tau\right) + \frac{G}{3\mathrm{Bi}_p} \tag{4.28}$$

and thereby Equation (4.19) also yields

$$E^*_{JC}(\tau) = \left(1 - \frac{G}{3\mathrm{Bi}_p}\right) \exp\left(-3\mathrm{Bi}_p \tau\right) + \frac{G}{3\mathrm{Bi}_p} \tag{4.29}$$

The energy profiles from the lumped capacitance model (LC), the Jeffreson correction (JC), and the exact solution are all plotted together in Figure 4.8. Barely visible under the JC solution are teh curves from the exact solution. The Jeffreson correction to the lumped capacitance method allows the simple modeling approach of the lumped capacitance method to capture the proper transient as well as steady-state values for this sphere with a moderately sized Biot number.

To look more closely, we view the instantaneous error (see Equation (4.23)) in Figure 4.9. For the value of $\mathrm{Bi} > 1$ due to either low conductivity (Figure 4.9a) or high heat transfer coefficient (Figure 4.9b), the error in the Jeffreson correction is always under 10%; often

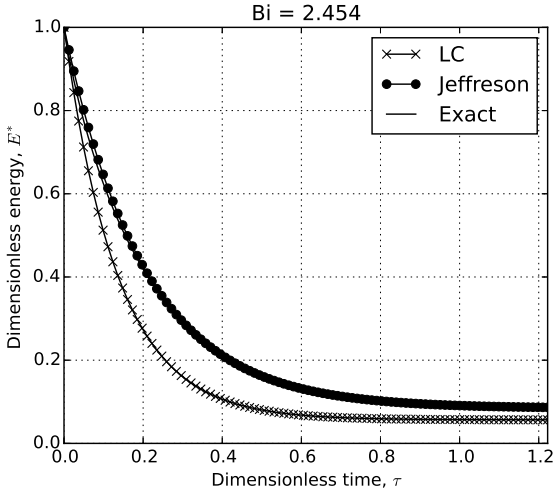

(a) The Biot number increased from a decrease in the solid conductivity.

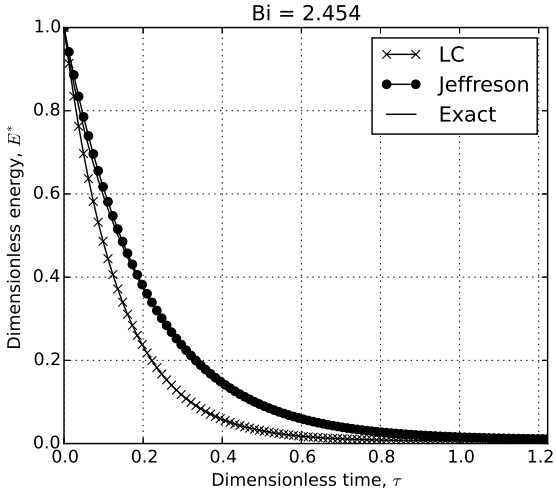

(b) The Biot number increased from an increase in the heat transfer coefficient.

Figure 4.8: Analytic, lumped capacitance model, and LC model with Jeffreson correction: Jeffreson correction corrects for transient and steady-state errors of lumped capacitance.

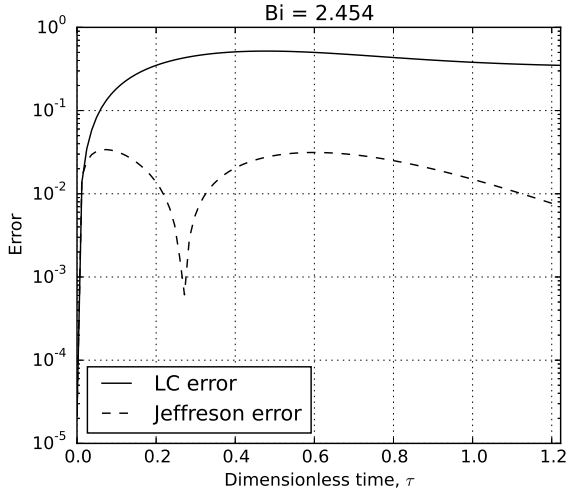

(a) The Biot number increased from a decrease in the solid conductivity.

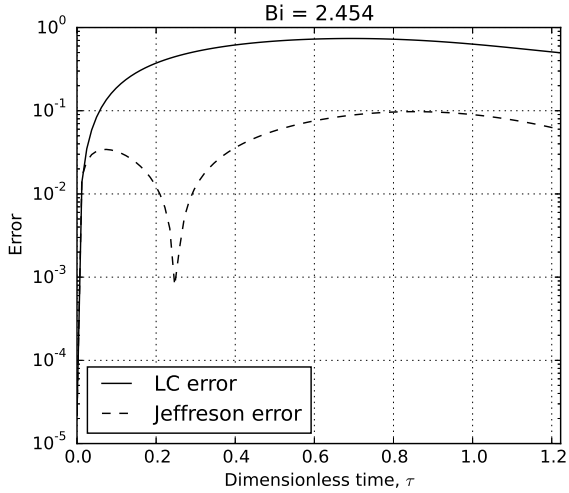

(b) The Biot number increased from an increase in the heat transfer coefficient.

Figure 4.9: Error of lumped capacitance and reduced error of the model with Jeffreson correction for moderate Biot number.

closer to only 1%. This is in opposition to the standard lumped capacitance method which has 50-80% error for both transient and steady-state values.

The lumped capacitance method allows researchers to simplify transient, conjugate heat transfer problems to a situation with an isothermal solid. In the discrete element method, the assumption of isothermal solid is innate in the framework of the method. With the implementation of the Jeffreson correction in the discrete element method, we have confidence in the fidelity of the heat transfer with the helium flow for moderately sized Biot numbers. The Jeffreson correction will be implemented into the DEM computations *via* Equation (4.27).

4.3 Benchmarking Solid-solid and Solid-fluid Heat Transfer Models for Pebble Beds

We will now validate the coupled CFD-DEM formulations of momentum and energy heat transfer. Momentum calculations will be validated via pressure drop calculations in the helium purge gas with empirical correlations for pressure drop of packed beds. Coupling of energy will be validated by means of calculating effective thermal conductivity of stagnant helium in a pebble bed with experimental measurements of effective thermal conductivity.

4.3.1 Validating Pressure Drop in Packed Beds with Flowing Helium Purge Gas

Our three-dimensional system consists of mono-dispersed particles of diameter d_p. The particles are constrained by two rigid walls in the x-direction at locations of $x = \pm 10 d_p$ and periodic boundary conditions in the y-direction located at $y = \pm 7.5 d_p$. Gravity acts in the downward z-direction and the particles are bound from below by a rigid wall at $z = 0$. The size of the system allows approximately 10 000 particles to fill to a height of approximately $z = 30 d_p$. The volume was chosen to represent the long, tall, narrow channels seen in many solid breeder module designs.[35,56,145] The fluid domain is constructed to include an inlet and outlet region of fluid to permit development of the flow profiles. The inlet region is 5 pebble diameters in length and the outlet is 30 pebble diameters. No-slip boundary conditions are

enforced at the walls at the x-limits of the region. To match the DEM domain, periodic boundary conditions are used in the y-limits. The inlet face of the fluid is specified at a constant $\mathbf{v} = (5, 0, 0)$ cm s^{-1}. The outlet face is specified with OpenFOAM's 'inletOutlet' command with a given pressure. This boundary condition allows the inlet pressure to float to value that satisfies the specified inlet velocity and outlet pressure.

The size of the CFD cells were chosen to be large enough to fit approximately 5 pebbles, for which the divided technique of computing void fraction is applicable (see § 4.1.3); the ratio of cell volume to particle volume was $V_{\text{cell}}/V_p = 7.46$. The helium, for this first validation, was modeled with constant fluid properties. The values are given in Table 4.1.

The Koch-Hill-Ladd drag model is employed in the style of Model B with an Archimedes pressure for buoyancy term. The terminology of these CFD coupling drag models is discussed in Ref.[214] The Nusselt number correlation of Li & Mason is used for calculating the Nusselt number. OpenFOAM's dummy turbulence model (which is nothing more than a laminar model) is used.

An implicit time marching scheme is employed with a time step in the fluid domain of $\Delta t_f = 1 \times 10^{-4}$ s. The small time step is not necessary to capture the fluid flow. The momentum equation is essentially not even transient as a steady-state laminar solution is achieved almost instantaneously in comparison to the long time span required to reach thermal steady state. The small time step is necessary for a relatively tight coupling to the pebble bed as the temperatures increase on the pebbles. Integration schemes of gradients, divergence terms, and laplacians are all Gauss linear or Gauss limitedLinear (as defined in OpenFOAM). The time step of the DEM is $\Delta t_s = 1 \times 10^{-7}$ s which must be small for stability of the DEM explicit integration. The coupling between CFD and DEM domains occurs every 10 time steps of the fluid domain - equating to every 10 000 in the pebble domain.

The layout of the pebble bed inside the CFD domain is shown in Figures 4.10 and 4.11. Notable of the layout is the relaxation of the mesh size in the direction of the periodic boundaries. The size is permitted as there are few variations in fluid or temperature in

the periodic direction. The meshes are made much smaller in the direction between cooling boundaries. In this direction (x-direction), we need the meshes small enough to resolve a temperature and velocity profiles across the bed between centerline and cooling boundaries. We also want to capture the behavior of near-wall arrangement of the pebble bed.

Table 4.1: Constant fluid properties of helium purge gas in CFD-DEM coupling.

ν	α	k	C_p	ρ
$(\mathrm{m^2\,s^{-1}})$	$(\mathrm{m^2\,s^{-1}})$	$(\mathrm{W\,m^{-1}\,K^{-1}})$	$(\mathrm{J\,kg^{-1}\,K^{-1}})$	$(\mathrm{kg\,m^{-3}})$
4.02×10^{-4}	6.06×10^{-4}	0.2	5192.8	0.175

The CFD-DEM model was run at various particle Reynolds numbers and the overall pressure drop of the packed bed was measured. The pressure drop is compared against the well-known Kozeny-Carman and Ergun equations. The Kozeny-Carman is known to fit better with experimental data at very small Reynolds numbers while the Ergun equation is a more general equation meant to span a large range of Reynolds numbers. In Figure 4.12 we see the CFD-DEM coupling model is providing bed-scale pressure drops that match very well with Kozeny-Carman over the Reynold's numbers applicable to helium purge flow in fusion reactors ($\mathrm{Re}_p \approx 1$).

Seki *et al.* experimentally studied the flow of helium purge gas in efforts to better understand tritium recovery.[163] They ran a representative volume of pebbles up to flow rates of $100\,\mathrm{L\,min^{-1}}$ and also found that Ergun's pressure drop prediction was highly accurate for the pebble beds as long as the viscous contribution (see the right-most term in Equation (2.56)) was small, *e.g.* when the Reynolds number of the packed bed is small. This result is a strong validation of the macroscopic results of pressure drop as calculated by the CFD-DEM simulation of a packed bed.

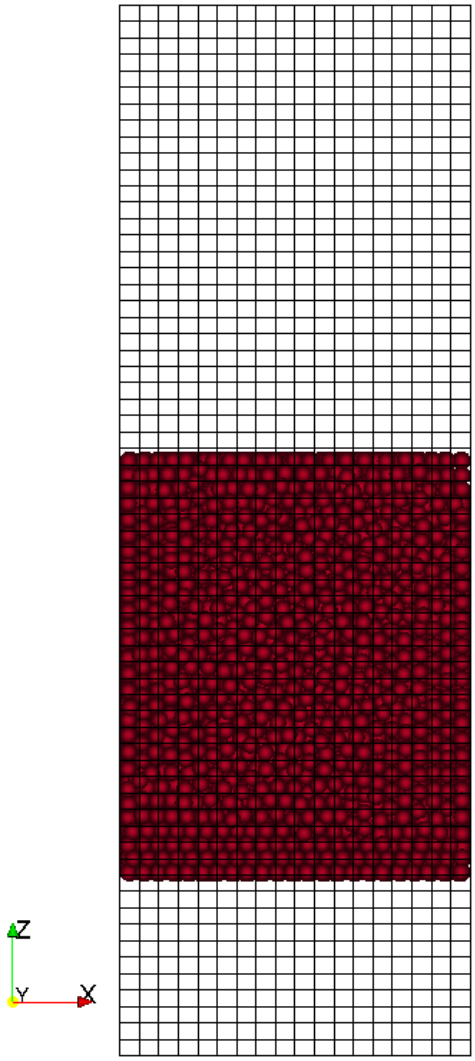

Figure 4.10: Front view of the pebble bed as it resides in the CFD mesh. The meshes in the direction of cooling are chosen to be large enough to fit many pebbles but small enough to provide a resolved temperature profile.

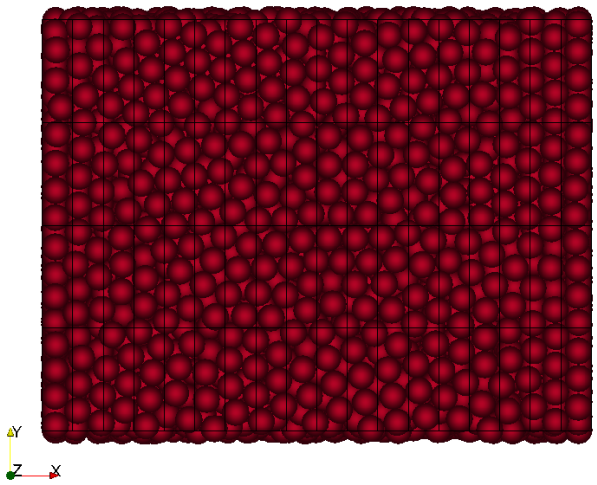

Figure 4.11: Top view of the pebble bed as it resides in the CFD mesh.

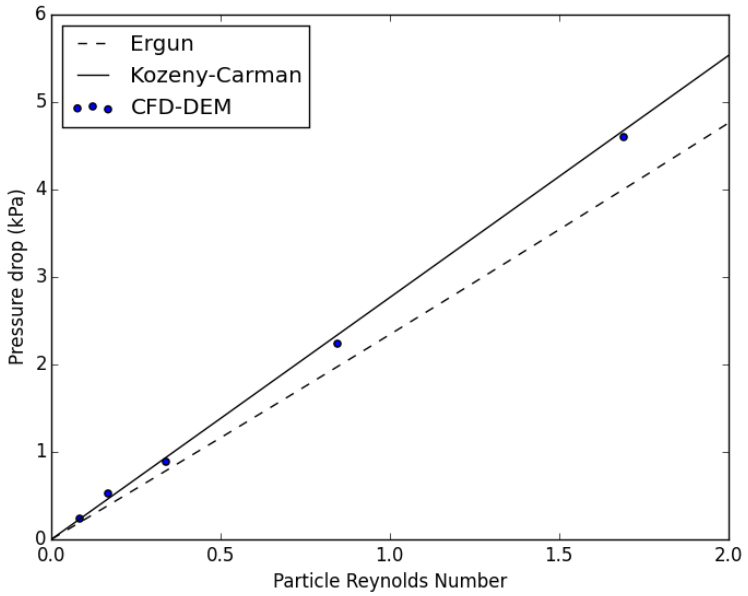

Figure 4.12: Pressure drop calculations across packed beds, solved by CFD-DEM, fit well to the Kozeny-Carman empirical relation.

4.3.2 Effective Thermal Conductivity from CFD-DEM with Stagnant Helium

In § 3.1.4 we saw that DEM models, including contact roughness modeling, were able to effectively model heat transfer of pebble beds in vacuum by means of measuring effective thermal conductivity of a representative pebble bed. We consider the same pebble bed but now immerse the pebbles in a stagnant helium gas. The fluid volume surrounding the pebble bed has equal dimensions in the x- and y-directions. A constant length $50d_p$ was used in the z-direction. The boundaries were: periodic in y, adiabatic in z, and constant temperature, $T_w = 573\,\mathrm{K}$ in x. A constant nuclear heating rate of $q_p''' = 8\,\mathrm{MW\,m^{-3}}$ was applied to the pebble volumes. The simulation is allowed to run to thermal steady-state.

After reaching a steady solution, temperature distributions of the pebbles are used to calculate an effective thermal conductivity. For the first set of pebble beds, the Jeffreson correction is not applied. The temperature distribution is given in Figure 4.13.

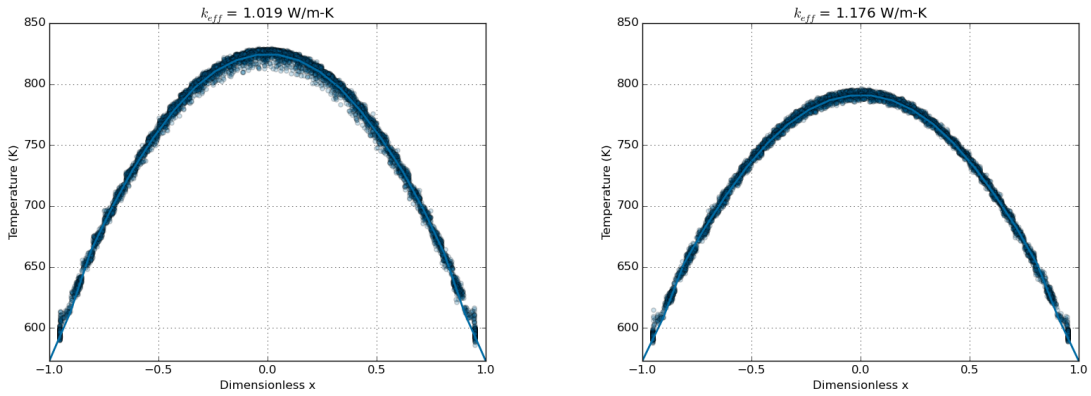

(a) $\phi_i = 62\%$ (b) $\phi_i = 64\%$

Figure 4.13: k_{eff} for packed beds in stagnant helium.

In addition, a grid-independence study was run. The grid size was reduced by 50% in each case and k_{eff} was calculated. The results for each grid are given in Figure 4.14. Negligible change was found between the two finer cases and consequently the results given here are of the finest mesh.

For stagnant helium, the Nusselt number is $\mathrm{Nu} = 2$ which leads to a heat transfer

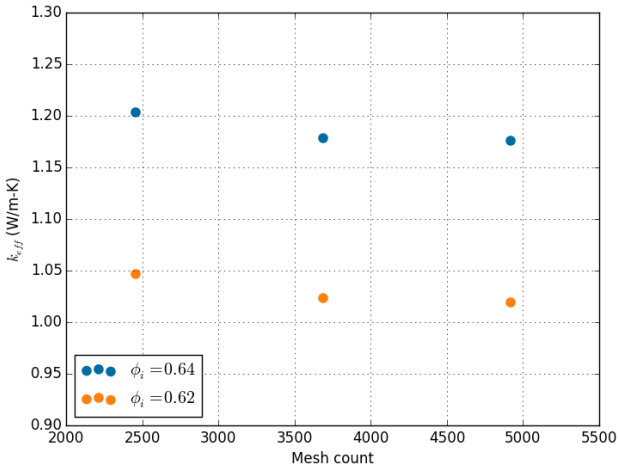

Figure 4.14: Effective thermal conductivity as a function of the grid size. The change between k_{eff} becomes negligible at the finer grid sizes.

coefficient of

$$h = \frac{k_f \text{Nu}}{d_p} \tag{4.30}$$

where k_f is the thermal conductivity of helium, $k_f = 0.34\,\text{W}\,\text{m}^{-1}\,\text{K}^{-1}$. The heat transfer coefficient is therefore $h = 680\,\text{W}\,\text{m}^{-2}\,\text{K}^{-1}$

The Biot number, using solid conductivity of $k_s = 2.4\,\text{W}\,\text{m}^{-1}\,\text{K}^{-1}$, is

$$\text{Bi} = \frac{h d_p}{k_s} = 0.283 \tag{4.31}$$

which is small enough that the Biot assumption should not be highly inaccurate. Nevertheless, a second set of pebble beds is run with Jeffreson correction applied. The corrected heat transfer coefficient is reduced to

$$h' = \frac{680\,\text{W}\,\text{m}^{-2}\,\text{K}^{-1}}{1 + 0.283/5} = 643\,\text{W}\,\text{m}^{-2}\,\text{K}^{-1} \tag{4.32}$$

which results in a 5% drop in heat transfer coefficient with the Jeffreson correction applied. Using the Jeffreson-corrected heat transfer coefficient for simulations, temperature profiles at thermal steady state are given in Figure 4.15. For the case of stagnant helium, the Jeffreson correction had negligible effect on determinations of temperature distributions in the two packed beds studied.

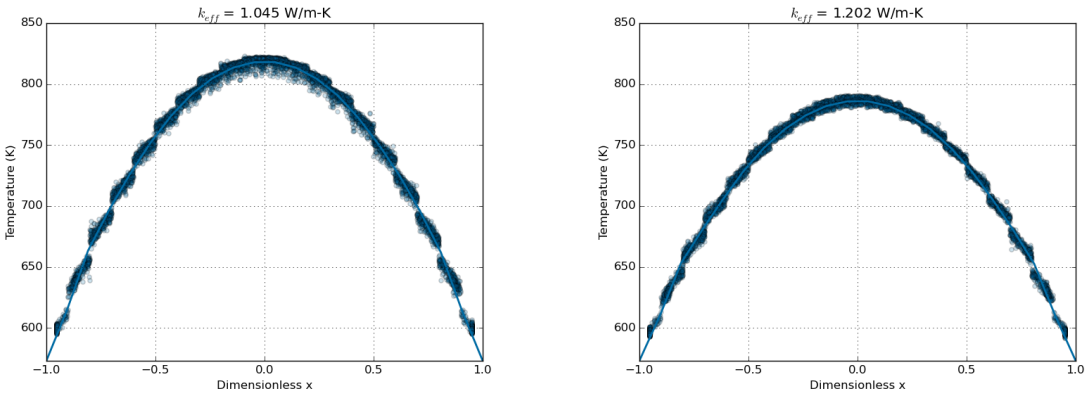

(a) $\phi_i = 62\%$ (b) $\phi_i = 64\%$

Figure 4.15: k_{eff} for packed beds in stagnant helium with Jeffreson correction to heat transfer coefficient.

Comparing the results of pebble beds with Jeffreson correction applied, for a stagnant fluid with Nu = 2, with material producing Bi = 0.29, there is a negligible change to the effective thermal conductivity of beds without the correction. Nevertheless, the correction is costs practically no computational time and is trivially applied during the convection calculation routine in the code. For cases when the Nusselt number increases locally, the effect may be larger and is therefore applied in general to CFD-DEM coupling code.

In the current framework, constant thermal properties are implemented for helium gas. The transport properties used in this study were from averages between 300 °C and 900 °C, a range over which the properties were all fairly linear. This is equivalent to reporting data at an average bed temperature of 600 °C. Hatano *et al.* reported the effective thermal conductivity of Li_2TiO_3 was reported for a packed bed of $d_p = 1.91\,\text{mm}$ as approximately $k_{\text{eff}} = 1.18\,\text{W}\,\text{m}^{-1}\,\text{K}^{-1}$ with the hot-wire technique.[87] Tanigawa *et al.* reported the effective thermal conductivity at 600 °C as a function of compressive strain and series cycle.[174] The results of Tanigawa *et al.* are reproduced in Figure 4.16; the values are approximately $k_{\text{eff}} = 1.3\,\text{W}\,\text{m}^{-1}\,\text{K}^{-1}$ above a stress state on the bed of 1 MPa. Abou-Sena *et al.* measured the effective thermal conductivity of uncompressed Li_2TiO_3 but only up to temperatures of 500 °C, and are therefore not relevant to comparison here.[3] Mandal *et al.* measured the effec-

tive thermal conductivity of Li_2TiO_3 pebbles in stagnant and flowing helium environment.[125] However, the results of Mandal *et al.* are much lower than data from other members, they report $k_{\text{eff}} = 0.274\,\text{W}\,\text{m}^{-1}\,\text{K}^{-1}$ in a stagnant helium environment at 200 °C which is 20% of values of other research centers. At their lowest superficial velocity, $u_s = 0.146\,\text{m}\,\text{s}^{-1}$, they find an effective conductivity of $k_{\text{eff}} = 0.65\,\text{W}\,\text{m}^{-1}\,\text{K}^{-1}$ with $d_p = 1\,\text{mm}$ pebbles.

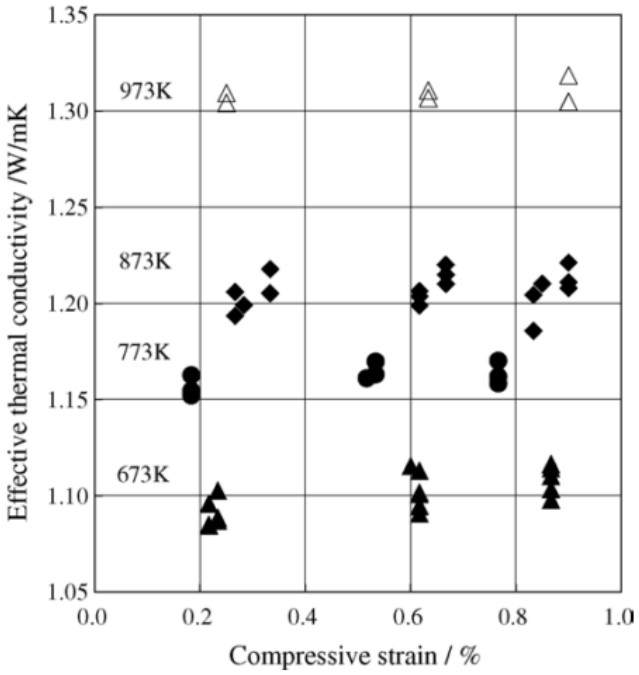

Figure 4.16: Effective thermal conductivity of a compressed Li_2TiO_3 pebble bed. Reproduced from.[174]

The results found here are in agreement with reported values from literature of uncompressed pebble beds at similar temperatures;[87] we found $k_{\text{eff}} = 1.05\,\text{W}\,\text{m}^{-1}\,\text{K}^{-1}$ when the initial packing fraction was $\phi_i = 0.62$. As the contact forces increased between the pebbles as is the case for initial packing of $\phi_i = 0.64$, we found $k_{\text{eff}} = 1.2\,\text{W}\,\text{m}^{-1}\,\text{K}^{-1}$. The results of this validation are plotted alongside experimental data in Figure 4.17.

Another important observation to be made from the pebble temperatures of CFD-DEM simulations is the lack of 'hot rattlers' that appeared in DEM simulations. For example, in Figure 3.8, there are many pebbles with temperatures much higher than the majority of nearby pebbles. These pebbles exist in localized pockets where their neighbors are carrying

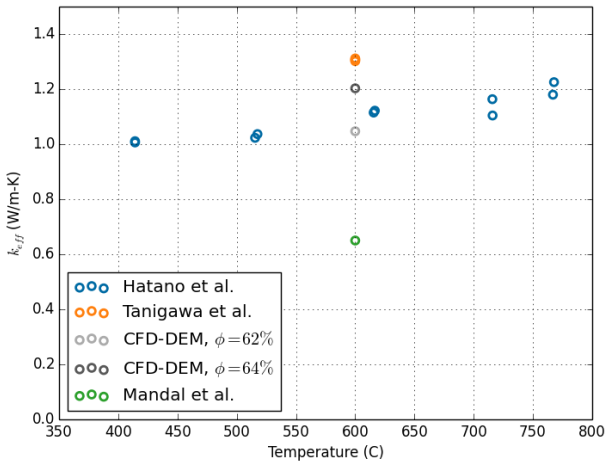

Figure 4.17: Comparison of effective conductivity measurements for Li_2TiO_3.

more contact force and they sit with relatively small forces at all contacts. The isolation allows nuclear heating to run away without temperature moderation. Including helium convection on pebble beds resulted in the complete disappearance of all hot rattlers. In Figure 4.15, all temperatures in a given region are tightly grouped around average temperatures. This demonstrates that the helium purge gas, while not intended to be a major carrier of heat in the system, plays a role in thermally equilibrating temperatures between pebbles and moderating temperatures of any mechanically isolated pebbles. This also has implications for fragmentation in pebble beds with helium. Small fragments were seen in § 3.3 to travel through beds before coming to rest with very small contact forces. We will see in § 6 that helium moderates fragmentation temperatures just as it did hot rattlers.

4.4 Summary of CFD-DEM Modeling of Solid Breeder Pebble Beds

The physics of heat transfer in solid breeder pebble beds are innately mixed-scale. On one hand, heat transfer through contact conductance is strongly dependent on the contact force network established in the packed bed of solids. During operation of the solid breeder in a fusion reactor, the force network and packing structure are bound to evolve due to, for

example, forces on pebbles and fragmentation of individual pebbles. The impact on heat transfer due to pebble-scale interactions is important to capture with numerical models because of the narrow operating temperature imposed on solid breeders. On the other hand, the slow-moving helium purge gas is a larger-scale interaction as the fluid transports heat well beyond the range of individual pebbles. Experimentally, helium's contribution to effective thermal conductivity has long been known to be larger than solid conductance and is critical to models of temperature distributions of solid breeder pebble beds.

Likewise, we use a microscale approach to heat transfer modeling of the pebble beds. Lithium ceramic pebbles are handled with the DEM code introduced in § 3. DEM models allow continual monitoring of inter-particle forces and individual particle temperatures such that any of the crush-prediction, fragmentation, or thermal expansion methods allow modeling changes of packing structures. Helium is treated with a continuum approach using volume-averaged versions of conservation equations of Navier-Stokes and energy. The volume-averaged approach of the fluid allow for an efficient overlaying of the fluid contribution to the thermophysical behavior of the pebble bed. Closure of coupled fluid conservation equations is easily performed *via* summed contributions of particles in fluid computational space.

We tested the validity of the lumped capacitance assumption when pebbles experience heat generation with a moderately large Biot number. Inaccuracies appeared for calculations of both transient and steady-state temperatures in a single pebble, with heat generation, when immersed in a passing fluid. The inaccuracies were larger for cases when solid conductivity decreased compared to cases when heat transfer coefficient increased – even if the two cases had the same Biot number. This was shown to be an effect of heat generation internal to the solid and standard lumped-capacitance validity on Biot number was invalidated. However, by incorporating the Jeffreson correction to heat transfer coefficients, we showed lumped-capacitance approximations (with Jeffreson correction) continues to be accurate even under the condition of volumetric heating of the solid. The Jeffreson correction is implemented in the CFD-DEM solver for solid breeder pebble beds.

A benchmarking effort was made to validate the application of this CFD-DEM model

for the specific conditions of solid breeder packed beds. A parametric study of Reynolds number showed that the coupled codes were able to recreate the pressure drop predicted by Kozeny-Carman correlation. From the point of view of heat transfer, CFD-DEM models of heat transfer in a stagnant helium bed were compared to experimental measurements of Li_2TiO_3 pebble beds and seen to be in sufficient agreement, considering the assumptions made for the computational models.

The CFD-DEM model is a powerful and efficient means of simulating helium flow through packed beds, while retaining heat transfer contributions of pebbles and their packing structure. However the simplicity of the volume-averaging model sacrifices the ability to resolve the complex flow fields that develop in the pebble bed. It is unclear if this simplification is completely acceptable. Therefore, in the next section we introduce another solid-fluid coupling technique which will solve for complete velocity and temperature fields of helium and ceramic in packed beds.

CHAPTER 5

Conjugate Heat Transfer in Solid Breeder Pebble Beds with Lattice-Boltzmann Modeling

The volume-averaged approach of the CFD-DEM coupling is an effective and efficient method for solving transiently-coupled heat transfer between flowing helium and pebble beds *via* volume-averaging techniques to handle the fluid conservation equations. However, the approach does not provide a complete view of the tortuous flow of interstitial helium because the CFD-DEM solver does not resolve the helium pathways on the particle scale. Therefore we have also investigated fluid-pebble interactions by means of linking DEM pebble beds with lattice-Boltzmann solvers which allows us the ability to solve the complete conjugate heat transfer of flowing helium through pebble beds within reasonable computational times.

The lattice-Boltzmann method (LBM) to simulate fluid flow is a growing field of numerical modeling with a rich historical development. As the LBM approach is relatively new and its governing equations have roots in both computer science and statistical mechanics, in this section we first review notable evolutions in modeling history and the background physics leading to the governing equations – which lend themselves to relatively straightforward numerical implementation. References[33,37,170,171,190] provide more thorough descriptions of the physics, modeling approaches, and applications of LBM theory to fluid dynamics problems.

5.1 Historical Development and Physics of LBM

We begin with a brief discussion of the Boltzmann equation describing the statistical behavior of non-equilibrium thermodynamic systems. Then we will introduce some of the lattice gas automata predecessors to the current lattice-Boltzmann method.

5.1.1 Discretized Boltzmann Equation

In the realm of statistical mechanics, suppose we wish to know, at a certain time t, how many particles exist at a given location, $\mathbf{x}$, that have momentum, $\mathbf{p}$. We define a number,

$$n = f(\mathbf{x}, \mathbf{p}, t)\mathrm{d}\mathbf{x}\mathrm{d}\mathbf{p} \tag{5.1}$$

as the number of n particles in the system that exist within the coordinates of $\mathrm{d}\mathbf{x}$ and momenta $\mathrm{d}\mathbf{p}$ at that instant. $f(\mathbf{x}, \mathbf{p}, t)$ is the probability density function representing the odds of finding a particle per phase space $(\mathbf{x}, \mathbf{p})$ at a moment in time, t.

Now let us assume we apply a small force, $\mathbf{F}$, to all the n particles and then increment time by $\mathrm{d}t$. Assuming further that none of the particles collide (with each other or any other particles in the system), the particles will have moved an amount $\mathbf{x} + \frac{\mathbf{p}}{m}\mathrm{d}t$. The particles will all also have had their momentum changed by an amount $\mathbf{p} + \mathbf{F}\mathrm{d}t = \mathbf{p} + \mathrm{d}\mathbf{p}$. In other words, those n particles are now found in the phase space of

$$n = f(\mathbf{x} + \frac{\mathbf{p}}{m}\mathrm{d}t, \mathbf{p} + \mathrm{d}\mathbf{p}, t + \mathrm{d}t)\mathrm{d}\mathbf{x}\mathrm{d}\mathbf{p} \tag{5.2}$$

The number of particles in the two moments of time are conserved, so we can also say

$$f(\mathbf{x} + \frac{\mathbf{p}}{m}\mathrm{d}t, \mathbf{p} + \mathrm{d}\mathbf{p}, t + \mathrm{d}t)\mathrm{d}\mathbf{x}\mathrm{d}\mathbf{p} = f(\mathbf{x}, \mathbf{p}, t)\mathrm{d}\mathbf{x}\mathrm{d}\mathbf{p} \tag{5.3}$$

Next we relax the assumption of no collisions. If we focus our attention of the phase space as before, some of the particles that began at $(\mathbf{x}, \mathbf{p}, t)$ will not arrive at the phase space of $(\mathbf{x} + \frac{\mathbf{p}}{m}\mathrm{d}t, \mathbf{p} + \mathrm{d}\mathbf{p}, t + \mathrm{d}t)$. By the same measure, some particles that began in some other phase space *will* arrive in $(\mathbf{x} + \frac{\mathbf{p}}{m}\mathrm{d}t, \mathbf{p} + \mathrm{d}\mathbf{p}, t + \mathrm{d}t)$. Now the number of particles is not conserved and we write the net number of particles having left/entered this phase space as

$$\Omega\mathrm{d}\mathbf{x}\mathrm{d}\mathbf{p}\mathrm{d}t \tag{5.4}$$

where Ω is classically referred to as the collision operator. This function dictates the evolution of particles after a collision (what phase space they leave/enter). Treatment of the collision operator is itself a source for discussion but we leave it as a generic operator. Thus the

balance of particles is now

$$f(\mathbf{x} + \frac{\mathbf{p}}{m}\mathrm{d}t, \mathbf{p} + \mathrm{d}\mathbf{p}, t + \mathrm{d}t)\mathrm{d}\mathbf{x}\mathrm{d}\mathbf{p} - f(\mathbf{x}, \mathbf{p}, t)\mathrm{d}\mathbf{x}\mathrm{d}\mathbf{p} = \Omega \mathrm{d}\mathbf{x}\mathrm{d}\mathbf{p}\mathrm{d}t \tag{5.5}$$

To be precise, to arrive at the collision operator, Ω, in the form we have used in Equation (5.5), it is required to make a few more assumptions on the system. Following Ludwig Boltzmann, we assume: the particles are dilute, point-like, and structureless that only interact *via* short-range two-body potentials. Another famous assumption from Boltzmann was of *Stosszahlansatz* (molecular chaos) which allow the inter-particle interactions to be described only in terms of their local binary collisions with very long paths through free space between collisions.[170] For the sake of this discussion, we will just accept the formulation of Equation (5.5) as the evolution equation for the particles in our system.

We consider a case where there are a discrete number of directions a particle may travel, such as toward discrete i directions of neighboring nodes in a lattice. In such a case, velocities point only toward those neighbors, $\mathbf{c} \to \mathbf{c}_i$. In Equation (5.5), we also normalize the mass such that $m = 1$, making $\mathbf{p}/m = \mathbf{p} = \mathbf{c}$. In discrete increments of time, we also write the collision operator in a discrete form, $\Omega \mathrm{d}t \to \Omega_i(\mathbf{x}, t)$. Thus, Equation (5.5) becomes,

$$f_i(\mathbf{x} + \mathbf{c}_i \Delta t, t + \Delta t) - f_i(\mathbf{x}, t) = \Omega_i(\mathbf{x}, t) \tag{5.6}$$

Lastly, if we assume that we are using time units that have also been normalized such that $\Delta t = 1$, the above becomes

$$f_i(\mathbf{x} + \mathbf{c}_i, t + 1) - f_i(\mathbf{x}, t) = \Omega_i(\mathbf{x}, t) \tag{5.7}$$

In the form of Equation (5.7), our discretized version of the Boltzmann equation for statistical mechanics will be seen to be identical to a lattice-based formulation that will be arrived at purely from the point of view of lattice gas automatons.

5.1.2 Lattice Gas Automata

In a broad sense, lattice gas automata (LGA) simulated the behavior of individual particles with a simple boolean approach where basic collision rules were defined at nodes in a lattice.

As particles approach nodes from neighbors at a given time, rules dictate the direction of the particle at the next moment in time. Computationally, the particles were simply represented with boolean operators that said either 1: a particle existed at that node in that direction; or 0: no particle existed at that node in that direction. Conceptually, the particles can be thought of as hard spheres that would collide on nodes of a lattice; collisions would send the particles rebounding along discrete directions toward neighboring nodes. The restraint on collision rules required that they obey conservation of mass and momentum.

The earliest LGA was a two-dimensional model by Hardy, Pomeau, and de Pazzis (HPP) in 1973.[86] The HPP model applied basic conservation rules that particles had to obey at each node. From the streaming particles, macroscopic units could be extracted. For instance, the particle density at a node is found from the total number of boolean particles at that node,

$$\rho(\mathbf{x}, t) = \sum_i n_i(\mathbf{x}, t) \tag{5.8}$$

where $n_i(\mathbf{x}, t)$ are the particles occupying the node at $\mathbf{x}$ at time t with a velocity of $\mathbf{c}_i$. As mentioned, the value of n is a boolean value of 1 or 0 if the particle is present or not, respectively. Similarly, the momentum at the node is found as,

$$\rho(\mathbf{x}, t)\mathbf{u}(\mathbf{x}, t) = \sum_i \mathbf{c}_i n_i(\mathbf{x}, t) \tag{5.9}$$

where $\mathbf{u}(\mathbf{x}, t)$ is the mean velocity of the particles at the node at that time.

Boolean nature of the HPP automata meant that the solution was not only exact (not susceptible to any round-off errors of floating point numbers) but each node required only four bits to completely describe the state (each bit described the four directions of traveling particles in the two dimensional node).[86] Furthermore, the HPP model benefited from the inherently parallel nature of all LGA simulations. The collision behavior at any given node is independent of all other nodes; the nodes only need to communicate when particles stream to neighbors.[170]

The LGA method was given considerable more attention after 1986 when Frish, Hasslacher, and Pomeau (FHP) showed it to be possible to solve lattice gas automata simulations that were ostensibly equivalent to Navier-Stokes equations (in two dimensions).[68] Descrip-

tions of the hexagonal lattice used in the FHP model can be found in the textbooks of Succi[170] and Sukop & Thorne.[171] The FHP method gave qualitatively beautiful reproductions of hydrodynamic phenomena.

Other such LGA models were developed with the same fundamental construction as the two models mentioned here. All the models followed the same basic form of evolution of the particles. Following the form of Ref.,[36]

$$n_i(\mathbf{x}_i + \mathbf{c}_i, t+1) - n_i(\mathbf{x}, t) = \Omega_i(\mathbf{x}, t) \tag{5.10}$$

where, in lattices, $\Delta t = 1$ is a standard normalization. After already deriving the Boltzmann equation, Equation (5.10) should appear quite familiar. The equation states that the particle occupation number at a specific location and time, $n_i(\mathbf{x}, t)$, evolves based on the collision rules, $\Omega_i(\mathbf{x}, t)$, defined at every node, $\mathbf{x}$. In the LGA framework, the collision operator is much simpler than the form used in the Boltzmann equation for statistical mechanics. Here, the rules are simplified and discretized so that Ω_i can exist in a simple look-up table or explicit function of n_i (with randomness).[36,171]

Collision operators are chosen such that they obey conservation of mass and momentum, expressed as,

$$\sum_i \Omega_i = 0 \tag{5.11a}$$

$$\sum_i \mathbf{c}_i \Omega_i = 0 \tag{5.11b}$$

With these simple rules applied to specific lattices, such as the LHP hexagons, it is possible to show the lattice gas automata, on a proper lattice, can be re-expressed to satisfy continuity and conservation of momentum (see Ref.[68,190]). The construction of LGA schemes were extremely simple yet, with their connection to conservation equations in the continuum, seemed promising as a perfect scheme for modeling fluid mechanics.

However, as exciting as the early LGA methods were, their drawbacks were very nearly as disheartening after being formally compared to the Navier-Stokes equations. Succi provides a thorough summary of the early issues with FHP (and all LGA approaches).[170] For the

sake of brevity we only mention that the main disadvantages were: lack Galilean invariance at higher Mach numbers (the results were not the same irrespective of inertial frame) and statistical noise in macroscopic quantities. The microscopic nature of LGAs – tracking the paths of individual particles – precluded the method from ever completely eliminating the issues such as statistical noise. The solution to the issues came in 1988 as a group zoomed-out from the microscopic into a mesoscopic formulation – the first version of what would eventually be the lattice-Boltzmann numerical method.

5.1.3 The Lattice-Boltzmann Equation

McNamara and Zanetti proposed a fix to the statistical noise in LGA *via* ensemble-averaging the boolean occupation numbers,[129]

$$f_i = \langle n_i \rangle = \frac{1}{q} \sum_{i=1}^{q} n_i \tag{5.12}$$

where q is the number of lattice directions from the node. The average quantity, f_i, was now identical in form to the distribution function of the Boltzmann equation. In the formulation of McNamara and Zanetti, we are no longer tracking individual boolean particles but a representative ensemble population of the particles.

Replacing the boolean occupation numbers in Equation (5.10) with the density function of Equation (5.12), we have

$$f_i(\mathbf{x} + \mathbf{c}_i, t + 1) - f_i(\mathbf{x}, t) = \Omega_i(\mathbf{x}, t) \tag{5.13}$$

which is precisely the form found for the discretized Boltzmann equation in Equation (5.7)! This is the essence of the lattice-Boltzmann method: it can be considered as a simplification of the Boltzmann concept *via* reduction of the continuous phase space into a finite number of discrete phase options; or it similarly can be considered as an ensemble-averaging of the lattice gas automata into calculations of mesoscopic distribution functions.

The boolean occupation numbers were simply imagined as the actual particles traveling from node to node in the LGA lattice. The ensemble average of these numbers, $f_i(\mathbf{x}, t)$, akin to the probability density function from kinetic theory, can be envisioned to be the

probability of finding a density of particles pointing in a certain direction, i, at a given node, $\mathbf{x}$, at a specific point in time, t. The values of f_i are direction-specific fluid densities and thus macroscopic fluid properties are still directly calculated from them,

$$\rho(\mathbf{x}, t) = \sum_i f_i(\mathbf{x}, t) \tag{5.14a}$$

$$\mathbf{u}(\mathbf{x}, t) = \frac{1}{\rho(\mathbf{x}, t)} \sum_i \mathbf{c}_i f_i(\mathbf{x}, t) \tag{5.14b}$$

The fluid pressure is related to the density for an ideal gas, so we can find the physical pressure in terms of the lattice density,

$$p = p_0 \frac{\rho(\mathbf{x}, t)}{\rho_0} \tag{5.15}$$

The density distribution function, while eliminating statistical noise, broke the exactness of calculations from the boolean numbers of n_i in LGA methods. The density distribution function is now a floating point number, requiring more memory storage per node and introducing round-off error into calculations. In Chapter 3 of Ref.[170] , Succi provides an excellent discussion of the early stages of LBM and the problems that the early models (such as those of McNamara and Zanetti) faced as well as their many great advantages. For our purposes, we accept Equation (5.13) as the fundamental equation driving the evolution of the density distribution function in a system.

5.1.3.1 Collision Operator for Lattice-Boltzmann Equation

The strength of Equation (5.13) hinges on the ability for the collision operator, $\Omega_i(\mathbf{x}, t)$, to allow reproduction of the Navier-Stokes equations. Up to this point we have only alluded to its function in the LGA and now LBM computations. While there are many potential collision operators (see Ref.[170]), we focus on the operator proposed by Qian, d'Humieres, and Lallemand.[146] Noting the similarities of LBM to kinetic theory, Qian, d'Humieres, and Lallemand proposed a collision operator similar in form to that proposed by Bhatnagar, Gross, and Krook in 1954 for the Boltzmann equation.[24] Thus the operator was named the

BGK collision operator and is given as,

$$\Omega_i = -\frac{1}{\tau}\left[f_i(\mathbf{x},t) - f_i^{\mathrm{eq}}(\mathbf{x},t)\right] \tag{5.16}$$

where τ, a free parameter, is the relaxation time of the lattice, and f_i^{eq} is the equilibrium distribution. Thus in the BGK formulation, the collision operator is a relaxation of the node towards equilibrium for the density distribution function.[24]

Inserting the operator of Equation (5.16) into the evolution of the density distribution function, Equation (5.13), we have the lattice-Boltzmann evolution equation with the BGK operator,

$$f_i(\mathbf{x}+\mathbf{c}_i, t+1) = f_i(\mathbf{x},t) - \frac{1}{\tau}\left[f_i(\mathbf{x},t) - f_i^{\mathrm{eq}}(\mathbf{x},t)\right] \tag{5.17}$$

In spite of the relaxation time being a free parameter, there are limits to its value. The kinematic viscosity in a lattice is,

$$\nu = c_s^2\left(\tau - \frac{1}{2}\right) \tag{5.18}$$

which shows that τ can not shrink to an arbitrarily small number. Numerical instabilities appear as $\tau \to 0.5$ and the kinematic viscosity $\nu \to 0$. Furthermore, if $\tau > 1$, we have subrelaxation and the distribution function will never completely relax to equilibrium. When $\tau < 1$, we have overrelaxation and the system out of equilibrium will advance toward it at different rates. When τ is small, the relaxation to f^{eq} is fast and thus the viscosity of the lattice can be considered to be small. A negative viscosity occurs if $\tau < 1/2$ and is not allowed.[33,37]

The equilibrium distribution function, f^{eq}, is derived from the Maxwell-Boltzmann velocity distribution in statistical mechanics. With clever application of the ideal gas law and the isothermal ideal gas pressure relation (see, for example, Refs.[37,190]), it is possible to find an equilibrium distribution that allows Ω_i to respect all conservation laws,

$$f_i^{\mathrm{eq}} = \rho(\mathbf{x},t)w_i\left[1 + \frac{\mathbf{u}\cdot\mathbf{c}_i}{c_s^2} + \frac{(\mathbf{u}\cdot\mathbf{c}_i)^2}{2c_s^4} - \frac{\mathbf{u}^2}{2c_s^2}\right] \tag{5.19}$$

where c_s is the speed of sound on the lattice and w_i are weighted lattice constants. In the development of the equilibrium function, it is assumed that the velocity of the fluid is small

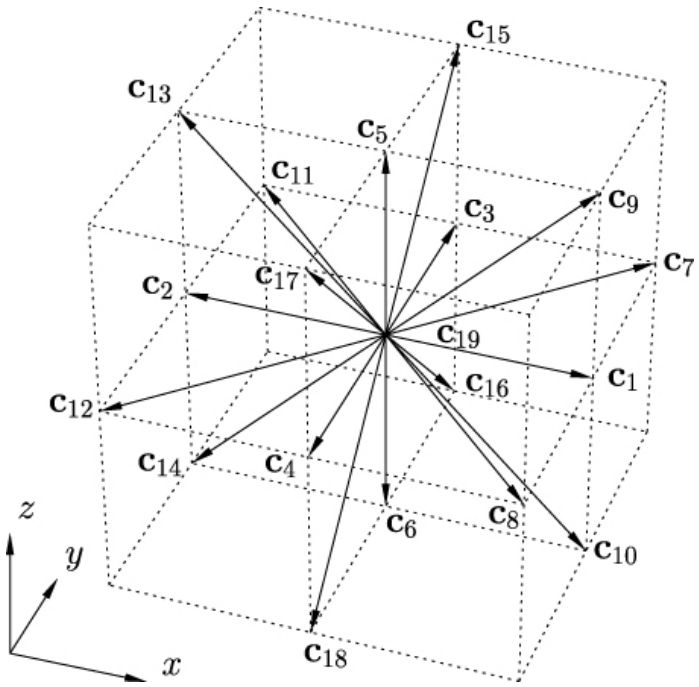

Figure 5.1: A representative node with directional vectors to the 18 neighbors (+1 central node) in the D3Q19 lattice (reproduced from Ref.[88]).

compared to the speed of sound on the lattice, in other words we require small Mach numbers: $\text{Ma} = \frac{|u|}{c_s} < 1$, on the lattice.[33,146] It is worth noting here that the equilibrium function of Equation (5.19) is defined entirely in terms of local velocity and density; everything is in terms of node i and no other neighboring node. This feature aids the LBM approach in being highly parallelizable in the same way the LGA method was.

There are several conditions a lattice must meet to satisfy the isotropy necessary to regain the Navier-Stokes equations in the macroscopic form.[116,190] A lattice structure in d dimensions with q lattice directions is commonly identified with the DdQq lattice label. In the three-dimensional flow of our packed beds, we use the D3Q19 lattice, *i.e.* $d = 3$ dimensions, and $q = 19$ nodes surround the node of interest (including the node itself). A representative node from the D3Q19 lattice is shown in Figure 5.1.

The numbered directions in the lattice of Figure 5.1 follows the standard practice of LBM. The index $i = 0$ corresponds to the node center. The indices $i = 1, 2, 3, \ldots, 6$ point to the six faces of the cube surrounding the node. Lastly, the indices $i = 7, 8, 9, \ldots, 18$ point

to the twelve midpoints of the edges of the cube. The weight constants, satisfying lattice symmetry, of the lattice structure of Figure 5.1 are calculated in Ref.[116] and given as,

$$w_i = \begin{cases} \frac{1}{3} & i = 0 \\ \frac{1}{18} & i = 1, 2, 3, \ldots, 6 \\ \frac{1}{36} & i = 7, 8, 9, \ldots, 18 \end{cases} \tag{5.20}$$

The lattice weights, w_i are necessary to account for the different vector lengths in the lattice. In principle, there is freedom in choosing the lattice speed of sound, c_s, requiring a change to the rest-weight of w_0 to maintain lattice symmetry. However, in practice, it is common to use $c_s^2 = \frac{1}{3}$ for numerical stability.[116,170]

5.1.3.2 Boundary Conditions

Techniques for implementation of no-slip boundary conditions in LBM are direct descendants of the bounce-back schemes from lattice gas automata. In the scheme, lattice nodes that exist at the boundary have particle directions that point into the wall. For example, see f_4, f_7, and f_8 in Figure 5.2 for a D2Q9 lattice. The scheme is 'bounce-back' because as particles stream into the wall, their distributions are scattered back in equal and opposite directions. Computationally, the bounce-back scheme is very attractive for the simplicity of implementing the method even in complex geometries. A fact which makes the use in LBM particularly attractive for packed bed simulations.[33] The bounce-back scheme has been shown to be first-order accurate for most three-dimensional flows, degrading the other-wise second order accuracy of the fluid bulk calculations.[33,217] To combat the loss in accuracy with increasing Reynolds number, several modifications to the bounce-back scheme have been proposed.[33] However, for the porous flow to be studied in ceramic pebble beds, it suffices to implement the bounce-back boundary condition to enforce no-slip at the fluid-particle interface.[33,122]

To treat velocity or pressure boundary conditions, the technique of Zou & He is used.[217] They proposed extending the bounce-back condition to the non-equilibrium distribution function in the direction normal to the boundary where $\mathbf{v}$ or p is specified. The approach

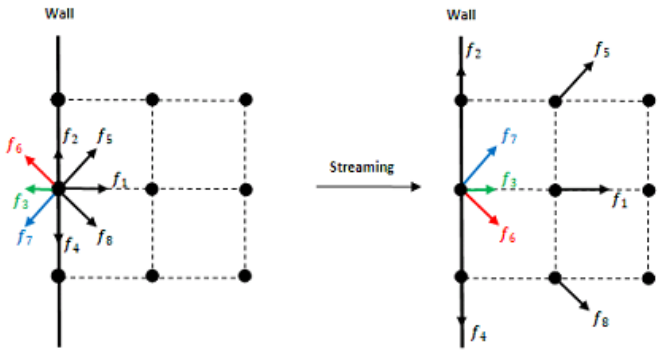

Figure 5.2: Sketch of the D2Q9 nodes showing at the boundary the distribution functions that would come from neighbors outside the boundary (at the wall) are unknown (drawing from correspondence with Dr. Bao, billbao@cims.nyu.edu).

allows closure of the algebraic calculation of distribution functions when we have a known velocity or pressure (see Eqs. 5.14). We note again that, in lattice units, determination of density is equivalent to determination of pressure *via* the ideal gas pressure law. Zou & He showed the approach provides second-order accurate results on these boundaries.[217]

5.1.3.3 Thermal LBM

Thus far the lattice-Boltzmann formulation has been shown to calculate mass and momentum transport of a fluid. But in the packed beds of fusion reactors, the transport of energy in the system is of utmost importance. To handle the thermal equations in the lattice-Boltzmann framework, we use the model of Guo *et al.*[85] Guo *et al.* introduced a second lattice upon which the distribution functions for temperature reside. The temperature distribution evolved with a coupling to the velocity distribution on the lattice solving the Navier-Stokes equations. The temperature was linked back to the Navier-Stokes lattice with a Boussinesq assumption that introduced a body force term to the fluid.[85] Guo *et al.* referred to their approach as the Coupled Lattice BGK (CLBGK) method.

On the thermal lattice in the CLBGK method, the temperature is a passive scalar that is transported by the velocity (it is specified at each node corresponding to nodes from lattice solving the Navier-Stokes equations). Therefore, the density distribution functions

on thermal lattices are in fact temperature distribution functions. The thermal lattice BGK equation is analogous to Equation (5.17) and written as,

$$g_i(\mathbf{x}+\mathbf{c}_i, t+1) = g_i(\mathbf{x}, t) - \frac{1}{\tau_g}\left[g_i(\mathbf{x}, t) - g_i^{\mathrm{eq}}(\mathbf{x}, t)\right] \tag{5.21}$$

where we have a second relaxation time for the thermal lattice, τ_g. The temperature field is reconstructed via

$$T = \sum_i^q g_i \tag{5.22}$$

A microscale Champan-Enskog expansion of Equation (5.21) can show that it is equivalent to the temperature form of the continuous energy conservation equation.[85] For the transport of the passive scalar, we can use a D3Q7 lattice which is sufficient to model the advection-diffusion of temperature.,[116,139] For such a lattice, the speed of sound is $c_{s,g}^2 = \frac{1}{2}$. We use a linear equilibrium function for g_i^{eq},

$$g_i^{\mathrm{eq}} = w_i T\left(1 + \frac{\mathbf{c}_i \cdot \mathbf{u}}{c_{s,g}^2}\right) \tag{5.23}$$

The thermal diffusivity (analogous to the viscosity in the momentum lattice) is

$$\alpha = c_{s,g}^2\left(\tau_g - \frac{1}{2}\right) \tag{5.24}$$

Thermal boundary conditions are handled *via* a decomposition of the boundary nodes into equilibrium and non-equilibrium parts and the values of the node extrapolated from neighboring nodes. Details can be found in the paper by Guo *et al.*.[85]

5.1.4 Realizing LBM Models Computationally

Because of the immensely simple implementation of no-slip boundary conditions for even the most complex geometry, the lattice-Boltzmann method was immediately seen as a powerful option of fluid modeling in porous networks. Chen & Doolen review many of the major accomplishments of implementing LBM models which verified Darcy's Law, the Cozeny-Karman equation, and Brinkmann equation, among other efforts.[33] Pan *et al.* evaluated the single-relaxation time BGK operator against models with multiple relaxation times as

well as models with different implementationsi of fluid-solid interface boundary conditions – among which was the bounce-back scheme we use here.[138] For the conditions we will consider, single-relaxation time models are sufficient.

For practical application of the LBM approach, as it will be used to simulate the conjugate heat transfer of the helium purge gas through ceramic pebble beds, there are two main objects required to define the structure of a lattice-Boltzmann model: collision operator, Ω_i, and constants which define the scaffolding of the lattice.

The computational domain of the fluid is discretized into a Cartesian grid with regularized spacing, δ_x, in every dimension. At each node are density functions, $f_i(\mathbf{x}, t)$, which represent the density at that node (found at $\mathbf{x}$), traveling in the direction of $\mathbf{c}_i$ at a moment in time, t. The density distribution function evolves according to Equation (5.13). It is helpful to look at the equation compartmentalized in the same manner it is handled computationally, thus we see the streaming and collision parts,

$$\underbrace{f_i(\mathbf{x} + \mathbf{c}_i, t + 1) = f_i(\mathbf{x}, t)}_{\text{streaming}} + \underbrace{\Omega_i(\mathbf{x}, t)}_{\text{collision}}$$

Conceptually the two steps of lattice evolution can be thought of as two distinct operations. First, the collision operator is calculated based only on each node's local information. Using the BGK approximation, given in Equation (5.16), the collision is calculated as,

$$\Omega_i = -\frac{1}{\tau}\left[f_i(\mathbf{x}, t) - f_i^{\text{eq}}(\mathbf{x}, t)\right]$$

Post-collision, in the streaming step, the information is passed from every node to its neighbors along the lattice directions shown in Figure 5.1. While the collision operation is exactly local, the streaming operation involves only nearest neighbors. After the streaming step, the nodes that lie along the boundary have the bounce-back scheme applied wherein distributions arriving at the boundary are reflected back to their incident directions.

Splitting the evolution of the distribution function into the two steps of collision and streaming, in addition to being a conceptual aid, is a natural partition of computational steps. In practice the algorithm proceeds as follows,[190]

1. using macroscopic properties of density and fluid velocity, the equilibrium distribution function is calculated at every node following Equation (5.19),

2. the BGK collision operator is calculated according to Equation (5.16) to find the post-collision distribution of every node,

3. information from each node streaming to neighboring nodes based on the evolution equation of Equation (5.13),

4. updated macroscopic properties are found from the new distribution functions according to Equation (5.14).

It is worth stressing again that the lattice-Boltzmann collision calculations are completely local, with the streaming step requiring only nearest inter-node communication for updating distribution functions which lends the method to extremely efficient parallelization.

5.1.5 Physical to Lattice Units

In LBM one typically works with lattice variables – differing from their physical counterparts simply through normalization. This is akin to achieving dynamic similarity in fluid mechanics experiments. Therefore the nondimensional form of governing equations is discussed, and then the nondimensional values are translated into lattice variables. We then see how tuning of some lattice variables will allow a sufficiently refined grid while still representing the physical system we are attempting to model. The notation of working with physical, nondimensional, and lattice variables can quickly become cumbersome. The convention here is to use $\hat{\psi}$ for physical variables, ψ^*, or nondimensional variables, and simply ψ for lattice variables.

Thus the Navier-Stokes equations, in physical units, for an incompressible fluid are

$$\hat{\nabla} \cdot \hat{\mathbf{u}} = 0 \tag{5.25}$$

and

$$\frac{\partial \hat{\mathbf{u}}}{\partial \hat{t}} + (\hat{\mathbf{u}} \cdot \hat{\nabla})\hat{\mathbf{u}} = -\frac{1}{\hat{\rho}_0}\hat{\nabla}\hat{p} + \hat{\nu}\hat{\nabla}^2\hat{\mathbf{u}} \tag{5.26}$$

I nondimensionalize the length scale based on the average diameter of pebble in our system, the velocity by the superficial velocity of our inlet, and pressure and time on derived forms of these two variables,

$$x^* = \frac{\hat{x}}{\hat{d}_p} \tag{5.27a}$$

$$\mathbf{u}^* = \frac{\hat{\mathbf{u}}}{|\hat{u}|_i} \tag{5.27b}$$

$$p^* = \frac{\hat{p}}{\hat{\rho}_0 |\hat{u}|_i^2} \tag{5.27c}$$

$$t^* = \frac{\hat{t}}{\frac{\hat{d}_p}{\hat{\mathbf{u}}_i}} \tag{5.27d}$$

Thus the nondimensional form of Navier-Stokes is the familiar,

$$\nabla^* \cdot \mathbf{u}^* = 0 \tag{5.28a}$$

$$\frac{\partial \mathbf{u}^*}{\partial t^*} + (\mathbf{u}^* \cdot \nabla^*)\mathbf{u}^* = -\nabla^* p^* + \frac{1}{\mathrm{Re}} \nabla^{*2} \mathbf{u}^* \tag{5.28b}$$

Note, too, that the physical limits of our system are describable in terms of the nondimensional units. In other words, if our system is $\hat{X}$ meters wide, the nondimensional width is $X^* = \frac{\hat{X}}{\hat{d}_p}$.

Next, the dimensionless kinematic viscosity, $\nu^* = 1/\mathrm{Re}$, is converted into a lattice viscosity as

$$\nu = \frac{\delta_t}{\delta_x^2} \frac{1}{\mathrm{Re}} \tag{5.29}$$

from which, we can finally calculate the relaxation time for our single-relaxation-time, D3Q19 lattice (calculated from Equation (5.18)) as,

$$\tau_{ns} = \frac{\nu}{c_s^2} + \frac{1}{2} \tag{5.30}$$

where the subscript $_{ns}$ denotes the relaxation time is specific for the fluid flow as described by the Navier-Stokes equations and the lattice speed of sound is $c_s^2 = \frac{1}{3}$.

To specify the velocity boundary condition (and similarly to convert our lattice velocity results back into physical values), we must have a translator between nondimensional and

lattice velocities,

$$\mathbf{u} = \frac{\delta_t}{\delta_x}\mathbf{u}^* \tag{5.31}$$

Translating from physical to lattice units is done via,

$$\mathbf{u} = \frac{\delta_t}{\delta_x}\frac{\hat{\mathbf{u}}}{|\hat{u}|_i} \tag{5.32}$$

The spatial discretization of the lattice is defined in terms of the resolution of our sphere in the discretization process. The values of lattice spacing, δx, and the total lattice nodes are calculated as,

$$\delta_x = \delta_y = \delta_z = \frac{1}{\text{res}} \tag{5.33a}$$

$$N_x = \text{res} \cdot X^* + 1 \tag{5.33b}$$

$$N_y = \text{res} \cdot Y^* + 1 \tag{5.33c}$$

$$N_z = \text{res} \cdot Z^* + 1 \tag{5.33d}$$

where res is defined as the number of nodes spanning the diameter of a pebble.

The only lattice parameter not defined at this point is the lattice time step, δ_t. In lattice-Boltzmann, δ_t and δ_x are linked *via* the incompressibility constraint in the lattice. At the same time, from Equation (5.31), the lattice velocity is directly related to the lattice time step size; and the magnitude of $\mathbf{u}$ may not be larger than the speed of sound on the lattice, c_s. The time step is further constrained when enforcing incompressibility of our fluid. The LB model is a quasi-compressible fluid solver which permits slight compressible regimes to enter the system to solve the pressure equation of the fluid. Compressibility effects will impact the numerical accuracy and should therefore be minimized. Compressibility effects scale like the square Mach-number, Ma^2, and thus effects can be minimized by enforcing a small Mach number. In LBM, the lattice Mach number is simply,

$$\text{Ma} = \frac{|\mathbf{u}_0|}{c_s} \tag{5.34}$$

where $|\mathbf{u}_0| = \frac{\delta_t}{\delta_x}$. Thus to say the compressibility error scales like $\epsilon \sim \text{Ma}^2$ is to say it scales like $\epsilon \sim \frac{\delta_t^2}{\delta_x^2}$. The compressibility error need not be smaller than the numerical error of the

LBM method itself. As LB is second-order accurate,[170] $\epsilon \sim \delta_x^2$, we can then determine the time step size relative to lattice spacing for which the two errors will be comparable in size,

$$\frac{\delta_t^2}{\delta_x^2} \sim \delta_x^2$$
$$\rightarrow \delta_t \sim \delta_x^2$$

Also, because the lattice spacing is directly dependent on our chosen resolution, the requirement on time step is alternatively written as

$$\delta_t \sim \frac{1}{\text{res}^2} \tag{5.35}$$

which shows, similar to standard CFD solvers, the time step requirement shrinks rapidly as we attempt to more finely represent the pebbles with more and more nodes. Thus care must be taken to balance the resolution with the time step requirements.

In the LBM model, we only treat the energy as a passive scalar transported by the fluid motion (*i.e.* we do not make the Boussinesq approximation to couple the fluid energy to momentum). The energy equation for the fluid in physical units is,

$$\frac{\partial \hat{T}_f}{\partial \hat{t}} + \hat{\nabla} \cdot (\hat{\mathbf{u}}\, \hat{T}_f) = -\hat{\alpha}_f \hat{\nabla}^2 \hat{T}_f \tag{5.36}$$

The temperature will be nondimensionalized based on a characteristic temperature of volumetric heating,

$$T^* = \frac{\hat{T} - \hat{T}_c}{\Delta \hat{T}} \tag{5.37}$$

and the time and length scales are nondimensionalized as in the Navier-Stokes equations. Thus the nondimensional energy equation is

$$\frac{\partial T_f^*}{\partial t^*} + \nabla^* (\mathbf{u}^* T_f^*) = \frac{1}{\text{Pe}_f} \nabla^{*2} T_f^* \tag{5.38}$$

where Pe is the Peclet number ($\text{Pe} = \text{Re} \cdot \text{Pr}$).

To discretize the dimensionless energy system into the lattice, we recognize the similarities between Equation (5.28) and Equation (5.38) to directly write the lattice thermal diffusivity of the fluid as

$$\alpha_f = \frac{\delta_t}{\delta_x^2} \frac{1}{\text{Pe}_f} \tag{5.39}$$

For the solid, the energy equation in dimensional units is

$$\frac{\partial \hat{T}_s}{\partial \hat{t}} = \hat{\alpha}_s \hat{\nabla}^2 \hat{T}_s + \frac{\hat{q}'''}{\hat{\rho}_s \hat{C}_{ps}} \tag{5.40}$$

which similarly nondimensionalizes to,

$$\frac{\partial T_s^*}{\partial t^*} = -\alpha_s^* \nabla^{*2} T_s^* + Q^{'''*} \tag{5.41}$$

where the dimensionless thermal diffusivity of the solid is $\alpha_s^* = \frac{\hat{\alpha_s}}{\hat{d}_p \hat{u}_i}$ and the dimensionless nuclear heating rate is $Q^{'''*} = \frac{\hat{q}''' \hat{d}_p}{\hat{u}_i \hat{\rho}_s \hat{C}_{ps} \Delta \hat{T}}$.

We can now directly write the lattice thermal diffusivity of the solid as

$$\alpha_s = \frac{\delta_t}{\delta_x^2} \frac{1}{\alpha_s^*} \tag{5.42}$$

The lattice heat rate is $Q = \delta_t Q^{'''*}$

On the thermal lattice, we need only use a D3Q7 to satisfy isotropy, for which the lattice speed of sound is only $c_s^2 = \frac{1}{2}$ (I will refer to it as $c_{s,ad}$ to distinguish). On this lattice, we are solving the energy equation for both the fluid and solid, so each material has a unique relaxation time. They are designated as the advection-diffusion (ad) and conjugate (cj) relaxation times, for short. They are,

$$\tau_{ad} = \frac{\alpha_f}{c_{s,ad}^2} + \frac{1}{2} \tag{5.43a}$$

$$\tau_{cj} = \frac{\alpha_s}{c_{s,ad}^2} + \frac{1}{2} \tag{5.43b}$$

and the size of lattice spacing and time steps are equal to those of the Navier-Stokes lattice.

To summarize the unit conversion process described above, our lattice needs to be defined in terms of lattice spacing and time step. The physics of the system are encompassed in the relaxation time – values which can be determined completely from lattice spacing and nondimensional values of the Reynolds, Peclet, and solid diffusivity values. Physical boundary conditions of velocity and temperature can be enforced in the lattice with translations into lattice variables as given above.

Lattice diffusivity values given in Equation (5.29), Equation (5.39), and Equation (5.42), respectively, are summarized together,

$$\nu = \frac{\delta_t}{\delta_x^2}\frac{1}{\mathrm{Re}}$$
$$\alpha_f = \frac{\delta_t}{\delta_x^2}\frac{1}{\mathrm{Pe}_f}$$
$$\alpha_s = \frac{\delta_t}{\delta_x^2}\frac{1}{\hat{\alpha}_s^*}$$

From which we calculate relaxation times:

$$\tau_{ns} = \frac{\nu}{c_s^2} + \frac{1}{2}$$
$$\tau_{ad} = \frac{\alpha_f}{c_{s,ad}^2} + \frac{1}{2}$$
$$\tau_{cj} = \frac{\alpha_s}{c_{s,ad}^2} + \frac{1}{2}$$

And relaxation parameters:

$$\omega_{ns} = \frac{1}{\tau_{ns}}$$
$$\omega_{ad} = \frac{1}{\tau_{ad}}$$
$$\omega_{cj} = \frac{1}{\tau_{cj}}$$

5.2 Numerical Implementation of LBM and DEM Coupling

As usual, the packing structure of our pebble bed is rendered with the code LIGGGHTS. Details of the software are described in § 3.1.3. The DEM solver is a highly parallel C++ code based on the Molecular Dynamics (MD) code LAMMPS.[144] The translation between the DEM packing and LBM nodal network is done with Python scripts created specifically to discretize and digitize the 'spherical' information of DEM into LBM. To solve the lattice-Boltzmann collision and streaming equations, we make use of the open-source code maintained by FlowKit Ltd named Palabos.[62] The Palabos library provides an interface for quick implementation of lattice-Boltzmann models in C++. Implemented models include the BGK and thermal flows with the Boussinesq approximation, among many others.

The lattices available are the common grids of D2Q9, D3Q13, D3Q15, D3Q19, or D3Q27. Zou/He, periodic, and bounce-back conditions are built into the LB kernel; implementation of Dirichlet or Neumann conditions with velocity or pressure are also available. The software is freely available under the terms of the open-source AGPLv3 license.[67] All mentioned models and ingredients are parallelized with MPI, including the I/O operations that are implemented in terms of MPI's Parallel I/O API.

5.3 DEM Mapping to LBM & Realizing Proper Hydrodynamics

Unlike the dynamic coupling between DEM and the volume-averaged CFD where information passed back and forth between fluid and particle, in the LBM construction we are simply translating a static packing structure from DEM into the LBM framework. The lattices of the LBGK solver use equally spaced nodes that discretize our volume into regular spacing. The pebble data from DEM is mapped onto the LBM nodes with a script *via* knowledge of the centroid and radius of each pebble. To demonstrate, in Figure 5.3, we have a sketch of the outline of a two-dimensional slice of a pebble projected onto a section of an LBM lattice. If the distance from a node to the centroid is less than pebble radius, the node is assigned as solid. All other nodes are assigned as fluids.

In the example of Figure 5.3, the resolution is only 9. Thus 9 nodes are needed to span the diameter of a single pebble and the lattice spacing is $\delta_x = 1/9$. In the second example shown in Figure 5.4, we see an individual pebble in three dimensions that has been mapped onto the LBM nodes with a resolution of 25 (thus $\delta_x = 1/25$). The trade-off between small lattice spacing is the ability to resolve the spherical surface of the pebble, stability, and even the ability to resolve a proper packing fraction in the pebble bed.

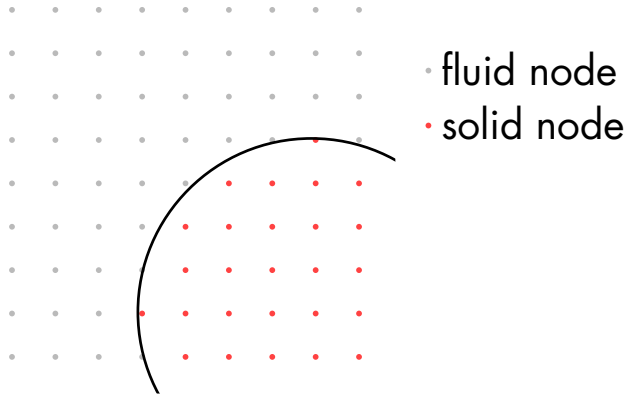

Figure 5.3: An example of the mapping process from DEM to LBM structures. Nodes are assigned as fluid or solid based on relative location of pebble centroid and radius. Here we have a resolution of 9 (*i.e.* 9 nodes per pebble diameter).

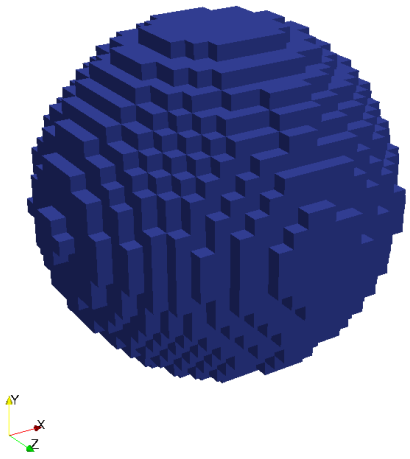

Figure 5.4: A three-dimensional DEM pebble as imported into the LBM lattice with a resolution of 25.

5.3.1 Consistency of Packing Fraction in Digitization

In the process of digitizing DEM onto lattice sites, the size of the sphere is often over-represented and the LBM lattice does not faithfully reproduce the correct void fraction from DEM. In order to capture proper macroscopic values of porosity on the lattice sites, a radius-reduction factor was introduced into the digitization process. Radii mapped into LBM are then $r_{lbm} = kr_{dem}$. The effects of the radius reduction factor can be seen in Figure 5.5, where the void fraction is calculated as discussed below.

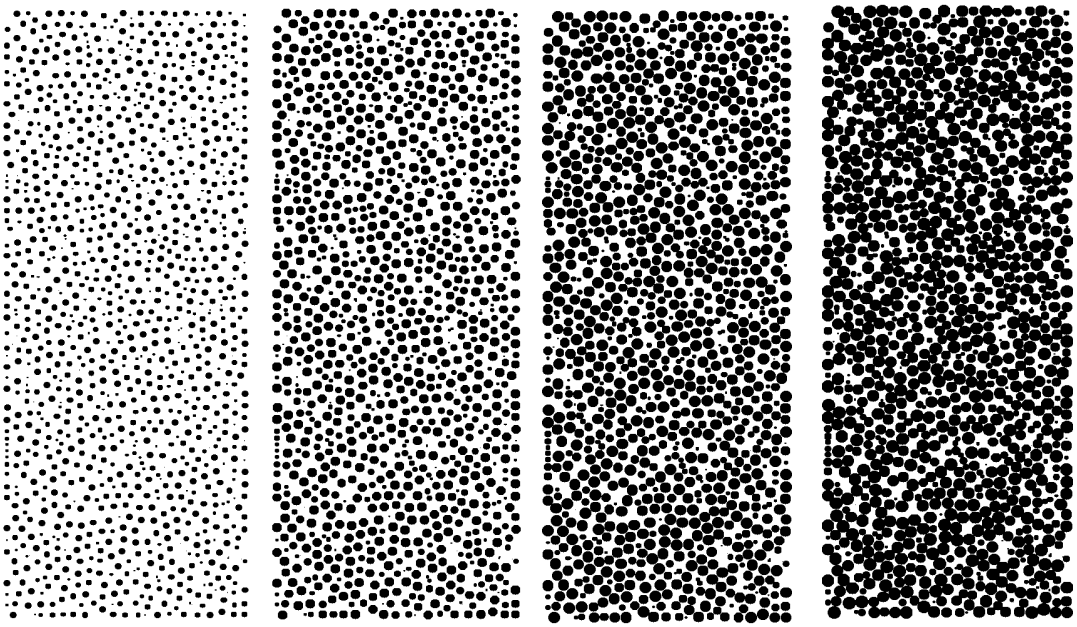

(a) $\phi = 0.181$ in pebble bed section with $k = 0.50$.

(b) $\phi = 0.389$ in pebble bed section with $k = 0.75$.

(c) $\phi = 0.555$ in pebble bed section with $k = 0.90$.

(d) $\phi = 0.667$ in pebble bed section with $k = 1.00$.

Figure 5.5: For a given resolution, the scaling parameter k will result in different packing fractions. These mappings were generated from a pebble bed with $\phi = 0.64$; only a specific k will yield that void fraction after mapping into LBM.

A digital void fraction for each mapping was measured numerically by comparing the

number of white pixels to black pixels in each bitmap slice,

$$\phi_{d,j} = \frac{N_{\text{black}}}{N_{\text{white}} + N_{\text{black}}} \tag{5.44}$$

Then the total digital packing fraction of the ensemble, as mapped into LBM, is simply

$$\phi_d = \frac{1}{J} \sum_{j}^{J} \phi_{d,j} \tag{5.45}$$

where there are J total slices. For example, we see in Figure 5.6 a plot of the digital packing fraction moving through a particular pebble bed. Digital packing fractions changed as a function of the radius-reduction factor and can be seen in Figure 5.5. The DEM packing from which these slices originated was a $\phi = 0.64$ initial packing of § 6.2.

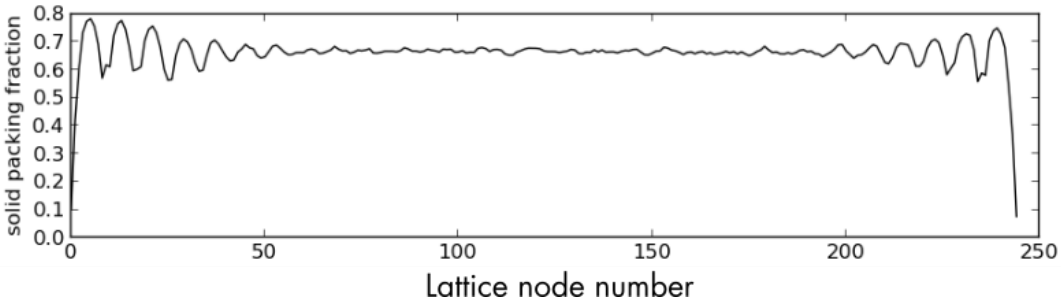

Figure 5.6: The digital packing fraction was measured at all slices through the height of the pebble bed. When the average value equaled the expected value, the mapping from DEM to LBM was considered consistent.

5.3.2 Pore Size Effects on Hydrodynamics

To model proper hydrodynamics with the lattice-Boltzmann method there are still several measures the lattice must satisfy. Several numerical experiments by Succi *et al.* have shown proper hydrodynamics of Pouiselle flow in channels requires 4 lattice sites for fluid in pores.[170] When spherical packings are digitized onto LBM lattices, constricted pores are consistently observed when resolutions are low and we thus must consider if there are regions of the lattice violating Succi's rule of 4 nodes (pixels). Taking DEM packings from § 6.2, we analyze the pore size distributions of different resolutions. The important pore size for a flow in the

x-direction is the transverse y-z-plane. Thus taking a digitized bitmap of the $\phi = 0.64$ DEM packings, we measure the pore size sweeping along the y- and z-axes to generate Figure 5.7 for various resolutions.

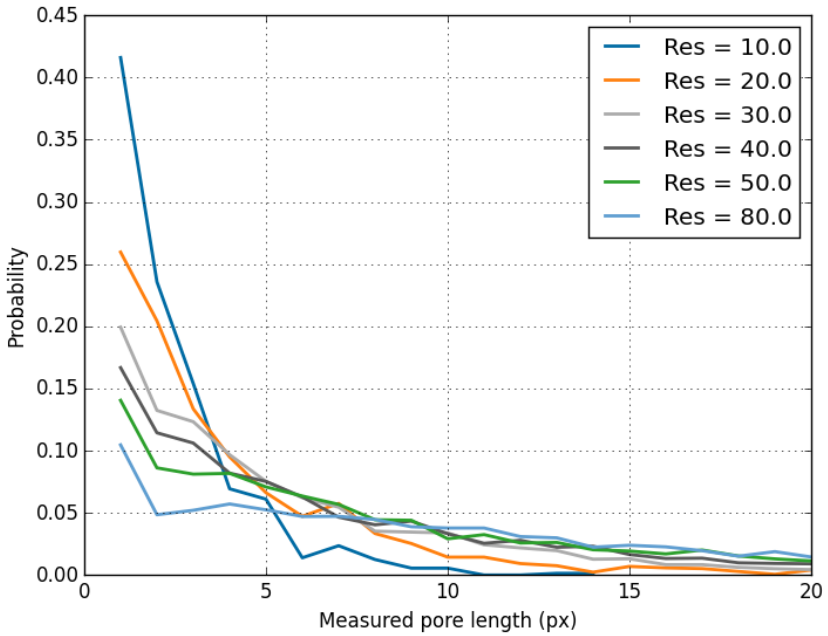

Figure 5.7: Normalized histogram of pore sizes with increasing resolution. Hydrodynamic fidelity is violated with average pore sizes less than 4 nodes on the LBM lattice.

Figure 5.8 shows the percentage of pore openings in the lattices that are less than the 4 nodes recommended for proper hydrodynamics. Adhering to Succi's criteria of 4 pixel-wide pore opening minimums, it is obvious that the lattice resolution of 10 is unacceptable in terms of faithful reproduction of packed bed flow hydrodynamics: nearly 90% of the pores in the lattice are less than 4 nodes wide. It is less evident if the violation of 4-node recommendation of other resolutions are allowable, so we instead consider the Knudsen criteria for continuous media for these resolutions.

The Knudsen number, the ratio of a gas's mean free path, λ_{mfp}, to a characteristic geometric length of the system, L,

$$\mathrm{Kn} = \frac{\lambda_{mfp}}{L} \tag{5.46}$$

is a key nondimensional parameter indicating when continuum assumptions, free molecule

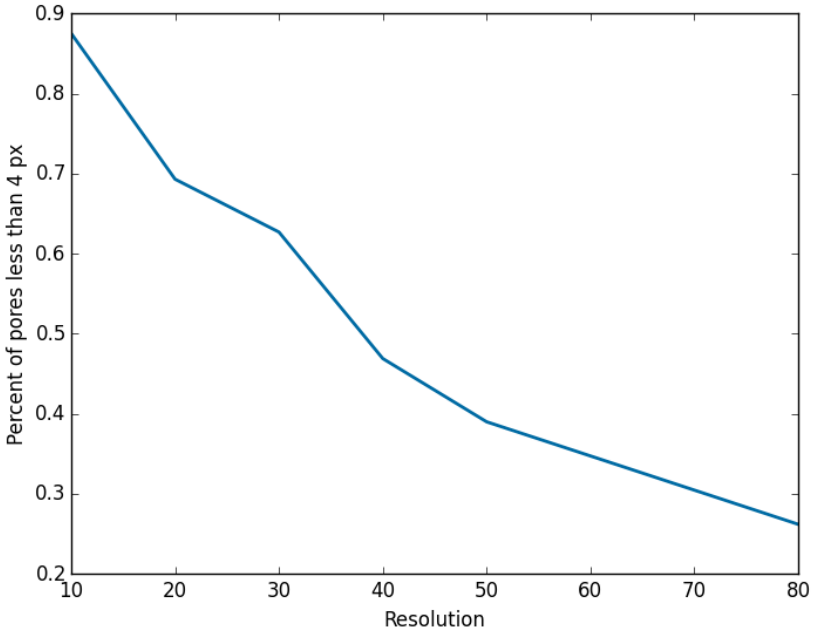

Figure 5.8: For small resolutions, the number of pore openings smaller than 4 lattice nodes is 87.5%. Increasing the resolution to 80 reduces this percentage to 26.2%.

solutions, or rarefaction take place in a gas flow. The mean free path for an ideal gas can be calculated as

$$\lambda_{mfp} = \frac{\mu}{\rho}\sqrt{\frac{\pi M}{2k_b T}} \tag{5.47}$$

where viscosity, μ, and density, ρ, are temperature-dependent. M is molecular mass, k_b the Boltzmann constant, and T absolute temperature.

A classification of flow regimes dictates that must be Kn $< 10^{-2}$ for the continuum assumption to hold.[106] The Knudsen number is calculated as a function of pore size and temperature for helium in Figure 5.9. To satisfy the Kn criteria for continuum modeling, pore sizes must be larger than 50 µm for helium at 400 °C and greater than 100 µm at 900 °C.

In packed beds of spheres, a large range of pore sizes appears; near the contact points of two pebbles, pore sizes can be extremely small. Simultaneously, pore sizes between some pebbles in the packing can be on the order of pebble diameters. The distribution of pore sizes for a $\phi = 0.64$ packing can be directly measured from very high resolution, res = 10 000, digitalizations of DEM. Pore size is converted into micro-meters from the translation

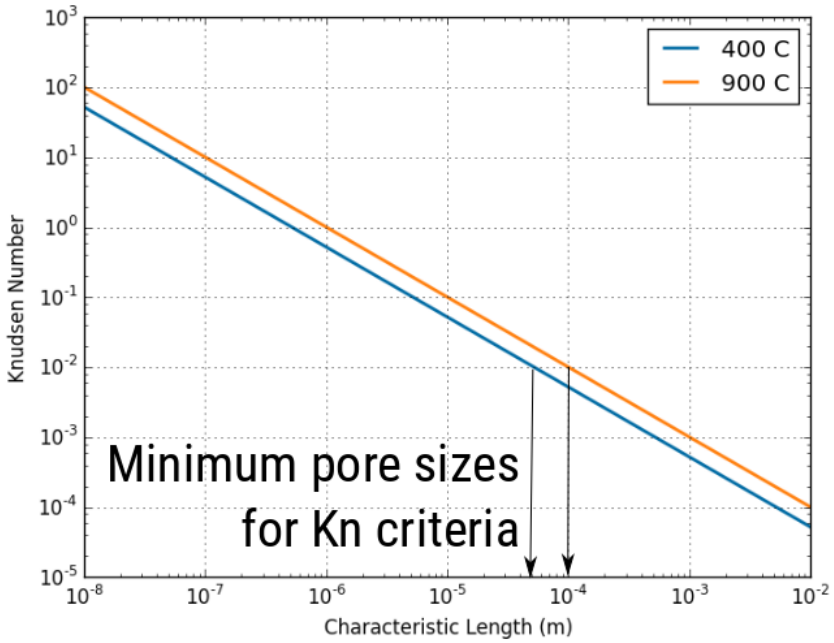

Figure 5.9: Knudsen number for helium at 400 °C and 900 °C as a function of characteristic pore size.

between resolution and pebble diameter (resolution = pixels/mm). The result is shown in Figure 5.10. Analysis of pore sizes tells us that this packed bed has 41.2% of its pores smaller than 100 µm and 22.5% of the pore openings are smaller than 50 µm. In other words, based on the Knudsen number of helium, at 400 °C, nearly a quarter of the gaseous space in the pebble bed is violating the assumption necessary for continuum treatment of the fluid. As the temperature increases to 900 °C, almost half of the gaseous space is in violation of the continuum assumption.

We are left with two, somewhat unsatisfying, conclusions from this present consideration. First, assuming a 64% packed bed that is digitized with a resolution of 40 voxels per mm at an average temperature of 400 °C, Succi's criteria of 4 voxels per throat necessary to model continuum mechanics is violated in nearly 50% of the packed bed. Second, in the same packed bed, Knudsen's criteria which allows treatment of the fluid as a continuum is also violated in nearly 22.% of the bed. Thus, we cannot directly ascertain if moderate resolution lattices (*i.e.* 20 to 80 voxels per mm) provide accurate hydrodynamics at high temperatures

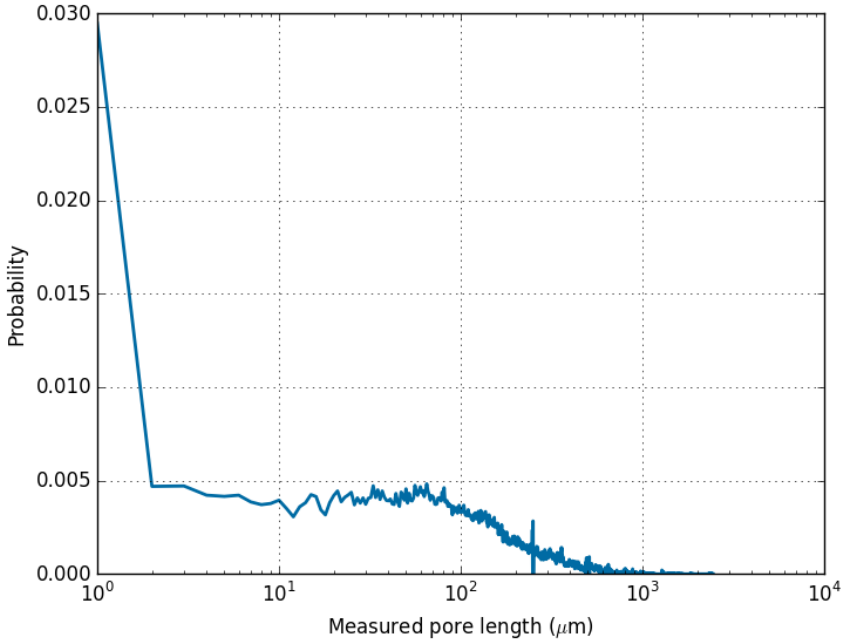

Figure 5.10: Measured pore sizes from digitized DEM packings at $\phi = 0.64$, determined from a lattice with res $= 10\,000$.

when Knudsen's criteria is violated. For the sake of this research, we must assume that these moderate resolution lattices are acceptable and leave the issue of violating Knudsen criteria in heated packed beds for future research consideration.

5.3.3 Parametric Study with Resolution and Packing Fractions

We now apply LBM models to a variety of DEM-generated pebble beds to find an optimum resolution which yields both tractable models in terms of computational time and stability. Packing fraction and resolution of slices have a direct impact on both of computational time and lattice stabilities. We consider several two-dimensional slices from a three-dimensional packing, such as the slices shown in Figure 5.5. Lattices were generated with varying values of both radius reduction factor, k, and resolution, res. Using simple boundary conditions of no-slip on the left and right walls, a Neumann boundary condition at the outlet (top) and constant velocity at the inlet (bottom), all latices were tested to find the stability of the resolutions and packings. To determine if a steady-state condition was reached, the velocity

of the entire lattice was integrated. The value has units of $\psi = [m/s][lu^2]$, with dimensionless lattice spacing units. The value of ψ is plotted in Figure 5.11; we see a steady-state velocity is reached in all of the low-packing fraction lattices. As the packing fraction increased, following the increase of k, we see the system velocity slowly becomes unstable. When $k = 0.9$, with a packing fraction of $\phi = 0.555$, the system approximately linearly increases into unstable values. Note, for the case when $k = 1$, the density calculated in this system blew up to ∞ in less than 300 steps, so the velocity profile does not have a chance to demonstrate the unstable increase. For that bed, the packing fraction was high enough that there was not a continuous path available between inlet and outlet.

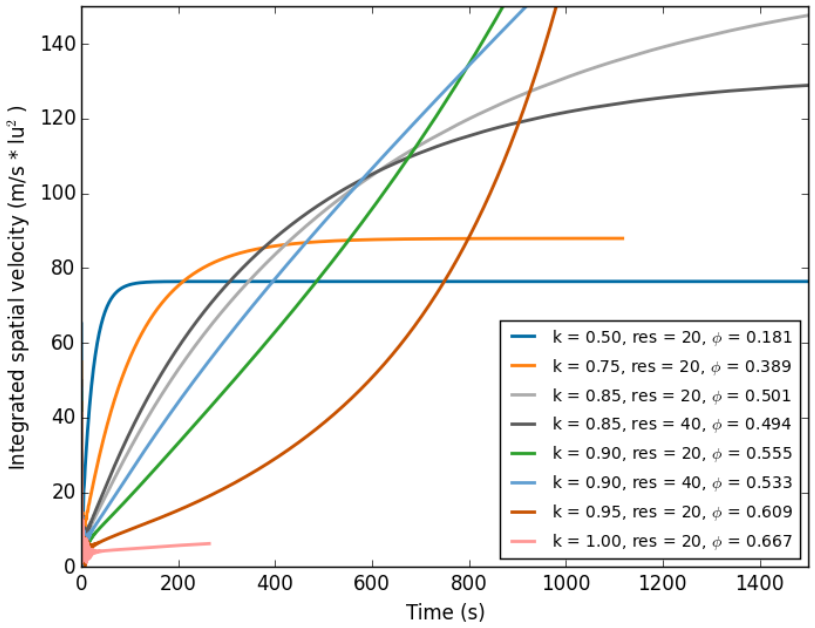

Figure 5.11: Integrated system velocity shows stable lattice configurations in two dimensions.

The two-dimensional study shows settings that lead to a stable lattice but, because of the limitations of two-dimensional lattices, such as rapid instability in such cases as $k = 1$, an additional study was done on a scaled-down pebble bed in three-dimensions (temporarily without consideration for the error of the modeled hydrodynamics). The simplified system considers a pebble bed with width of $6d_p$, periodic depth of $1d_p$, and height of approximately $6d_p$. The pebble bed is discretized using the same numeric schemes and loaded onto three-

dimensional lattices. The pebble bed, as visualized from DEM data, is shown in Figure 5.12. When the simplified pebble bed is mapped onto discrete LBM nodes, we see the effects of resolution in Figure 5.13. Here we have chosen resolutions of 10, 20, and 40, respectively. For each resolution, the coarseness of discretization requires varying radius reduction factors in order to achieve a consistent digital packing fraction; k = 0.92, 0.947, and 0.97, respectively. Details of the lattices are given below in Table 5.1.

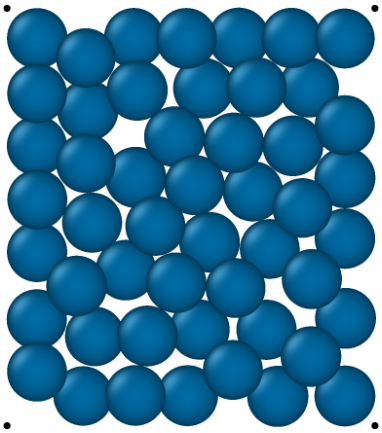

Figure 5.12: Simplified three-dimensional pebble bed, packing generated with DEM.

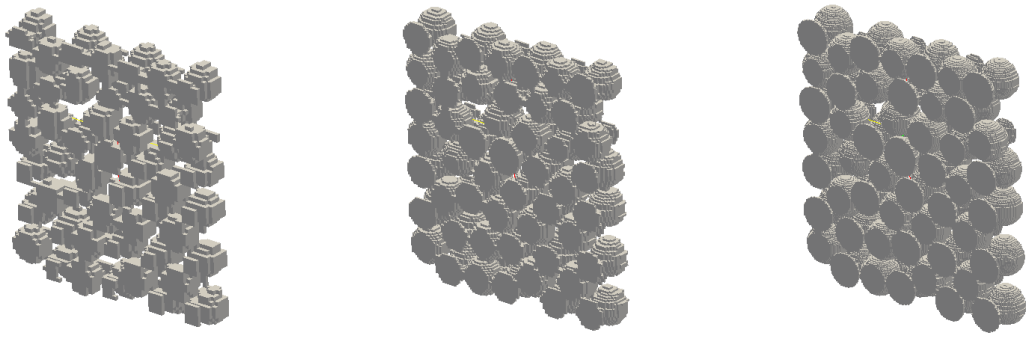

(a) $k = 0.92$, res = 10. (b) $k = 0.947$, res = 20. (c) $k = 0.97$, res = 40.

Figure 5.13: For a specified packing fraction, 62.4%, different resolution lattices require different radius scaling factors. The increased resolution is seen in increasing accuracy of spherical modeling on the discretized lattice.

In Figure 5.14, the lattices shown in Figure 5.13 and others have their overall average

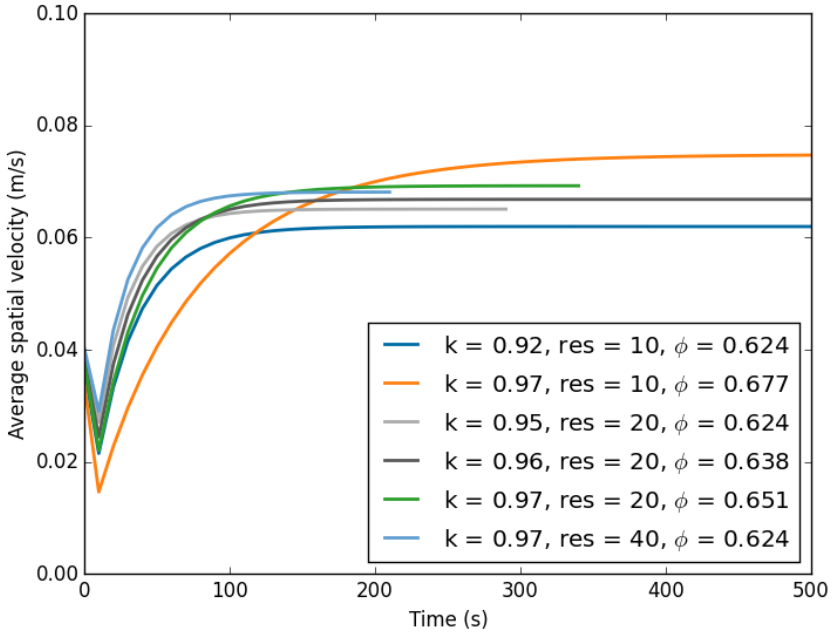

Figure 5.14: Averaged system velocity shows pebble beds with the same digital packing fraction and different resolutions will have different average system velocities.

velocity plotted. In this case, the magnitude of steady-state velocity is important so the integrated velocity has been divided by the total fluid space in the simulation. We see from Figure 5.14 that a lattice with the same packing fraction will have slightly different rates at which steady-state is approached.

At a location along the axial midpoint, velocity profiles across the pebble bed are shown in Figure 5.15. The velocity jets in the near-wall region, caused by low packing fraction from ordered packing, are not well-captured by the low resolution (res = 10) lattice. Other features of velocity are qualitatively seen in the low resolution packing, such as the velocity near $x = 2$ lu, but the res = 20 shows much greater correspondence with the profiles predicted by the highest resolution packing.

Considerations of the velocity in the packed bed are important because the impact of tortuous velocity pathlines are what we seek to understand with implementation of the DEM-LBM study. However, hydrodynamically, an important measure of the physical fidelity of the packing simulation is the pressure drop across the bed. In Figure 5.16, the pressure

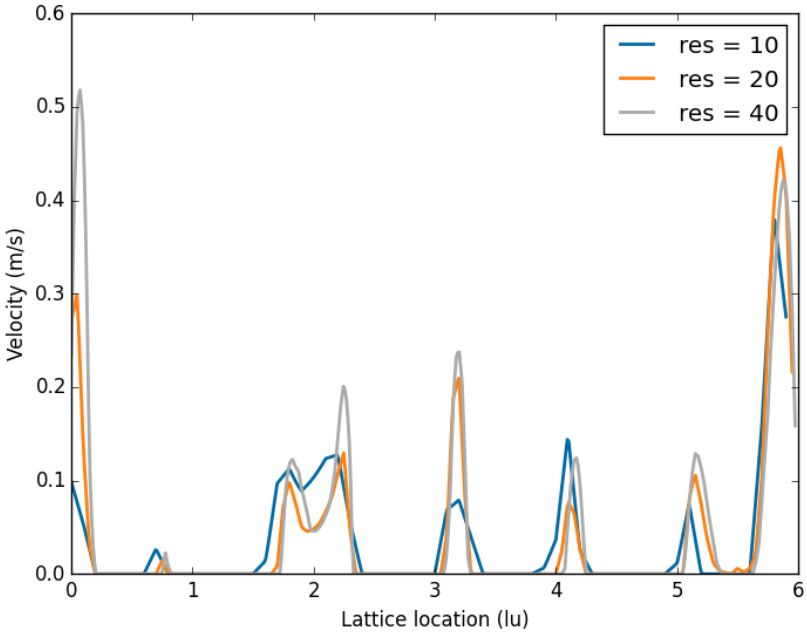

Figure 5.15: Low resolution lattices show qualitatively similar behavior but have insufficient resolution to capture jet velocity magnitudes.

drop between inlet and outlet as a function of time are given for the three packings with equal packing fraction (the beds of Figure 5.13). The pressure drop predicted by the Kozen-Carman relationship is approximately 66 Pa. The steady state value of the res = 40 lattice is 61 Pa. The lower resolution, res = 20, lattice comes close to the KC prediction; the steady-state pressure drop is 64 Pa. The lowest resolution pebble bed lattice is unstable and the density blows up shortly after 200 sec.

The last aspect to consider in the execution of the LBM model is the duration of a complete simulation. The last row in Table 5.1 shows the product of total timesteps (to reach 200 s) and total lattice nodes. Assuming a perfect scalability of the simulation, this value is approximately the number of calculations performed to solve for steady-state on the lattice. Normalizing against the res = 10 lattice, we see that it requires 16 times longer to run the res = 20 lattice and more than 255 times longer to run the res = 40 lattice. The same scaling rules will apply to the full pebble bed lattices that we wish to study. Thus, like most models of packed beds, we are forced to concede some accuracy in physics of

the model for simplifications that allow reasonable computational times. For this reason, we conclude that the res = 20 lattice, with k chosen to satisfy digital porosity, is the appropriate setting to continue pebble bed simulations. The res = 20 lattice had reasonable accuracy on hydrodynamic measurements of pressure drop and showed acceptable ability to capture features of the flow velocity such as the near-wall jets.

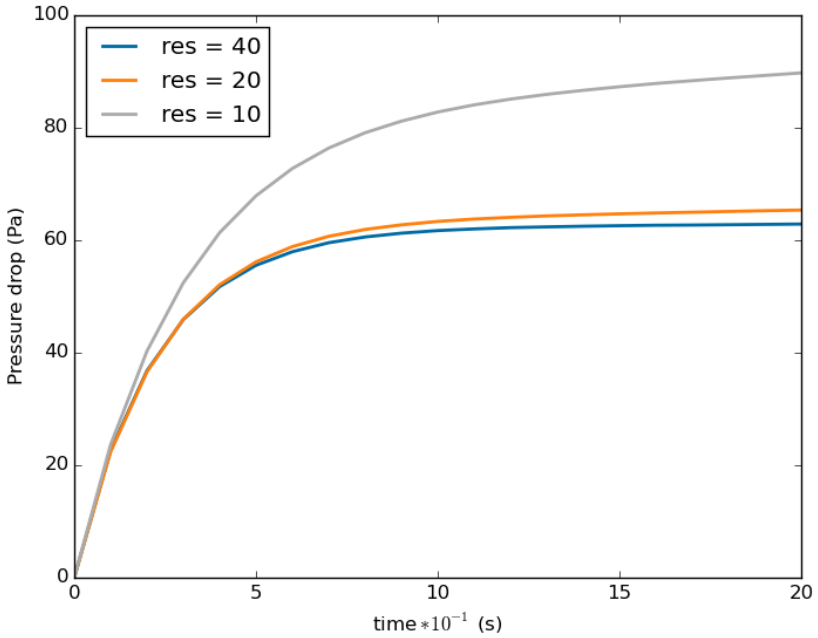

Figure 5.16: Pressure drops across the simplified pebble bed approaching steady-state in time. The low resolution pebble bed greatly over-predicts the pressure drop. Increased resolution appears to converge to approximately 61 Pa.

Table 5.1: Comparison of lattice parameters for simplified pebble bed model.

res	10	20	40
N_x	60	120	240
N_y	10	20	40
N_z	138	276	553
N_{tot}	82.8×10^3	662.4×10^3	5308.8×10^3
ω_{ns}	1.131	0.789	0.491
δ_x	0.1	0.05	0.025
δ_t	0.001	0.0005	0.00025
N_t	200×10^3	400×10^3	800×10^3
$N_{\text{tot}} \times N_t$	16.6×10^9	264.9×10^9	4247.0×10^9

5.4 Summary of LBM Modeling Development

The lattice-Boltzmann method of modeling fluid flow was introduced and its merits for application to porous flow discussed. We have shown a method for mapping data of packing structures, generated in DEM, onto nodes of lattices solving momentum/mass and energy conservation with collision-streaming operations of the lattice-Boltzmann method. The LBM approach was chosen in place of finite element or finite volume methodology because of, firstly, the extreme ease with which boundary conditions can be applied inside the highly complex packing structure of ceramic pebble beds; enforcing no-slip conditions on complex geometry is trivially realized with bounce-back rules on distribution functions. Furthermore, discretization of fluid domains in lattice-Boltzmann frameworks requires no special meshing in the highly-skewed regions near contacting pebbles, such as is necessary with standard CFD/FEM solvers. The multi-relaxation-time lattices for momentum and energy offer complete modeling of complex geometry and conjugate heat transfer with far less computational overhead compared to FEM models.

We also showed that proper selection of lattice properties can lead to stable solutions that

are also faithful to the macroscopic fluid mechanics being modeled. Consistency in packing structure representation is maintained between DEM and LBM through modification of pebble radii when mapped on LBM voxels; accomplished through measurements of digital packing fraction in LBM lattices. We then considered the effects of grid sizing and resolution on stability of packed bed simulations. For densely packed beds, we found a resolution of 20 pixels/nodes per pebble diameter was sufficient for results that were: stable, capable of reproducing correct hydrodynamics, and computationally tractable.

CHAPTER 6

Applied Modeling of Solid Breeders

In the preceding chapters, descriptions of the microscale models established for this thesis were given. The new models were created to permit studying the internal packing structure of solid breeder pebble beds, specifically under fault conditions (*i.e.* crushed pebbles, altered packing structures), and the subsequent ability to maintain heat removal of deposited nuclear energy. In this chapter we finally apply all the models toward studying heat transfer in fusion-relevant pebble bed configurations. There will be three main topics considered: (i) changes to effective conductivity due to irradiation damage of ceramic solids, (ii) the effect of pebble bed orientation, initial packing fraction, and pebble fragmentation on temperature distributions in pebble beds, and (iii) helium tortuosity effects on heat transfer after pebble fragmentation.

6.1 Irradiation Effects on Effective Thermal Conductivity

Ceramic materials primarily conduct heat by phonon transport. Irradiation-induced vacancies act as phonon scattering centers and consequently thermal conductivity of ceramics is reduced under irradiation.[95] Fast neutron damage can produce large populations of defects and thereby reduce room-temperature thermal conductivity of ceramics by orders of magnitude with doses $\leq$ 1 dpa.[168] Analysis of breeding blanket modules for ITER indicate a maximum expected neutron damage in steel to be about 3 dpa over a span of 20 years of operation. By comparison, dpa levels required for DEMO are greater than 70 dpa.[76] Reduced thermal conductivity due to fast neutron damage is a concern for blanket designers and this study is meant to address pebble bed thermal reactions to irradiated pebbles.

Neutron fluence in ITER is targeted to reach $0.3\,\mathrm{MW\,yr\,m^{-2}}$.[1,182] In terms of 14 MeV neutrons, this equates to a fluence of $4.22 \times 10^{24}\,\mathrm{n\,m^{-2}}$. Kawamura *et al.* carried out irradiation experiments on Li_2TiO_3 pebble beds to detect changes in effective thermal diffusivity. They found a reduction in thermal diffusivity of 30% compared to unirradiated pebble beds at 400 °C but report that no change in effective thermal conductivity is detectable up to thermal neutron fluence of $1 \times 10^{24}\,\mathrm{n\,m^{-2}}$.

An experimental irradiation campaign has been carried out in Petten, Netherlands as part of the European program for development of HCPB blanket concept, a high fluence irradiation project, HICU (High neutron fluence Irradiation of pebble staCks for fUsion). The high fluence irradiation of lithium ceramics was meant to be up to DEMO-relevant values of 20 to 25 dpa, even with a neutron spectra not including 14.1 MeV.[89,186] Temperatures in ceramic regions dropped during the experimental campaign, trailing somewhat the tritium production rate and lithium burn-up. On-line temperatures were measured during the year-long experiment, temperatures in ceramic pebble regions were measured between 600 K to 800 K. Similar to Kawamura *et al.*, a significant increase in temperatures as a result of decreased thermal conductivity was not witnessed. However, careful thermal characterizations of ceramic pebble beds under irradiation were not evaluated.

The experiment of Kawamura *et al.* reached neutron fluence of the same order of magnitude of a years operation in ITER though only with thermal neutrons. HICU matched much of the neutron energy spectrum, save for the highly energetic fusion neutrons. Both experiments did not detect significant reductions in thermal conductivity. The results are providential for ceramic breeder regions far from first walls. Nevertheless, damage from fast neutrons in near-wall regions remains a concern.

In this study, we investigate the effects on effective conductivity as impacted by two orders of magnitude reduction in solid conductivity. To simulate neutron damage of Li_2TiO_3 in solid breeder pebble beds, we will parametrically reduce the solid conductivity as $\eta = k_{\mathrm{irr}}/k_{\mathrm{unirr}}$, where k_{irr} is a proxy value for the solid conductivity of material that has been damaged by neutron irradiation and $k_{\mathrm{unirr}} = 2.4\,\mathrm{W\,m^{-1}\,K^{-1}}$. In this study η is varied from $\eta = 1$ down to $\eta = 0.01$ to cover a broad range of reduction. The nuclear heat generation rate

is $8\,\mathrm{MW\,m^{-3}}$. We calculate an effective thermal conductivity of pebble beds with damaged ceramics. The pebble bed geometries are duplicates of those used for validation in § 3.1.4. The initial packing fraction of the pebble bed is $\phi_i = 0.61$. At thermal steady-state, temperature scatters of pebbles and binned average values are plotted for the neutron-damaged pebble beds in Figure 6.1. A k_{eff} is calculated for each bed and plotted alongside its fit in Figure 6.2; the effective thermal conductivity for irradiated beds is normalized against the case of non-irradiated bed, $k_{\mathrm{eff}} = 0.398\,\mathrm{W\,m^{-1}\,K^{-1}}$. As a consequence of irradiation damage to conductivity, maximum temperatures in the pebble beds increased dramatically; average maximum values are plotted in Figure 6.3.

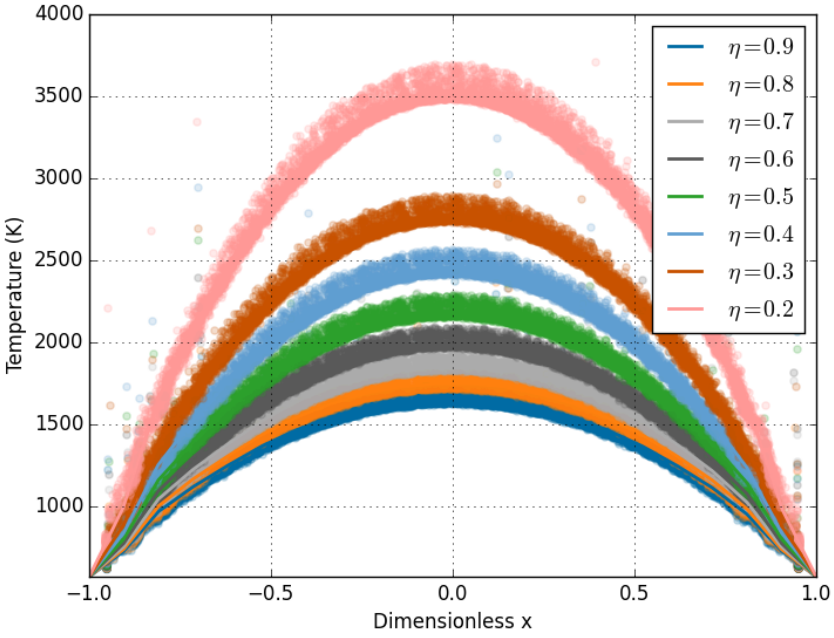

Figure 6.1: Temperature scatters and average profiles for DEM models of ceramic pebbles with irradiation-damage-induced reductions in thermal conductivity.

The effective thermal conductivity is fit to the following fifth-order polynomial, with $R^2 = 0.9999$,

$$k_{\mathrm{eff}}[\mathrm{W\,m^{-1}\,K^{-1}}] = 1.39\eta^5 - 4.649\eta^4 + 6.061\eta^3 - 3.964\eta^2 + 2.124\eta + 0.03875 \qquad (6.1)$$

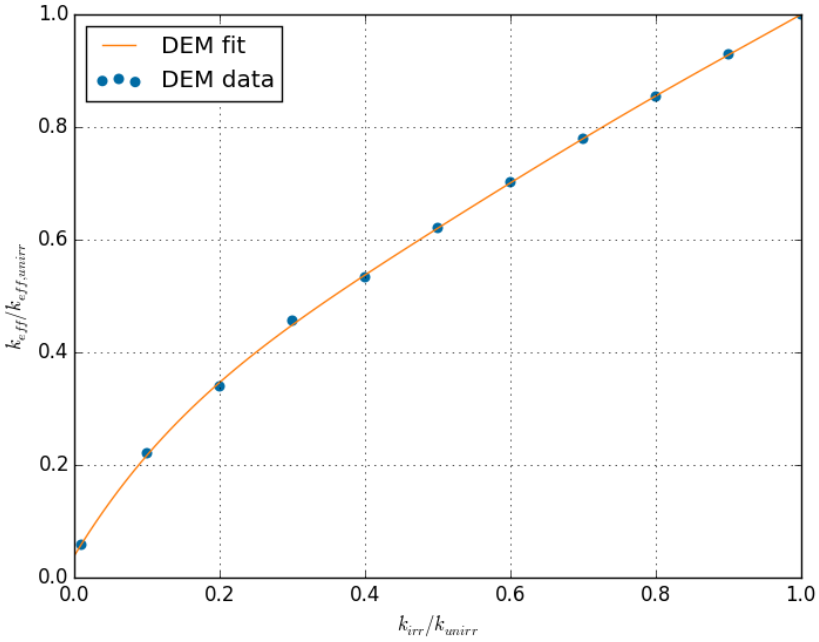

Figure 6.2: In DEM-based simulations, k_{eff} of pebble beds rapidly decreases as the solid conductivity drops by more than a single order of magnitude.

Data for mid-line temperatures was fit to the following power law, with $R^2 = 0.9993$,

$$T_{\text{mid}}[\text{K}] = 1536.2\eta^{-0.526} \tag{6.2}$$

In the DEM model, heat transport between constituents in pebble beds proceeds only through points of contact as if in vacuum. In the idealized situation considered here, as solid conductivity reduces due to neutron damage, $k_{\text{irr}} \to 0\,\text{W}\,\text{m}^{-1}\,\text{K}^{-1}$, the effective thermal conductivity must similarly converge to $k_{\text{eff}} \to 0\,\text{W}\,\text{m}^{-1}\,\text{K}^{-1}$. The pebble temperatures of these beds will thereby increase to $T_p \to \infty$ because of the lack of the material to transport heat. This behavior is seen in Figure 6.2 and Figure 6.1.

Bearing in mind that heat transfer in vacuum is not directly relevant to blanket operation but the results do facilitate observation of contact conductance's role in pebble bed heat transfer. For instance, when $\eta > 0.4$, reduction in irradiated k_{eff} is approximately linear with a slope of 0.77. In other words, the effective thermal conductivity of beds of irradiated pebbles drops only 77% of the reduction in solid conductivity of the irradiated pebbles

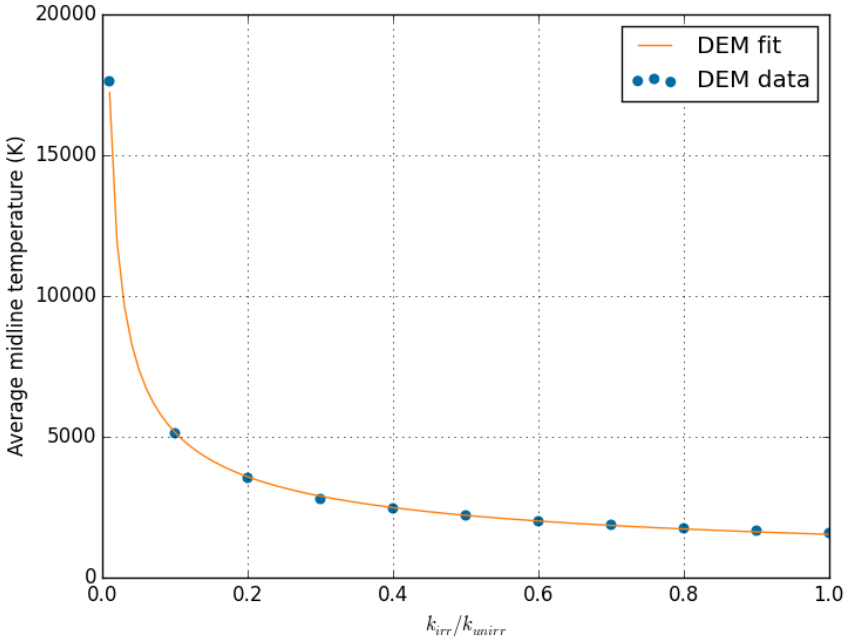

Figure 6.3: In DEM-based simulations, mid-line temperatures increase sharply as $\eta < 0.1$.

themselves. Returning for a moment to Equation (3.16), heat conductance between two pebbles is directly related to solid conductivity and radius of the contact area between them, a. However, there is not a one-to-one reduction in H_c due to reductions in k_s. Nor is there an inflection point where the magnitude of k_s decreases to be on the same order of magnitude, or less, than the contact radius; at an irradiated conductivity as low as $\eta = 0.01$, $k_{s,irr}$ is still, generally, three orders of magnitude larger than the contact radius, a. The reduction in k_{eff} for irradiated pebble beds, is instead due to combined effects of solid conductivity, coordination number, and contact forces. A thorough look into the relationship between heat transfer and parameters describing packing structures was reported by Van Lew *et al.*.[184]

The results in vacuum are interesting and illustrative, but not directly pertinent for blanket designers. Thus we now consider a more fusion-appropriate case of reduction in effective thermal conductivity due to neutron damage in the presence of helium. In this case, the pebble beds are re-creations of those from § 4.3, with packing fractions of $\phi_i = 0.62$ and stagnant helium. Again, pebble temperature scatter plots and binned average values are plotted for the neutron-damaged pebble beds in Figure 6.5, k_{eff} is given in Figure 6.6;

the effective thermal conductivity for irradiated beds is normalized against the case of non-irradiated bed, $k_{\text{eff}} = 1.02\,\text{W}\,\text{m}^{-1}\,\text{K}^{-1}$, average maximum values are plotted in Figure 6.9.

In the case of reduced solid conductivity, the Jeffreson correction to heat transfer coefficient becomes more pronounced. A sphere in a stagnant fluid has a Nusselt number of $\text{Nu} = 2$, equating to a heat transfer coefficient of $h = 680\,\text{W}\,\text{m}^{-2}\,\text{K}^{-1}$ for these pebbles in helium. The Biot number is a function of solid conductivity, $\text{Bi} = hd_p/k_s$, inversely related to solid conductivity. The Biot number for irradiated pebbles is given in Figure 6.4. Jeffreson correction accounts for large Biot numbers and reduces the heat transfer coefficient as $h_p = h/(1 + \text{Bi}/5)$. Reduced heat transfer coefficients are also given in Figure 6.4. The Biot number and heat transfer coefficients are normalized against the unirradiated condition. We see that, for example, when $\eta = 0.1$, meaning one order of magnitude reduction in solid conduction, the heat transfer coefficient reduces to 40% of the original value.

For the zero-velocity helium in this consideration, the fluid's volume-averaged energy equation at steady-state reduces to

$$\nabla\left(\epsilon_k \nabla T_f\right) = \frac{1}{V_k \rho_f C_f} \sum_{\forall i \in k} h_i A_i \Delta T_{if} \tag{6.3}$$

If an uncorrected heat transfer coefficient was introduced into this energy equation, the term on the right-hand-side would introduce large errors into the fluid temperature profile. Without the Jeffreson correction, the lumped capacitance assumption in the DEM framework would greatly over-estimate the amount of energy capable of being transported from pebble internals to fluid at the surface.

In the presence of stagnant helium, the effective thermal conductivity is fit to the following linear equation with $R^2 = 0.9998$,

$$k_{\text{eff}}[\text{W}\,\text{m}^{-1}\,\text{K}^{-1}] = 0.545\eta + 0.458 \tag{6.4}$$

Interestingly, as $k_{\text{irr}} \to 0\,\text{W}\,\text{m}^{-1}\,\text{K}^{-1}$, interstitial helium causes $k_{\text{eff}} \to 0.46\,\text{W}\,\text{m}^{-1}\,\text{K}^{-1}$. Interstitial helium plays a significant role in the ability of the overall pebble bed to transport heat, even when its conductivity (as used in this modeling effort) is only $k_f = 0.34\,\text{W}\,\text{m}^{-1}\,\text{K}^{-1}$. Normalized reductions in effective conductivity for irradiated pebbles in DEM and CFD-DEM environments are compared directly in Figure 6.7. Figure 6.7 shows the contribution

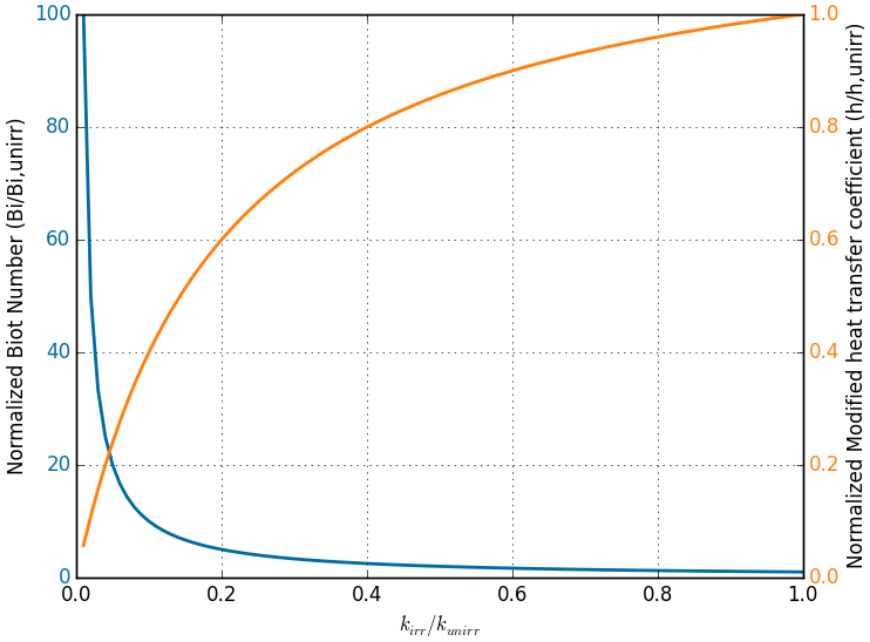

Figure 6.4: Biot number as a function of normalized solid conductivity (left), modified heat transfer coefficient *via* Jeffreson correction (right).

of helium at maintaining effective thermal conductivity of pebble beds after the solid material is damaged due to neutron-induced vacancies. Large reductions in solid conductivity, *i.e.* more than one order of magnitude, almost completely destroys the ability of pebbles to transport heat out of the assembly. Interstitial helium provides a limit to how far effective conductivity can drop in beds. We see a linear decrease in effective conductivity at a rate that is half as fast as the linear reduction in solid conductivity; evident from the slope of 0.55.

Plotted in Figure 6.8 are the results from our CFD-DEM model plotted alongside much other experimental data from Ref.[178] as well as the heat transfer correlations for stagnant interstitial gas (discussed in § 2.2.1). As a reminder, $\kappa = \frac{k_s}{k_f}$. From Figure 6.8, we see at larger values of solid conductivity, the CFD-DEM results compare well with many correlations from literature. However, for the two smallest values of κ (of $k_{irr} = 0.1, 0.01$), the results from CFD-DEM are above theoretical predictions and experimental data by almost double. At $\kappa = 1$, fluid and solid conductivities are equal and as such, the effective thermal conductivity

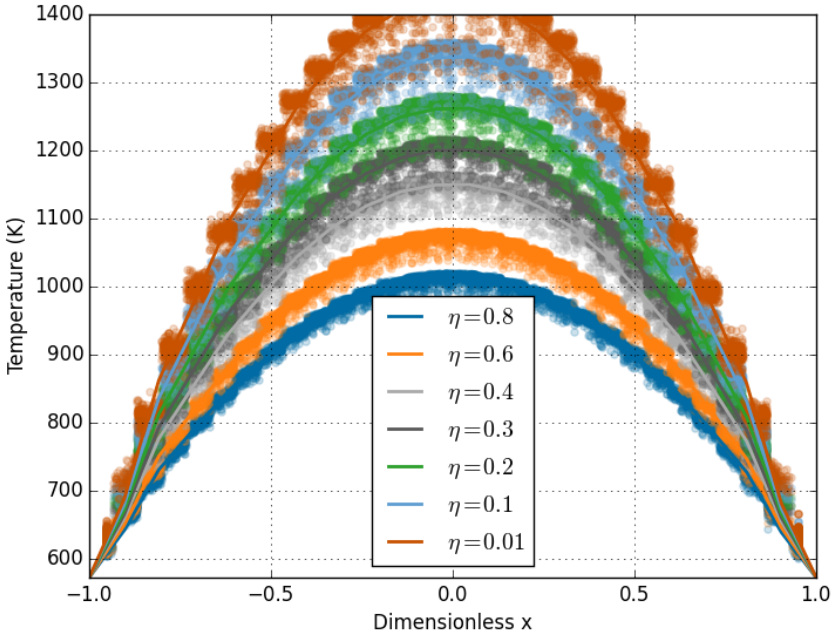

Figure 6.5: Temperature scatters and average profiles for CFD-DEM models of ceramic pebbles with irradiation-damage-induced reductions in thermal conductivity.

should similarly be unity. The fact that the CFD-DEM results yield data twice as high as theory suggests more investigation is required.

In mapping Lagrangian data from DEM into Eulerian CFD fields (for *e.g.* calculating porosity and inter-phase exchange coefficients), the divided technique is employed (see Figure 4.3). Mapping fluid temperatures back onto DEM, however, employed the simpler particle-centroid technique. A validation effort was performed to define proper fluid mesh sizes in the unirradiated pebble bed condition.

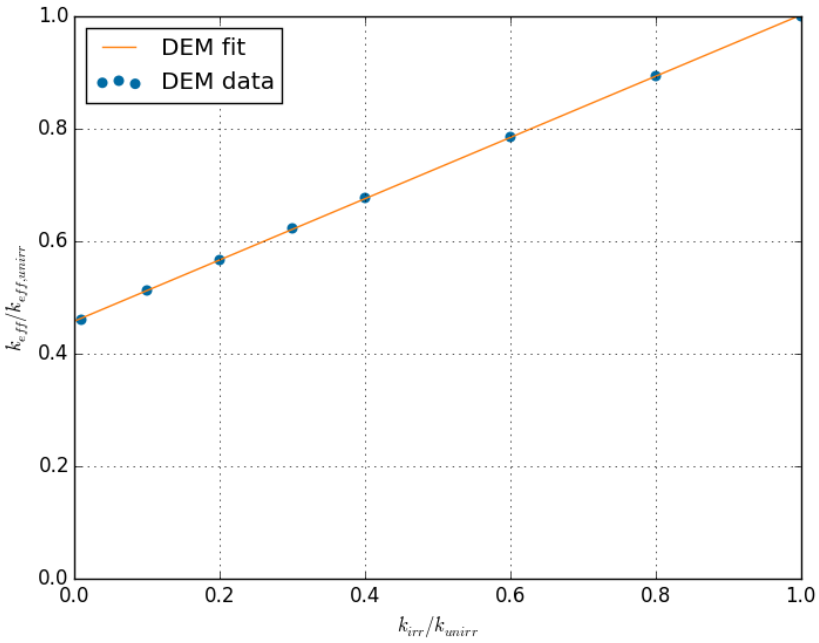

Figure 6.6: In CFD-DEM-based simulations, k_{eff} of pebble beds decreases linearly with reduced solid conductivity to a limit of $k_{\text{eff}} \to 0.46\,\text{W}\,\text{m}^{-1}\,\text{K}^{-1}$ when solid conductivity is reduced.

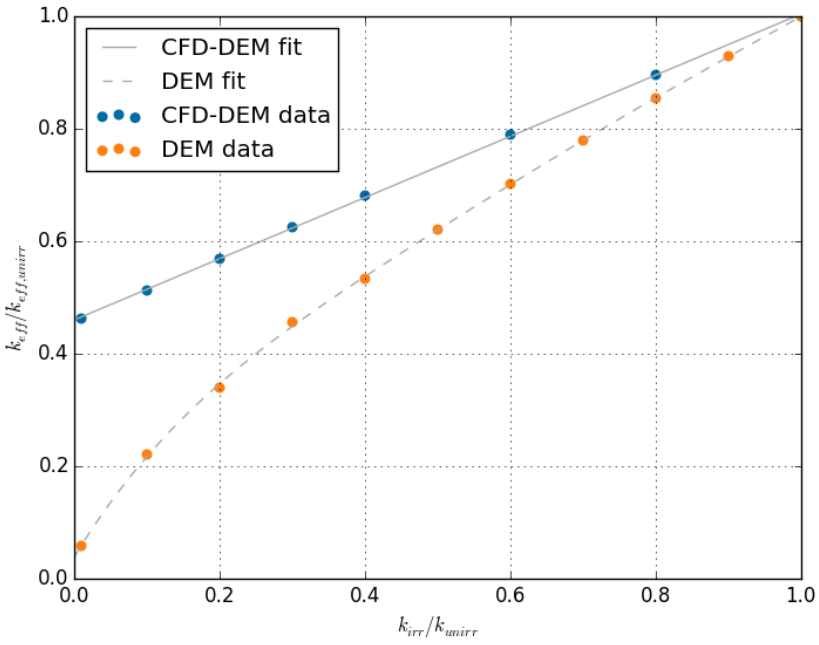

Figure 6.7: Helium's contribution maintains a minimum of k_{eff} even as contact-conductance heat transfer reduces to 0, as demonstrated by k_{eff} of DEM-based results.

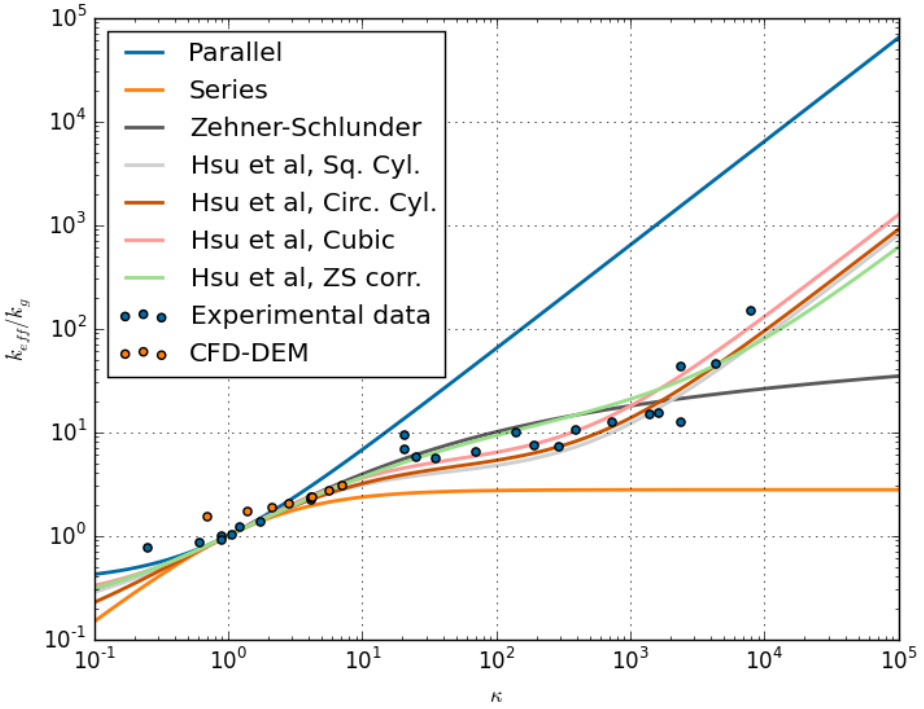

Figure 6.8: Values of k_{eff} measured for irradiated pebbles with CFD-DEM for all but the smallest solid conductivity values compare well with correlations and other experimental data.

Again mid-line temperatures for the considered pebble beds are given in Figure 6.9.

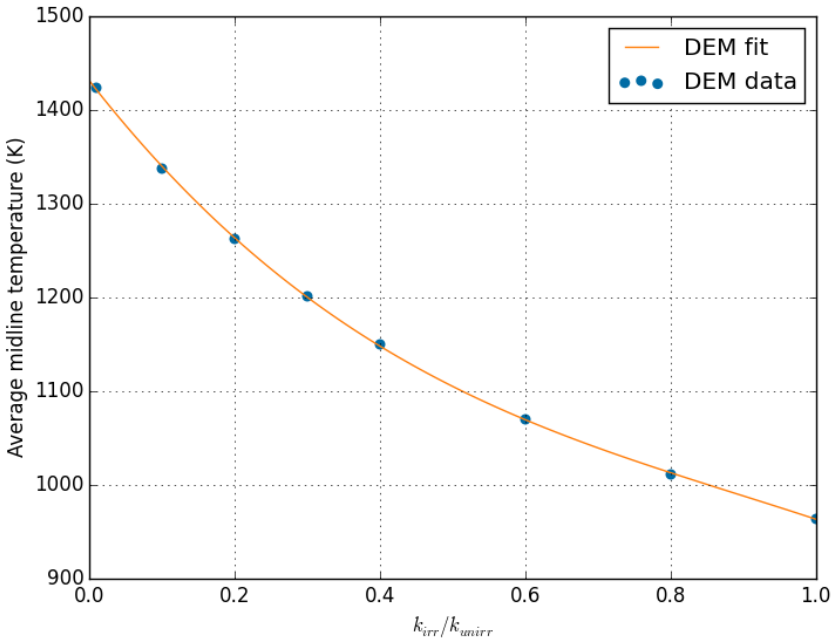

Figure 6.9: In CFD-DEM-based simulations, mid-line temperatures increase as solid conductivity drops; the increase is governed by helium heat transfer continuing in spite of large reductions in solid conductivity.

Data for mid-line temperatures was fit to the following third-order polynomial with $R^2 = 0.9999$ equation,

$$T_{\text{mid}}[\text{K}] = -314.1\eta^3 + 840.1\eta^2 - 994\eta + 1431 \tag{6.5}$$

In the pebble bed with non-irradiated pebbles, the average maximum temperature in the mid-line was 964 K. Wall temperatures are always held at 573 K. As an example, when neutron damage causes solid conductivity to drop by an order of magnitude, the pebble bed centerline temperature increases to 1337 K, an increase of nearly 40%. The temperature curves given here are, however, for a generic volume under the average maximum heat generation rate expected for Korean designs of HCPBs, namely 8 MW m^{-3} and no consideration was given for design margins of temperatures in beds. As such, the magnitude of temperature given here may not match design targets of a real blanket. It is thus illustrative to consider a

non-dimensional temperature and view its increase. To that end, a second set of pebble beds was run with a nuclear heat rate of $5.12\,\mathrm{MW\,m^{-3}}$. Maximum bed temperatures are reported in non-dimensional terms; bed temperatures are normalized against the unirradiated result,

$$\Theta = \frac{T_{\mathrm{mid}}(\eta) - T_{\mathrm{wall}}}{T_{\mathrm{mid,unirr}} - T_{\mathrm{wall}}} \tag{6.6}$$

With this transformation from temperature magnitude, the results of any nuclear heat generation rate or bed geometry will collapse into a single curve, shown in Figure 6.10. The curve is fit with the following relationship

$$\Theta = -0.803\eta^3 + 2.148\eta^2 - 2.541\eta + 2.194 \tag{6.7}$$

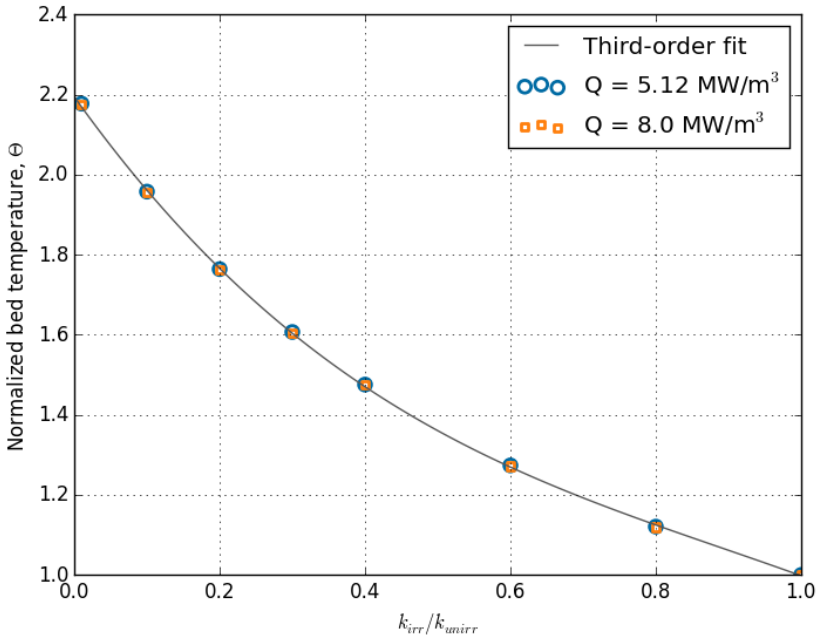

Figure 6.10: Non-dimensional temperatures of different pebble beds collapse into a single curve, allowing direct comparison of pebble bed temperature increases for irradiated beds with different operating parameters (of nuclear heat rate and geometry).

As an example of the applicability of these results, suppose we wish to find the amount of irradiated damage is allowable in a ceramic breeder region. In this scenario, a blanket

designer chooses to allow a maximum operating temperature with 10% margin away from 950 °C. The planned bed mid-line temperature would therefore be 855 °C. To find the amount of damage allowable within the 10% margin, we then know $\Theta = \frac{950-573}{855-573} = 1.34$. Thus, solving for η in Equation (6.7) yields $\eta = 0.52$; a solid conductivity of $k_{s,irr} = 1.25\,\mathrm{W\,m^{-1}\,K^{-1}}$. The last step would require knowledge of a relationship between solid conductivity and dpa. With such information, allowable dpa could be ascertained and the 10% design margin on temperature evaluated.

Neutrons from fusion plasma are highly energetic and it is important to consider how these neutrons will affect heat transport internal to lithium ceramics during their operation in a fusion reactor. In this study, we varied solid thermal conductivity parametrically as a proxy to represent material damaged by neutron irradiation. When stagnant helium gas is included in the calculation, the results fit well within limits of correlations and theoretical limits above $\kappa \approx 1$. We also arrived at correlations relating effective thermal conductivity and maximum bed temperatures as a function of irradiated solid conductivity. At present we have no data indicating the precise quantity of expected dpa in lithium ceramics, nor a correlation between dpa and reduced conductivity. There is, however, irradiation data from a high-dose fission experiment, HICU, in which it appears conductivity values did not decrease dramatically at the temperatures and dpa experienced. Next steps should be to study precisely the relationship between dpa and conductivity in the lithiated ceramic materials considered for use in ITER and future DEMO reactors.

6.2 Temperature Distributions with Breeder Orientation, Pebble Fragmentation

We apply coupled computational fluid dynamics and discrete element method (CFD-DEM) modeling tools with new numerical implementations of pebble fragmentation to study the combined effects of granular crushing and ensemble restructuring, granular fragment size, and initial packing for different breeder volume configurations. In typical solid breeder modules, heat removal from beds relies on maintaining pebble-pebble and pebble-wall contact

integrity. However, contact is disrupted when an ensemble responds to individually-crushed pebbles. Furthermore, restructuring of metastable packings after crushing events are, in part, dependent on gravity forces acting upon the pebbles. We investigate two representative pebble bed configurations under constant volumetric heat sources; modeling heat removed from beds *via* inter-particle conduction, purge gas convection, and contact between pebble beds and containers. In one configuration, heat is removed from at walls oriented parallel to the gravity vector (no gap formation possible); in the second, heat is removed at walls perpendicular to gravity, allowing for the possibility of gap formation between bed and wall. Judging beds on increase in maximum temperatures as a function of crushed pebble amount, we find that both pebble bed configurations to have advantageous features that manifest at different stages of pebble crushing. However, all configurations benefit from achieving high initial packing fractions.

6.2.0.1 Simulation domain, boundary conditions, and material properties

Two ITER-relevant volumes are considered in this study, sketched in Figures 6.11a and 6.11b. They are differentiated from each other by gravity's direction in the configuration. Because of their similarity, we use generic coordinate systems (χ, ζ). Thus χ-configurations, shown in Figure 6.11a, have $\chi = y$ and $\zeta = x$ while ζ-configurations, Figure 6.11b, have $\chi = x$ and $\zeta = y$. The ζ-configuration in this study is meant to represent the orientation of European Union's TBM,[90] while the χ configuration is an orientation adopted by many other current TBM designs in ITER.[35,60]

In terms of the generic coordinates, outflow of bed heat to coolant is along ζ. Constant temperature boundaries, T_w, exist at the edges of that dimension. As sketched in Figure 6.11, gravity resettling in the χ configuration will not allow gap formation between bed and wall. However, in the ζ-config it is possible for a gap to form between top coolant walls and pebbles after gravity resettling. A constant nuclear heat rate was applied to every particle in the bed which is representative of the highest source term anticipated in current ITER designs of solid breeder blankets, $q''' = 8 \times 10^6\,\mathrm{W\,m^{-3}}$.

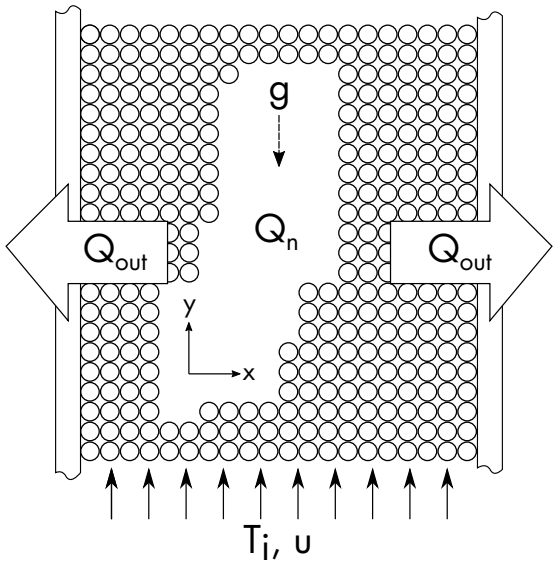

(a) χ-configuration: heat removed in the x-direction.

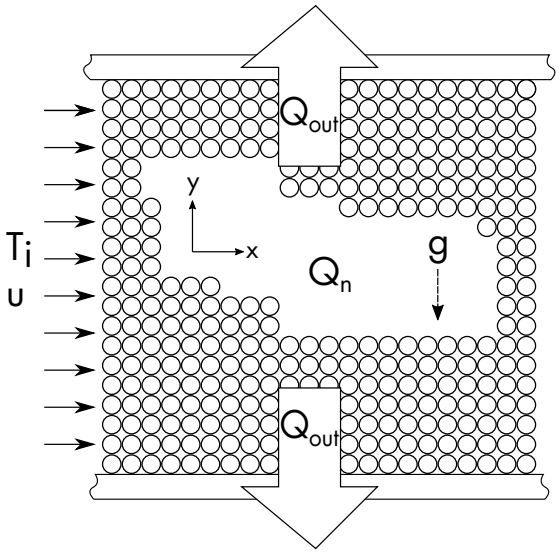

(b) ζ-configuration: heat removed in the y-direction

Figure 6.11: Sketches of the two breeder orientations show that gravity settling will not allow gaps between pebbles and walls in the χ-configuration. However for the ζ-configuration, gravity-induced resettling can create a gap between pebbles and upper wall.

The simulation consists of pebbles of diameter $d_p = 1\,\text{mm}$, in beds filled to two initial packing fractions, $\phi_{1,2} = 62, 64\%$. Mechanical properties of the pebbles are given in Table 6.1. To note is the elastic modulus chosen for pebbles in this study. In a past experimental study, Van Lew *et al.* found that individual pebbles behaved in a manner indicative of having a elastic modulus from 20 to 60% of values reported in literature for sintered blocks of Li_2TiO_3 and Li_4SiO_4.[185] Therefore to maintain some generality to this study, we have chosen a elastic modulus at a nominal value of $E = 60\,\text{GPa}$ to generically represent either ceramic pebble.

Pebble bed widths in ζ are 20 mm, a size comparable to breeding volumes of many ITER TBM designs.[35,60,90] Bed depths (in the z-direction, in/out of the page in Figures 6.11a and 6.11b) are 5 mm, with periodic boundary conditions. Bed lengths in χ vary to accommodate 6000 pebbles, initially, with given initial packing fractions; the length is approximately 50 mm. Virtual walls are placed at extents of χ and ζ dimensions. Walls in ζ had

constant temperature boundaries of $T_{w,s}$, all walls have mechanical and thermal properties of structural steel, given in Table 6.2.

Fluid domains, overlaid on DEM pebbles, have fluid inlet and outlet regions of lengths 10 mm and approximately 51 mm, respectively. The side walls of the fluid domain were adiabatic in inlet and outlet regions and had constant temperature boundaries where they contacted the pebble bed, $T_{w,f}$. Fluid entered with a constant velocity magnitude of $5\,\mathrm{cm\,s^{-1}}$ and constant temperature T_i. At present, temperature-dependencies of helium properties have not been incorporated into the model. Over the range of 400 °C to 900 °C, increases in helium momentum and thermal diffusivities are both essentially linear and thus an arithmetic mean for properties over that range is used as a first approximation. Future models will incorporate temperature-dependence of fluid properties. Fluid transport properties are given in Table 6.3.

Table 6.1: Mechanical and thermal properties of ceramic pebbles in the DEM domain. Aside from E_s, properties come from[78] with $\epsilon = 0.2$

Property	Symbol	Value
elastic modulus (GPa)	E_s	60.0
Poisson ratio	ν_s	0.24
thermal conductivity ($\mathrm{W\,m^{-1}\,K^{-1}}$)	k_s	1.79
diameter (m)	d_p	0.001
pebble-pebble friction coefficient	μ_s	0.2
pebble-wall friction coefficient	μ_w	0.2
heat capacity ($\mathrm{J\,kg^{-1}\,K^{-1}}$)	c_s	1.45×10^3
thermal expansion coefficient ($\mathrm{K^{-1}}$)	β_s	1.77×10^{-5}
density ($\mathrm{kg\,m^{-3}}$)	ρ_s	3.44×10^3

6.2.0.2 Modeling crush events

Models have been proposed in the past which translate experimental measurements of granular crushing into contact forces in an ensemble to predict granular crushing, *e.g.* Refs.,[10,74,160,185,211] but no validation has set any model apart as yet. Here, packed beds experience artificial pebble-crushing events for which a chosen percentage, η, of initial pebbles

Table 6.2: Mechanical and thermal properties and boundary conditions of structural container in the DEM domain.[66]

Property	Symbol	Value
elastic modulus (GPa)	E_w	175.0
Poisson ratio	ν_w	0.30
thermal conductivity ($\mathrm{W\,m^{-1}\,K^{-1}}$)	k_w	29.0
wall temperature (K)	$T_{w,s}$	573

Table 6.3: Transport properties of helium and boundary conditions in the CFD domain; mean values over the temperature range 400 °C to 900 °C.

Property	Symbol	Value
thermal conductivity ($\mathrm{W\,m^{-1}\,K^{-1}}$)	k_f	3.40×10^{-1}
heat capacity ($\mathrm{J\,kg^{-1}\,K^{-1}}$)	c_f	5.19×10^{3}
density ($\mathrm{kg\,m^{-3}}$)	ρ_f	5.38×10^{-2}
kinematic viscosity ($\mathrm{m\,s^{-2}}$)	λ_f	8.52×10^{-4}
thermal diffusivity ($\mathrm{m\,s^{-2}}$)	α_f	1.28×10^{-3}
wall temperature (K)	$T_{w,f}$	573
inlet temperature (K)	T_i	573

(at randomized locations) fragment. Four pebble crush percentages are used: $\eta = 0, 1, 3, 5\%$. Numerical models of crush events themselves have received attention. Annabattula, Zhao, and Gan attempted to model a crushing event as either a reduction in radius of the crushed pebble or a reduction in elastic modulus.[11,12,212] Van Lew *et al* made similar simplifications when they considered a crushed pebble as being removed from the force network, thus being removed from the DEM domain.[184]

In this work, we replace a parent pebble of radius r with N_c smaller daughter fragments, each of equal radius, r_c. After a crushing event, fragments are free to resettle through interstitial gaps in the pebble bed and original pebbles respond in kind with re-arrangement into a new metastable packing structure. To conserve volume between pre- and post-crush, we can relate the number of daughter fragments to the radius ratio between fragments and parent, $r^* = r_c/r$, as $N_c = (1/r^*)^3$. Conservation of energy of crush events is enforced by

setting the temperature of daughter fragments equal to the parent pebble at the moment of crushing.

Numeric techniques to handle overlap after crush events, as a consequence of volume conservation, were shown in § 3.3. To summarize the approach, in our fragmentation procedure, overlap and the associated high contact forces between the daughter fragments is permitted. Directly following a fragmentation event, a cut-off distance is applied to the velocity-Verlet integration of daughter fragments which prevents instabilities in position; *e.g.* in any given timestep fragments are only allowed to travel x_{cutoff}, regardless of the distance calculated in integration. A short time is permitted for the daughter fragments to relax away from the highly-overlapped state; relaxation time was a function of number of pebble fragments and pebble fragment size. Contact forces in the system were monitored and when average values returned to pre-fragmentation levels, the relaxation procedure concluded, cut-off distance was removed, and standard velocity-Verlet integration of daughter pebbles was reinstated.

Experimental studies of crushing brittle pebbles show many different modes of fragmentation, often with highly irregular sizes (see *e.g.* Ref.[196]). As a first effort, we compare the effect of fragmentation size by studying two different values, $r_1^* = 0.32$ and $r_2^* = 0.2$ which results in $N_{c,1} = 23$ and $N_{c,2} = 125$ daughters per crushed parent (at $\eta = 5\%$, for r_2^* the system expands to 43 200 pebbles).

6.2.1 Results & Discussion

In Figure 6.12, a bed of 64% initial packing with 5% of pebbles broken into fragments of size $r_2^* = 0.2$ is shown; vectors of flow field, colored by fluid temperature, are seen moving through the bed. The inset image qualitatively demonstrates how the fluid field aids in equilibrating temperatures of fragments with neighboring larger pebbles in spite of light physical contact between pebbles.

Several cross-sections are created at mid-planes in z. Representative results are taken from 64% packings of ζ- and χ-configurations and compared against their respective $\eta = 5\%$, r_2^* conditions, shown in Figures 6.13 and 6.14. The numbered zones of the beds will be

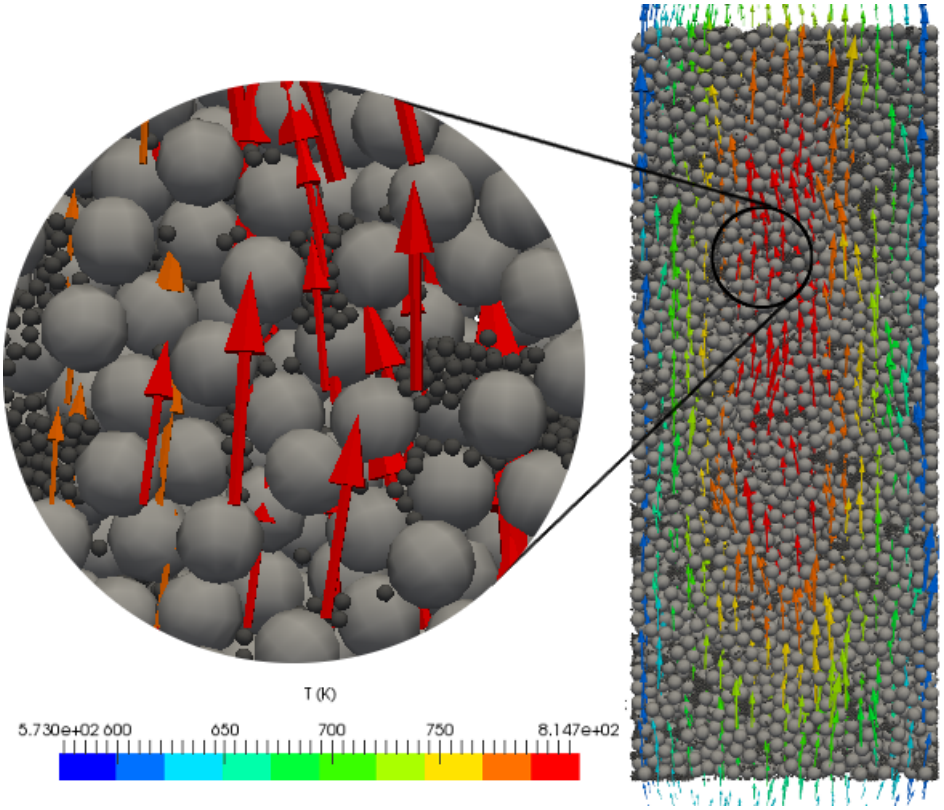

Figure 6.12: Showing the case for $\phi_2 = 0.64$, $\eta = 5\%$ with fluid velocity vectors colored by temperature. Inset image reveals size discrepancies between fragments and pebbles and the ensemble interaction with fluid flow.

discussed shortly.

Wall offset temperatures $(T - T_w)$ in beds are found in slices of width $\Delta\zeta$ along ζ. Pebble-weighted mean values are found as $\langle T \rangle = \frac{1}{V_n} \sum_j^n (T_j - T_w) V_j$, for n pebbles of temperature T_j consuming a total volume V_n in the slice. Demonstrative cases of $\phi_2 = 0.64$ with $r_2^* = 0.2$ are given in Figure 6.15 as functions of granular crushing percentage.

We report the overall hydrostatic pressure of pebble beds, $p = \sigma_{ii}/3$, at steady-state heating. Bed stress tensors can be calculated as,[8,72,127]

$$\boldsymbol{\sigma} = \frac{1}{V} \left(\sum^{N} \delta_{ij} f_{n,ij} \mathbf{n} \otimes \mathbf{n} + \sum^{N} \delta_{ij} f_{t,ij} \mathbf{n} \otimes \mathbf{t} \right) \tag{6.8}$$

where $\mathbf{n}$ and $\mathbf{t}$ are unit vectors of the normal and tangential directions, respectively, and f_n and f_t are the magnitudes of force in the normal and tangential directions, respectively.

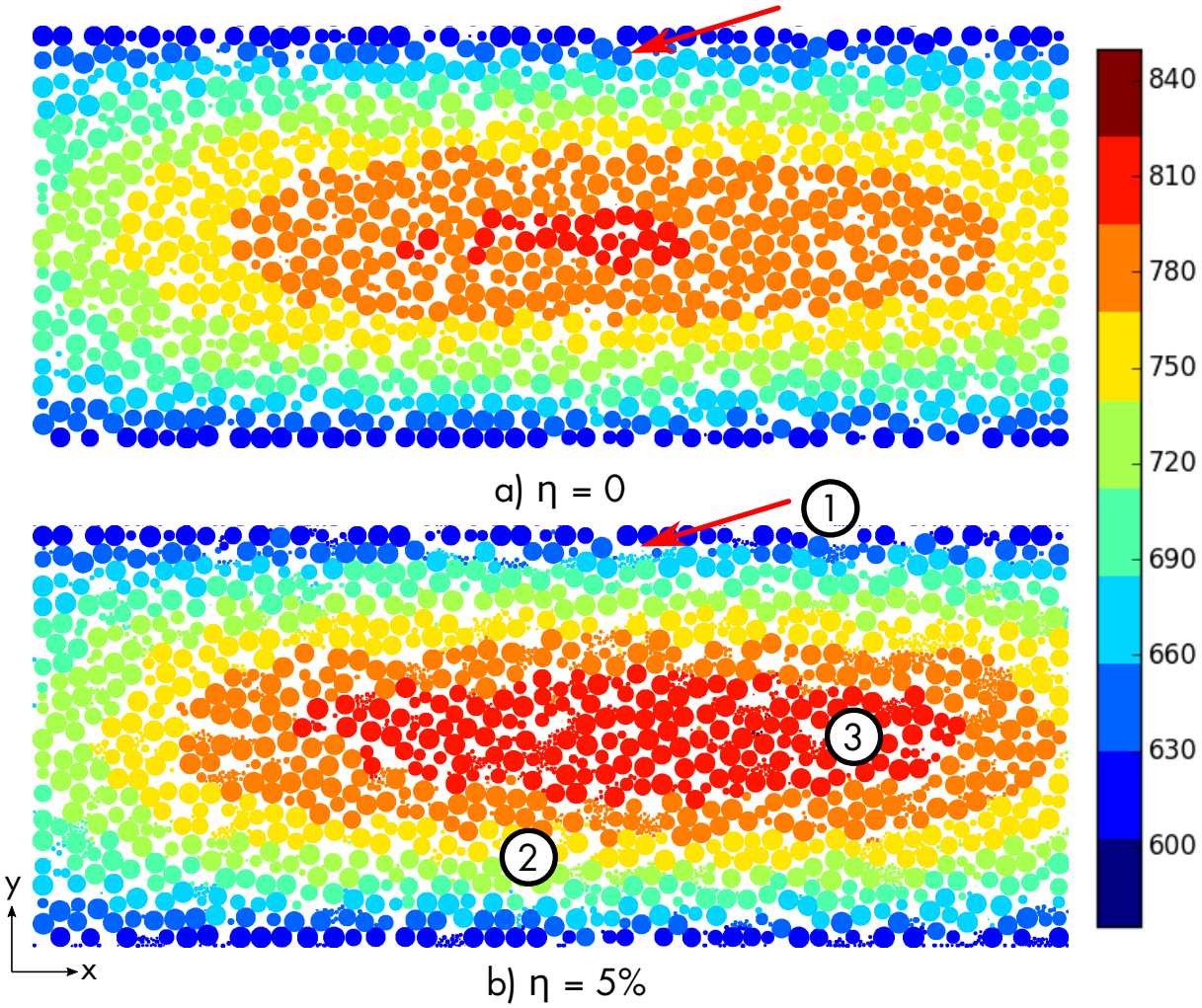

Figure 6.13: Cuts at the mid-plane of z for ζ-config beds. (a) bed initially packed to ϕ_2, and (b) bed with crushing of η_5 pebbles with particle size r_2^*.

Hydrostatic pressure values are normalized against initial ($\eta = 0$) beds for respective configurations. Hydrostatic pressure is given in Figure 6.16.

A total mean bed temperature is found from all pebbles in the system as $\langle T \rangle_{tot} = \frac{1}{V_N} \sum_j^N (T_j - T_w) V_j$ where N is the total number of ensemble pebbles. The total mean bed temperature is also normalized against initial packing cases of each respective set of beds. Results for all beds are given in Figure 6.17. Maximum temperature rises of every bed are also found, $T_m = \max(T) - T_w$, and normalized against the maximum temperature in the initial packing of each respective set of beds. To avoid aberrant results from a bed which might have a single, very high temperature pebble, the maximum temperature, $\max(T)$, is

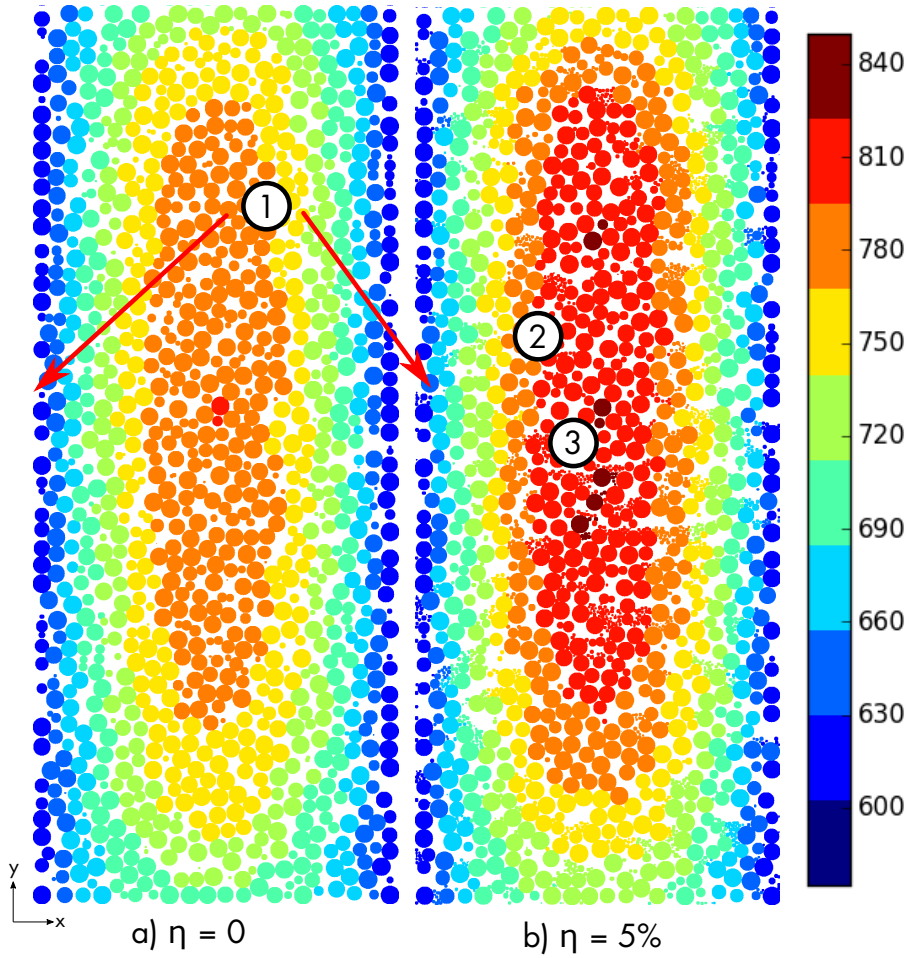

Figure 6.14: Cuts at the mid-plane of z for χ-config beds. (a) bed initially packed to ϕ_2, and (b) bed with crushing of η_5 pebbles with particle size r_2^*.

calculated as a mean value of the 50 highest temperature pebbles. The results are given in Figure 6.18. In addition to total mean bed temperature, maximum temperature rise is also an important factor in evaluation of a pebble bed.

Lastly, we consider how far pebble fragments travel in the bed after a crushing event. Total displacements from the moment of crush event to final resting, $|\Delta h|$, are normalized against the original pebble diameter, $|\Delta h|/d_p$. Histograms for 64% packing fractions of χ- and ζ-configurations at 5% pebble crushing with fragment sizes r_2^* are given in Figure 6.19. These two beds saw the most settling, all other beds tested saw considerably less fragment travel.

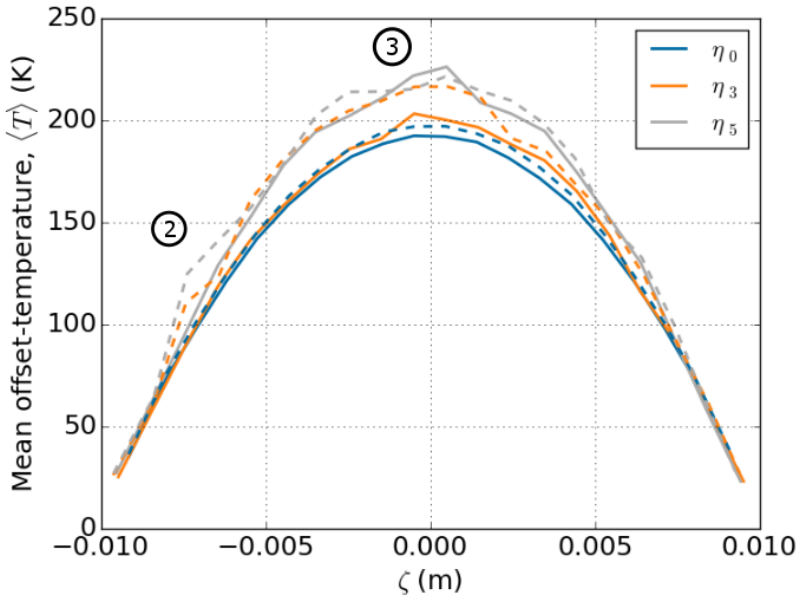

Figure 6.15: Mean offset temperature profiles, $\langle T \rangle$, along ζ in beds with initial packing fractions $\phi_2 = 0.64$, fragmentation sizes were r_2^*. Solid lines are χ configurations, dashed lines are ζ configurations. Fragmentation settling of ζ-configs are seen in 'lumps' near Zone (2) and in the χ-config spike in zone (3).

Analyzing results of all the pebble beds in this study revealed two main contributors to bed temperatures with resettling from pebble crushing: final settling location of fragment particles and overall contact force relaxation. The two interacting contributors were found to be expressed to different extents depending on crush amount and bed configuration.

Hydrostatic pressure (a global measure of inter-particle contact forces) is predominately a function of initial packing fraction alone, as seen in Figure 6.16. Smaller initial packing fractions had their internal hydrostatic pressures reduced more rapidly as pebbles crushed in the ensemble. Breeder orientation appears to have less impact on stress relief than size of crush fragments. Due to the inter-connected nature of the force network, and geometry of beds studied here, resettling in beds and contact force relaxation is uniform throughout the beds. Thus we expect reductions in contact forces to directly result in an overall increase of bed temperatures. This is reflected in the curves of Figure 6.17. Total mean temperatures of $\phi_1 = 0.62$ beds increased between 16 to 19% at $\eta = 5\%$. Yet beds initially packed to

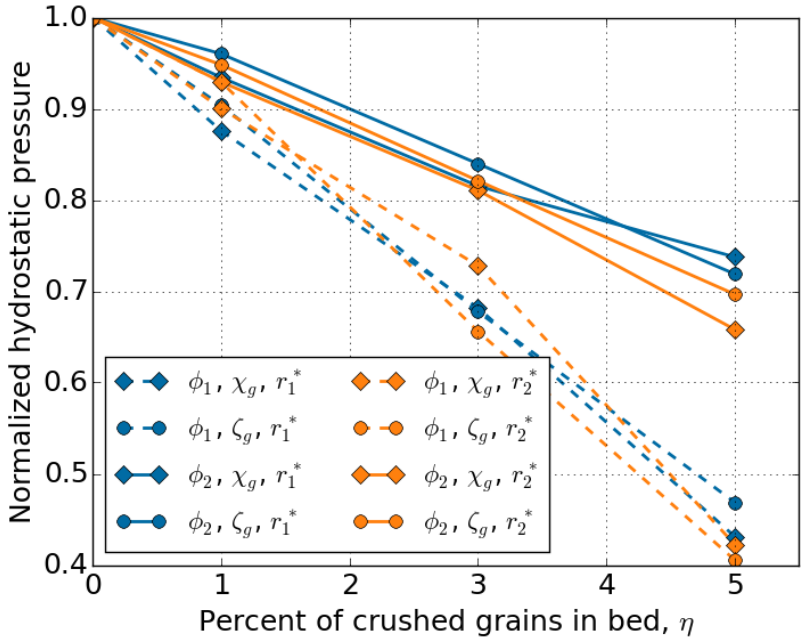

Figure 6.16: Dashed lines represent the lower packing fraction, $\phi_1 = 0.62$, solid lines are $\phi_2 = 0.64$. Markers are: $\circ$ for ζ-config, $\diamondsuit$ for χ-config. Color differentiates the fragment radius ratio. Contact force relaxation is more rapid for lower packing fractions.

$\phi_2 = 0.64$ increased by only 10 to 13% at the same value of crushed pebble amount.

Fragment settling location, on the contrary, is strongly dependent on fragment size and breeder orientation. Larger pebble fragments generally did not travel far, settling loosely in regions near the point of fragmentation. Smaller fragments were seen to be capable of traveling much further through interstitial gaps between pebbles before also coming to rest with loose settlings. The looseness of the fragment settling is indicated by their ensemble-average coordination number (counting only the fragments) for r_1* and r_2^*, respectively, as $\langle Z \rangle = 3.2$ and $\langle Z \rangle = 2.8$. Contacts with walls or floors are not counted in this coordination number. A consequence of loose packings of fragments is poor thermal conductance to neighboring pebbles. Fragment temperatures are therefore mostly regulated by convection with interstitial helium and their influence on bed temperatures is much more complex.

To identify the effects of fragment settling, we look to Figure 6.19 and the several zones demarcated in the results of Figures 6.13 and 6.14. The majority of fragments, even in this

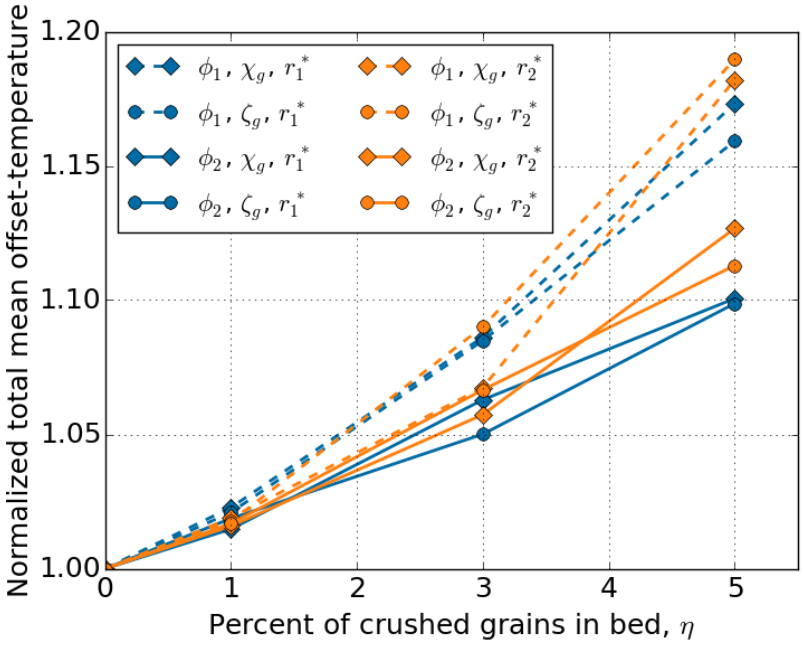

Figure 6.17: Dashed lines represent the lower packing fraction, $\phi_1 = 0.62$, solid lines are $\phi_2 = 0.64$. Markers are: $\circ$ for ζ-config, $\diamondsuit$ for χ-config. Color differentiates the fragment radius ratio. Lower packing fraction is the most dominant parameter for overall bed temperature. Amongst the same packing fraction, fragment size is most influential factor.

case of smallest fragment size and largest crushing amount, remain approximately at the location of the parent pebble; for both configurations, approximately 60% travel less than 1 pebble diameter (1 mm). However, in both configurations, approximately 8% of fragments travel more than 2 diameters, and those pebbles have a significant impact on the ensembles overall thermal response.

In ζ-configuration beds, pebbles traveling more than a few pebble diameters will move between colored isotherms drawn in Figure 6.13. For example we can see the fragment group identified in Zone (1) as moving downward, away from the top wall. Similarly, when pebbles in Zone (3) are crushed, some of the fragments tumble downward into Zone (2) before coming to rest where they continue to receive volumetric heating. Thus the fragments, with poor thermal conductance, increase heating in the regions where they settle. The effect is seen in the $\eta = 3, 5\%$ temperature profiles in Figure 6.15 that are asymmetric with lower temperatures in the top half (above Zone (3)) and higher temperatures in the region near

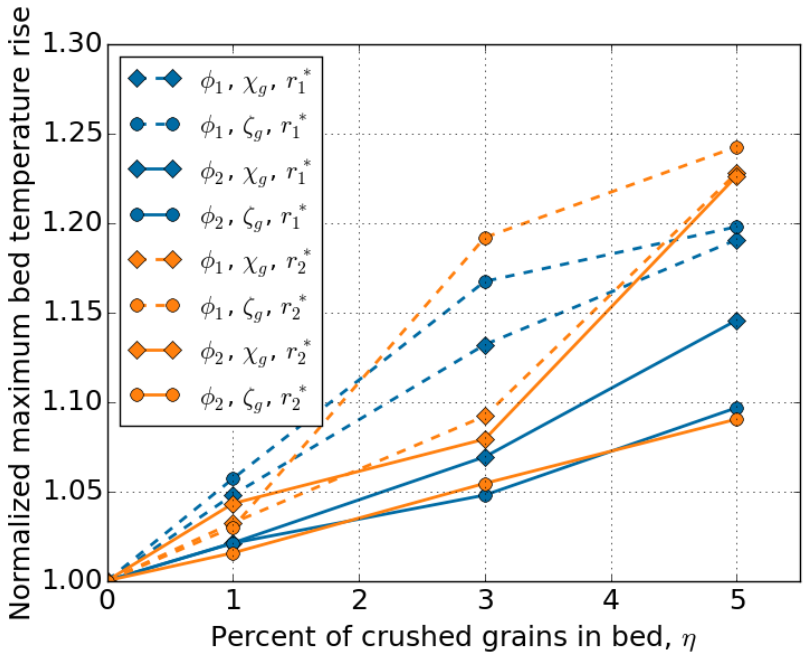

Figure 6.18: Dashed lines represent the lower packing fraction, $\phi_1 = 0.62$, solid lines are $\phi_2 = 0.64$. Markers are: $\circ$ for ζ-config, $\diamondsuit$ for χ-config. Color differentiates the fragment radius ratio. The dominant parameter influencing maximum bed temperature varies as a function of the number of crushed pebbles in the bed.

Zone (2).

In contrast, χ-config beds respond much differently to pebble fragment settling. We again see from cross-sections in Figure 6.14 a pebble identified in Zone (1) that breaks but remains in that zone after settling. The trend continues in other regions of the bed. When pebbles are crushed in the χ-config beds, gravity causes them to fall downward but remain generally in the same isotherm, as drawn in Figure 6.14. According to Figure 6.15, the effect of pebble crushing has little effect up to 3% of damaged pebbles. But suddenly at $\eta = 5\%$, the combination of reduced overall bed pressure and fragmentation heating causes the maximum bed temperature to jump above all other $\phi = 64\%$ beds (see Figure 6.15 and Figure 6.18). The temperature increase in this χ-config bed is due to the accumulation of pebble fragments that remain in Zone (3), only tumbling to lower heights. Helium that enters the χ-configuration bed reaches higher temperatures more quickly due to the increased

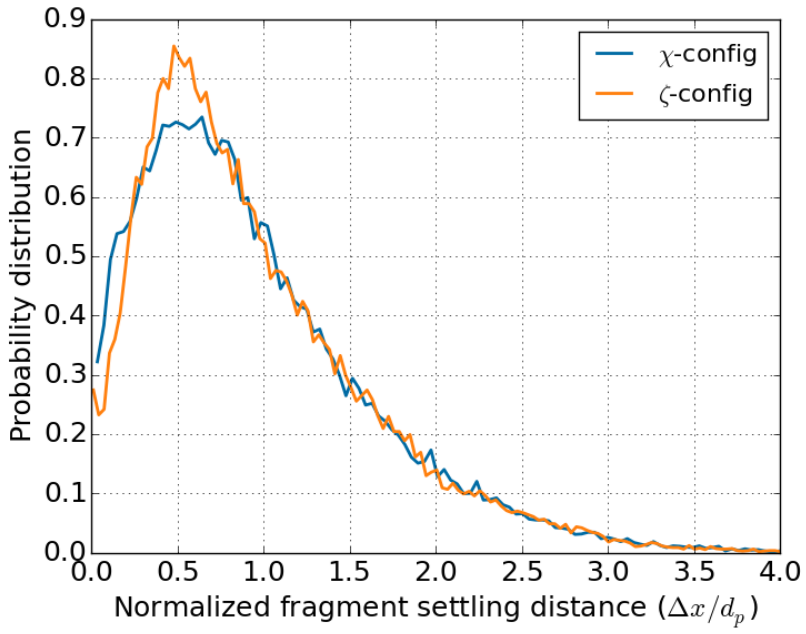

Figure 6.19: Normalized displacement histograms for fragment sizes of $r_2^* = 0.2$ with $\eta = 5\%$. χ-config: 59.7% of fragments travel up to 1 mm and 8.2% travel more than 2 mm; ζ-config: 60.7% of fragments travel up to 1 mm, 7.9% travel more than 2 mm.

heating from fragments which settled at lower heights of y. Helium then continues to heat from the many fragments in Zone (3) which ultimately results in the highest maximum bed temperatures (for the given packing fraction). This can also be seen with comparison between Figures 6.13 and 6.14: the χ-config bed reaches the 780 K contour at a much lower height than the ζ-configuration.

Travel of pebble fragments also manifests in changes to local packing fraction. In Figures 6.20 to 6.23, we see the changes local packing fraction distribution, for all pebble beds of χ-configuration, due to fragmentation and resettling. Similarly, in Figures 6.24 to 6.27, we see the local packing fraction distributions for all pebble beds of the ζ-configuration. These figures are alternative depictions of fragmentation travel, illustrating global changes to pebble beds after pebble crushing. The images are generated from binning particles in grids of x and z and considering all pebbles in the depth y.

Comparing Figure 6.20 with Figure 6.22, two sets of beds with the same configuration and fragment size but different initial packing fraction, we see pebble beds with lower initial

packing fractions have an amplified response to crushing than beds with higher packing fraction. Likewise, if we flip the orientation such as in Figure 6.24 and Figure 6.26, there is again a more widespread change in local packing fraction for beds of smaller initial packing fractions.

The effect of pebble fragment size to local packing fraction is also revealed in these images. For both configurations, and all initial packing fractions, the beds with smaller fragment size, r_2^*, would result in accumulation of mass (*i.e.* higher packing fraction) at the base of the pebble beds and a reduction of mass near the top wall. Among this subset of pebble beds with smaller fragments, we again clearly see that lower initial packing fractions; beds of either configuration with $\phi = 0.62$ have larger regions of $\Delta\phi = 0.07$ than any of the $\phi = 0.64$ beds.

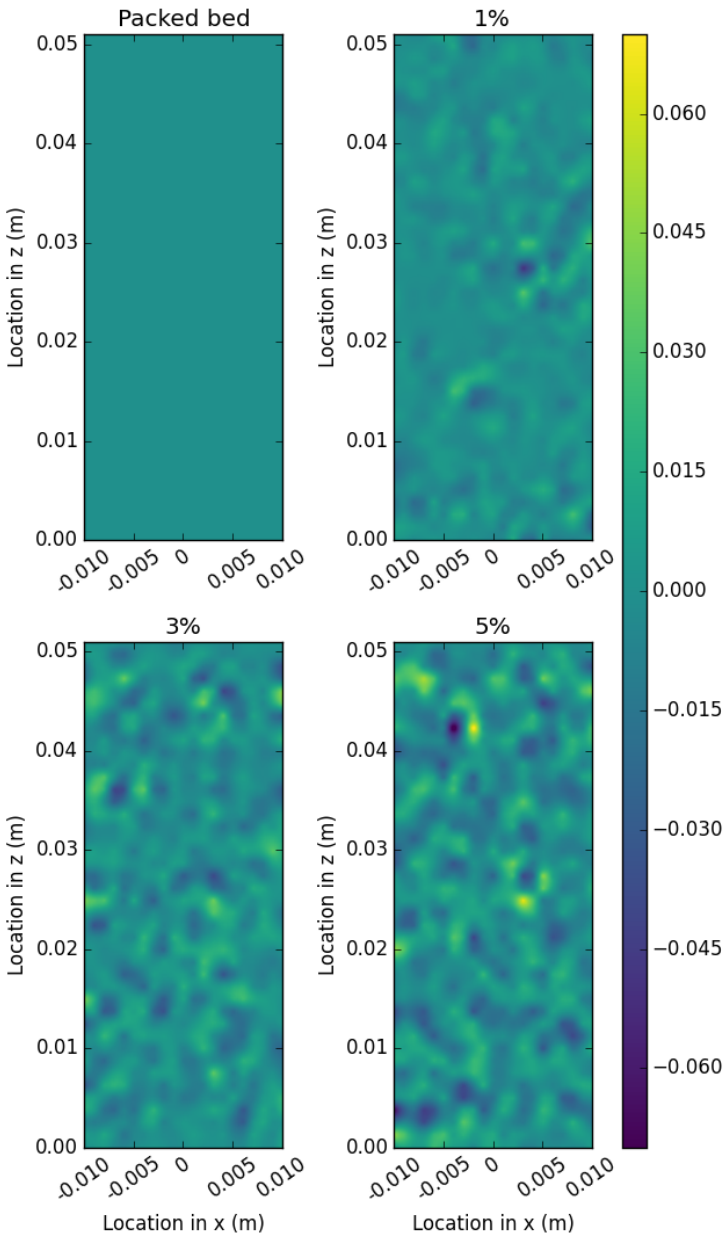

Figure 6.20: Distribution of local changes in packing fraction $(\phi_\eta - \phi_i)$ for χ-config, $\phi = 0.62$, $r^* = 0.32$

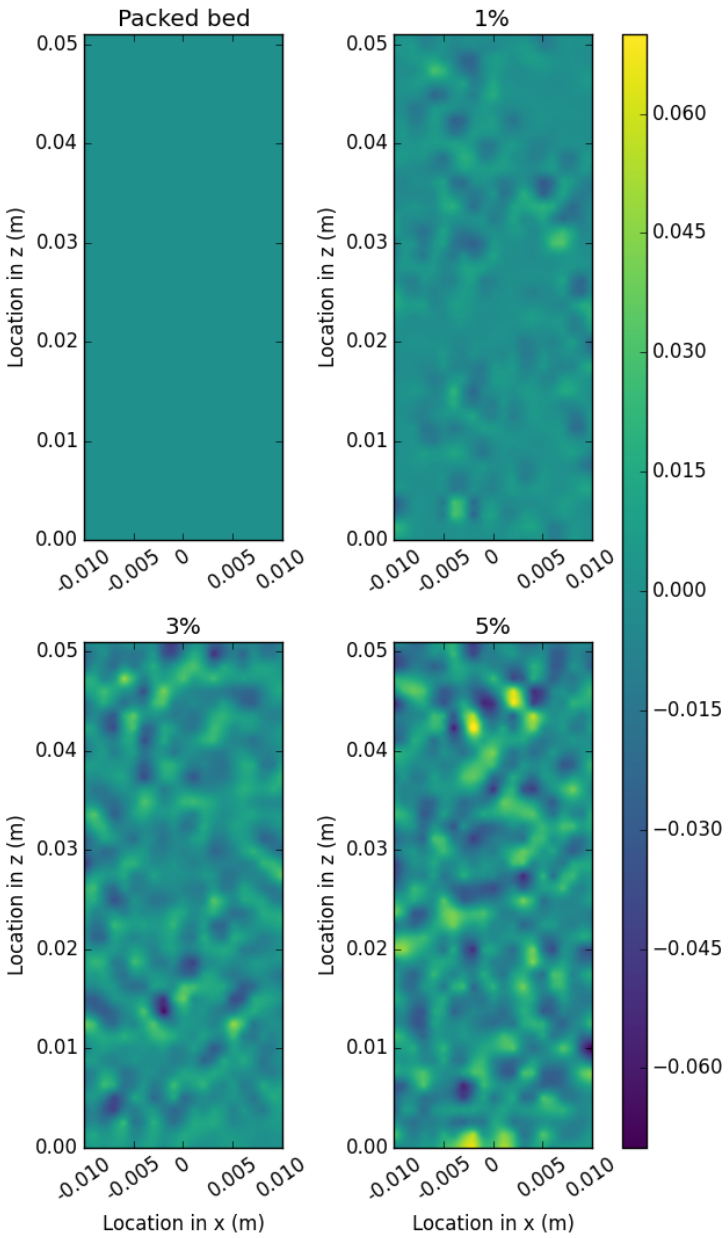

Figure 6.21: Distribution of local changes in packing fraction $(\phi_\eta - \phi_i)$ for χ-config, $\phi = 0.62$, $r^* = 0.2$

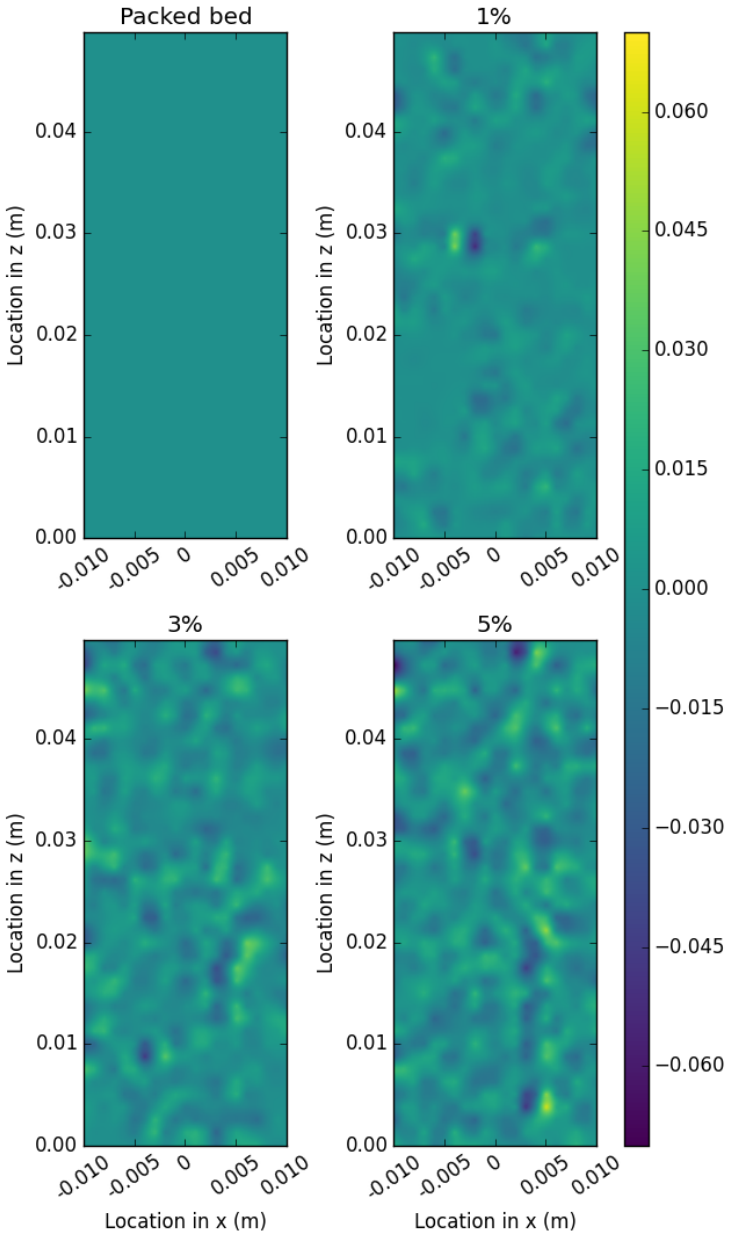

Figure 6.22: Distribution of local changes in packing fraction $(\phi_\eta - \phi_i)$ for χ-config, $\phi = 0.64$, $r^* = 0.32$

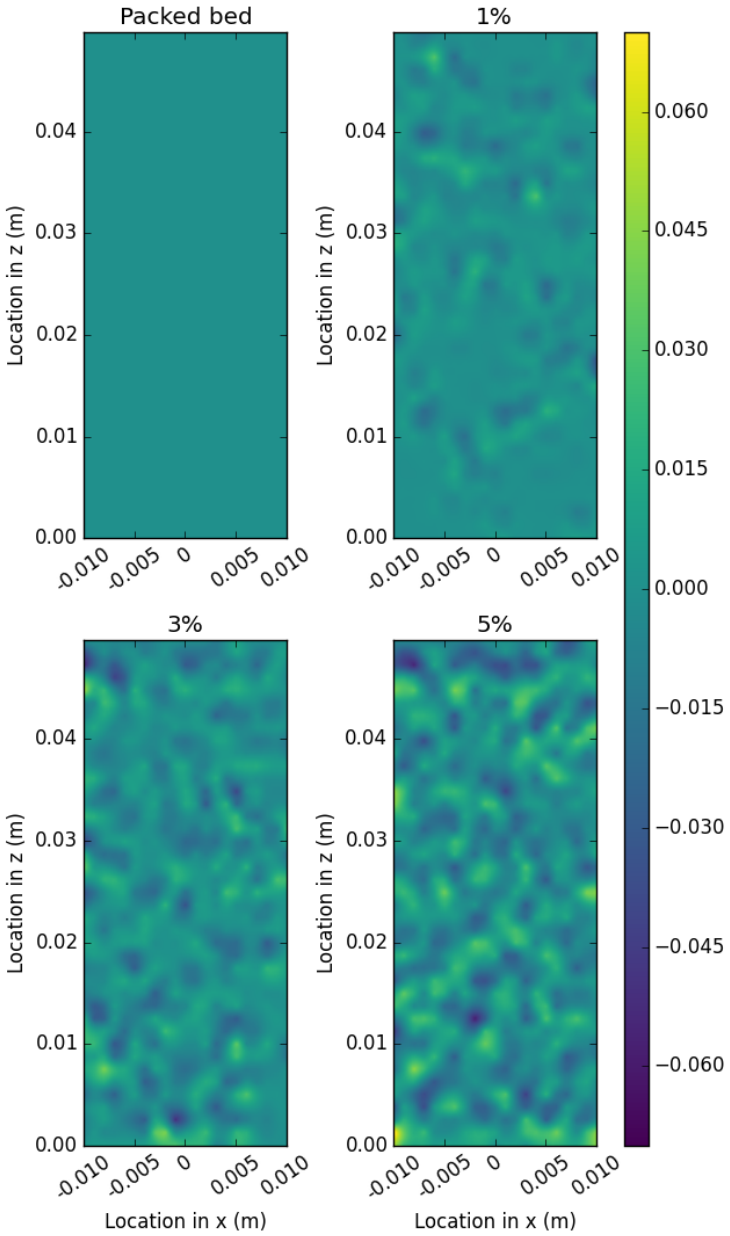

Figure 6.23: Distribution of local changes in packing fraction $(\phi_\eta - \phi_i)$ for χ-config, $\phi = 0.64$, $r^* = 0.2$

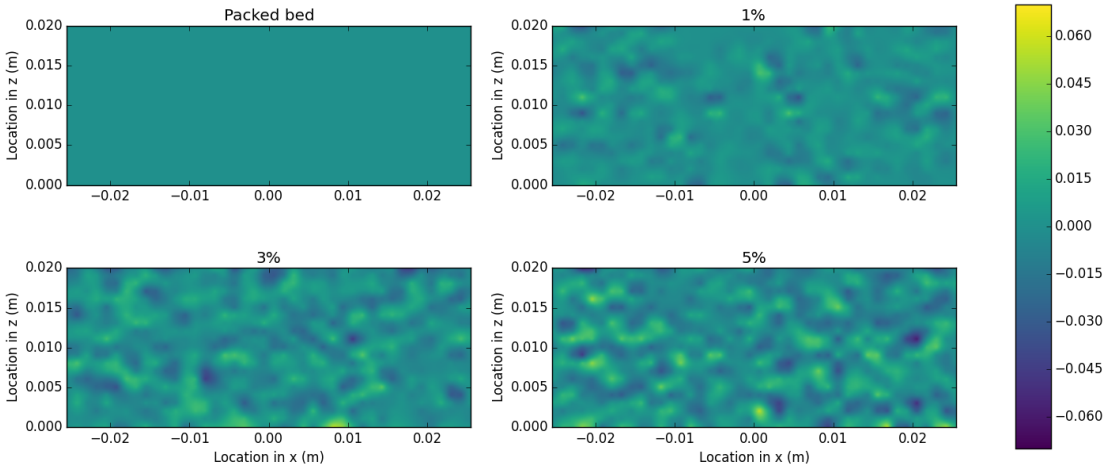

Figure 6.24: Distribution of local changes in packing fraction $(\phi_\eta - \phi_i)$ for ζ-config, $\phi = 0.62$, $r^* = 0.32$

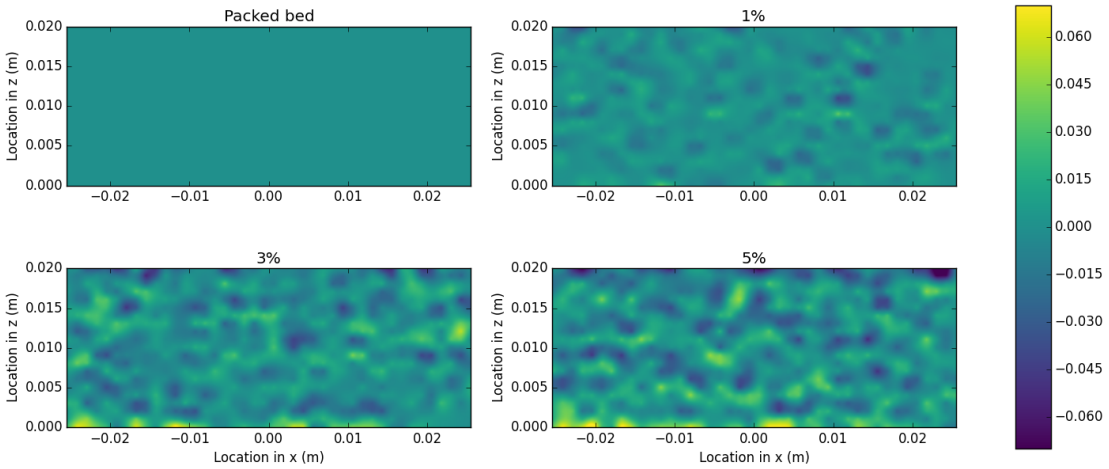

Figure 6.25: Distribution of local changes in packing fraction $(\phi_\eta - \phi_i)$ for ζ-config, $\phi = 0.62$, $r^* = 0.2$

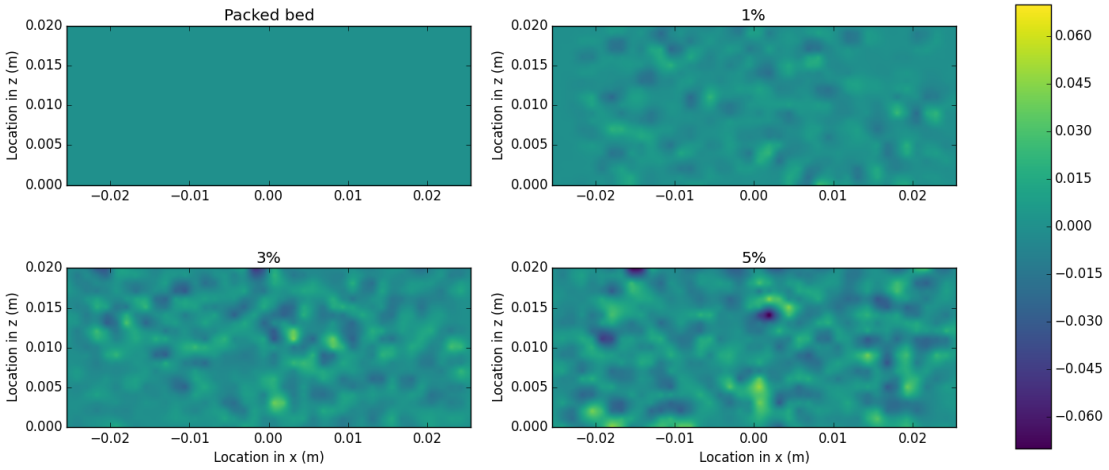

Figure 6.26: Distribution of local changes in packing fraction $(\phi_\eta - \phi_i)$ for ζ-config, $\phi = 0.64$, $r^* = 0.32$

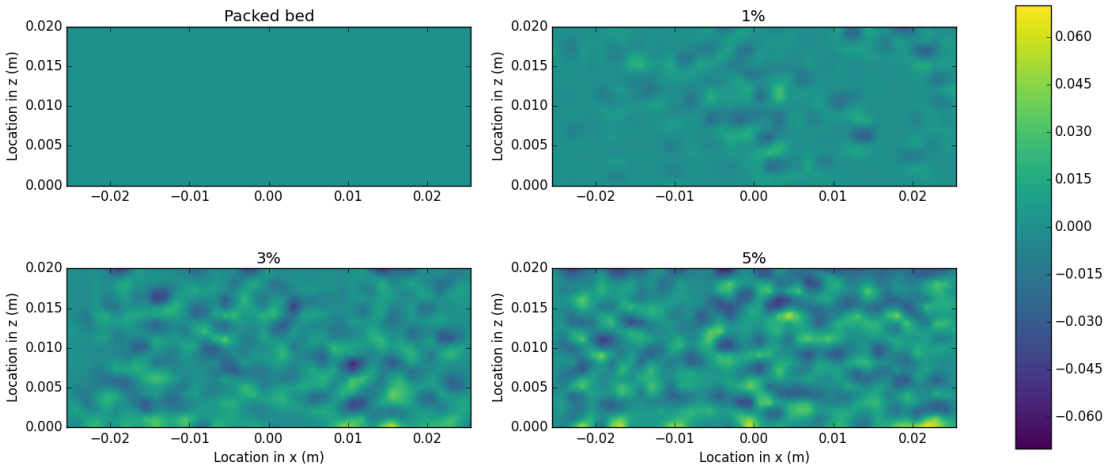

Figure 6.27: Distribution of local changes in packing fraction $(\phi_\eta - \phi_i)$ for ζ-config, $\phi = 0.64$, $r^* = 0.2$

6.2.2 Conclusions

We conducted several microscale simulations of granular heat transfer using coupled CFD-DEM simulations of representative tritium-breeding ceramic pebble bed volumes with parametric variations of: bed orientation with respect to gravity, pebble crushing amount, initial packing fraction, and crushed fragmentation size.

There was one general trend observed that reiterates past conclusions from solid breeder research. Namely, more persistent behavior is witnessed in pebble beds with higher initial packing fractions. In this study, the most dominant parameter observed to affect temperatures in pebble beds was the initial packing fraction: beds with higher initial packing fraction had smaller increases in bed temperatures due to pebble crushing. We therefore conclude that manual densification, from either long-term vibration packing or load-induced pre-compaction, must be done to ceramic pebble bed volumes to gain some temperature control during operation in a fusion reactor. To achieve packing fractions of 64% in the relatively small sizes of this study, for example, a load of over 1 MPa was necessary. In the assembly of tritium breeding modules, it must be kept in mind that similar pre-compaction may need to be performed.

As stated earlier, a concern with the ζ design is the possibility of gap formation between pebble bed and upper walls after bed resettling, particularly after pebble fragmentation. In this study, we found pebble beds initially packed to $\phi = 62\%$ experienced the highest increases in both total average bed temperature as well as maximum temperature rise. The comparably looser packing allowed a quick reduction in hydrostatic pressures and consequently a reduction in heat conduction to the upper wall. Nevertheless, no gaps were detected even at 5% of pebbles crushed. However, temperatures in pebble beds packed to 64% showed a resistance to fragmentation; overall average temperatures were comparable to χ-configurations, and in fact these EU-style beds had the lowest maximum temperatures for beds with many crushed pebbles. We showed that freedom of fragments to travel between zones in these beds prevented a build-up of loose fragments (and thereby avoided build-up of heating) in the hottest regions.

As for the χ-configurations, we found that when there were not many broken pebbles ($\eta \leq 3\%$), these beds generally had lower temperatures in comparison to similar ζ-config beds. But as η went above 3% for many of the beds, the averaged bed temperature and, importantly, the maximum temperature rise actually jumped above the ζ-configurations. We showed that for these beds it was the inability for fragments to move between zones which left many small fragments to settle in the hottest region, further contributing to heating.

From the results we have shown, it is obvious that pebble crushing and bed resettling effects on temperature are complicated, non-linear responses and are particular to breeder design and ceramic material employed. We found indications of certain operational spaces for which different designs responded less severely to pebble crushing. For instance, from the point of view of temperature response in pebble beds, if one were to employ a material known to have a limited crush strength, one might accept that many pebbles could break (at least up to 5%, as studied here) over the life of the breeder and choose to employ the ζ-style which avoided large increases in temperature after long operation of the breeder. Alternatively, if one had a ceramic material with a larger crush strength, the χ-design would be preferable as it generally retained lower overall and maximum bed temperatures when fewer pebbles in the ensemble were crushed.

It must be pointed out that the findings discussed here are concerned primarily with temperature distribution, without consideration for other consequences of pebble crushing such as blocking of helium purge, and thereby tritium extraction, by clogging from fragment dust or particulates. Clogging of purge flow is specific to each pebble bed design and must receive future attention in its own right.

This study was performed on some generic geometries and has provided some generalized conclusions. But in light of the pebble beds' complex responses, as breeder designs continue to evolve into their final form before deployment in ITER, CFD-DEM models should continuously be employed to study the specific thermomechanical responses to pebble crushing and bed resettling unique to each design.

6.3 Lattice-Boltzmann Method Modeling of Temperature Distributions in Pebble Beds

In this section, lattice-Boltzmann method (LBM) numerical models are used to study the complete interstitial flow of helium through a packed bed of lithium ceramics. A discussion on the development of the LBM method was given in § 5. To review, for implementation of DEM and LBM coupling, pebble packing structures are generated with DEM simulations then mapped into the LBM nodal grids where the thermofluid and conjugate heat transfer models solve momentum and thermal conservation equations. The DEM-LBM approach is a one-way coupled approach in that LBM results are not currently fed back into DEM simulations for future packing evolution. The sacrifice of two-way coupling (that is currently possible with volume-averaged CFD-DEM models) offers instead to understand the tortuous helium flow and its impact on thermal transport in the tritium breeding ceramic pebble beds.

In the lattice-Boltzmann formulation, we will consider representative pebble bed volumes. The system spans $6d_p$ and $4d_p$ in the x and y directions, respectively. Primitive walls are placed at the limits of x, periodic boundary conditions are used in the extent of y. The limit in the flow direction, z, is set to satisfy the desired packing fraction of $\phi = 0.61$ with an ensemble of $N = 200$ pebble,

$$z_{\text{lim}} = \frac{N\pi d_p^3}{6x_{\text{lim}}y_{\text{lim}}\phi} \tag{6.9}$$

where x_{lim} and y_{lim} are the limits given above. The result is approximately 7 pebble diameters of height ($7.16d_p$) in the flow direction. Primitive walls are also placed at the limits of z.

The damaged pebble bed case considers fragments of size $r^* = 0.2$ and a damage amount of $\eta = 5\%$ (following the syntax developed in § 6.2). A resolution of res = 40 is chosen in order to properly resolve the smaller fragments of the bed with damaged pebbles. Such a resolution dictates lattices of size $N_x = 241$, $N_y = 161$, and $N_z = 368$ for a total of approximately 14.2 million LBM nodes. The grid spacing is $\delta_x = 25 \times 10^{-3}$. A lattice velocity is chosen as $u_{0,lb} = 0.02$ which sets the lattice timestep size as $\delta_t = 500 \times 10^{-6}$.

The relaxation parameters, ω, for the lattice solving the momentum equation (ω_{ns}), the

lattice nodes representing the solid in the energy equation (ω_{cj}) and the lattice nodes for the fluid in the energy equation (ω_{ad}) are given in Table 6.4.

The simulation procedure begins with creating volumes in DEM of a well-packed pebble bed and a pebble bed with crushed and fragmented particles. The two pebble beds are shown in their DEM representation in Figure 6.28. In order to highlight the differences between modeling methods, the pebble-fluid system will also be simulated in the CFD-DEM framework.

Table 6.4: The momentum relaxation constants for fluid (ns), thermal relaxation constants for fluid (ad), and thermal relaxation constants for the solid (cj) used in the simulation.

ω_{ns}	ω_{ad}	ω_{cj}
0.6569	0.3925	0.6995

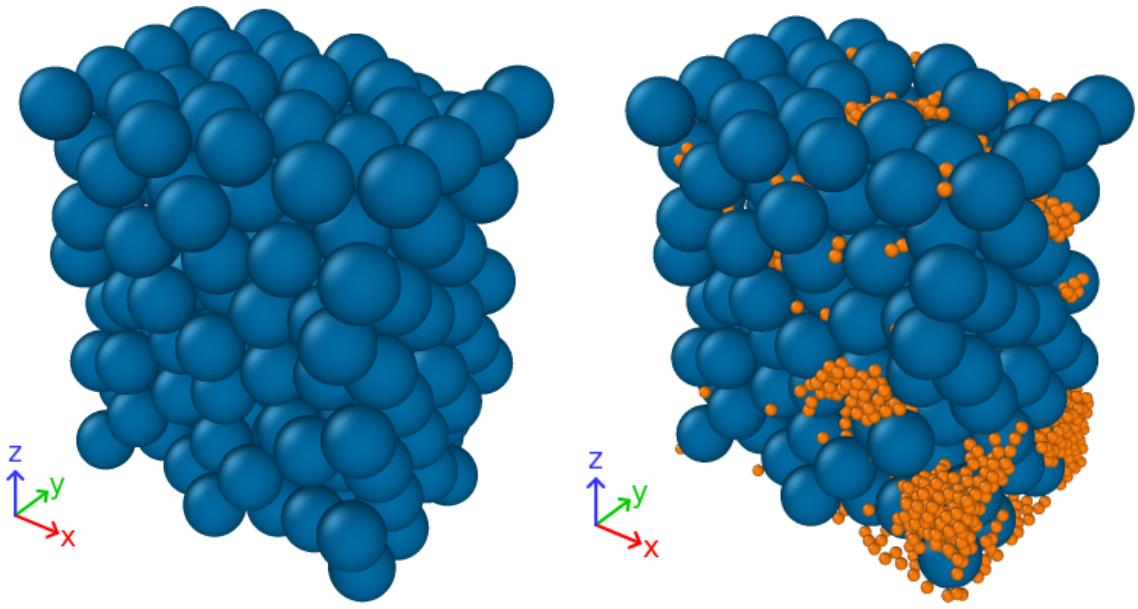

(a) Representative pebble bed having filled the volume to $\phi = 0.61$ with DEM.

(b) Pebble bed with $r^* = 0.2$ and $\eta = 0.05$ constructed with DEM.

Figure 6.28: DEM pebble beds are generated to provide pictures of packings to be loaded into LBM lattices.

6.3.1 Results & Discussion

After mapping DEM pebbles onto LBM lattices, they are run to thermal steady-state. Pebbles, as realized in LBM, are shown in Figures 6.29 to 6.31, colored by temperature.

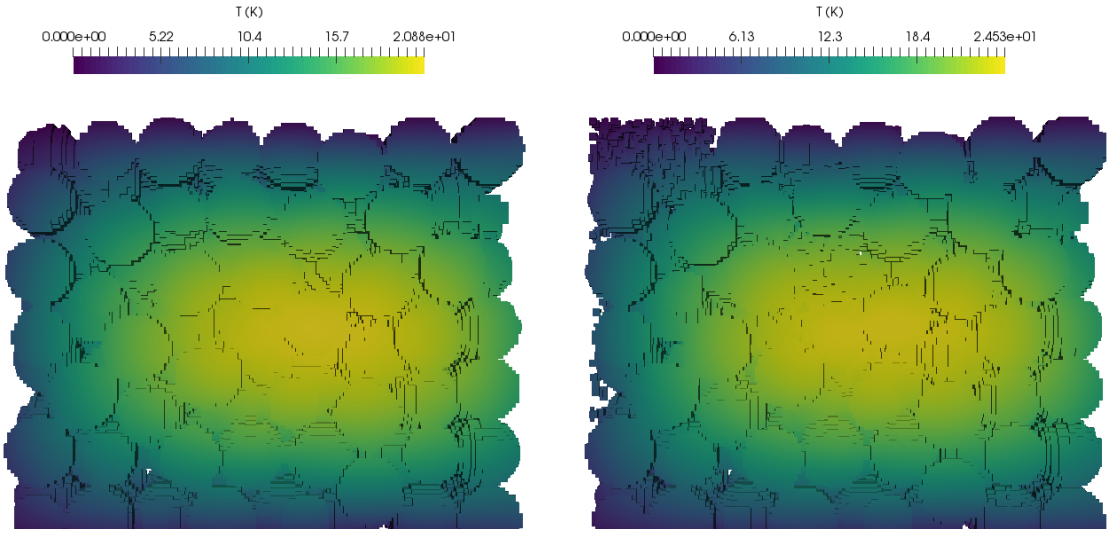

(a) Filled (b) Crushed

Figure 6.29: Frontal view of pebbles realized in LBM lattices (y-normal, fluid moving left to right).

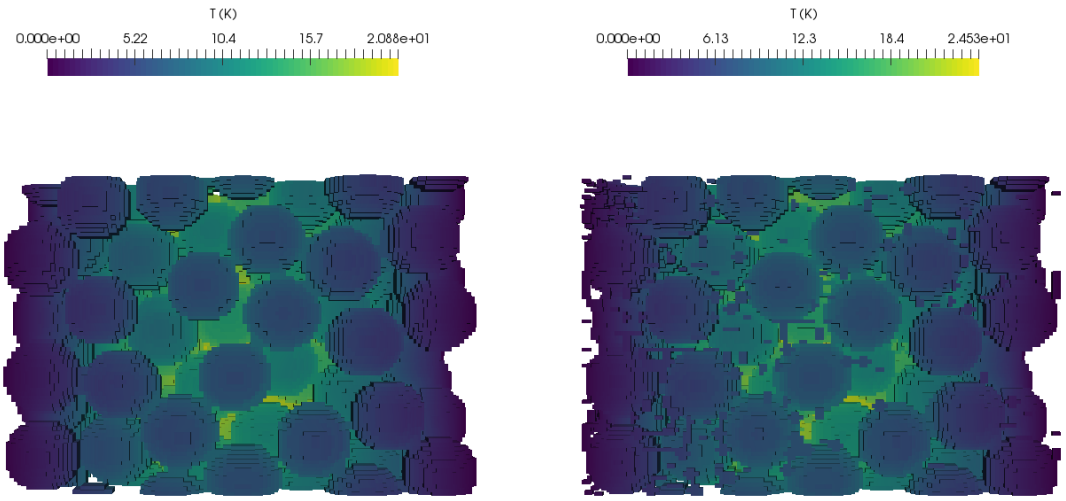

(a) Filled (b) Crushed

Figure 6.30: Bottom view of pebbles realized in LBM lattices (z-normal, fluid moving into page).

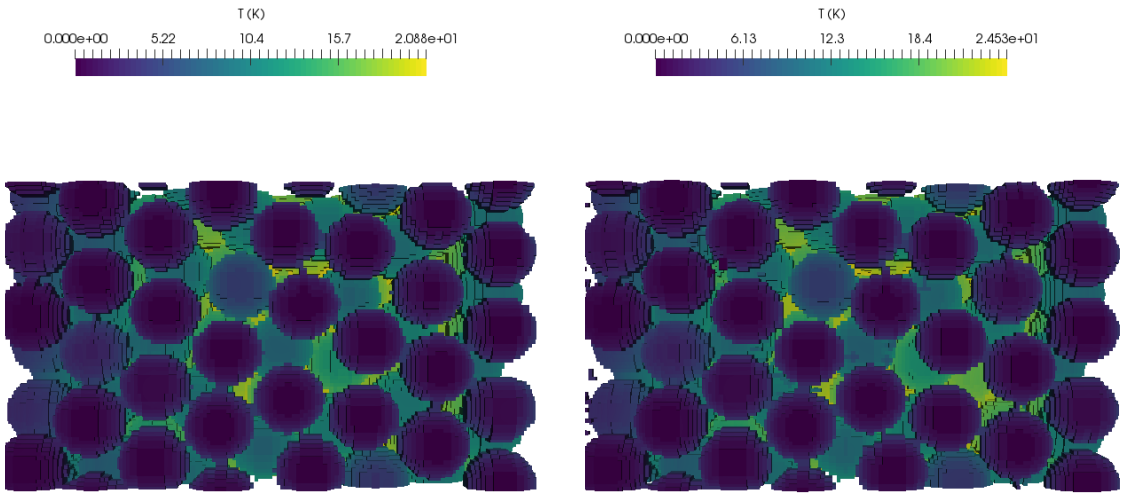

(a) Filled (b) Crushed

Figure 6.31: Side view of pebbles realized in LBM lattices (x-normal, fluid moving left to right).

Streamlines from LBM results are given in Figures 6.32 to 6.34. In the pebble bed with crushed fragments, the helium flow is clearly more tortuous than the pebbled bed with solid,

well-packed pebbles.

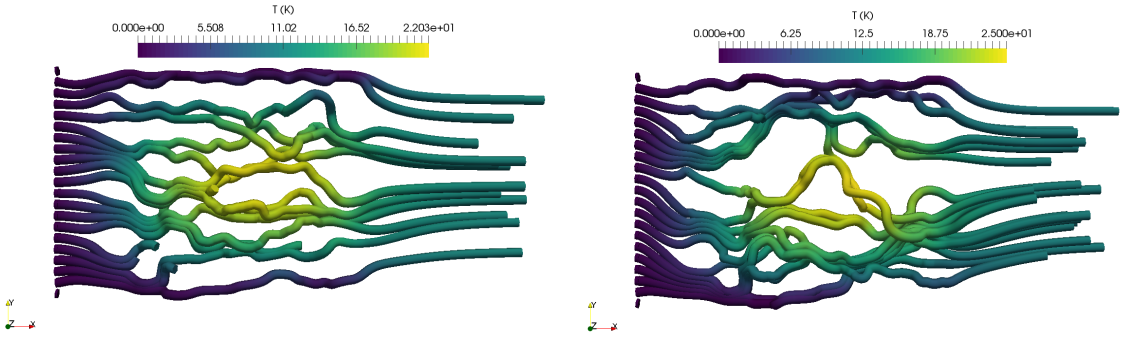

(a) Filled (b) Crushed

Figure 6.32: Top view of streamlines generated along in a line parallel to x-axis (fluid moving left to right).

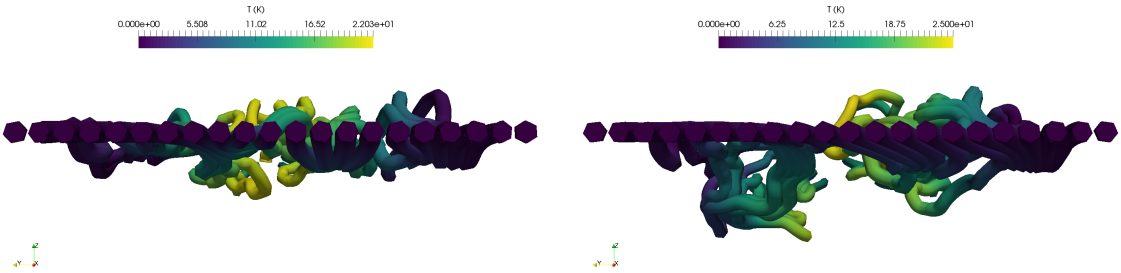

(a) Filled (b) Crushed

Figure 6.33: Rear view of streamlines generated along in a line parallel to x-axis (fluid moving into page).

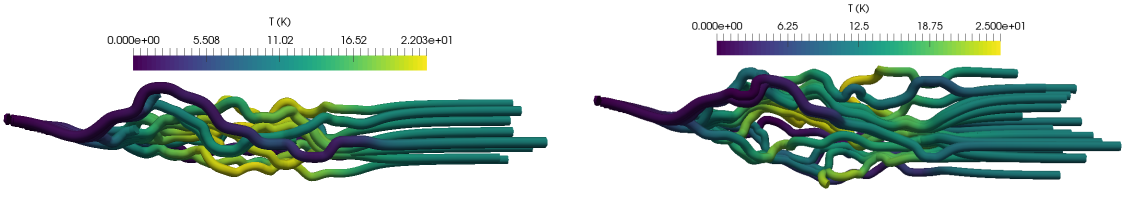

(a) Filled (b) Crushed

Figure 6.34: Side view of streamlines generated along in a line parallel to x-axis (fluid moving left to right).

A quantitative description of the extra paths taken by fluid packets moving through the crushed pebble bed is tortuosity. Tortuosity was first introduced to studies of porous media by PC Carman in 1937.[30] Tortuosity is described as the ratio between the effective length of travel of a packet of fluid through a packed bed against the characteristic length of the packed bed (the length the packet would travel in unimpeded flow),

$$\mathscr{T} = \frac{L_{\text{eff}}}{L} \tag{6.10}$$

Matyka & Koza provide a method for calculating tortuosity from readily available numerical data.[128] Their formula reads,

$$\mathscr{T} = \frac{\langle u \rangle}{\langle u_x \rangle} \tag{6.11}$$

where $\langle u \rangle$ is the average magnitude of the intrinsic velocity over the entire system volume. And $\langle u_x \rangle$ is the average of the component of velocity along the macroscopic flow direction.

Taking advantage of the regularly spaced lattices in LBM, tortuosity can then be calculated directly from LBM results along all nodes,

$$\mathscr{T} = \frac{\sum_{\mathbf{r}} u(\mathbf{r})}{\sum_{\mathbf{r}} u_x(\mathbf{r})} \tag{6.12}$$

Tortuosity is found for the filled pebble bed to be $\mathscr{T} = 1.245$; for crushed pebble bed it is calculated to be $\mathscr{T} = 1.329$. The crushed pebble fragments caused an increase of 6.7% to tortuosity of fluid flow.

In Figures 6.35 and 6.36, many contours of velocity, normalized against the inlet magnitude, are shown for the filled and crushed pebble beds ($\mathbf{u}/U_0$). Redistribution of particles from fragmentation result in clogging certain regions and thus localized increases in velocity, compared to the well-packed pebble bed. The velocity jets manifest in regional averages in the pebble bed as well. The results of LBM are integrated along z and y to provide profiles along the direction of interest. Velocity profiles and void fraction are given in Figure 6.37 for the cases of well-packed and crushed pebble beds.

In Figure 6.38, velocity profiles as calculated with LBM and CFD-DEM models are given. Comparisons of packing fraction calculated with the two modeling approaches are similarly given in Figure 6.39.

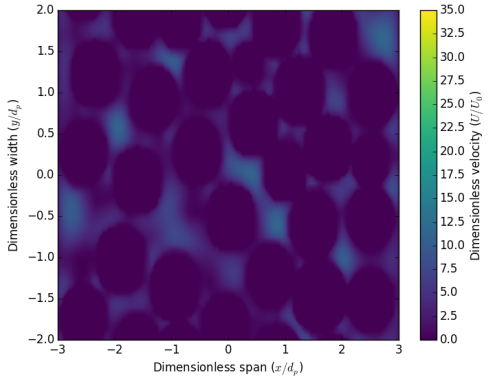

(a) Filled, height of $2d_p$

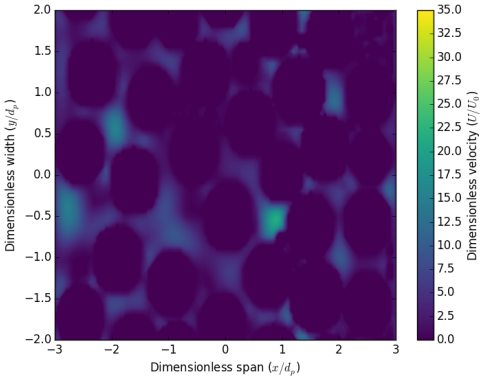

(b) Crushed, height of $2d_p$

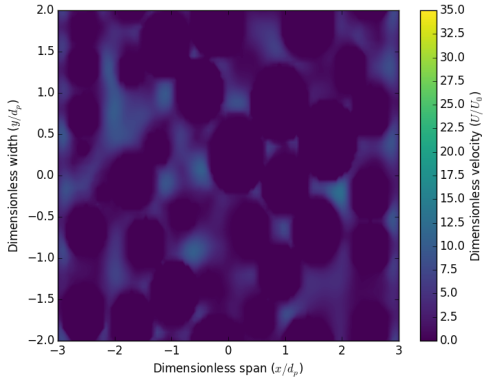

(c) Filled, height of $3d_p$

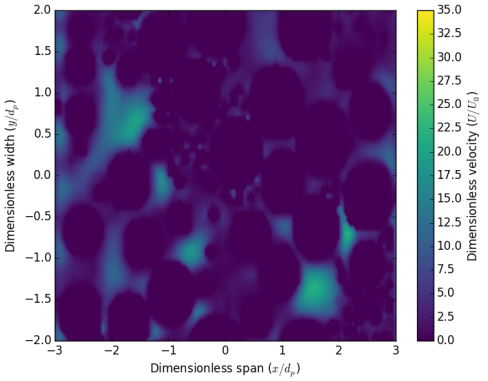

(d) Crushed, height of $3d_p$

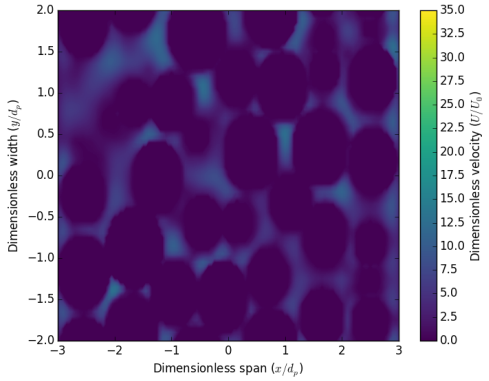

(e) Filled, height of $4d_p$

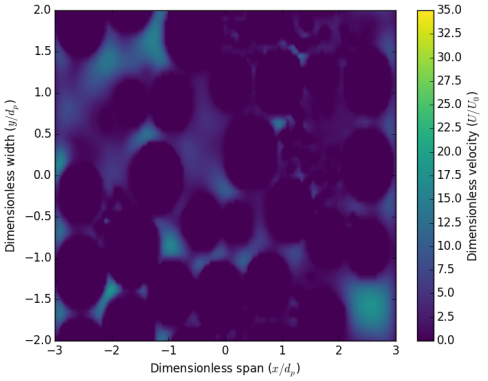

(f) Crushed, height of $4d_p$

Figure 6.35: x-y-plane contours from heights of $2d_p$ to 4_dp show localized peaks of velocity in crushed pebble beds.

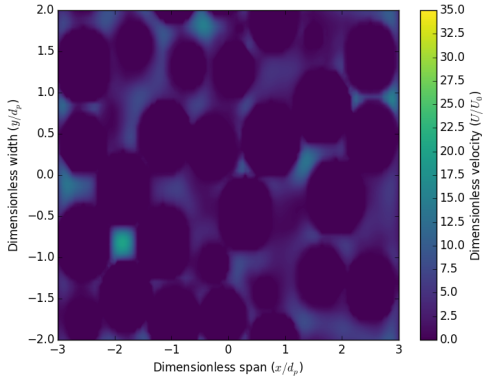

(a) Filled, height of $5d_p$

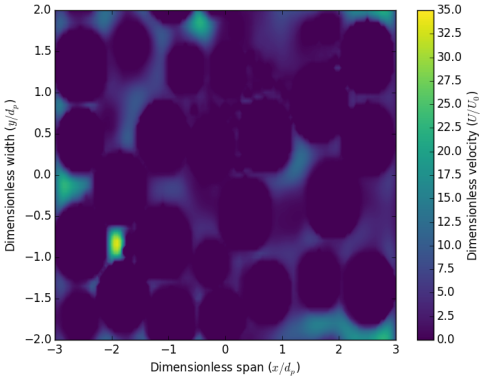

(b) Crushed, height of $5d_p$

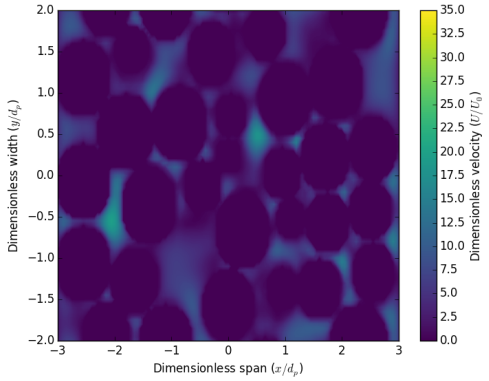

(c) Filled, height of $6d_p$

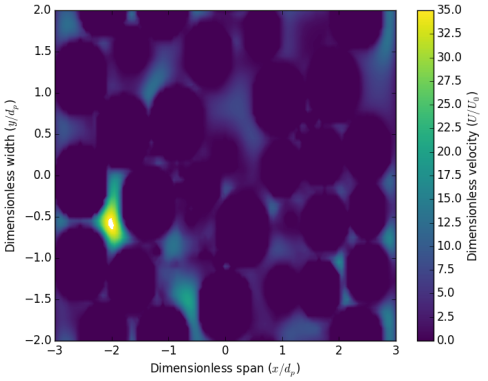

(d) Crushed, height of $6d_p$

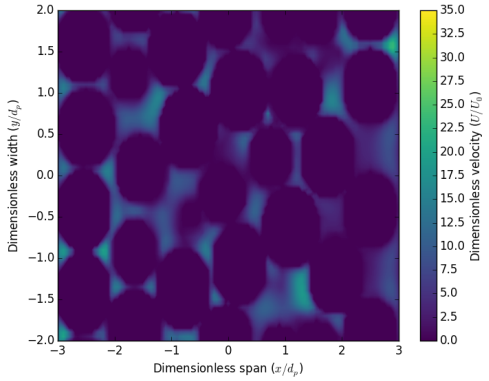

(e) Filled, height of $7d_p$

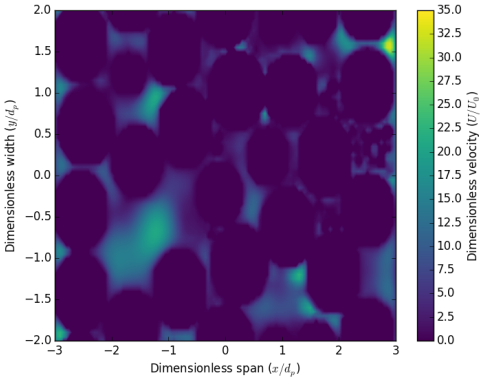

(f) Crushed, height of $7d_p$

Figure 6.36: x-y-plane contours from heights of $5d_p$ to 7_dp show localized peaks of velocity in crushed pebble beds.

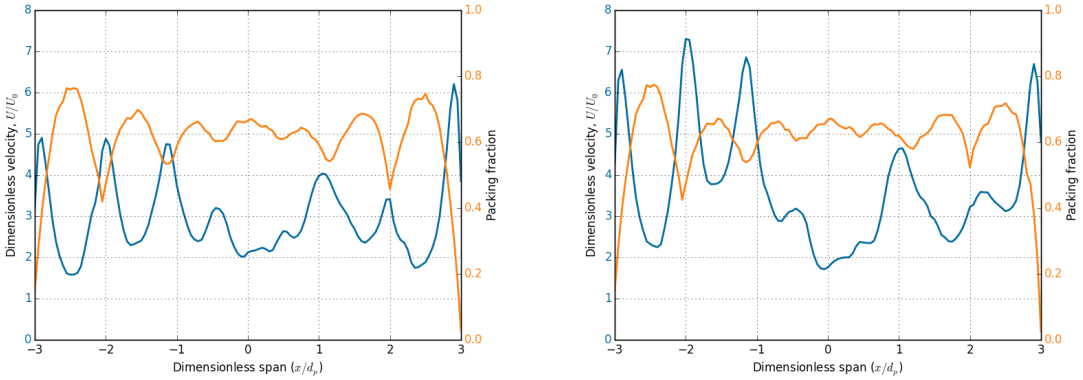

(a) Filled (b) Crushed

Figure 6.37: y-z-plane averages of normalized velocity (left) and packing fraction (right) demonstrating the oscillatory behavior of flow from ordered packing forced by physical boundaries.

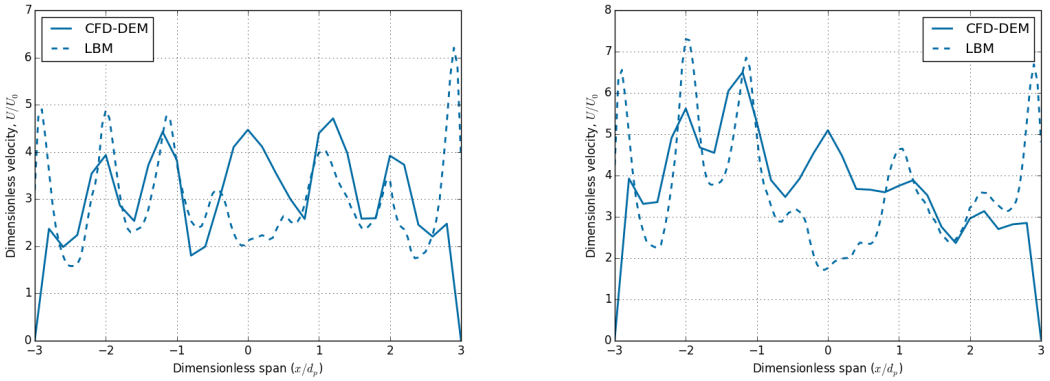

(a) Filled (b) Crushed

Figure 6.38: y-z-plane averages of normalized velocity for LBM (dashed) and CFD-DEM (solid).

Thermal dispersion is the spreading of heat caused by variations in velocity about a mean in a fluid. In a packed bed with stagnant interstitial fluid, molecular thermal diffusion is the dominant mode of heat transfer. Mechanical dispersion of heat and fluid flow becomes significant with increased Reynolds number in pores, leading to additional heat transfer. We will quantify thermal dispersion with a commonly-applied temperature-gradient assumption

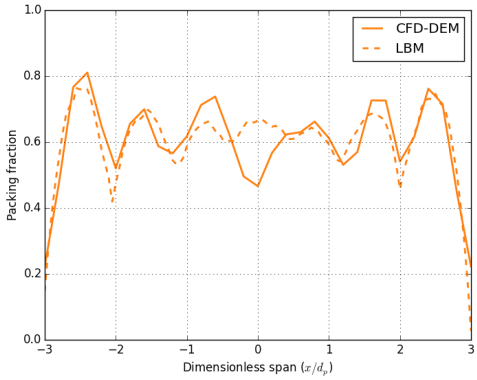

(a) Filled

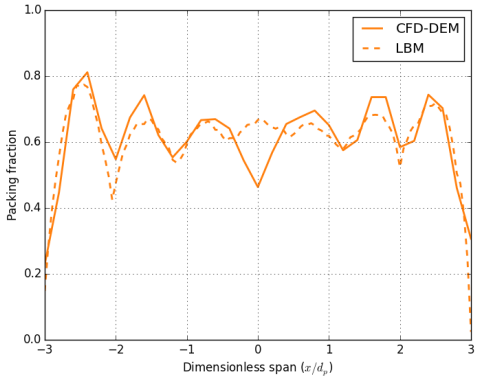

(b) Crushed

Figure 6.39: y-z-plane averages of normalized packing fraction for LBM (dashed) and CFD-DEM (solid).

to calculated a dispersion conductivity.[112,132,199]

Applying volume-averaging-theory (VAT), the intrinsic energy equation for a fluid in porous media in a representative elemental volume (REV) is given in Sbutega *et al.*,[162]

$$\epsilon\rho_f C_{pf}\langle\mathbf{u}\rangle^f \cdot \nabla\langle T_f\rangle^f = \nabla\left(\mathbf{k}_{f,\text{eff}} \cdot \nabla\langle T_f\rangle^f\right) + hS_w\left(\langle T_s\rangle^s - \langle T_f\rangle^f\right) \tag{6.13}$$

where $\langle T_f\rangle^f$ is the intrinsic volume average of fluid temperature and $\langle T_s\rangle^s$ is the intrinsic volume average of solid phase temperature. h is a closure term for heat transfer coefficient between solid and fluid phases which is applied over the volumetric interfacial surface area, $S_w = A_{fs}/V$, in the REV. The effective conductivity for the fluid is a tensor that is composed of the stagnant thermal conductivity, including diffusive conductivity and the 'tortuousity' conductivty, and the dispersion conductivity,

$$\mathbf{k}_{f,\text{eff}} \cdot \nabla\langle T_f\rangle^f = \mathbf{k}_{i,\text{stag}} \cdot \nabla\langle T_f\rangle^f + \mathbf{k}_{i,\text{disp}} \cdot \nabla\langle T_f\rangle^f \tag{6.14}$$

where

$$\mathbf{k}_{f,\text{stag}} \cdot \nabla\langle T_f\rangle^f = \epsilon k_f \nabla\langle T_f\rangle^f + \frac{1}{V}\int_{Afs} T_f \,\mathrm{d}\mathbf{A} \tag{6.15}$$

$$\mathbf{k}_{f,\text{disp}} \cdot \nabla\langle T\rangle^f = -\epsilon\rho_f C_{pf}\langle T'_f\mathbf{u}'_f\rangle^f \tag{6.16}$$

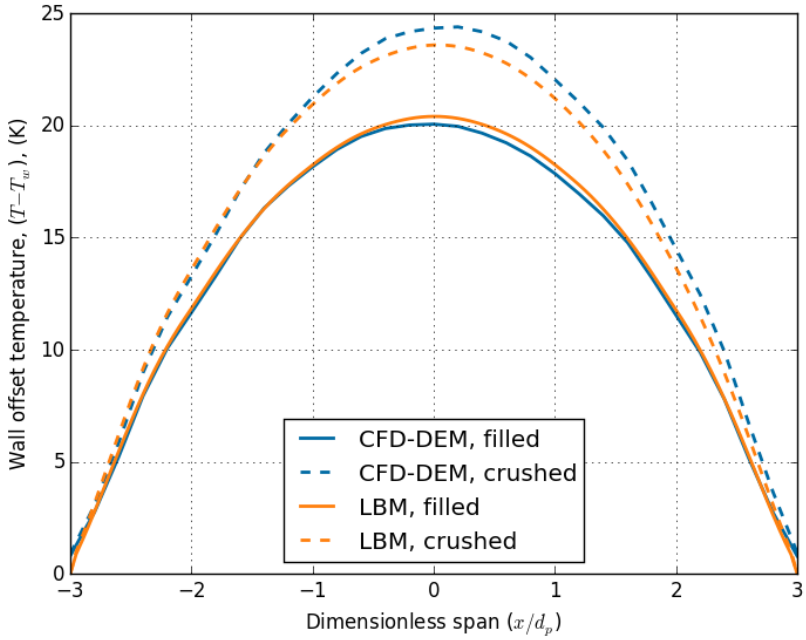

Figure 6.40: Temperature profiles in pebble beds that are fully filled (solid), and with 5% crushed (dashed) using both CFD-DEM (blue) and LBM (orange) models.

Sbutega *et al.* and Kuwahara *et al.*[113,162] show that the dispersion conductivity is negligible at low Peclet number but dominates at high Peclet. In the pebble beds of solid breeders, low Peclet numbers are expected due to slow moving purge gas and small Prandtl number of helium. As a consequence, we can expect that temperatures calculated *via* the lattice-Boltzmann method should not be fundamentally different from CFD-DEM computations. Nevertheless, data of the LBM model allow us to calculate dispersion conductivities; for the well-packed bed we find the average of the y-component of dispersive conductivity to be only $k_{f,\mathrm{disp}}|_y = 0.0043\,\mathrm{W\,m^{-1}\,K^{-1}}$; for the bed with crushed pebbles the y-componenet of dispersive conductivity is $k_{f,\mathrm{disp}}|_y = 0.0053\,\mathrm{W\,m^{-1}\,K^{-1}}$; an increase of 23.2% for crushed pebbles. Nevertheless, in both cases the amount of spreading due to dispersive conductivity is negligibly small. Therefore, in the beds we have analyzed with small Peclet number, the results of CFD-DEM and LBM are predictably similar. Temperature profiles, averaged in slices of y- and z-directions, calculated from LBM and CFD-DEM for well-packed and crushed beds are given together in Figure 6.40.

Figure 6.41: Over-estimates of contact area of fragments contributes to higher heat conductance in LBM model than CFD-DEM.

In Figure 6.40, we see extremely good agreement between CFD-DEM and LBM results, particularly for well-packed pebble beds.. While the velocity profiles between the two methods showed only qualitative similiarties, the lack of mechanical dispersion of heat from the $\langle T'_f \mathbf{u}'_f \rangle^f$ term allows the volume-averaged approach of CFD-DEM to model heat transfer as faithfully as LBM. In pebble beds with fragmentation, the agreement between CFD-DEM and LBM is less. The temperatures from LBM are 6% higher at the midpoint. Lower temperatures in LBM are, in part, not physical but attributable to the resolution when mapping DEM pebbles into LBM. A resolution of 20 pixels was chosen to represent pebbles. Fragments of size $r^* = 0.2$ result in 4 pixels per diameter for fragments. As an example, a slice of pebble bed (pebbles in black, fluid in white) is shown in Figure 6.41. In this cross-section, the small fragments mapped into LBM have larger contact areas than Hertzian predictions provide in DEM.

6.3.2 Conclusions

Much effort was made to accurately model the tortuous flow of helium in packed beds. Using the lattice-Boltzmann method, we looked into pore-scale influences of crushing on

void fraction distribution and consequently velocity fields of pebble beds. We found that when 5% of pebbles are fragmented, tortuosity of the pebble bed increased by nearly 7% while the dispersive conductivity increased over 23%. In spite of the increase in dispersive conductivity, the impact on temperature profile spreading remained negligibly small due to the low Peclet number flow expected in tritium breeding blankets. The result, however, does inspire a path of research toward allowing higher power density in solid breeders. The pebble bed with crush fragments studied here can be considered as a low-porosity, polydisperse pebble bed. Polydispersity in pebble beds can lead to very high packing fractions.

Yang & Nakayama provide a correlation for transverse dispersive conductivity in regularized packings as a function of a modified Peclet number,[199]

$$\frac{k_{\text{diss}}}{k_f} = 0.0075 \frac{\text{Pe}_D^2}{2 + 1.1 \frac{\text{Pe}_D^{0.6}}{\text{Pr}^{0.27}}} \tag{6.17}$$

where the Peclet number,

$$\text{Pe}_D = \rho_f C_{pf} \frac{\langle u \rangle d_p}{k_f} \tag{6.18}$$

is based on the Darcian velocity, $\langle u \rangle = \frac{U_0}{\epsilon}$. Because the Darcian velocity increases with more tightly packed beds (smaller void fraction), there appears to be some control over dispersive conductivity by means of polydisperse packings. Using material properties for helium and 1 mm pebbles (neglecting for a moment the influence of polydispersity), we can calculate dispersive conductivity as a function of void fraction. In Figure 6.42, the example calculation is shown as a function of packing fraction. Experimentally, packing fractions in polydisperse beds can easily reach $\phi = 0.80$.[150] From Figure 6.42, dispersive conductivity (again, calculated assuming single sized pebbles) increases by an order of magnitude for packing fractions around $\phi = 0.88$.

Large packing fractions are generally avoided in solid breeder blankets in order to avoid their concomitant increase in pressure drop. However, from the investigation performed with heat transfer in lattice-Boltzmann simulations, it is worth revisiting the topic from the point of view of energy management and the ability for packed beds to sustain larger power densities.

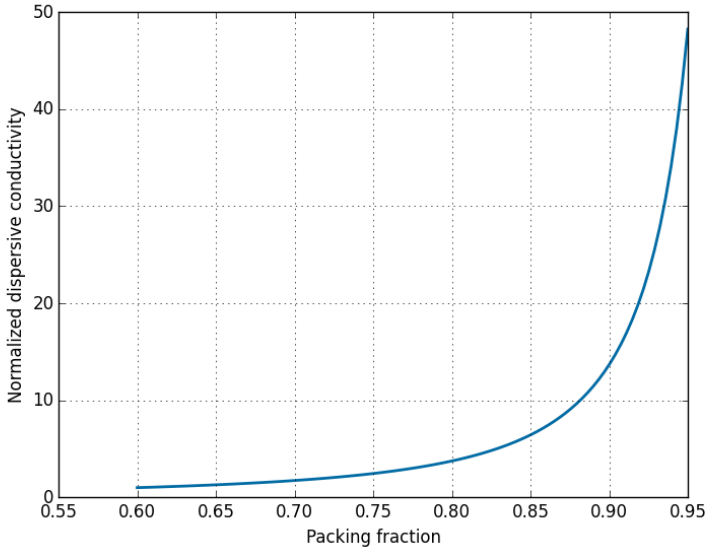

Figure 6.42: Dispersive conductivity for pebble beds increases rapidly as packing fraction approaches unity.

The lattice-Boltzmann method allowed us to study the tortuous path of helium through packed beds of spheres with and without crush fragments. Unlike traditional CFD methods for packed beds, no simplifications of contact regions was required and a direct mapping, which maintained consistency of packing fractions, was performed when digitizing DEM packing structures onto LBM lattice nodes. LBM simulations were run on a machine with quad-core, 3 GHz Intel Xeon E6-1607. Computation times for the lattices with a resolution of 20 voxels per diameter, up to 400 seconds of real time simulation were generally around 30 hours. On the same machine, CFD-DEM simulations generally concluded in approximately 4 hours. Scaling up to a full-size pebble bed would require significant computational expenses. Yet, owing to the small Peclet number of pebble beds under consideration, there does not appear to be any evidence that considerations of the entire helium flow field is necessary when attempting to model thermomechanical interactions of solid breeders. The lattice-Boltzmann technique can, however, help in studying novel concepts for increasing heat transfer in packed beds in order to increase power density, such as the increase in dispersive conductivity due to mixed pebble beds and high packing fractions.

CHAPTER 7

Summary, Closing Remarks, & Future Work

7.1 Summary

Ceramic pebble beds as tritium breeding volumes in fusion reactors must endure high power densities while maintaining both continued transport of high quality heat into coolants for power production as well as ceramic temperatures within relatively-narrow prescribed operating windows. The ceramic pebble beds, as non-cohesive granular material, exist with metastable packing structures that will evolve from the external and internal forces acting upon them during long-term operation as tritium breeders. As a consequence, predictive models of solid breeder heat transfer characteristics must contend with transient packing structures and the changing modes of heat transfer they present. To provide such predictive modeling, microscale numerical models were developed to allow investigation of thermal transport in pebble beds operating in environmental conditions relevant to planned fusion reactors. Specifically, this involved development and validation of: transient, three-dimensional, thermal DEM models of packed beds; fragmentation models to simulate pebble crushing in ensembles; fully-coupled, transient, volume-averaged CFD-DEM models of fluid-solid heat transfer; and one-way-coupled, transient DEM-LBM models of conjugate heat transfer in packed beds.

In the course of validating DEM-formulations of heat transfer in packed bed ensembles, new phenomenological descriptions of contact conductance and material properties were constructed. Experimental measurements of elastic response for individual pebbles showed a wide scatter that violates a purely-Hertzian prediction of contact force based on the elastic modulus measured of sintered ceramic blocks. However, it was shown that the force-travel

response of individual pebbles follows the proper relationship predicted by Hertzian contact, namely $F_n \propto s^{3/2}$. Therefore we introduced a statistical distribution with an *apparent* elastic modulus fit to experimental measurements. The statistical spread was reproduced numerically in DEM simulations when applying elastic modulus to pebbles. In numeric simulations of uniaxial compression of DEM packed beds, volumes with the distributed apparent elastic moduli were seen to have nearly 40% more strain for the same stress state. Additionally, a roughness model was introduced into DEM formulations of contact conductance. Comparing DEM results of effective thermal conductivity, models with roughness parameters (estimated from similar ceramic materials) reduced error by more than 120%.

A new phenomenological model of pebble crushing, which models fragmentation as assemblies of smaller spheres, was developed for DEM to simulate crushed pebbles and concomitant effects on pebble bed thermomechanics. The modeling approach inserts fragments of chosen size into the system in an energy- and mass-conserving fashion. A parametric study on fragment sizes revealed that smaller pebble fragments were seen to be capable of traveling relatively long distances before re-settling; approximately 10% of pebbles traveled more than the original pebble diameter. Redistribution of mass was seen in increased local packing fractions of beds. Nuclear heating of the beds will also be affected by mass redistribution and was one topic studied during applications of the models for ITER-relevant pebble beds (to be discussed shortly).

The work of this thesis represents the first application of CFD-DEM modeling approach to solid breeder research for which nuclear heat generation in solids, tight-packed structures, and slow-moving purge gas fluid phase are dominate physical phenomena. Due to the unique operating conditions of solid breeders, advancements to the CFD-DEM code were also required to complete the research objectives of this work. Using an exact analytic solution for a single sphere with heat generation in a quiescent fluid, I showed that lumped capacitance, an assumption inherent to DEM, remains valid for both transient and steady-state solutions only after a so-called Jeffreson correction is used in the calculation of heat transfer coefficient. Without the Jeffreson correction, nuclear heating of low conductivity pebbles caused error in both transient and steady-state calculations of temperatures in pebbles, even if a low

Biot number indicates the validitiy of lumped capacitance assumption. The algebraic form of Jeffreson correction was implemented in the coupling between CFD-DEM with negligible computational overhead. Corrected versions of heat transfer coefficients compensated for low-Biot number errors due to low solid conductivity with large volumetric heat sources.

Once the correction factor was implemented for calculations of inter-phase heat transfer exchange coefficients, temperature predictions of CFD-DEM models were validated against experimental measurements of effective conductivity with stagnant helium with excellent agreement. Numeric predictions of effective thermal conductivity at 600 °C reported values of $1.05\,\mathrm{W\,m^{-1}\,K^{-1}}$ and $1.20\,\mathrm{W\,m^{-1}\,K^{-1}}$ for beds of 62% and 64% packing fractions, respectively. Experimental measurements at similar temperatures ranged between $1.18\,\mathrm{W\,m^{-1}\,K^{-1}}$ and $1.3\,\mathrm{W\,m^{-1}\,K^{-1}}$. Furthermore, the pressure drop measured in CFD-DEM packed bed models were shown to match the Kozeny-Carman correlation over the range of all Reynolds numbers relevant to solid breeder designs.

This thesis is also the first application of the lattice-Boltzmann method for modeling the conjugate heat transfer of flowing helium and volumetric heating of pebble beds in solid breeders. As a first of its kind study, much attention was paid to the method's ability to faithfully reproduce hydrodynamics in a computationally tractable manner. It was shown that proper selection of lattice spacing and resolution of digital mapping between DEM and LBM lattices are important for LBM simulations of fluid flow and heat transfer. Recommendations from literature suggest 4 nodes per throat are necessary for capturing hydrodynamics of channel flow. It was shown that when a 1 mm pebble is represented by only 10 nodes, nearly 90% of pore sizes were less than 4 nodes/pixels wide. For more reasonable resolutions of 20 and 40 pixels per mm, the violation of 4 node criteria was compared to the error in packed beds due to violating Knudsen criteria for continuum assumptions. The criteria for a gas to act as a continuum is that $\mathrm{Kn} < 10^{-2}$, for slightly greater Kn, modified slip-conditions will exist at solid-fluid interfaces, and at large values of Knudsen number, fluids enter rarefied regimes. It was shown that the mean-free-path of helium from 400 °C to 900 °C results in packed beds violating Knudsen criteria in 22% and 41% of the void space, respectively. Therefore, without a quantifiable method to determine if matching continuum

hydrodynamics is critical when the fluid itself is not matching continuum conditions, and for computational accessibility, resolutions of 20 and 40 pixels per mm were determined to be currently acceptable. It was then shown that beds with a resolution of 20 provided numerically stable solutions and error in velocity profiles for packed beds with a resolution of 20 were acceptable compared to res = 40 beds and that computational times for the former beds were nearly 20 times faster. Ultimately, lattice-Boltzmann simulations applied in this thesis maintained with lattices of 20 nodes per pebble diameter (*i.e.* 20 pixels per mm).

Once the models and modeling approaches were established and validated, they were applied to studying critical issues in solid breeder pebble beds. First, the thermomechanical impact of irradiation damage on ceramic materials was studied. Effective thermal conductivity values were numerically measured for pebble beds with irradiation-induced reductions in solid thermal conductivity. It was shown that effective thermal conductivity reduced linearly at a rate of $k_{\text{eff}}[\text{W m}^{-1}\,\text{K}^{-1}] = 0.545\eta + 0.458$ with $\eta = k_{irr}/k_{unirr}$. Helium purge gas was seen to help maintain thermal transport in packed beds as solid conductivity dropped. The trend was compared with SBZ correlations for effective thermal conductivity, a correlation which is itself a function of solid conductivity, and the numerical results agreed well for all values greater than $\kappa > 1$. The fit to SBZ is another validation of the numeric formulations of heat transfer in CFD-DEM, yet the models developed here can be expanded into predictive spaces well beyond the limited applicability of SBZ correlations.

Next, CFD-DEM models were applied to study representative tritium-breeding ceramic pebble bed volumes with altered packing structures as a result of crushed pebbles, with a specific intent of understanding the presence, or lack thereof, of gap formation between pebble beds and structural materials. The studies were performed with parametric variations of: bed orientation with respect to gravity (χ or ζ configurations), pebble crushing amount (η), initial packing fraction (ϕ), and crushed fragmentation size (r^*). One one general trend was observed that reiterates past conclusions from solid breeder research. Namely, more persistent behavior is witnessed in pebble beds with higher initial packing fractions. Total mean temperatures of $\phi_1 = 0.62$ beds increased between 16 to 19% at $\eta = 5\%$. Yet beds initially packed to $\phi_2 = 0.64$ increased by only 10 to 13% at the same value of crushed

pebble amount. We therefore conclude that manual densification, from either long-term vibration packing or load-induced pre-compaction, should be performed on ceramic pebble bed volumes to gain some temperature control during operation in a fusion reactor. To achieve packing fractions of 64% in the relatively small sizes of this study, for example, a load of over 1 MPa was necessary. In the assembly of tritium breeding modules, it must be kept in mind that similar pre-compaction may need to be performed.

One purpose of the study was to identify the effects of breeder orientation on heat transfer after pebble fragmentation. In configurations where heat transfer out of the pebble bed is in parallel directions with gravity (ζ-configuration), concerns have always focused on development of gap formation between pebble bed and upper walls. Over all the crush percentages studied here, up to 5% total crushed pebbles, no gaps were detected at the upper wall. In fact, this configuration of breeder bed demonstrated the lowest maximum temperatures for beds with many crushed pebbles. We showed that freedom of fragments to travel between zones in these beds prevented a build-up of loose fragments (and thereby avoided build-up of heating) in the hottest regions. By comparison, beds with heat removal directions perpendicular to gravity (χ-configuration) as η went above 3%, maximum temperature rise jumped well-above the ζ-configurations. We showed that for these beds it was the inability for fragments to move between zones which left many small fragments to settle in the hottest region, further contributing to heating.

Lastly, using lattice-Boltzmann method simulations of helium flow through pebble beds, we looked into pore-scale influences of crushing on void fraction distribution and consequently velocity fields of pebble beds. We found that when 5% of pebbles are fragmented, tortuosity of the pebble bed increased by nearly 7% while the effective dispersive thermal conductivity increased over 23%. In spite of the increase in dispersive conductivity, the impact on temperature profile spreading remained negligibly small due to the low Peclet number flow, as expected in tritium breeding blankets. LBM models confirmed that packed beds with low-Peclet flows were, in fact, well characterized by the considerably less computationally draining volume-averaging techniques of CFD-DEM, as measured by comparison of temperature profiles between LBM-DEM and CFD-DEM. Therefore, CFD-DEM coupling

is the preferred method for packed beds with low Reynolds flow.

In the course of model application, the issue of natural convection arose for configurations which develop an adverse temperature gradient, such as in the EU HCPB. A short investigation into natural convection in porous material was carried out and is given in Appendix F. The conclusion of the investigation was that the narrowness of the solid breeder volume prevents buoyant and momentum terms from ever overcoming viscous and thermal forces in helium. Natural convection simply has no space to develop convective cells in spite of the extremely large temperature gradient (*e.g.* 500 K per cm).

7.2 Closing Remarks & Recommendation for Future Work

There were two main sources of inspiration for the microscale methodology chosen for thermal, thermofluid, and fragmentation modeling in this thesis. The first came from results of post-irradiation experiments and crush load measurements of early Li_4SiO_4 pebbles. Indications were that the brittleness of the pebbles may not allow them to survive the harsh environment of fusion reactors without significant fragmentation. There was uncertainty on both the effects of fragmentation and the extent to which it should be expected in solid breeders. The second inspiration was the specter of gap formation between pebble beds and the containing structure that has haunted solid breeder researchers from the beginning. The fear was that if pebble bed settling (*i.e.* densification of the packing structure) were to cause separation between bed and wall, heat transport out of the breeding zone could be disastrously reduced. Both questions were addressed with the numerical models developed in this thesis and thorough analyses of representative volumes were performed.

However, over the time of this thesis progression, fusion researchers have developed processes which yield stronger pebbles – crush loads an order of magnitude larger than the early Li_4SiO_4 pebbles – and our DEM models have suggested contact forces on these stronger pebbles will be low enough to avoid fragmentation initiation. Even so, this advantage has not come without a price. Our recent pebble bed experiments at fusion-relevant temperatures (>750 °C) and pressures (>2 MPa) have shown that pebbles, although not fragmenting, are

displaying the effects of contact creep and forming sintered clumps. Creep/contact sintering is the next major phenomena that must be considered in predictive models of temperature distributions in pebble beds. Fortunately, the modular approach of DEM modeling, as implemented in this thesis, allows all previous fragmentation modules to be implemented entirely in tandem with future models describing the cohesive nature of contact creep.

In regards to studies on gap formation, we must review what it means to form a 'gap' between a pebble bed and its containing structure. For even in a well-packed (random-packed) bed of spheres, void fraction (volume fraction of fluid in a porous media) is essentially $\epsilon = 1$ at the wall, dropping to a minimum of approximately $\epsilon = 0.2$ at a distance of one pebble radius. Solid-solid contact with a pebble bed and its container occurs only in extremely small contact areas between the first layer of well-ordered pebbles in the ensemble. Therefore, what does it mean to have a 'gap' between two material interfaces for which fluid volume is already filling 100% of the space in the near-contact region? Moreover, as has been discussed in this thesis, we have experimentally observed that effective conductivity of a granular medium in vacuum is around $0.2\,\mathrm{W\,m^{-1}\,K^{-1}}$. When we add a fluid, with thermal conductivity of only around $0.3\,\mathrm{W\,m^{-1}\,K^{-1}}$, the overall effective conductivity is not simply the superposition of the two values, but instead the effective conductivity of the two phase medium increases to nearly $1\,\mathrm{W\,m^{-1}\,K^{-1}}$! Thus, even in the ideal condition of a pebble bed, the task of heat transfer from pebble to wall is facilitated in large part by helium. Gap formation, or, local increases to the void fraction of helium, is simply a repartitioning of single modes of a multi-mode heat transfer phenomena occurring at bed/structure interfaces. To conclude on the topic, future work must not separate the issue of mechanical relief at interfaces without also considering in detail the synergistic effects of helium alongside pebbles and structure.

Up to this point, pebble bed modeling has been focused on prediction and potential avoidance of negative consequences to pebble bed heat transfer during operation. These efforts are unquestionably important, but they miss the fact that a pebble bed with effective thermal conductivity of, at best, around $1\,\mathrm{W\,m^{-1}\,K^{-1}}$ will never be able to handle heat loads of DEMO reactors without substantial impact on tritium breeding capabilities due to increased structure volume. Based on the level of sophistication of the models presented

in this thesis, their future application should move beyond consideration of current-bed technologies and toward studying methods for increasing heat transfer capabilities of solid breeders.

For example, pebble beds of mixed breeder/multiplier, such as Japanese-proposed titanium beryllides (*e.g.* $Be_{12}Ti$), have received attention from the point of view of chemical stability, higher operating temperature, better oxidation, and acceptable swelling. Mixed volumes of both neutron multiplier and tritium breeder may have high tritium breeding ratios with acceptable tritium inventory of the beryllides. Moreover, the dense packing available from potentially large differences of pebble radii in conjunction with high solid conductivity of beryllides can have advantageous impacts on heat transfer in pebble beds. DEM/CFD-DEM models can play a leading role in the exploration of thermomechanical performance of mixed breeder/multiplier volumes, and any issues associated with them such as contact forces, contact conductance, and possible segregation of material after many thermal cycles, before experimental campaigns are launched.

Another potential for increased heat transfer in pebble beds springs from the DEM-LBM study on the serpentine helium purge flow. Large packing fractions are generally avoided in solid breeder blankets in order to prevent their concomitant increase in pressure drop. However, the investigation performed with heat transfer in lattice-Boltzmann simulations suggests it is worth revisiting the topic from the point of view of energy management and the ability for packed beds to sustain larger power densities. We observed that transverse thermal dispersion was negligible at low Peclet numbers and with mono-sized pebble packings in the LBM-based study. Increasing flow velocity will increase Peclet number and pressure drop, though at different rates. On the one hand, pressure drop is linearly proportional to u_f until about Re = 100. As an example, the Korean TBM design has a particle Re ≈ 1. This could allow a hundred-fold increase in velocity with only a linearly similar increase in pressure drop. On the other hand, Kuwahara *et al.* fit a correlation for k_{disp} to be proportional to $\text{Pe}^{1.4}$, and thus $u_f^{1.4}$ and $\epsilon^{-1.4}$. As a consequence, dispersive conductivity increases at a much more rapid rate than pressure drop and heat transfer enhancements due to dispersive conductivity may overwhelm the negative effects of increased pressure drop.

Therefore, there is potential to study packed beds with high packing fraction and increased Reynolds number to ascertain the benefits of higher dispersion on overall effective thermal conductivity.

The suggestions for future work provided in this section are based on observations I've made over the course of this thesis development and my current understanding of the complicated modes of heat transfer in lithium ceramic pebble beds. But it is also my sincere hope that the tools developed for this thesis will find their way into the hands of future researchers. And that they use the tools to come at fusion problems with fresh eyes and fresh ideas to forge paths into new and fruitful veins of research. For, as the great Bob Dylan says "strike another match, go start anew. And it's all over now, Baby Blue."

APPENDIX A

Solution of Steady State Energy Equation for One Dimensional Slab with Heat Generation

Before considering the heat equation in a sphere, it is instructive to first consider the simpler problem of a one-dimensional slab with volumetric heat generation, q'''_g and convective cooling at the surfaces.

Assuming we can find the Nusselt number for the convective cooling, we write the heat flux from the surface to the fluid as

$$q''_s = h(T_s - T_f) \tag{A.1}$$

where T_f is the bulk fluid temperature and T_s is the surface temperature. At steady-state the amount of heat moved across the fluid-surface interface must necessarily be equal to the total amount of heat generated into the slab. Therefore,

$$q''_w = q'''_g L = h(T_f - T_s) \tag{A.2}$$

where L is the half-width of the slab. For the sake of discussion, we re-write the above in terms of the temperature delta from surface to fluid in terms of nuclear heating,

$$T_f - T_s = \frac{q'''_g L}{h} \tag{A.3}$$

Inside the slab, at steady-state the energy equation is simply a balance of heat conduction and nuclear generation.

$$0 = k\frac{\mathrm{d}^2T}{\mathrm{d}x^2} + q'''_g \tag{A.4}$$

The boundary conditions are symmetry about the centerline and known surface temperature

$$q_{L=0} = 0 \tag{A.5a}$$

$$T(L) = T_s \tag{A.5b}$$

The ODE of Eq.A.4 is solved with simple separation and integration. When the boundary conditions are applied we have

$$T(x) = \frac{q'''_g L^2}{2k}\left(1 - \frac{x^2}{L^2}\right) + T_s \tag{A.6}$$

We can find the temperature at the centerline of the slab, $x = 0$ as

$$T_{cl} = \frac{q'''_g L^2}{2k} + T_s \tag{A.7}$$

Or,

$$T_{cl} - T_s = \frac{q'''_g L^2}{2k} \tag{A.8}$$

From Eqs. A.3 and A.8, we see that the temperature differences between the surface and the fluid or the centerline and the surface are dictated by the heat generation rate relative to the speed at which that heat can be transported, *via* convection or conduction, respectively.

We will divide Equation (A.8) by Equation (A.3),

$$\frac{T_{cl} - T_s}{T_f - T_s} = \frac{1}{2}\frac{hL}{k} \tag{A.9}$$

Careful observation of this equation can tell us much about the relative importance of the different modes of heat transfer to/from the surface. If the thermal transport away

from the surface occurs at a much slower pace than thermal transport of energy through the solid to the surface, then the change in temperature across the solid $T_{cl} - T_s$ will be small compared to the change in temperature from the interface of solid to the bulkd fluid temperature, $T_s - T_f$. If the temperature across the solid is negligibly small in comparison to the surface-fluid difference, we are safe in the assumption that the solid is isothermal.

The group of terms on the right-hand-side of Equation (A.9) is recognized as the Biot number,

$$\text{Bi} = \frac{hL}{k} = \frac{R_{cond}}{R_{conv}} \tag{A.10}$$

whose value is used to quantify the importance of internal conduction in the analysis of the solid interacting with convective heat transfer. If Bi $<<$ 1, it is safely assumed that there is no temperature gradient in the solid material. A conclusion that will prove helpful in later analysis.

It is interesting to note that in this derivation of Biot number, we had considered nuclear heating as the source for temperature gradients across the pebble yet the rate of nuclear heating still does not appear in the Biot number. This implies that traditional assumptions of the validity of the lumped capacitance method hold even when dealing with a heat generation term in our energy balance.

APPENDIX B

Hertzian Contact

In § 3.1.1, we will lay out the contact interaction mechanics implemented in the discrete element method which include normal and tangential forces and damping. While all the mechanics are important for the fidelity and stability of the DEM simulation, we will focus here purely on the normal elastic contact of two interacting bodies, the analysis which was first performed by Heinrich Hertz in 1882. The results of the so-called Hertzian contact law is vital to many other sections of this work so it is instructive to have the analysis laid out.

We consider two non-conforming solids approaching and then contacting under load. Picture a line connecting the center points of the two bodies and an $x - y$ plane existing at the midpoint between the bodies and oriented normal to their connecting line. On that surface, there is a radius, r extending from the connecting line that is related to the $x - y$ coordinates as $r^2 = x^2 + y^2$.

Because we are restricting ourselves to two spheres, the surface of curvature of the two bodies may be written as

$$z_1 = \frac{1}{2R_1} r^2 \tag{B.1a}$$

$$z_2 = \frac{1}{2R_2} r^2 \tag{B.1b}$$

respectively. As the two bodies approach, just before the surfaces are in contact, points on the two surfaces are separated by a distance $h(r)$,

$$h = z_1 - z_2$$
$$h = \left(\frac{1}{R_1} + \frac{1}{R_2}\right)\frac{r^2}{2} \tag{B.2}$$

Noticing this term in the separation, we define the relative radius of curvature as

$$\frac{1}{R^*} = \frac{1}{R_1} + \frac{1}{R_2} \tag{B.3}$$

and then the separation is simply $h = (1/2R^*)r^2$.

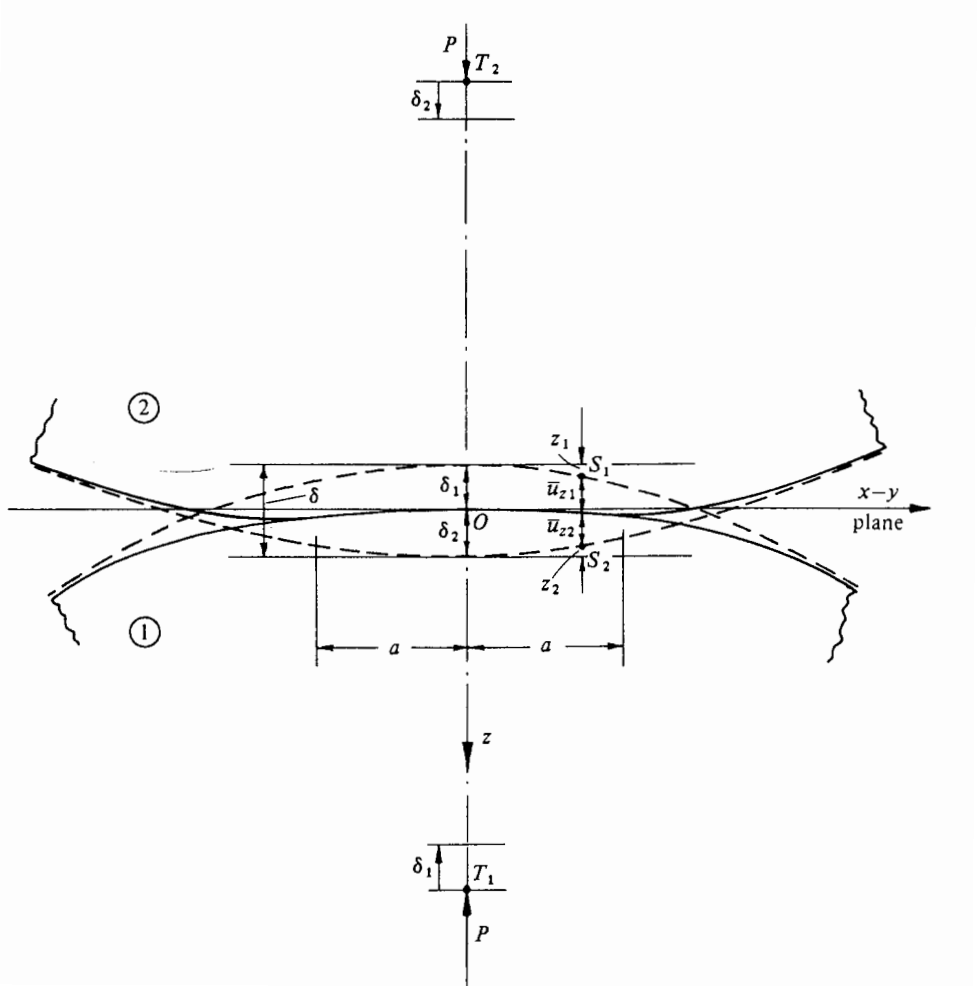

Figure B.1: Geometry of interacting bodies in Hertzian formulation

The two bodies continue their approach towards each other until finally, under an external load F, come into contact. The cross-section of these bodies after contact are shown in

Figure B.1. If we first imagine that the two surfaces do not interact and their surfaces pass through each other unimpeded, their surfaces would be overlapped to a distance δ. In such a case, we examine two points deep within the bodies, along the axis of contact, calling them T_1 and T_2. These points will have moved δ_1 and δ_2, respectively. The total overlap is obviously related to these displacements by $\delta = \delta_1 + \delta_2$.

However, under actual interaction, the two surfaces are going to deform as the load F presses them into contact. So now we consider two points on the surfaces, such as S_1 and S_2. Before contact, these two points are initially are separated by a distance h (from Equation (B.2)), then displace by $\bar{u}_{z1}$ and $\bar{u}_{z2}$ due to contact pressure.

If the points S_1 and S_2 are inside of the contact region under load, these distances are related by

$$\bar{u}_{z1} + \bar{u}_{z2} + h = \delta \tag{B.4}$$

Then using Equation (B.2), we have an expression for the elastic displacements as

$$\bar{u}_{z1} + \bar{u}_{z2} = \delta - \frac{1}{2R^*} r^2 \tag{B.5}$$

Alternatively, if after deformation the points S_1 and S_2 are outside of the contact region, this is simply

$$\bar{u}_{z1} + \bar{u}_{z2} > \delta - \frac{1}{2R^*} r^2 \tag{B.6}$$

It now is necessary to find a pressure distribution that satisfies these boundary conditions of displacement. Hertz's great contribution was to simplify the solution of expressions Eqs. B.5 and B.6 by regarding each body as an elastic half-space upon which the load is applied over a small, elliptical region (the contact area). This simplification allows for treatment of the highly concentrated stresses near the region of contact without consideration of either the general response of stresses in the bulk of the body or the manner in which they are supporting the load. This assumption is justifiable if the dimensions of each body as

well as the relative radii of curvature are very large compared to the contact area. These assumptions are sufficient to proceed with the analysis, but the curious are pointed to an excellent discussion and background of Hertz's theory as given in KE Johnson's textbook.[105]

For solids of revolution, a distribution of pressure to satisfy the displacements of Equation (B.6) is proposed by Hertz as

$$p = p_0 \left[1 - \left(\frac{r}{a}\right)^2\right]^{1/2} \tag{B.7}$$

where a is the radius of the contact area.

The total load, F is found from the pressure distribution as

$$\begin{aligned} F &= \int_0^a p(r) 2\pi r \, \mathrm{d}r \\ F &= \frac{2}{3} p_0 \pi a^2 \end{aligned} \tag{B.8}$$

From the distributed load over the circular region, stresses and deflections are found from superposition of point loads. The pressure is integrated (see Ref.[105]) to find the normal displacement for either solid body as

$$\bar{u}_z = \frac{1-\nu^2}{E} \frac{\pi p_0}{4a} \left(2a^2 - r^2\right) \tag{B.9}$$

This is applied to both bodies and plugged into Equation (B.5) to yield

$$\frac{\pi p_0}{4aE^*} \left(2a^2 - r^2\right) = \delta - \left(\frac{1}{2R^*}\right) r^2 \tag{B.10}$$

where we have introduced the now-common term of pair elastic modulus,

$$\frac{1}{E^*} = \frac{1-\nu_1^2}{E_1} + \frac{1-\nu_2^2}{E_2} \tag{B.11}$$

for simplification.

With the solution of Equation (B.10), if we consider $r = a$ and $\delta(a) = 0$, we find the radius of the contact circle is

$$a = \frac{\pi p_0 R^*}{2E^*} \tag{B.12}$$

and when $r = 0$, we find the overlap as

$$\delta = \frac{\pi a p_0}{2E^*} \tag{B.13}$$

and alternatively we find the pressure as a function of overlap

$$p_0 = \frac{2E^*\delta}{\pi a} \tag{B.14}$$

The radius, overlap, and pressure relations are inserted into Equation (B.8) to find the force (from now on referred to as the Hertz force) as a function of overlap, relative radius, and pair elastic modulus,

$$F = \frac{4}{3} E^* \sqrt{R^*}\, \delta^{3/2} \tag{B.15}$$

as a last step, to differentiate the force from other terms to be derived later, we specify it as the normal force between sphere i and sphere j as

$$F_{n,ij} = \frac{4}{3} E^*_{ij} \sqrt{R^*_{ij}}\, \delta^{3/2}_{n,ij} \tag{B.16}$$

Equation B.16 defines the normal contact forces between any two contacting, elastic spheres. This extremely important result acts as the basis of all discrete element method codes since the concept was first introduced for granular materials by Cundall & Strack in 1979.[42]

It is very appealing to use the Hertz force in a numerical model such as DEM because there are very few assumptions built in to the theory; the material must be elastic and satisfy

$$\frac{a}{R^*} \ll 1 \tag{B.17}$$

In which case the force of Equation (B.16) is calculated from material and geometric properties alone and no phenomenological, empirical fits are necessary.

APPENDIX C

Calculating Critical Strain Energy

It is impractical, if not impossible, to experimentally measure accurate contact forces between all the pebbles in a densely-packed, three-dimensional ensemble. In investigating the probability of pebbles becoming damaged (*i.e.* crushed or cracked) in a packed bed, we therefore rely on the combined information gained from indirect measurements of the entire pebble bed, crush experiments of individual pebbles, and the predictive capabilities of DEM simulations. With the rise of micro-mechanical tools and computing power, attempting to predict when ceramic pebbles will crush in an ensemble, based on inter-particle contact forces, has received considerable attention.[126,143] Research on pebble damage has also been taken up by others in the fusion community to predict the onset of pebble crushing as a function of an external pressure and the resulting changes to mechanical properties such as the stress-strain of the pebble bed.[12,211,212]

Statistical probability arguments were applied to the study of packed beds of brittle grains by Marketos and Bolton.[126] The fundamental assumption in their predictive method was the independence of crushing events. They used their model to predict the initiation of crushing as well as the evolution of the packing after crushing. They created somewhat arbitrary probability distributions of the strength of their granular particles,

$$h(\Phi) = \frac{0.0395}{\sqrt{\Phi}} \tag{C.1}$$

where Φ is a characteristic strength parameter falling between 160 and 640 N. The form of their distribution was based on single crushing tests on quartz particles from Nakata *et al.*.

A common alternative distribution is to use a form first proposed by Weibull for a material

under uniform stress.[114,131,143,212,213] The form, as written by Zhao *et al.* is,

$$P_s = 1 - \exp\left[-\left(\frac{W_c}{W_{\text{mat}}}\right)^m\right] \tag{C.2}$$

where W_c is the energy absorbed by the pebble and W_{mat} and m characterize the material. An important note is how to calculate the critical strain energy for the pebble. Refs.[126] and[213] note the necessity to consider the coordination number dependence on total strain energy. In other words, the total strain energy is the cumulative total of strain energy at every contact. Zhao *et al.* give the critical strain as

$$W_c = \sum_{i=1}^{Z} \left(\frac{9}{80R_{ij}^*}\right)^{1/3} \left(\frac{1}{E_{ij}^*}\right)^{2/3} F_{n,ij}^{5/3} \tag{C.3}$$

where Z is the coordination number of pebble i.

However, Russell *et al.*, analyzed simple, ideal granular assemblies for which they could find analytical solutions to stress distributions inside of pebbles.[160] In their work, failure of a granular particle initiates at the location of maximum stress invariant ratios. In the contact of elastic spheres, the stress fields near the contact areas are highly localized. Because of the highly localized effects, Russell *et al.* find that in granular assemblies the contributions to failure initiation are not additive. They discovered that the initiation of failure is always located adjacent to the largest force irrespective of the material properties or geometric size of the pebbles in an ensemble. Russell *et al.* conclude: *the largest contact force acting upon a particle is the primary agent driving the damage of the individual.*[160] Based upon the failure criterion developed for brittle materials, crushing of an individual does not directly depend upon the presence or magnitude of any lesser contact forces acting on the particle. Although their results were obtained for idealized assemblies, the results are generally true for any situation where multiple contact forces are present.

Based on the compelling arguments of Russell *et al.*, we define a pebble in an ensemble to crush *when a single contact force surpasses a defined critical value for that pebble.* The definition of the critical force is an empirical value derived from experiments on single pebbles. Because the normal force between two elastic objects is a function of the material properties of the interacting objects (see, *e.g.*, Equation (B.16)), we cannot directly compare

the forces between the pebble and test stand with pebble-pebble contacts in an ensemble. An alternative is to integrate the force along displacement, resulting in strain energy of the contact. The strain energy can then relate the contact forces between different material interactions, in a similar manner to Refs.[12,212]

We begin by integrating the Hertzian force along the overlap of contact to find the strain energy W_ϵ, of contact between any two materials,

$$W_\epsilon = \int_0^{\delta_c} F_n(\delta')\,\mathrm{d}\delta' \tag{C.4}$$

where the upper limit of the integration is the critical overlap δ_c. Inserting the Hertzian relation of Equation (B.16) into Equation (C.4) gives,

$$W_\epsilon = \int_0^{\delta_c} \frac{4}{3} E^* \sqrt{R^*}\,\delta'^{3/2}\,\mathrm{d}\delta' \tag{C.5}$$

$$W_\epsilon = \frac{8}{15} E^* \sqrt{R^*}\,{\delta_c}^{5/2} \tag{C.6}$$

We call the strain energy of the pebble compressed between platens as the lab strain energy, $W_{\epsilon,L}$. In pebble crushing experiments, we record the strain energy absorbed up to the point of crushing, the data for Li_4SiO_4 and Li_2TiO_3 pebbles are shown in Figure C.1 and Figure C.2, respectively. The strain energy of two particles in contact will be the bed strain energy, $W_{\epsilon,B}$. The assumption is made that, if each contact interaction computed in DEM simulations is integrated to the proper critical overlap, the strain energies will be equal at that contact. Thus lab strain energy is equated to bed strain energy to find the critical ensemble overlap value, $\delta_{c,B}$, in terms of experimental values,

$$W_{\epsilon,L} = W_{\epsilon,B} = \frac{8}{15} E_B^* \sqrt{R_B^*}\,{\delta_{c,B}}^{5/2} \tag{C.7}$$

the critical pebble bed overlap is therefore,

$$\delta_{c,B} = \left[\frac{15 W_{\epsilon,L}}{8 E_B^* \sqrt{R_B^*}}\right]^{2/5} \tag{C.8}$$

This overlap can be reinserted to the Hertz force of Equation (B.16) to find the critical force (crush force) of the interacting particles in the numeric ensemble as a function of the

critical strain energy of the lab. Doing this, we find,

$$F_{c,B} = C E_B^{*\,2/5} R_B^{*\,1/5} W_{\epsilon,L}^{3/5} \tag{C.9}$$

where $C = \frac{4}{3}\left(\frac{15}{8}\right)^{3/5}$.

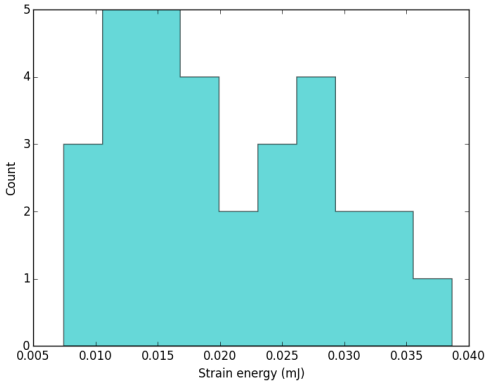

Figure C.1: Histogram of the absorbed strain energy at the moment of crushing for Li_4SiO_4 pebbles as measured in single pebble crush experiments.

Equation (C.9) is a generic translation between lab materials and packed bed materials. We will use the equation as the basis for our pebble crushing prediction in DEM simulations. During the DEM run, we can find the maximum normal force acting on each pebble,

$$F_c = \max F_{n,ij} \tag{C.10}$$

We then define in a straightforward way a pebble crushing event as occurring when the pebble's maximum normal force is greater than the critical bed force defined in Equation (C.9),

$$F_c > F_{c,B} = \frac{4}{3}\left(\frac{15}{8}\right)^{3/5} E_B^{*\,2/5} R_B^{*\,1/5} W_{\epsilon,L}^{3/5} \tag{C.11}$$

Example values of critical crush forces, predicted from Equation (C.11) are given in Figure C.3. From § 3.2, elastic Modulus was seen to vary widely among tested pebbles; for this calculation a range of 10 GPa to 100 GPa is used along with a generic Poisson ratio of 0.24 for finding E^*. A constant pebble radius of $R_p = 0.5$ mm is used. A large variation of measured strain energy was seen between Li_4SiO_4 and Li_2TiO_3; a range of 0.1 µJ to 1 µJ is chosen for this calculation.

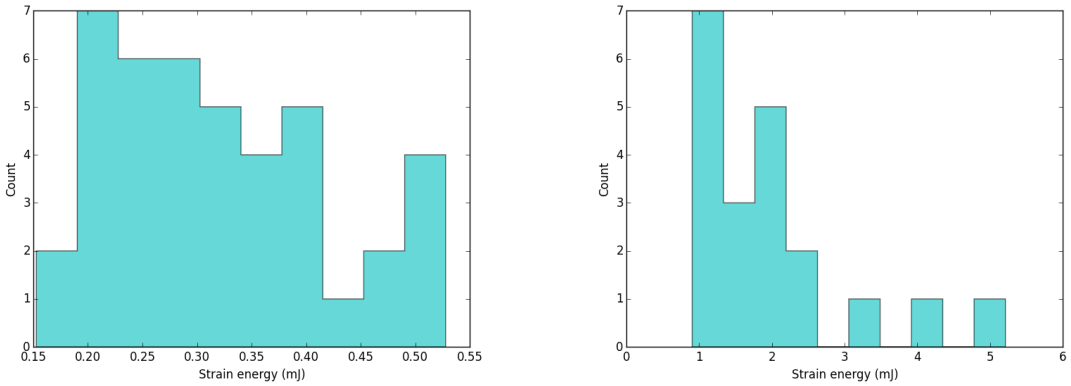

(a) $\bar{d}_p = 1$ mm (b) $\bar{d}_p = 1.5$ mm

Figure C.2: Histogram of the absorbed strain energy at the moment of crushing for Li_2TiO_3 pebbles as measured in single pebble crush experiments.

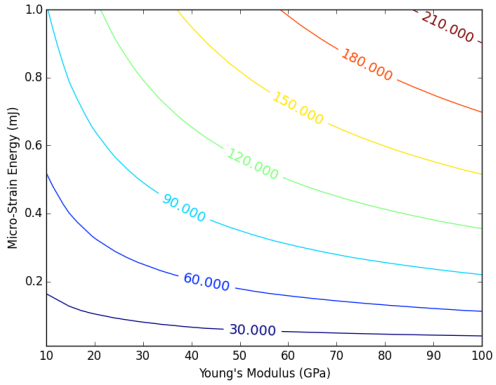

Figure C.3: Contour map of critical crush force values as a function of elastic Modulus and micro strain energy.

For implementation in DEM, the crush force prediction becomes probabilistic naturally due to the distribution of strain energies measured in experiments; therefore imparting a distribution shape to the $F_{c,B}$ prediction. Cumulative distribution functions are generated for the experimental strain energy data for which we fit Weibull distribution curves, of the form

$$\Xi = \lambda \left[-\ln(W_\epsilon) \right]^{1/\sigma} \tag{C.12}$$

where the shape parameter, σ, is fit to the specific curve of each set of experimental data and the second parameter, λ is defined as

$$\lambda = \bar{W}_\epsilon - \min W_\epsilon$$

In Figure C.4 and Figure C.5 we see the experimental data and the Weibull fits specific to the ceramic material and batch. The figures illustrate goodness of Weibull fits. The Weibull distribution functions are recreated numerically in the assignment of each pebbles 'critical bed force' value.

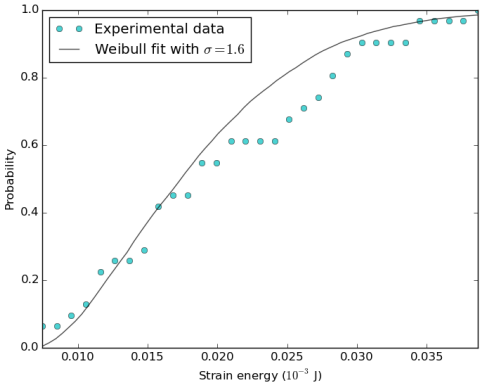

Figure C.4: Cumulative distribution function for strain energy with a Weibull distribution fit with shape parameter specific for the Li_4SiO_4 pebbles. The shape parameters are used in numeric replications.

In this section we have proposed a numerical basis for predicting pebble crushing in a ceramic pebble bed based on translations of strain energy distribution functions of experimental data. Implementation in DEM simulations requires defining an array of strain energies, the distribution of which must satisfy Weibull distributions matching experimental

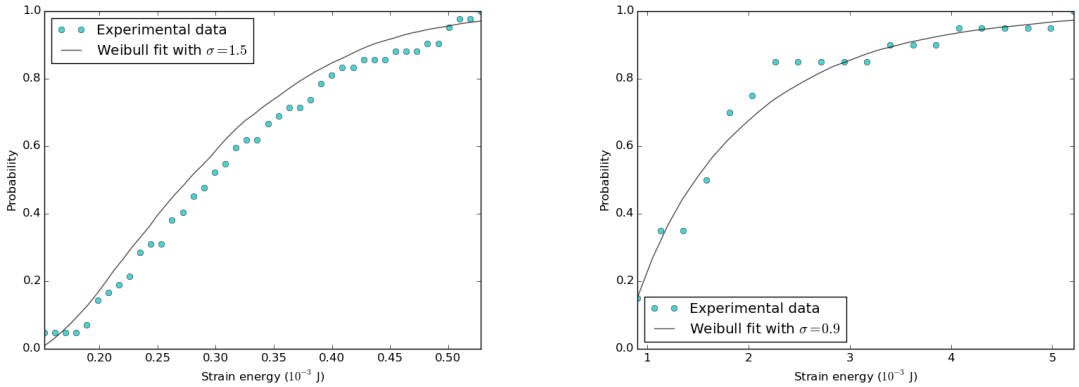

(a) $\bar{d}_p = 1$ mm (b) $\bar{d}_p = 1.5$ mm

Figure C.5: Cumulative distribution function for strain energy with a Weibull distribution fit with shape parameter specific for the two batches of Li_2TiO_3 pebbles. The shape parameters are used in numeric replications.

data for the specific pebble under consideration. The array of strain energies is loaded as a dictionary variable with the DEM pebble identification number as key and strain energy as value. Then we loop through all pebble IDs in the ensemble and check the criteria defined in Equation (C.11). If a pebble's maximum force exceeds the crush criteria, the pebble is flagged for fragmentation. Similar to implementation of thermal expansion, it is possible at every time step to check for broken pebbles. However, the stress on pebbles is due to thermal expansion and is therefore nonsensical to check for broken pebbles more frequently than updating pebble diameters with thermal expansion; therefore the same timestep is used in both of these custom numerical routines.

The equations established here present the framework for implementing crush prediction in DEM models. However, there is currently no experimental data with which to validate or calibrate the model. A parametric study of pebble crushing in uniaxial compression tests could be performed, as has been done by others (See Refs.[12,212]). But without necessary experimental data, the impact of their results is also somewhat lacking.

APPENDIX D

Solution of Transient Energy Equation for Sphere with Heat Generation

We solve for the temperature distribution inside a single sphere of constant thermal conductivity with constant heat generation with a convective heat transfer boundary condition. To simplify to homogeneous boundary conditions, the temperature we solve for will be in reference to the fluid temperature, $\mathbb{T} = T - T_f$.

The energy equation in spherical coordinates with axial symmetry is,

$$\frac{1}{r}\frac{\partial^2}{\partial r^2}(r\mathbb{T}) + \frac{g}{k} = \frac{1}{\alpha}\frac{\partial \mathbb{T}}{\partial t} \tag{D.1}$$

which is subject to the boundary conditions of a constant heat transfer coefficient at the surface, h,

$$\left[\frac{\partial \mathbb{T}}{\partial r} + \frac{h}{k}\mathbb{T}\right]_{r=b} = 0 \tag{D.2}$$

and an axisymmetry at the center,

$$\left[\frac{\partial \mathbb{T}}{\partial r}\right]_{r=0} = 0 \tag{D.3}$$

The sphere will be at an isothermal initial temperature,

$$\mathbb{T}(r, 0) = \mathbb{T}_0 \tag{D.4}$$

D.1 Transformations

We first transform the system into the nondimensional forms as defined in § 4.2,

$$\theta = \frac{\mathbb{T}}{\mathbb{T}_0}$$
$$\rho = \frac{r}{b}$$
$$\tau = \frac{t}{b^2/\alpha}$$

The energy equation is then,

$$\frac{1}{\rho}\frac{\partial^2}{\partial\rho^2}(\rho\theta) + G = \frac{\partial\theta}{\partial\tau} \tag{D.5}$$

where $G = \frac{gb^2}{k\mathbb{T}_0}$

The next transformation will be to introduce $U(\rho,\tau) = \rho\theta(\rho,\tau)$ as a transformation variable to simplify the differential equation of energy conservation. In the new variable formulation, the energy equation is,

$$\frac{\partial^2 U}{\partial\rho^2} + G\rho = \frac{\partial U}{\partial\tau} \tag{D.6}$$

The boundary conditions are likewise transformed into,

$$\left[\frac{\partial U}{\partial\rho} + (\mathrm{Bi} - 1)\,U\right]_{\rho=1} = 0 \tag{D.7}$$

and

$$U\big|_{\rho=0} = 0 \tag{D.8}$$

with initial condition

$$U(\rho,0) = U_0 = \theta_0 r^* = r^* \tag{D.9}$$

D.2 Solution approach

Because of the non-homegeneous form of the energy equation (due to the heat generation term), we will solve Equation (D.6) by breaking it up into two simpler problems,

1. A non-homogeneous, steady-state problem defined by $U_{ss}(r)$
2. A homogeneous, time-dependent problem defined by $U_h(r,t)$

The steady-state distribution U_{ss} is found from the solution of

$$\frac{\partial^2 U_{ss}}{\partial \rho^2} + G\rho = 0 \tag{D.10}$$

subject to the same boundary condition given by Eqs. D.7,D.8. Separation and integration gives.

$$U_{ss} = -\frac{G}{6}\rho^3 + C_1\rho + C_2 \tag{D.11}$$

Applying Equation (D.8) directly gives $C_2 = 0$ and, with some algebra Equation (D.7) gives,

$$C_1 = \left(\frac{G}{6} + \frac{G}{3\mathrm{Bi}}\right)$$

valid for $\mathrm{Bi} > 0$. Thus the steady-state distribution of our transformed variable is

$$U_{ss} = \left(\frac{G}{6} + \frac{G}{3\mathrm{Bi}} - \rho^2\right)\rho \tag{D.12}$$

The next step is to find the homogeneous solution of

$$\frac{\partial^2 U_h}{\partial \rho^2} = \frac{\partial U_h}{\partial \tau} \tag{D.13}$$

Again, subject to Eqs. D.7,D.8, but now with a modified initial condition of

$$
\begin{aligned}
U_{h,0} &= U_0 - U_{ss} \\
&= \left[1 - \left(\frac{G}{6} + \frac{G}{3\mathrm{Bi}} - \rho^2\right)\right] \rho
\end{aligned} \tag{D.14}
$$

This is a standard homogeneous partial differential equation. The solution is of the form

$$
U_h = R(\rho)\Gamma(\tau) \tag{D.15}
$$

The solution for Γ is given as

$$
\Gamma = \exp(-\zeta^2 \tau) \tag{D.16}
$$

The space-variable function $R(\zeta, \rho)$ satisfies the following eigenvalue problem:

$$
\frac{\mathrm{d}^2 R}{\mathrm{d}\rho^2} + \zeta^2 R = 0 \tag{D.17}
$$

subject to

$$
R_{\rho=0} = 0 \tag{D.18}
$$

and

$$
\left[\frac{\mathrm{d}R}{\mathrm{d}\rho} + (\mathrm{Bi} - 1)R\right]_{\rho=1} = 0 \tag{D.19}
$$

This eigenvalue problem is a special case of the Sturm-Liouville problem. The solution for U_h can be constructed from known eigenvalue solutions,

$$
U_h(\rho, \tau) = \sum_{n=1}^{\infty} c_n R(\zeta_n, \rho) \exp(-\zeta^2 \tau) \tag{D.20}
$$

Application of the initial condition gives,

$$F(\rho) = \sum_{n=1}^{\infty} c_n R(\zeta_n, \rho) \tag{D.21}$$

where $F(\rho)$ is the initial condition defined from Eq D.9,

$$F(\rho) = \left[1 - \frac{G}{6}\left(1 + \frac{2}{\mathrm{Bi}} - \rho^2\right)\right]\rho \tag{D.22}$$

The coefficients of c_n can be determined by applying the operator $\int_0^1 R(\zeta_n, \rho)\,\mathrm{d}\rho$ and utilizing the orthogonality property of eigenfunctions. The coefficients are found in the form

$$c_n = \frac{1}{N(\zeta_n)} \int_0^1 R(\zeta_n, \rho') F(\rho')\,\mathrm{d}\rho' \tag{D.23}$$

The norm, N is a function of the eigenvalues,

$$N(\zeta_n) = \int_0^1 \left[R(\zeta_n, \rho)\right]^2\,\mathrm{d}\rho \tag{D.24}$$

The eigenfunctions for Equation (D.17) are

$$R(\zeta_n, \rho) = \sin(\zeta_n \rho) \tag{D.25}$$

where the eigenvalues are the root of the following transcendental equation,

$$\zeta_n \cot(\zeta_n) = -H \tag{D.26}$$

the roots of which will be found numerically. The normalization integral is then solved as

$$\frac{1}{N(\zeta_n)} = 2\frac{\zeta_n^2 + H^2}{\zeta_n^2 + H^2 + H} \tag{D.27}$$

where $H = (\mathrm{Bi} - 1)$.

We substitute the coefficients of Equation (D.23), they can be substituted back into Equation (D.20) and we have a solution for the homogeneous, transient distribution,

$$U_h(\rho,\tau) = \sum_{n=1}^{\infty} \exp(-\zeta^2\tau)\frac{R(\zeta_n,\rho)}{N(\zeta_n)}\int_0^1 R(\zeta_n,\rho')F(\rho')\,\mathrm{d}\rho' \tag{D.28}$$

In order to explicitly express the solution, we will first set the integral equal to a function $Z(\zeta_n)$ and evaluate as,

$$\begin{aligned} Z(\zeta_n) &= \int_0^1 R(\zeta_n,\rho')F(\rho')\,\mathrm{d}\rho' \\ &= \int_0^1 \sin(\zeta_n\rho')\left[1-\left(\frac{G}{6}+\frac{G}{3\mathrm{Bi}}-\rho'^2\right)\right]\rho'\,\mathrm{d}\rho' \\ &= \left[1-\left(\frac{G}{6}+\frac{G}{3\mathrm{Bi}}\right)\right]\int_0^1 \sin(\zeta_n\rho')\rho'\,\mathrm{d}\rho' + \frac{G}{6}\int_0^1 \sin(\zeta_n\rho')\rho'^3\,\mathrm{d}\rho' \end{aligned} \tag{D.29}$$

The two unique integrals are evaluated as

$$\begin{aligned} C_n &= \int_0^1 \sin(\zeta_n\rho')\rho'\,\mathrm{d}\rho' = \frac{\sin\zeta_n - \zeta_n\cos\zeta_n}{\zeta_n^2} \\ K_n &= \int_0^1 \sin(\zeta_n\rho')\rho'^3\,\mathrm{d}\rho' = \frac{3(\zeta_n^2-2)\sin\zeta_n - \zeta_n(\zeta_n^2-6)\cos\zeta_n}{\zeta_n^4} \end{aligned}$$

Thus our Z function is

$$Z(\zeta_n) = \left[1-\left(\frac{G}{6}+\frac{G}{3\mathrm{Bi}}\right)\right]C_n + \frac{G}{6}K_n \tag{D.30}$$

The homogeneous solution is then written in a compact form as,

$$U_h(\rho,\tau) = \sum_{n=1}^{\infty}\exp(-\zeta^2\tau)\sin(\zeta_n\rho)\frac{Z(\zeta_n)}{N(\zeta_n)} \tag{D.31}$$

The complete solution is then a superposition of Equation (D.12) and Equation (D.31),

$$U(\rho,\tau) = \left(\frac{G}{6}+\frac{G}{3\mathrm{Bi}}-\rho^2\right)\rho + \sum_{n=1}^{\infty}\exp(-\zeta^2\tau)\sin(\zeta_n\rho)\frac{Z(\zeta_n)}{N(\zeta_n)} \tag{D.32}$$

We now transform back to our dimensionless temperature,

$$\theta(\rho,\tau) = \left(\frac{G}{6} + \frac{G}{3\text{Bi}} - \rho^2\right) + \sum_{n=1}^{\infty} \exp(-\zeta^2\tau)\frac{\sin(\zeta_n\rho)}{\rho}\frac{Z(\zeta_n)}{N(\zeta_n)} \tag{D.33}$$

D.3 Energy

We will want to compare the solution of Equation (D.33) to that of a sphere with the lumped capacitance assumption. To facilitate comparison, we look to a measure of the energy of the sphere (with radial dependence removed *via* integration of Equation (D.33)). The energy will be nondimensionalized as,

$$E^*(\tau) = \frac{E(\tau)}{E_0} \tag{D.34}$$

where E_0 is the initial energy of the sphere,

$$E_0 = \rho_r C_r V \mathbb{T}_0 \tag{D.35}$$

Thus the nondimensional energy of the sphere at a given time, τ is

$$\begin{aligned} E^*(\tau) &= \int \frac{\rho_r C_r \mathbb{T}(\rho,\tau)\text{d}V}{\rho_r C_r V \mathbb{T}_0} \\ E^*(\tau) &= \frac{1}{V}\int \theta(\rho,\tau)\,\text{d}V \end{aligned} \tag{D.36}$$

For a circle in spherical coordinates:

$$\text{d}V = r^2\sin(\phi)\text{d}r\text{d}\phi\text{d}\theta \tag{D.37}$$

For our sphere, this becomes:

$$\text{d}V = 4\pi b^3\rho^2\text{d}\rho = 3V\rho^2\text{d}\rho \tag{D.38}$$

The integral for dimensionless energy of our sphere is then,

$$E = 3\int_0^1 \left[\frac{G}{6}\left(1 + \frac{2}{\mathrm{Bi}} - \rho^2\right) + \sum_{n=1}^{\infty} \exp(-\zeta^2\tau)\frac{\sin(\zeta_n\rho)}{\rho}\frac{Z(\zeta_n)}{N(\zeta_n)}\right]\rho^2\,\mathrm{d}\rho \tag{D.39}$$

This ultimately reduces to,

$$E^* = \left(\frac{G}{15} + \frac{G}{3\mathrm{Bi}}\right) + 3\sum_{n=1}^{\infty} \exp(-\zeta^2\tau)\frac{Z(\zeta_n)}{N(\zeta_n)}C_n(\zeta_n) \tag{D.40}$$

APPENDIX E

DEM Time Integration and Stability

The force field defined by Equation (3.1a) is rewritten in terms of the acceleration of the particle. Note that the per-particle subscripts (i, j, etc.) will be temporarily omitted and instead, time-varying quantities will have a subscript to refer to their temporal location t. Equation (3.1a) becomes

$$\mathbf{a}_t = \mathbf{g} + \frac{\mathbf{f}_t}{m} \tag{E.1}$$

The first step in the velocity-Verlet algorithm is to integrate the position of the particle by a full time step based on the current time step's velocity and acceleration. Note that the initial condition of the particle must specify both position and velocity for this step to be evaluated at the start, from then on the velocity is explicitly updated.

$$\mathbf{r}_{t+\Delta t} = \mathbf{r}_t + \mathbf{v}_t \Delta t + \frac{1}{2}\mathbf{a}_t \Delta t^2 \tag{E.2}$$

The particles at new positions interact as a function of their overlaps (see Eqs. 3.4). Acceleration at the full time step is then calculated from the updated forces (of Equation (E.1)). In the last computational step, the velocity at the full time step is found from an average acceleration,

$$\mathbf{v}_{t+\Delta t} = \mathbf{v}_t + \frac{\mathbf{a}_t + \mathbf{a}_{t+\Delta t}}{2}\Delta t \tag{E.3}$$

The velocity-Verlet algorithm is an efficient means of explicitly integrating the kinematic equations for all the particles in the ensemble. The algorithm is stable with a global error of approximately $O(\Delta t^2)$ for displacement.[83] But, as an explicit method, the size of the time step must be carefully chosen to avoid instabilities in the system.

As mentioned when the integration algorithm was introduced in § 3.1.1, the velocity-Verlet algorithm is a computationally efficient, second-order accurate means of updating the kinematics of all the particles in the ensemble.[111] The time step of the integration, however, must often be very small to ensure that it is less than the time taken for a pressure wave to propagate through the particle. The time step is further constrained by the quasistatic assumption used to derive the Hertzian contact force such that inertial and relaxation effects may be neglected.[26] We will also show that, in order to avoid heat energy to propagate further than a single pebble during a single time step, the thermal time step requirement is orders of magnitude larger than the mechanical time step equivalent. And that the overall minimum time step is thus driven by the mechanical stability.

In tandem with the requirement on very small time step, the thermal time-constants in the ceramic breeder zones can be many hundreds of seconds. These two conditions seem to conspire to force an unacceptably large requirement on the number of time steps for a thermal DEM simulation and thus make numerical experiments impractical.

In this section we will analyze the calculation of a critical time step based on the speed of a Rayleigh wave propagating along the surface of a particle. Then, with that knowledge in hand, we will argue for scaling certain physical properties to allow for faster simulations without sacrificing fidelity to the real physics of the problem.

E.1 Critical Dynamic time step

If we wish to choose a time step sufficiently small such that a pressure wave originating from the contact of one particle does not propagate to other neighboring particles during the time step, we must choose a time step smaller than the critical time step defined by Rayleigh wave traveling through the solid.

When a force is applied to the surface of an elastic body, the force propagates along the surface at the wave speed first solved by John William Strutt, 3rd Baron Rayleigh[149] (when he wasn't discovering the scattering phenomenon explaining why the sky is blue or winning the Nobel prize for discovering Argon),

$$u_{\mathrm{Ra}} = K\sqrt{\frac{G}{\rho}} \tag{E.4}$$

where, again, G is the shear modulus and ρ is the density of the elastic material. The K coefficient is a complicated function coming from Rayleigh's solution but can be approximated as[165]

$$K = 0.1631\nu + 0.876605 \tag{E.5}$$

which is valid for realistic values of Poisson's ratio, ν, of elastic materials. From the inverse of the Rayleigh wave frequency, we can directly find a time step for Rayleigh waves on a sphere of radius, R,

$$\delta t_{\mathrm{Ra}} = \frac{\pi R}{u_{\mathrm{Ra}}} \tag{E.6}$$

When we write this for any particle, i in the ensemble (exchanging the shear for elastic modulus),

$$(\delta t_{\mathrm{Ra}})_i = \frac{\pi R_i}{0.1631\nu_i + 0.876605}\sqrt{\frac{2(1+\nu_i)\rho_i}{E_i}} \tag{E.7}$$

We allow for the particles in the system to have varying density, elastic modulus, and size. Therefore the critical time step for the entire system is governed by the minimum value of any particle's Rayleigh time step.

$$\delta t_c = \min_{\forall i}\left[(\delta t_{\mathrm{Ra}})_i\right] \tag{E.8}$$

The ceramic materials identified for breeders have relatively high elastic moduli, on the order of $10 \times 10^{10}\,\mathrm{Pa}$. The smallest radius will be on the order of $10 \times 10^{-4}\,\mathrm{m}$. The ceramic density is approximately on the scale of $10 \times 10^{4}\,\mathrm{kg\,m^{-3}}$. These values lead to a necessary time step of

$$\delta t_c \propto 10 \times 10^{-7}\,\mathrm{s} \tag{E.9}$$

For a simulation that may last several hundreds of seconds of real time, this then requires more than 10×10^9 time steps. If we have 10×10^4 particles in the simulation, each having their position integrated over a billion times, it becomes obvious that computational time is a major issue for our simulations of nuclear heating of ceramic breeder pebbles. If we are able to reduce the critical time step (while perhaps decreasing the simulation time), the simulations will be much more practical for research use.

E.2 Critical Thermal time step

In § 3.1.2, we introduced the dynamics of heat transfer between contacting particles in an ensemble. As we integrate the energy of an individual particle in time, we must also ensure that energy would not propagate through a particle faster than a single time step can capture. In analogy to the critical time step for mechanical stability (e.g. Eq.E.6), we write for particle i,

$$\delta t_{\mathrm{Bi}} = \frac{\rho_i C_i V_i}{H_c} \tag{E.10}$$

where $\rho_i C_i V_i$ represents the inertial resistance to changing the temperature of T_i and the conductance, H_c represents the speed at which energy is delivered to T_i from contact conduction. Then from the definition of H_c we have given for smooth elastic spheres, this is also written as

$$\delta t_{\mathrm{Bi}} = \frac{(4/3)\pi R_i^2 \rho_i C_i}{2k^*} \frac{R_i}{a} \tag{E.11}$$

For the material properties of lithium ceramics, as discussed for mechanical stability, we can expect

$$\frac{(4/3)\pi R_i^2 \rho_i C_i}{2k^*} \approx \frac{(10^{-4})^2 10^4 10^3}{10^0} = 10^{-1}$$

But from the requirements on Hertz theory in appendix B, we have required that $\frac{a}{R_i} \ll 1$. Thus the time step for stability in the energy calculation is utterly negligible compared to the mechanical stability.

Vargas and McCarthy[187] make similar arguments, giving the criteria as,

$$\frac{\mathrm{d}T_i}{T_i - T_j} \ll 1 \tag{E.12}$$

and too note that the time step requirement for thermal calculations are orders of magnitude less restrictive than the analogous restriction of the particle dynamics.

Thus we can be confident that any time step chosen for dynamic stability in the DEM simulation will automatically satisfy the time step for thermal stability.

APPENDIX F

Considering Natural Convection

Consider the simplest case of stagnant fluid in a packed bed, the momentum equation is

$$-\nabla P + \rho \mathbf{g} = 0 \tag{F.1}$$

Taking the curl of the above yields

$$\nabla \rho \times \mathbf{g} = 0 \tag{F.2}$$

In the Boussinesq approximation, density is only a function of temperature, thus we may say

$$\nabla T \times \mathbf{g} = 0 \tag{F.3}$$

Which shows the numerical condition for stability in a fluid is a vertical temperature gradient. In horizontally-configured solid breeder volumes such as the European HCPB design, large adverse temperature gradients exist from breeder zone center-line to the coolant structure above, see the illustration of the EU HCPB in Figure F.1. Therefore it is worth considering whether natural convective cells will arise in the purge helium flow.

Intrapore natural convection may increase effective conductivity of a medium and has therefore received attention in the engineering field since the 1940s. The problem can be considered as a porous medium analog to the Rayleigh-Benard problem and the solution for a simple duct to be shown next follows similar mathematical constructs.

We consider a duct such that the upper boundary is at $z = H$ and lower boundary at $z = 0$, with respective temperatures of T_0 and $T_0 + \Delta T$. The adverse temperature gradient $\Delta T/H$ will give rise to natural convection under certain circumstances. Assuming that the medium in this duct is homogeneous, isotropic, Darcy's law is valid, and the Boussinesq

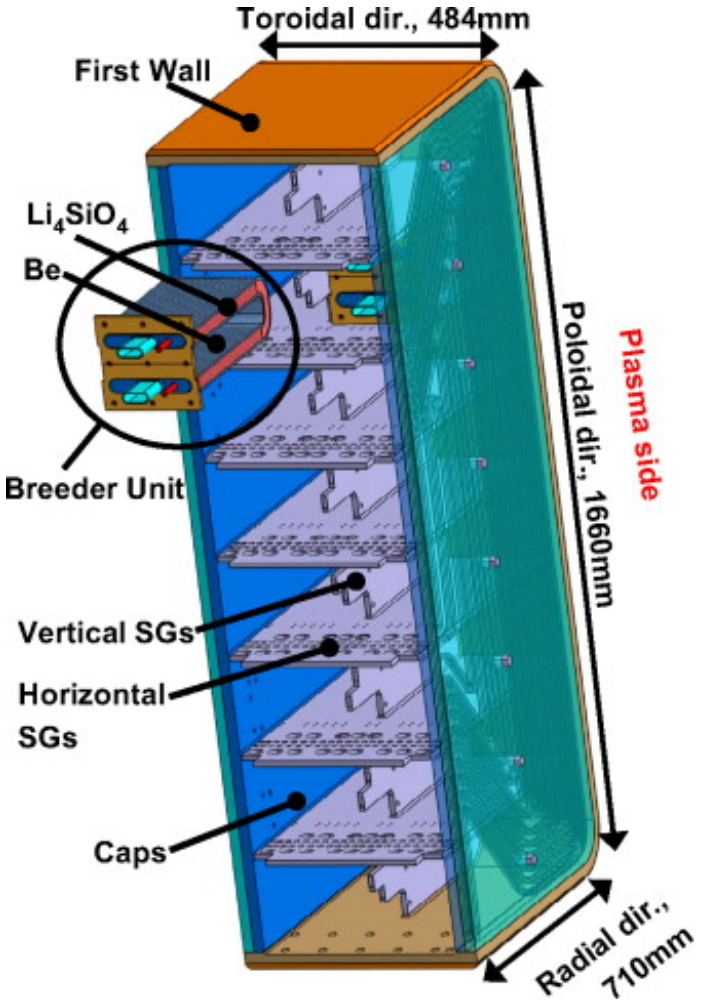

Figure F.1: breeder units in EU design of HCPB feature breeding zones layered horizontally with coolant above and below.

approximation is valid, the governing equations reduce to

$$\nabla \cdot \mathbf{v} = 0 \tag{F.4}$$

$$c_a \rho_0 \frac{\mathrm{d}\mathbf{v}}{\mathrm{d}t} = -\nabla P - \frac{\mu}{K}\mathbf{v} + \rho_f \mathbf{g} \tag{F.5}$$

$$(\rho c)_m \frac{\mathrm{d}T}{\mathrm{d}t} + (\rho c_P)_f \mathbf{v} \cdot \nabla T = k_m \nabla^2 T \tag{F.6}$$

where c_a is an acceleration coefficient, unique to porous media. Its definition is described in more detail in Ref.[133] . Temperature dependence enters density via $\rho_f = \rho_0[1 - \beta(T - T_0)]$. K is the permeability of the packed bed, its calculation will be shown later.

For any variable with subscript as ψ_m, it is calculated as the two-phase average,

$$\psi_m = (1-\epsilon)\psi_s + \epsilon\psi_f \tag{F.7}$$

One solution to Equation (F.4) is the stagnant, pure-conduction condition,[133]

$$\mathbf{v}_b = 0 \tag{F.8}$$

$$T_b = T_0 + \Delta T(1 - \frac{z}{H}) \tag{F.9}$$

$$P_b = P_0 - \rho_0 g\left[z + \frac{1}{2}\beta\Delta T\left(\frac{z^2}{H} - 2z\right)\right] \tag{F.10}$$

Natural convection may be considered an instability in the conduction solution. Therefore we consider the sensitivity of the above to small perturbations. The variables are then

$$\mathbf{v} = \mathbf{v}_b + \mathbf{v}' \tag{F.11}$$

$$T = T_b + T' \tag{F.12}$$

$$P = P_b + P' \tag{F.13}$$

which, when inserted back into the conservation equations and higher order perturbation terms are neglected, yield

$$\nabla \cdot \mathbf{v}' = 0 \tag{F.14}$$

$$a\rho_0 \frac{\mathrm{d}\mathbf{v}'}{\mathrm{d}t} = -\nabla P' - \frac{\mu}{K}\mathbf{v}' - \beta\rho_0 T'\mathbf{g} \tag{F.15}$$

$$(\rho c)_m \frac{\mathrm{d}T'}{\mathrm{d}t} - (\rho c_P)_f \frac{\Delta T}{H} w' = k_m \nabla^2 T' \tag{F.16}$$

We next nondimensionalize Equation (F.14) with the following dimensionless variables,

$$x^* = \frac{x}{H} \tag{F.17}$$

$$t^* = \frac{\alpha_m t}{\sigma H^2} \tag{F.18}$$

$$\mathbf{v}^* = \frac{H\mathbf{v}'}{\alpha_m} \tag{F.19}$$

$$T^* = \frac{T}{\Delta T} \tag{F.20}$$

$$P^* = \frac{KP'}{\mu\alpha_m} \tag{F.21}$$

where σ is a heat capacity ratio,

$$\sigma = \frac{(\rho c)_m}{(\rho c_p)_f} \tag{F.22}$$

With nondimensional parameters, we arrive at the following form of nondimensionalized equations

$$\nabla \cdot \mathbf{v}^* = 0 \tag{F.23}$$

$$\gamma_a \frac{\mathrm{d}\mathbf{v}^*}{\mathrm{d}t} = -\nabla P^* - \mathbf{v}^* + \mathrm{Ra} T^* \mathbf{k} \tag{F.24}$$

$$\frac{\mathrm{d}T^*}{\mathrm{d}t} - w^* = \nabla^2 T^* \tag{F.25}$$

where $\mathbf{k}$ is the unit vector in the z direction. The dimensionless parameters arising in the momentum equation are

$$\mathrm{Ra} = \frac{\rho_0 g \beta K H \Delta T}{\mu \alpha_m} \tag{F.26}$$

$$\gamma_a = \frac{c_a K}{\sigma \mathrm{Pr}_m H^2} \tag{F.27}$$

$$\mathrm{Pr}_m = \frac{\nu_0}{\alpha_m} \tag{F.28}$$

Ra is the Darcian Rayleigh number, differentiated from the standard Rayleigh number by the contribution of permeability, K. Pr_m is the overall Prandtl number of the two-phase medium. And γ_a is a dimensionless acceleration coefficient of the fluid.

From Equation (F.24), we see the strength of the coupling between energy and momentum is dependent on the magnitude of Ra; above a critical value, temperature gradients in the medium will induce motion in the fluid.

Nield & Bejan provide a solution for the set of equations Equations (F.23) to (F.25) assuming the acceleration parameter is negligibly small, $\gamma_a = 0$.[133] The Darcy number, K/H^2 is generally quite small and is, in the case of ceramic breeder beds indeed small, and their assumption is applicable. The homogeneous equations form an eigenvalue system for which the eigenvalue is Ra. Ultimately, a stable and real solution is determinable provided that

$$\mathrm{Ra} = \frac{(j^2\pi^2 + \omega^2)^2}{\omega^2} \tag{F.29}$$

where ω is an overall horizontal wavenumber and $j = 1, 2, 3, \ldots$.[133] The minimum of the above occurs when $j = 1$ and $\omega = \pi$ and thus the critical Rayleigh number is $\mathrm{Ra}_c = 4\pi^2 \approx 39.48$. This result suggests that conduction state remains stable for cases of Darcian Rayleigh number less than $4\pi^2$, *i.e.* $\mathrm{Ra} < 39.48$. For Rayleigh numbers larger than this value, convective cells of cellular motion will appear in the porous media fluid.

Combarnous and Bia experimentally studied buoyancy-induced secondary flows through a porous medium in rectangular duct.[41] They found that in cases of large horizontal to vertical aspect ratios, axial flow did not affect the critical Rayleigh number predicted by linear stability theory. In horizontally-configured solid breeder volumes, aspect ratios are on the order of $A \approx 30$ and thus the critical Rayleigh number defined from perturbation theory, $\mathrm{Ra} < 39.48$, is applicable.

Thus we must finally calculate the Darcian Rayleigh number for a condition such as the European HCPB. Permeability is defined from the relationship to the superficial velocity, viscosity, and pressure drop,

$$\bar{U} = -\frac{K}{\mu}\nabla P \tag{F.30}$$

or

$$K = -\frac{\bar{U}\mu}{\nabla P} \tag{F.31}$$

where the pressure gradient of a spherical-packed bed can be determined from the Cozeny-Karman relation given in Equation (2.48). Therefore, we write

$$K = \bar{U}\mu \frac{d_p^2}{180\bar{U}\mu} \frac{\epsilon^3}{(1-\epsilon)^2} \tag{F.32}$$

which reduces to

$$K = \frac{d_p^2}{180} \frac{\epsilon^3}{(1-\epsilon)^2} \tag{F.33}$$

For a well-packed bed, $\epsilon = 0.36$, of 1 mm pebbles, the permeability is found to be $K = 6.33 \times 10^{-10}\,\mathrm{m}^2$.

Taking a half-width of the EU HCPB of 1 cm with a temperature gradient of 400 K, we may take fluid properties at an average value across the bed to ultimately find that the Darcian Rayleigh number is $\mathrm{Ra} = 1.23 \times 10^{-5}$ which is significantly less than the critical

Rayleigh number, $1.23 \times 10^{-5} \ll 39.5$. We may therefore conclude that under standard operating conditions of ITER-like solid breeder pebble beds natural convection *will not occur*.

We may also consider the situation when there is no porous medium present in the duct. In the condition of pure helium, standard Rayleigh number may be calculated,

$$\mathrm{Ra}_f = \frac{\rho_0 g \beta H \Delta T}{\mu \alpha} \tag{F.34}$$

which, for helium between two constant temperatures separated by 1 cm results in a Rayleigh number of only $\mathrm{Ra}_f = 4.86$. For Rayleigh-Benard convective cells to form, the critical Rayleigh number is around $\mathrm{Ra}_f = 1000$, which is significantly higher than what we have found. Ultimately, the narrowness of the solid breeder volume prevents buoyant forces from ever overcoming viscous forces in the two-phase form of helium and lithium ceramic.

References

[1] M. A. Abdou, N. B. Morley, S. Smolentsev, A. Ying, S. Malang, A. Rowcliffe, and M. Ulrickson. Blanket/first wall challenges and required R&D on the pathway to DEMO. *Fusion Engineering and Design*, 100:2–43, 2015.

[2] M. A. Abdou, L. J. Wittenberg, and C. W. Maynard. A Fusion Design Study of Nonmobile Blankets with Low Lithium and Tritium Inventories. *Nuclear Technology*, 1975.

[3] A. Abou-Sena, A. Ying, and M. A. Abdou. Experimental measurements of the effective thermal conductivity of a lithium titanate (Li2TiO3) pebbles-packed bed. *Journal of Materials Processing Technology*, 181(1-3):206–212, 2007.

[4] A. Abou-Sena, A. Y. Ying, and M. A. Abdou. Effective Thermal Conductivity of Lithium Ceramic Pebble Beds for Fusion Blankets: A Review. *Fusion Science and Technology*, 47(4):1094–1100, 2005.

[5] H. T. Aichlmayr and F. A. Kulacki. The Effective Thermal Conductivity of Saturated Porous Media. *Heat Transfer: Volume 1*, pages 265–273, 2005.

[6] A. Amritkar, S. Deb, and D. Tafti. Efficient parallel CFD-DEM simulations using OpenMP. *Journal of Computational Physics*, 256:501–519, 2014.

[7] Z. An, A. Ying, and M. A. Abdou. Numerical characterization of thermo-mechanical performance of breeder pebble beds. *Journal of Nuclear Materials*, 367-370:1393–1397, 2007.

[8] Z. An, A. Y. Ying, and M. A. Abdou. Application of discrete element method to study mechanical behaviors of ceramic breeder pebble beds. *Fusion Engineering and Design*, 82(15-24):2233–2238, 2007.

[9] T. B. Anderson and R. O. Y. Jackson. A Fluid Mechanical Description of Fluidized Beds. *Industrial & Engineering Chemistry Fundamentals*, 6(4):527–539, 1967.

[10] R. K. Annabattula. Size-Dependent Crush Analysis of Lithium Orthosilicate Pebbles. *Fusion Science & Technology*, 66(1), aug 2014.

[11] R. K. Annabattula, Y. Gan, and M. Kamlah. Mechanics of binary and polydisperse spherical pebble assembly. *Fusion Engineering and Design*, pages 2–7, mar 2012.

[12] R. K. Annabattula, Y. Gan, S. Zhao, and M. Kamlah. Mechanics of a crushable pebble assembly using discrete element method. *Journal of Nuclear Materials*, 430(1-3):90–95, nov 2012.

[13] V. Antonetti and M. Yovanovich. Thermal Contact Resistance in Microelectronic Equipment. *Thermal Management Concepts in Microelectronic Packaging From Component to System, ISHM Technical Monograph Series*, 1984-003:135–151, 1984.

[14] D. Aquaro and N. Zaccari. Experimental and numerical analyses on LiSO4 and Li2TiO3 pebble beds used in a ITER test blanket module. *Journal of Nuclear Materials*, 367-370(SPEC. ISS.):1293–1297, aug 2007.

[15] M. Bahrami, J. R. Culham, M. Yovanovich, and G. E. Schneider. Thermal Contact Resistance of Nonconforming Rough Surfaces, Part 2: Thermal Model. *Journal of Thermophysics and Heat Transfer*, 18(2):218–227, 2004.

[16] M. Bahrami, M. Yovanovich, and J. R. Culham. Effective thermal conductivity of rough spherical packed beds. *International Journal of Heat and Mass Transfer*, 49(19-20):3691–3701, 2006.

[17] G. C. Barker and A. Mehta. Transient phenomena, self-diffusion, and orientational effects in vibrated powders. *Physical Review E*, 47(1):184–188, jan 1993.

[18] G. Batchelor and R. O'Brien. Thermal or Electrical Conduction Through a Granular Material. *Proceedings of the Royal Society of London. Series A, Mathematical and Physical Sciences1*, 355(1682):313–333, 1977.

[19] R. Bauer and E. U. Schlunder. Effective Radial Thermal-Conductivity of Packings in Gas-Flow. 2. Thermal-Conductivity of Packing Fraction without Gas-Flow. *International Chemical Engineering*, 18(2):189–204, 1978.

[20] O. Ben-Nun and I. Einav. The role of self-organization during confined comminution of granular materials. *Philosophical Transactions of the Royal Society A: Mathematical, Physical and Engineering Sciences*, 368(1910):231–247, 2010.

[21] O. Ben-Nun, I. Einav, and A. Tordesillas. Force attractor in confined comminution of granular materials. *Physical Review Letters*, 104(10):10–13, 2010.

[22] R. F. Benenati and C. B. Brosilow. Void fraction distribution in beds of spheres. *AIChE Journal*, 8(3):359–361, 1962.

[23] S. Benyahia, M. Syamlal, and T. J. O'Brien. Extension of Hill–Koch–Ladd drag correlation over all ranges of Reynolds number and solids volume fraction. *Powder Technology*, 162(2):166–174, mar 2006.

[24] P. L. Bhatnagar, E. P. Gross, and M. Krook. A Model for Collision Processes in Gases. I. Small Amplitude Processes in Charged and Neutral One-Component Systems. *Physical Review*, 94(3):511–525, 1954.

[25] G. Breitbach and H. Barthels. The radiant heat transfer in the high temperature reactor core after failure of the afterheat removal systems. *Nuclear Technology*, 49(3):392–399, 1980.

[26] N. Brilliantov, F. Spahn, J. Hertzsch, and T. Pöschel. Model for collisions in granular gases. *Physical review. E, Statistical physics, plasmas, fluids, and related interdisciplinary topics*, 53(5):5382–5392, may 1996.

[27] L. Bühler and J. Reimann. Thermal creep of granular breeder materials in fusion blankets. *Journal of Nuclear Materials*, 307-311:807–810, dec 2002.

[28] G. Buonanno, A. Carotenuto, G. Giovinco, and L. Vanoli. Effective Thermal Conductivity of Rough Spheres Packed Bed. In *Heat Transfer: Volume 1*, pages 251–256. ASME, 2003.

[29] P. Calderoni, A. Ying, T. Sketchley, and M. A. Abdou. Experimental study of the interaction of ceramic breeder pebble beds with structural materials under thermomechanical loads. *Fusion Engineering and Design*, 81(1-7):607–612, 2006.

[30] P. Carman. Fluid flow through granular beds. *Transactions, Institution of Chemical Engineers*, 15:150–166, 1937.

[31] P. Carman. *Flow of Gas Through Porous Media*. London Butterworths Scientific Publications, 1956.

[32] K. Chen, A. Harris, J. Draskovic, and P. Schiffer. Granular fragility under thermal cycles. *Granular Matter*, 11(4):237–242, may 2009.

[33] S. Chen and G. D. Doolen. Lattice Boltzmann method for fluid flows. *Annual review of fluid mechanics*, 30(Kadanoff 1986):329–364, jan 1998.

[34] G. Cheng, A. Yu, and P. Zulli. Evaluation of effective thermal conductivity from the structure of a packed bed. *Chemical Engineering Science*, 54(4199):4209, 1999.

[35] S. Cho, M.-Y. Ahn, D. H. Kim, E. S. Lee, S. Yun, N. Z. Cho, and K. J. Jung. Current status of design and analysis of Korean Helium-Cooled Solid Breeder Test Blanket Module. *Fusion Engineering and Design*, 83(7-9):1163–1168, dec 2008.

[36] B. Chopard and M. Droz. *Cellular automata*. Springer, 1998.

[37] B. Chopard, A. Dupuis, A. Masselot, and P. Luthi. Cellular Automata And Lattice Boltzmann Techniques: An Approach To Model And Simulate Complex Systems. *Advances in Complex Systems*, 05(02n03):103–246, jun 2002.

[38] K. Chu and A. Yu. Numerical simulation of complex particle–fluid flows. *Powder Technology*, 179(3):104–114, jan 2008.

[39] F. Cismondi, S. Kecskés, M. Ilic, G. Légrádi, B. Kiss, O. Bitz, B. Dolensky, H. Neuberger, L. Boccaccini, and T. Ihli. Design update, thermal and fluid dynamic analyses of the EU-HCPB TBM in vertical arrangement. *Fusion Engineering and Design*, 84:607–612, 2009.

[40] R. Clemmer. The Development of Tritium Breeding Blankets for DT-Burning Fusion Reactors. In *Fourth ANS Topical Meeting on the Technology of Controlled Nuclear Fusion*, 1980.

[41] M. A. Combarnous and P. Bia. Combined Free and Forced Convection in Porous Media.

[42] P. A. Cundall and O. D. L. Strack. A discrete numerical model for granular assemblies. *Geotechnique*, 29(1):47–65, 1979.

[43] J. A. Currie. Gaseous diffusion in porous media. Part 3 - Wet granular materials. *British Journal of Applied Physics*, 12(6):275–281, 2002.

[44] N. G. Deen, M. Van Sint Annaland, M. Van der Hoef, and J. A. Kuipers. Review of discrete particle modeling of fluidized beds. *Chemical Engineering Science*, 62(1-2):28–44, jan 2007.

[45] R. G. Deissler and J. S. Boegli. An investigation of effective thermal conductivites of powders in various gases. *ASME Transactions*, 80(7):1417– 1425, 1958.

[46] G. Dell'Orco, P. A. Di Maio, R. Giammusso, A. Malavasi, L. Sansone, A. Tincani, and G. Vella. Progress in the benchmark exercise for analyzing the lithiate breeder pebble bed thermo-mechanical behaviour. *Fusion Engineering and Design*, 81(1-7):169–174, feb 2006.

[47] G. Dell'Orco, P. A. Di Maio, R. Giammusso, A. Tincani, and G. Vella. A constitutive model for the thermo-mechanical behaviour of fusion-relevant pebble beds and its application to the simulation of HELICA mock-up experimental results. *Fusion Engineering and Design*, 82(15-24):2366–2374, oct 2007.

[48] G. Dell'Orco, P. A. Di Maio, R. Giammusso, A. Tincani, and G. Vella. On the theoretical–numerical study of the HEXCALIBER mock-up thermo-mechanical behaviour. *Fusion Engineering and Design*, 85(5):694–706, aug 2010.

[49] F. P. Di Maio, A. Di Renzo, and D. Trevisan. Comparison of heat transfer models in DEM-CFD simulations of fluidized beds with an immersed probe. *Powder Technology*, 193(3):257–265, aug 2009.

[50] P. A. Di Maio, G. Dell'Orco, R. Giammusso, A. Malavasi, I. Ricapito, A. Tincani, and G. Vella. Experimental tests and thermo-mechanical analyses on the HEXCALIBER mock-up. *Fusion Engineering and Design*, 83(7-9):1287–1293, dec 2008.

[51] P. A. Di Maio, R. Giammusso, and G. Vella. On the hyperporous non-linear elasticity model for fusion-relevant pebble beds. *Fusion Engineering and Design*, 85(7-9):1234–1244, 2010.

[52] A. Di Renzo and F. P. Di Maio. Comparison of contact-force models for the simulation of collisions in DEM-based granular flow codes. *Chemical Engineering Science*, 59(3):525–541, feb 2004.

[53] T. Divoux, H. Gayvallet, and J.-C. Géminard. Creep Motion of a Granular Pile Induced by Thermal Cycling. *Physical Review Letters*, 101(14):148303, oct 2008.

[54] D. C. Drucker and W. Prager. Soil mechanics and plastic analysis or limit design. *Quarterly of Applied mathematics*, 10, 1952.

[55] J. Duran. *Sands, powders, and grains: an introduction to the physics of granular materials*. Springer Science & Business Media, 2012.

[56] M. Enoeda, Y. Kosaku, T. Hatano, T. Kuroda, N. Miki, T. Honma, M. Akiba, S. Konishi, H. Nakamura, Y. Kawamura, S. Sato, K. Furuya, Y. Asaoka, and K. Okano. Design and technology development of solid breeder blanket cooled by supercritical water in Japan. *Nuclear Fusion*, 43:1837–1844, 2003.

[57] M. Enoeda, Y. Ohara, N. Roux, A. Ying, G. Pizza, and S. Malang. Effective thermal conductivity measurement of the candidate ceramic breeder pebble beds by the hot wire method. *Fusion Technology*, 39(2):612–616, 2001.

[58] H. Enwald, E. Peirano, and A. E. Almstedt. Eulerian two-phase flow theory applied to fluidization. *International Journal of Multiphase Flow*, 22(1975):21–66, 1996.

[59] S. Ergun. Fluid flow through packed columns. *Chemical engineering progress*, 48, 1952.

[60] K. M. Feng, C. H. Pan, G. S. Zhang, T. Y. Luo, Z. Zhao, Y. J. Chen, Y. J. Feng, X. F. Ye, G. Hu, K. H. He, R. W. Niu, Z. X. Li, P. H. Wang, B. Xiang, L. Zhang, Q. J. Wang, F. C. Zhao, Q. X. Cao, F. Wang, T. Yuan, G. Y. Zheng, Y. Liu, Y. Zhong, and M. C. Zhang. Progress on design and R&D for helium-cooled ceramic breeder TBM in China. *Fusion Engineering and Design*, 87:1138–1145, 2012.

[61] Y. Feng and K. Han. An accurate evaluation of geometric view factors for modelling radiative heat transfer in randomly packed beds of equally sized spheres. *International Journal of Heat and Mass Transfer*, 55(23-24):6374–6383, nov 2012.

[62] FlowKit Ltd. Palabos, 2015.

[63] S. Flueckiger, B. D. Iverson, S. V. Garimella, and J. E. Pacheco. System-level simulation of a solar power tower plant with thermocline thermal energy storage. *Applied Energy*, 113:86–96, jan 2014.

[64] S. Flueckiger, Z. Yang, and S. V. Garimella. An integrated thermal and mechanical investigation of molten-salt thermocline energy storage. *Applied Energy*, 88(6):2098–2105, jun 2011.

[65] S. Flueckiger, Z. Yang, and S. V. Garimella. Thermocline Energy Storage in the Solar One Power Plant: An Experimentally Validated Thermomechanical Investigation. In *ASME 2011 5th International Conference on Energy Sustainability, Parts A, B, and C*, pages 775–781. ASME, 2011.

[66] J. H. Fokkens. Thermo-mechanical Finite Element Analyses for the HCPB In-pile Test Element, 2003.

[67] Free Software Foundation Inc. Gnu Affero General Public License. (November):1–16, 2007.

[68] U. Frisch, B. Hasslacher, and Y. Pomeau. Lattice-gas automata for the Navier-Stokes equation. *Physical Review Letters*, 56(14):1505–1508, 1986.

[69] Y. Gan and M. Kamlah. Identification of material parameters of a thermo-mechanical model for pebble beds in fusion blankets. *Fusion Engineering and Design*, 82(2):189–206, feb 2007.

[70] Y. Gan and M. Kamlah. Thermo-mechanical analysis of pebble beds in HELICA mock-up experiments. *Fusion Engineering and Design*, 83(7-9):1313–1316, dec 2008.

[71] Y. Gan and M. Kamlah. Thermo-mechanical analyses of HELICA and HEXCALIBER mock-ups. *Journal of Nuclear Materials*, 386-388:1060–1064, apr 2009.

[72] Y. Gan and M. Kamlah. Discrete element modelling of pebble beds: With application to uniaxial compression tests of ceramic breeder pebble beds. *Journal of the Mechanics and Physics of Solids*, 58(2):129–144, feb 2010.

[73] Y. Gan and M. Kamlah. Thermo-mechanical modelling of pebble bed–wall interfaces. *Fusion Engineering and Design*, 85(1):24–32, jan 2010.

[74] Y. Gan, M. Kamlah, H. Riesch-Oppermann, R. Rolli, and P. Liu. Crush probability analysis of ceramic breeder pebble beds under mechanical stresses. *Journal of Nuclear Materials*, pages 10–13, dec 2010.

[75] T. Gensane. Dense packings of equal spheres in a larger sphere: a list of result. *Les Cahiers du LMPA J. Liouville*, 188, 2003.

[76] L. Giancarli, V. Chuyanov, M. A. Abdou, M. Akiba, B. Hong, R. Lässer, C. Pan, and Y. Strebkov. Breeding Blanket Modules testing in ITER: An international program on the way to DEMO. *Fusion Engineering and Design*, 81(1-7):393–405, 2006.

[77] D. Gidaspow. *Multiphase flow and fluidization: continuum and kinetic theory descriptions*. Academic Press, 1994.

[78] P. J. Gierszewski. Review of properties of lithium metatitanate. *Fusion Engineering and Design*, 39-40:739–743, sep 1998.

[79] F. A. Gilabert, J. N. Roux, and A. Castellanos. Computer simulation of model cohesive powders: Influence of assembling procedure and contact laws on low consolidation states. *Physical Review E - Statistical, Nonlinear, and Soft Matter Physics*, 75:1–26, 2007.

[80] V. Gnielinski. Berechnung des Wärme-und Stoffaustauschs in durchströmten ruhenden Schüttungen. *Verfahrenstechnik*, 16(1):36–39, 1982.

[81] C. Goniva, C. Kloss, N. G. Deen, J. A. Kuipers, and S. Pirker. Influence of Rolling Friction on Single Spout Fluidized Bed Simulation. *Particuology*, 10(5):582–591, oct 2012.

[82] K. Gruber. *Sediment transport in open channel flows - Experimental investigation and numerical simulation of local scour development downstream of a weir*. PhD thesis, Johannes Kepler University Linz, 2012.

[83] H. Grubmuller, H. Heller, A. Windemuth, and K. Schulten. Generalized verlet algorithm for efficient molecular dynamics simulations with long-range interaction. *Molecular Simulation*, 6:121–142, 1991.

[84] D. Gunn. Transfer of heat or mass to particles in fixed and fluidised beds. *International Journal of Heat and Mass Transfer*, 21(4):467–476, apr 1978.

[85] Z. Guo, B. Shi, and C. Zheng. A coupled lattice BGK model for the Boussinesq equations. *International Journal for Numerical Methods in Fluids*, 39(4):325–342, jun 2002.

[86] J. Hardy, Y. Pomeau, and O. De Pazzis. Time Evolution of a Two-Dimensional Classical Lattice System. *Physical Review Letters*, (5):276 – 279, 1975.

[87] T. Hatano, M. Enoeda, S. Suzuki, Y. Kosaku, and M. Akiba. Effective thermal conductivity of a Li2TiO3 pebble bed for a demo blanket. *Fusion Science and Technology*, 44(1):94–98, 2003.

[88] M. Hecht and J. Harting. Implementation of on-site velocity boundary conditions for D3Q19 lattice Boltzmann simulations. *Journal of Statistical Mechanics: Theory and Experiment*, 2010(01):P01018, 2010.

[89] J. Hegeman, E. van Essen, M. Jong, J. G. van der Laan, and J. Reimann. Thermomechanical behaviour of ceramic breeder pebble stacks for HICU. *Fusion Engineering and Design*, 69(1-4):425–429, sep 2003.

[90] F. Hernández, M. Kolb, M. Ilić, a. Kunze, J. Németh, and a. Von Der Weth. Set-up of a pre-test mock-up experiment in preparation for the HCPB Breeder Unit mock-up experimental campaign. *Fusion Engineering and Design*, 88(9-10):2378–2383, 2013.

[91] J. M. Hill and A. Selvadurai. *Mathematics and Mechanics of Granular Materials*. Springer, 2005.

[92] R. J. Hill, D. L. Koch, and A. J. C. Ladd. Moderate-Reynolds-number flows in ordered and random arrays of spheres. *Journal of Fluid Mechanics*, 448:243–278, nov 2001.

[93] R. J. Hill, D. L. Koch, and A. J. C. Ladd. The first effects of fluid inertia on flows in ordered and random arrays of spheres. *Journal of Fluid Mechanics*, 448:213–241, nov 2001.

[94] B. Hoomans, J. A. Kuipers, W. Briels, and W. van Swaaij. Discrete particle simulation of bubble and slug formation in a two-dimensional gas-fluidised bed: A hard-sphere approach. *Chemical Engineering Science*, 51(1):99–118, jan 1996.

[95] G. R. Hopkins and R. J. Price. Fusion reactor design with ceramics. *Nuclear Engineering and Design*, 2:111–143, 1985.

[96] A. Horvat, M. Leskovar, and B. Mavko. Comparison of heat transfer conditions in tube bundle cross-flow for different tube shapes. *International Journal of Heat and Mass Transfer*, 49(5-6):1027–1038, 2006.

[97] C. T. Hsu, P. Cheng, and K. W. Wong. A Lumped-Parameter Model for Stagnant Thermal Conductivity of Spatially Periodic Porous Media. *Journal of Heat Transfer*, 117(2):264, 1995.

[98] M. Hunt and C. Tien. Non-darcian flow, heat and mass transfer in catalytic packed-bed reactors. *Chemical Engineering Science*, 45(1):55–63, 1990.

[99] R. I. Issa. Solution of the implicitly discretised fluid flow equations by operator-splitting. *Journal of Computational Physics*, 62(1):40–65, 1986.

[100] H. Jaeger, S. Nagel, and R. P. Behringer. Granular solids, liquids, and gases. *Reviews of Modern Physics*, 68(4):1259–1273, 1996.

[101] H. M. Jaeger, S. R. Nagel, and R. P. Behringer. The Physics of Granular Materials. *Physics Today*, 49(4), 1996.

[102] C. Jeffreson. Prediction of Breakthrough Curves in Packed Beds: 1. Applicability of Single Parameter Models. *American Institute of Chemical Engineers*, 18(2):409–416, mar 1972.

[103] C. Johnson and R. Clemmer. Solid Breeder Materials. *Journal of Nuclear Materials*, 103 & 104:547–553, 1981.

[104] C. Johnson, K. Kummerer, and E. Roth. Ceramic breeder materials. *Journal of Nuclear Materials*, 155-157:188–201, jul 1988.

[105] K. Johnson. *Contact Mechanics*. Cambridge University Press, 1985.

[106] G. Karniadakis, A. Beskok, and N. Aluru. *Microflows and nanoflows: fundamentals and simulation*, volume 29. Springer Science & Business Media, 2006.

[107] C. Kloss and C. Goniva. LIGGGHTS - Open Source Discrete Element Simulations of Granular Materials Based on LAMMPS. *Supplemental Proceedings: Materials Fabrication, Properties, Characterization, and Modeling*, 2:781–788, 2011.

[108] C. Kloss, C. Goniva, A. Hager, S. Amberger, and S. Pirker. Models, algorithms and validation for opensource DEM and CFD-DEM. *Progress in Computational Fluid Dynamics*, 12(2/3):140–152, 2012.

[109] J. B. Knight, C. G. Fandrich, C. N. Lau, H. M. Jaeger, and S. R. Nagel. Density relaxation in a vibrated granular material. *Physical Review E*, 51(5):3957–3963, may 1995.

[110] D. L. Koch and R. J. Hill. Inertial Effects in Suspension and Porous-Media Flows. *Annual Review of Fluid Mechanics*, 33(1):619–647, jan 2001.

[111] H. Kruggel-Emden, M. Sturm, S. Wirtz, and V. Scherer. Selection of an appropriate time integration scheme for the discrete element method (DEM). *Computers & Chemical Engineering*, 32(10):2263–2279, oct 2008.

[112] F. Kuwahara, A. Nakayama, and H. Koyama. A Numerical Study of Thermal Dispersion in Porous Media. *Journal of Heat Transfer*, 118(3):756, 1996.

[113] F. Kuwahara, M. Shirota, and A. Nakayama. A numerical study of interfacial convective heat transfer coefficient in two-energy equation model for convection in porous media. *International Journal of Heat and Mass Transfer*, 44(6):1153–1159, 2001.

[114] C. Y. Kwok and M. D. Bolton. DEM simulations of soil creep due to particle crushing. *Géotechnique*, (16):1–12, 2013.

[115] P. A. Langston, U. Tlrzon, and D. M. Heyes. Discrete element simulation of granular flow in 2D and 3D hoppers: dependence of discharge rate and wall stress on particle interactions. *Chemical Engineering Science*, 50(6):967–987, 1995.

[116] J. Lätt. *Hydrodynamic limit of lattice Boltzmann equations*. Phd thesis, University of Geneva, 2007.

[117] J. Li and D. J. Mason. A computational investigation of transient heat transfer in pneumatic transport of granular particles. *Powder Technology*, 112(3):273–282, oct 2000.

[118] J. Li, D. J. Mason, and A. S. Mujumdar. A Numerical Study of Heat Transfer Mechanisms in Gas–Solids Flows Through Pipes Using a Coupled CFD and DEM Model. *Drying Technology*, 21(9):1839–1866, dec 2003.

[119] J. M. Link, L. A. Cuypers, N. G. Deen, and J. A. Kuipers. Flow regimes in a spout-fluid bed: A combined experimental and simulation study. *Chemical Engineering Science*, 60:3425–3442, 2005.

[120] Z. Lu. *Numerical Modeling and Experimental Measurement of the Thermal and Mechanical Properties of Packed Beds*. PhD thesis, University of California Los Angeles, 2000.

[121] Z. Lu, A. Y. Ying, and M. A. Abdou. Numerical and experimental prediction of the thermomechanical performance of pebble beds for solid breeder blanket. *Fusion Engineering and Design*, 49-50:605–611, 2000.

[122] L.-s. Luo. Lattice Boltzmann Methods for Computational Fluid Dynamics. *Review Literature And Arts Of The Americas*, page 53, 2003.

[123] A. Magielsen, M. M. W. Peeters, J. Hegeman, M. Stijkel, and J. G. van der Laan. Analysis of the in-pile operation and preliminary results of the post-irradiation dismantling of the pebble bed assemblies, presented at the 8th ISFNT, 2007.

[124] H. Makse, N. Gland, D. Johnson, and L. Schwartz. Granular packings: Nonlinear elasticity, sound propagation, and collective relaxation dynamics. *Physical Review E*, 70(6):061302, dec 2004.

[125] D. Mandal, D. Sathiyamoorthy, and M. Vinjamur. Experimental measurement of effective thermal conductivity of packed lithium-titanate pebble bed. *Fusion Engineering and Design*, 87(1):67–76, jan 2012.

[126] G. Marketos and M. D. Bolton. Quantifying the extent of crushing in granular materials: A probability-based predictive method. *Journal of the Mechanics and Physics of Solids*, 55(10):2142–2156, oct 2007.

[127] C. L. Martin. Elasticity, fracture and yielding of cold compacted metal powders. *Journal of the Mechanics and Physics of Solids*, 52(8):1691–1717, 2004.

[128] M. Matyka and Z. Koza. How to calculate tortuosity easily? In *AIP Conference Proceedings*, volume 1453, pages 17–22, 2012.

[129] G. R. McNamara and G. Zanetti. Use of the boltzmann equation to simulate lattice-gas automata. *Physical Review Letters*, 61(20):2332–2335, 1988.

[130] G. E. Mueller. Narrow annular packed-bed radial void fraction correlation. *AIChE Journal*, 48(3):644–647, 2002.

[131] Y. Nakata, A. F. L. Hyde, M. Hyodo, and H. Murata. A probabilistic approach to sand particle crushing in the triaxial test. *Geotechnique*, 49(5):567–583, 1999.

[132] A. Nakayama, F. Kuwahara, and Y. Kodama. An equation for thermal dispersion flux transport and its mathematical modelling for heat and fluid flow in a porous medium. *Journal of Fluid Mechanics*, 563:81, 2006.

[133] D. A. Nield and A. Bejan. *Convection in Porous Media*. Springer New York, New York, NY, 2013.

[134] H. Niessen and S. Ball. Heat Transport and Afterheat Removal for Gas Cooled Reactors Under Accident Conditions. Technical report, 2000.

[135] Y. Nomoto, S. Suzuki, K. Ezato, T. Hirose, D. Tsuru, H. Tanigawa, T. Hatano, M. Enoeda, and M. Akiba. Structural concept of Japanese solid breeder test blanket modules for ITER. *Fusion Engineering and Design*, 81(1-7):719–724, feb 2006.

[136] I. Nozad, R. Carbonell, and S. Whitaker. Heat conduction in multiphase systems—I: Theory and experiment for two-phase systems. *Chemical Engineering Science*, 40(5):843–855, 1985.

[137] OpenCFD Ltd. OpenFOAM - The Open Source CFD Toolbox, 2014.

[138] C. Pan, L.-S. Luo, and C. T. Miller. An evaluation of lattice Boltzmann schemes for porous medium flow simulation. *Computers and Fluids*, 35(8-9):898–909, 2006.

[139] A. Parmigiani. *Lattice Boltzmann calculations of reactive multiphase flows in porous media*. Phd thesis, University of Geneva, 2011.

[140] N. Patankar and D. Joseph. Modeling and numerical simulation of particulate flows by the Eulerian–Lagrangian approach. *International Journal of Multiphase Flow*, 27(10):1659–1684, oct 2001.

[141] Z. Peng, E. Doroodchi, C. Luo, and B. Moghtaderi. Influence of void fraction calculation on fidelity of CFD-DEM simulation of gas-solid bubbling fluidized beds. *AIChE Journal*, 60(6):2000–2018, jun 2014.

[142] G. Piazza, J. Reimann, E. Günther, R. Knitter, N. Roux, and J. D. Lulewicz. Characterisation of ceramic breeder materials for the helium cooled pebble bed blanket. *Journal of Nuclear Materials*, 307-311(0):811–816, dec 2002.

[143] R. Pitchumani, O. Zhupanska, G. M. Meesters, and B. Scarlett. Measurement and characterization of particle strength using a new robotic compression tester. *Powder Technology*, 143-144:56–64, jun 2004.

[144] S. Plimpton. Fast Parallel Algorithms for Short-Range Molecular Dynamics. *Journal of Computational Physics*, 117(1):1–19, mar 1995.

[145] Y. Poitevin, L. Boccaccini, M. Zmitko, I. Ricapito, J. Salavy, E. Diegele, F. Gabriel, E. Magnani, H. Neuberger, R. Lässer, and L. Guerrini. Tritium breeder blankets design and technologies in Europe: Development status of ITER Test Blanket Modules, test & qualification strategy and roadmap towards DEMO. *Fusion Engineering and Design*, 85(10-12):2340–2347, dec 2010.

[146] Y. H. Qian, D. D'Humières, and P. Lallemand. Lattice BGK models for Navier-Stokes equation. *EPL (Europhysics Letters)*, 17(6):479, 1992.

[147] A. R. Raffray and M. A. Abdou. Modeling of Tritium Behavior in Solid Breeders. In I. J. Hastings and G. W. Hollenberg, editors, *Fabrication and Properties of Lithium Ceramics*. American Ceramic Society, 1989.

[148] W. Ranz and W. Marshall. Evaporation From Drops, Part I. *Chemical Engineering Progress*, 48(3):141–146, 1952.

[149] J. W. S. Rayleigh. On waves propagated along the plane surface of an elastic solid. *Proceedings of the London Mathematical Society*, 17:4–11, 1885.

[150] J. Reimann, E. Arbogast, M. Behnke, S. Müller, and K. Thomauske. Thermomechanical behaviour of ceramic breeder and beryllium pebble beds. *Fusion Engineering and Design*, 49-50:643–649, 2000.

[151] J. Reimann, L. Boccaccini, M. Enoeda, and A. Ying. Thermomechanics of solid breeder and Be pebble bed materials. *Fusion Engineering and Design*, 61-62:319–331, nov 2002.

[152] J. Reimann, D. Ericher, and G. Wörner. Influence of pebble bed dimensions and filling factor on mechanical pebble bed properties. *Fusion Engineering and Design*, 69(1-4):241–244, 2003.

[153] J. Reimann and H. Harsch. Thermal creep of beryllium pebble beds. *Fusion Engineering and Design*, 75-79:1043–1047, nov 2005.

[154] J. Reimann and S. Hermsmeyer. Thermal conductivity of compressed ceramic breeder pebble beds. *Fusion Engineering and Design*, 61-62:345–351, nov 2002.

[155] J. Reimann and G. Wörner. Thermal creep of Li4SiO4 pebble beds. *Fusion Engineering and Design*, 58-59:647–651, nov 2001.

[156] S. Rickelt, F. Sudbrock, S. Wirtz, and V. Scherer. Coupled DEM/CFD simulation of heat transfer in a generic grate system agitated by bars. *Powder Technology*, 249:360–372, 2013.

[157] L. Roblee, R. Baird, and W. Tierney. Radial Porosi Variations in Packed Beds. *AIChE Journal*, pages 460–464, 1958.

[158] S. J. P. Romkes, F. M. Dautzenberg, C. M. van den Bleek, and H. P. A. Calis. CFD modelling and experimental validation of particle-to-fluid mass and heat transfer in a packed bed at very low channel to particle diameter ratio. *Chemical Engineering Journal*, 96:3–13, 2003.

[159] N. Roux, J. Avon, A. Floreancing, J. Mougin, B. Rasneur, S. Ravel, A. Floreancig, J. Mougin, B. Rasneur, and S. Ravel. Low-temperature tritium releasing ceramics as potential materials for the ITER breeding blanket. *Journal of Nuclear Materials*, 233-237:1431–1435, oct 1996.

[160] A. R. Russell, D. Muir Wood, and M. Kikumoto. Crushing of particles in idealised granular assemblies. *Journal of the Mechanics and Physics of Solids*, 57(8):1293–1313, aug 2009.

[161] O. Sadovskaya, V. Sadovskii, and H. Altenbach. *Mathematical Modeling in Mechanics of Granular Materials*. 2012.

[162] K. Sbutega and I. Catton. Efficient Hydraulic and Thermal Analysis of Heat Sinks Using Volume Averaging Theory and Galerkin Methods. *Multiphase Science and Technology*, 25(2-4):311–338, 2013.

[163] Y. Seki, M. Enoeda, and S. Fukada. A study on fluid flow of helium purge gas with tritium transfer released from lithium titanate in a solid breeder test blanket module. In *Proceedings of the 17th IEA International Workshop on Ceramic Breeder Blanket Interactions (CBBl-17)*, 2013.

[164] J. Shafer, S. Dippel, and D. E. Wolf. Force Schemes in Simulations of Granular Materials. *Journal de Physique I*, 6(1):5–20, jan 1996.

[165] Y. Sheng, C. Lawrence, B. Briscoe, and C. Thornton. Numerical studies of uniaxial powder compaction process by 3D DEM. *Engineering Computations*, 21(2/3/4):304–317, 2004.

[166] L. Silbert, G. Grest, and J. Landry. Statistics of the contact network in frictional and frictionless granular packings. *Physical Review E*, 66(6):061303, dec 2002.

[167] L. E. Silbert, D. Ertaş, G. Grest, T. Halsey, D. Levine, and S. Plimpton. Granular flow down an inclined plane: Bagnold scaling and rheology. *Physical Review E*, 64(5):051302, oct 2001.

[168] L. L. Snead, S. J. Zinkle, and D. P. White. Thermal conductivity degradation of ceramic materials due to low temperature, low dose neutron irradiation. *Journal of Nuclear Materials*, 340(2-3):187–202, 2005.

[169] S. Song and M. Yovanovich. Relative contact pressure-Dependence on surface roughness and Vickers microhardness. *Journal of thermophysics and heat transfer*, 2(1):43–47, 1988.

[170] S. Succi. *The Lattice-Boltzmann Equation*. Oxford University Press, 2001.

[171] M. C. Sukop and D. T. Thorne. *Lattice Boltzmann Modeling*. Springer, 2007.

[172] T. Swasdisevi, W. Tanthapanichakoon, T. Charinpanitkul, T. Kawaguchi, T. Tanaka, and Y. Tsuji. Prediction of gas–particle dynamics and heat transfer in a two-dimensional spouted bed. *Advanced Powder Technology*, 16(3):275–293, jun 2005.

[173] H. Tanigawa, M. Enoeda, and M. Akiba. Measurement of thermal expansion of Li2TiO3 pebble beds. *Fusion Engineering and Design*, 82(15-24):2259–2263, oct 2007.

[174] H. Tanigawa, T. Hatano, M. Enoeda, and M. Akiba. Effective thermal conductivity of a compressed Li2TiO3 pebble bed. *Fusion Engineering and Design*, 75-79:801–805, nov 2005.

[175] H. Tanigawa, Y. Tanaka, and M. Enoeda. Packing behaviour of a Li2TiO3 pebble bed under cyclic loads. *Journal of Nuclear Materials*, 417(1-3):2010–2012, dec 2010.

[176] Y. Tsuji, T. Kawaguchi, and T. Tanaka. Discrete particle simulation of two-dimensional fluidized bed. *Powder Technology*, 77(1):79–87, oct 1993.

[177] Y. Tsuji, T. Tanaka, and T. Ishida. Lagrangian numerical simulation of plug flow of cohesionless particles in a horizontal pipe. *Powder Technology*, 71(3):239–250, sep 1992.

[178] W. van Antwerpen, C. du Toit, and P. G. Rousseau. A review of correlations to model the packing structure and effective thermal conductivity in packed beds of mono-sized spherical particles. *Nuclear Engineering and Design*, 240(7):1803–1818, jul 2010.

[179] M. S. van Buijtenen, W.-J. van Dijk, N. G. Deen, J. A. Kuipers, T. Leadbeater, and D. Parker. Numerical and Experimental Study on Multiple-spout Fluidized Beds. *Chemical Engineering Science*, 66(11):2368–2376, jun 2011.

[180] M. Van der Hoef, R. Beetstra, and J. A. Kuipers. Lattice-Boltzmann simulations of low-Reynolds-number flow past mono- and bidisperse arrays of spheres: results for the permeability and drag force. *Journal of Fluid Mechanics*, 528:233–254, apr 2005.

[181] J. G. van der Laan, A. Fedorov, S. van Til, and J. Reimann. Ceramic Breeder Materials. Technical report, 2011.

[182] D. van Houtte, K. Okayama, and F. Sagot. ITER operational availability and fluence objectives. *Fusion Engineering and Design*, 86(6-8):680–683, oct 2011.

[183] J. T. Van Lew. *Transient Heat Delivery, Storage Process, and Optimization of a Packed Bed Thermocline Thermal Energy Storage System*. Master's thesis, University of Arizona, 2010.

[184] J. T. Van Lew, A. Ying, and M. A. Abdou. A discrete element method study on the evolution of thermomechanics of a pebble bed experiencing pebble failure. *Fusion Engineering and Design*, 89(7-8):1151–1157, oct 2014.

[185] J. T. Van Lew, A. Ying, and M. A. Abdou. Coupling Discrete Element Models of Ceramic Breeder Pebble Beds to Thermofluid Models of Helium Purge Gas Using Volume-Averaged Navier-Stokes and the Lattice-Boltzmann Method. *Fusion Science and Technology*, 68(2):288–294, sep 2015.

[186] S. van Til, A. Fedorov, and A. Magielsen. Study of ceramic pebble beds in Post Irradiation Examination of the Pebble Bed Assemblies irradiation experiment. *Fusion Engineering and Design*, 87(5-6):885–889, aug 2012.

[187] W. L. Vargas and J. J. McCarthy. Heat Conduction in Granular Materials. *AIChE Journal*, 47(5), 2001.

[188] W. L. Vargas and J. J. McCarthy. Conductivity of granular media with stagnant interstitial fluids via thermal particle dynamics simulation. *International Journal of Heat and Mass Transfer*, 45(24):4847–4856, nov 2002.

[189] W. L. Vargas and J. J. McCarthy. Thermal expansion effects and heat conduction in granular materials. *Physical Review E*, 76(4):1–8, oct 2007.

[190] E. M. Viggen. *The lattice Boltzmann method with applications in acoustics*. Master's thesis, Norwegian University of Science and Technology, 2009.

[191] C. J. Visser. *Modelling Heat And Mass Flow Through Packed Pebble Beds: A Heterogeneous Volume-Averaged Approach*. Master's thesis, University of Pretoria, 2007.

[192] N. Wakao and T. Funazkri. Effect of fluid dispersion coefficients on particle-to-fluid mass transfer coefficients in packed beds. *Chemical Engineering Science*, 33(10):1375–1384, jan 1978.

[193] N. Wakao and S. Kagei. *Heat and mass transfer in packed beds*, volume 1. Taylor & Francis, 1982.

[194] S. Whitaker. The method of volume averaging. Theory and applications of transport in porous media. *Kluwer Academic Publishers, Dordrecht, The Netherlands*, 1999.

[195] J. T. Wu, Y. Q. Dai, Z. W. Wang, and F. X. Liu. Study on the Heat Transfer in Granular Materials by DEM. *Advanced Materials Research*, 233-235:2949–2954, may 2011.

[196] S. Wu, K. Chau, and T. Yu. Crushing and fragmentation of brittle spheres under double impact test. *Powder Technology*, 143-144:41–55, jun 2004.

[197] B. Xu, P. Li, and C. L. Chan. Extending the validity of lumped capacitance method for large Biot number in thermal storage application. *Solar Energy*, 86(6):1709–1724, jun 2012.

[198] B. Xu and A. Yu. Numerical simulation of the gas-solid flow in a fluidized bed by combining discrete particle method with computational fluid dynamics. *Chemical Engineering Science*, 52(16):2785–2809, aug 1997.

[199] C. Yang and A. Nakayama. A synthesis of tortuosity and dispersion in effective thermal conductivity of porous media. *International Journal of Heat and Mass Transfer*, 53(15-16):3222–3230, 2010.

[200] Z. Yang and S. V. Garimella. Thermal analysis of solar thermal energy storage in a molten-salt thermocline. *Solar Energy*, In Press,, 2010.

[201] A. Ying, J. Reimann, L. Boccaccini, M. Enoeda, M. Kamlah, R. Knitter, Y. Gan, J. G. van der Laan, L. Magielsen, P. A. Di Maio, G. Dell'Orco, R. K. Annabattula, J. T. Van Lew, H. Tanigawa, and S. van Til. Status of ceramic breeder pebble bed thermo-mechanics R&D and impact on breeder material mechanical strength. *Fusion Engineering and Design*, 87(7-8):1130–1137, aug 2012.

[202] A. Y. Ying, H. Huang, and M. A. Abdou. Numerical simulation of ceramic breeder pebble bed thermal creep behavior. *Journal of Nuclear Materials*, 307-311:827–831, dec 2002.

[203] M. Yovanovich, S. Burde, and J. Thompson. Thermal Constriction Resistance of Arbitrary Planar Contacts with Constant Flux. In *AIAA 11th Thermophysics Conference*, 1976.

[204] P. Zehner and E. U. Schlünder. Wärmeleitfähigkeit von Schüttungen bei mäßigen Temperaturen. *Chemie Ingenieur Technik - CIT*, 42(14):933–941, jul 1970.

[205] P. Zehner and E. U. Schlünder. Einfluß der Wärmestrahlung und des Druckes auf den Wärmetransport in nicht durchströmten Schüttungen. *Chemie Ingenieur Technik - CIT*, 44(23):1303–1308, 1972.

[206] C. Zhang, A. Ying, and M. A. Abdou. FEM Modeling of Pebble Bed/Structural Wall Separation. *Fusion Science and Technology*, 68(3):612–617, oct 2015.

[207] H. Zhang and H. Makse. Jamming transition in emulsions and granular materials. *Physical Review E*, 72(1):011301, jul 2005.

[208] M. Zhang, K. Chu, F. Wei, and a.B. Yu. A CFD–DEM study of the cluster behavior in riser and downer reactors. *Powder Technology*, 184(2):151–165, may 2008.

[209] J. Zhao and T. Shan. Coupled CFD-DEM simulation of fluid-particle interaction in geomechanics. *Powder Technology*, 239:248–258, 2013.

[210] S. Zhao. *Multiscale Modeling of Thermomechanical Properties of Ceramic Pebbles*. PhD thesis, Karlsruhe Institute of Technology, 2010.

[211] S. Zhao, Y. Gan, and M. Kamlah. Spherical ceramic pebbles subjected to multiple non-concentrated surface loads. *International Journal of Solids and Structures*, 49(3-4):658–671, feb 2012.

[212] S. Zhao, Y. Gan, and M. Kamlah. Failure initiation and propagation of Li4SiO4 pebbles in fusion blankets. *Fusion Engineering and Design*, 88(1):8–16, jan 2013.

[213] S. Zhao, Y. Gan, M. Kamlah, T. Kennerknecht, and R. Rolli. Influence of plate material on the contact strength of Li4SiO4 pebbles in crush tests and evaluation of the contact strength in pebble–pebble contact. *Engineering Fracture Mechanics*, 100:28–37, mar 2013.

[214] Z. Zhou, S. B. Kuang, K. W. Chu, and a. B. Yu. Discrete particle simulation of particle–fluid flow: model formulations and their applicability. *Journal of Fluid Mechanics*, 661:482–510, aug 2010.

[215] Z. Zhou, A. Yu, and P. Zulli. Particle scale study of heat transfer in packed and bubbling fluidized beds. *AIChE Journal*, 55(4):868–884, apr 2009.

[216] H. Zhu, Z. Zhou, R. Yang, and A. Yu. Discrete particle simulation of particulate systems: Theoretical developments. *Chemical Engineering Science*, 62(13):3378–3396, jul 2007.

[217] Q. Zou and X. He. On pressure and velocity boundary conditions for the lattice Boltzmann BGK model. *Physics of Fluids*, 9(6):1591, 1997.